

A modeling framework to understand and optimize ultrasound neuromodulation

Présentée le 18 janvier 2021

à la Faculté des sciences et techniques de l'ingénieur
Chaire Fondation Bertarelli en neuro-ingénierie translationnelle
Programme doctoral en génie électrique

pour l'obtention du grade de Docteur ès Sciences

par

Théo LEMAIRE

Acceptée sur proposition du jury

Prof. D. Ghezzi, président du jury
Prof. S. Micera, Dr E. Neufeld, directeurs de thèse
Prof. M. Shapiro, rapporteur
Dr G. Hwang, rapporteuse
Prof. W. Gerstner, rapporteur

Acknowledgements

These four years have been a thrilling adventure. I entered this journey full of innocence, with the hope of making an impact my scientific field, and more generally in society. I now know that I have probably not changed the world, but I am nonetheless very grateful for this experience. I have learnt a lot about science and I now have a much better appreciation for its beauty and complexity. I have also learnt a lot about myself, and I am confident that I am ending this journey a more complete scientist and human being. For that I have many people to thank.

First off, I would like to express my gratitude to Prof. Silvestro Micera for giving me the opportunity to conduct my doctoral thesis in his lab. Four years ago, none of us knew much about the field of ultrasound neuromodulation, and I do not believe we could foresee the vast majority of challenges encountered throughout this journey (with among other things a civil war and a pandemic). However, his leadership brought me back on track when I got lost along the way, and his genuine optimism kept me going when I questioned the value of my work. I am also profoundly indebted to Dr Esra Neufeld, whose support has been of vital importance. At first glance, computational modeling can seem a straightforward endeavor carried out in the comfort of the numerical world. However, it also entails many unforeseen complexities, and a simple problem can quickly turn into an inextricable maze. When it seemed there was no solution, Esra used all of his expertise to devise, with an implacable consistency, a path towards the light. By contrast, when I wanted to take an easy route, he also reminded me that every modeling choice entails an associated set of assumptions that cannot be overlooked. Altogether, he has deeply contributed to making me the scientist I am today. Finally, I am immensely thankful to Drs Wulfram Gerstner, Grace Hwang and Mikhail Shapiro for their in-depth reviews of this thesis, as well as their valuable insights and constructive critiques during my oral defense.

Throughout this journey, I have also had the chance to work with very committed and talented students. All of them have contributed, in one way or another, to take this project a bit further. Hence, I would like to thank Simon Narduzzi, Valentin Bruttin, Mariia Popova, Justine Costaz and finally Elena Vicari, who has brilliantly embarked into this project and to whom I wish the best of luck on her own journey.

To everyone at the TNE lab: the pleasant, stimulating and human working environment that you have sustained during these years have made my work all the more enjoyable. I have met here some incredibly talented people, some of which have been a big inspiration for my past, present and future work. I regret that we did not find more opportunities to work together, but this has been compensated by rich social interactions, and I hope our paths will cross again in the future.

With all my heart, I would also like to thank my parents that have been by my side not only during these four years, but throughout my entire life up to this point. Your unconditional love and support have been an invaluable help throughout these years. I would also like to thank my friends for constantly reminding me, in very concrete ways, that there is much more to life than models and equations. Finally, I would like to thank Beatrice, who has been my first supporter for the last 3 years, has taught me to look ahead with curiosity rather than fear, and with whom I look forward to build a future.

Geneva, November 30th 2020

Abstract

Over the last decade, Low Intensity Focused Ultrasound Stimulation (LIFUS) has emerged as an attractive technology to modulate the activity of deep neural targets without invasive procedures. However, the underlying mechanisms by which ultrasonic waves can excite neurons are still unclear, which prevents a reliable and targeted application of the LIFUS technology and hinders its translation into clinical settings.

The Neuronal Intramembrane Cavitation Excitation (NICE) model hypothesizes that ultrasound excites neurons through the nucleation and resonance of nanoscale membrane structures (bilayer sonophores) that can alter membrane capacitance and induce depolarizing currents. The model predictions of LIFUS neuromodulatory effects match a wide range of empirical observations in the brain. However, because it neglects cellular morphology, the NICE model cannot address important questions on the interaction of ultrasonic waves with neural structures.

In this thesis, I propose several strategies to address these limitations, and to bridge the gap towards an experimental validation of this mechanism.

I begin with an introduction establishing the background, describing the state-of-the-art and issues plaguing the field of ultrasound neuromodulation, and motivating the global objectives that will be pursued throughout the thesis.

In a second part, I provide a mathematical description of the two pillars of the NICE model, namely a cavitation model describing mechanical membrane oscillations, and a point-neuron model describing the membrane electrical response. In doing so, I also discuss the inherent model assumptions, the potential implications for its validity range, and its sensitivity to key parameters.

In a third part, I present a novel multi-Scale Optimized Neuronal Intramembrane Cavitation (SONIC) model that alleviates the stiffness of the NICE model by numerically separating its two constituent time scales. I demonstrate how this approach drastically reduces computational costs and confers interpretability to LIFUS neuromodulatory effects in terms of effective membrane dynamics.

In a fourth part, I present a morphological expansion of the SONIC model (termed morphoSONIC) allowing to simulate intramembrane cavitation in a wide variety of realistic neuron models. With this framework, I investigate LIFUS neuromodulatory effects in peripheral nerve fibers. I predict that myelinated and unmyelinated axons can be distinctively and selectively recruited by LIFUS, thereby opening exciting avenues for peripheral neuromodulation.

In a fifth part, I present the results of a parallel collective effort to track down the mechanisms of ultrasound neuromodulation in sensory neurons extracted from the medicinal leech. We found that LIFUS can reliably induce spiking activity within an optimal intensity range, and identified common and differing response features between acoustically and electrically evoked spikes. This chapter ends with a discussion of the implications of our findings for the validity of the intramembrane cavitation hypothesis.

The achievements presented in this thesis provide an increased understanding of the mechanisms by which ultrasound modulates neural activity, as well as computational tools for their investigation.

Moreover, they pave the way towards the development of reliable modeling frameworks to simulate ultrasound neuromodulatory effects across spatial, temporal and functional scales, helping to propel LIFUS into the clinics.

Keywords

ultrasound neuromodulation, intramembrane cavitation, computational modeling, temporal multiscale, electrophysiological interpretability, morphological expansion, peripheral nerve stimulation, fiber-selective neuromodulation, medicinal leech, intracellular recording.

Résumé

Au cours de la dernière décennie, la stimulation par ultrasons focalisés de faible intensité (LIFUS) est apparue comme une technologie prometteuse pour moduler l'activité de structures neurales profondes sans recourir à des procédures invasives. Pour autant, les mécanismes sous-jacents par lesquels les ondes ultrasonores peuvent exciter les neurones sont encore abscons, ce qui empêche une application fiable et ciblée de la technologie LIFUS et entrave son transfert dans l'univers clinique.

Le modèle d'excitation neuronale par cavitation intramembranaire (NICE) émet l'hypothèse que les ondes ultrasonores excitent les neurones par la nucléation et résonance de structures membranaire nanométriques qui peuvent modifier la capacité de la membrane et induire des courants de dépolarisation. Les prédictions du modèle quant aux effets neuromodulateurs de la stimulation LIFUS concordent avec une vaste gamme d'observations empiriques dans le cerveau. Cependant, du fait qu'il néglige la morphologie cellulaire, le modèle NICE n'est pas en mesure de répondre à des questions essentielles sur l'interaction des ondes ultrasonores avec les structures neurales.

Dans cette thèse, je propose plusieurs stratégies pour résoudre ces limitations et combler le fossé vers une validation expérimentale de ce mécanisme.

Je commence par une introduction établissant le contexte, décrivant l'état de l'art et les enjeux du domaine de la neuromodulation par ultrasons, et motivant les objectifs globaux qui seront poursuivis tout au long de la thèse.

Dans une seconde partie, je propose une description mathématique des deux piliers du modèle NICE, à savoir un modèle de cavitation décrivant les oscillations mécaniques de la membrane, et un modèle de neurone ponctuel décrivant sa réponse électrique. Ce faisant, je discute également des hypothèses intrinsèques du modèle, les implications potentielles pour sa plage de validité, et sa sensibilité à des paramètres clés.

Dans une troisième partie, je présente un nouveau modèle de cavitation intramembranaire neuronale optimisé multi-échelles (SONIC) qui allège la rigidité du modèle NICE en séparant numériquement ses deux échelles de temps constitutives. Je démontre comment cette approche réduit considérablement les coûts de calcul et confère une interprétabilité quant aux effets neuromodulateurs de la stimulation LIFUS en termes de dynamique membranaire « efficace ».

Dans une quatrième partie, je présente une expansion morphologique du modèle SONIC (appelée morphoSONIC) permettant de simuler la cavitation intramembranaire dans une grande variété de modèles de neurones réalistes. Avec cet outil, j'étudie les effets neuromodulateurs de la stimulation LIFUS dans les fibres nerveuses périphériques. Je prédis que les axones myélinisés et non myélinisés peuvent être recrutés distinctivement et sélectivement par stimulation LIFUS, ouvrant ainsi des voies passionnantes pour la neuromodulation périphérique.

Dans une cinquième partie, je présente les résultats d'un effort collectif parallèle pour traquer les mécanismes de neuromodulation par ultrasons dans des neurones sensoriels extraits de la sangsue médicinale. Nous avons constaté que la stimulation LIFUS peut induire une activité neuronale de ma-

nière fiable dans une plage d'intensité optimale, et identifié les caractéristiques communes et différentes entre les réponses évoquées par stimulation acoustique et électrique. Ce chapitre se termine par une discussion sur les implications de nos résultats quant à la validité de l'hypothèse de cavitation intramembranaire.

Les avancées présentées dans cette thèse permettent de mieux comprendre les mécanismes par lesquels les ultrasons modulent l'activité neurale, et fournissent des outils de calcul pour leur investigation. De plus, ils ouvrent la voie au développement de cadres de modélisation fiables pour simuler les effets neuromodulateurs des ultrasons à travers les échelles spatiales, temporelles et fonctionnelles, aidant ainsi à propulser la technologie LIFUS dans l'univers clinique.

Mots-clés

Neuromodulation ultrasonique, cavitation intramembranaire, modélisation computationnelle, multiscale temporel, interprétabilité électrophysiologique, expansion morphologique, stimulation de nerfs périphériques, neuromodulation sélective de fibres, sangsue médicale, enregistrement intracellulaire.

Contents

Acknowledgements.....	i
Abstract.....	iii
Keywords.....	iv
Résumé.....	v
Mots-clés.....	vi
List of Figures	xi
Chapter 1 Introduction.....	1
1.1 The nervous system.....	1
1.2 Neuromodulation	2
1.2.1 Traditional approaches.....	2
1.2.2 Modern approaches.....	3
1.3 Ultrasound neuromodulation	4
1.3.1 The physics of ultrasound.....	4
1.3.2 Ultrasound parameters.....	7
1.3.3 Neuromodulation by ultrasound: a review of the literature.....	7
1.3.4 Candidate mechanisms	10
1.4 Advantages and current limitations of LIFUS.....	12
1.5 Objectives and outline of the thesis.....	14
Chapter 2 The Neuronal Intramembrane Cavitation (NICE) Model.....	16
2.1 Biomechanical part: the bilayer sonophore model	16
2.1.1 Steady-state system.....	16
2.1.2 Perturbation.....	18
2.1.3 Quasi-steady system.....	20
2.1.4 Dynamical system	21
2.1.5 Assumptions.....	34
2.1.6 Parameters.....	35
2.1.7 Numerical resolution.....	38
2.1.8 Dynamical behavior	38

2.1.9	Numerical stiffness and computational cost	41
2.1.10	Conclusions	41
2.2	Electrical part: the Hodgkin-Huxley formalism	41
2.2.1	Membrane equivalent electrical circuit	42
2.2.2	Ionic conductances	42
2.2.3	Dynamical behavior	43
2.3	Bi-directional coupling.....	44
2.3.1	Mechano-electrical coupling	44
2.3.2	Electro-mechanical coupling	45
2.3.3	Dimensional considerations.....	47
2.3.4	Differential system	48
2.4	Dynamical behavior	48
2.4.1	Typical behavior	49
2.4.2	Dependency on stimulus parameters	50
2.5	Predictive power	51
2.6	Conclusions	53
Chapter 3	The multi-Scale Optimized Intramembrane Cavitation (SONIC) model	55
3.1	Abstract	56
3.2	Introduction	56
3.3	Methods	57
3.3.1	The NICE electromechanical model	57
3.3.2	A multi-Scale Optimized Neuronal Intramembrane Cavitation (SONIC) model.....	60
3.3.3	Comprehensive characterization of neural responses	63
3.3.4	A multi-compartmental SONIC model to study spatially-distributed nanoscale interactions.....	63
3.4	Results	65
3.4.1	LIFUS-dependent effective variables.....	65
3.4.2	Model validation.....	67
3.4.3	The SONIC model boosts algorithmic efficiency by at least 3 orders of magnitude	69
3.4.4	Cell-type-specific excitability and spiking activity depends on multiple LIFUS parameters	71
3.4.5	Excitation thresholds are sensitive to LIFUS parameters and sonophore geometry	74
3.5	Discussion	75
3.5.1	Interpretability of the SONIC model.....	75

3.5.2	Effects of partial sonophore membrane coverage on neural responses	76
3.5.3	Influence of sonophore size and density on neural excitability	77
3.5.4	Relevance for experimental validation	78
3.5.5	Generalizability and integration	79
3.5.6	Advantage over other simplification strategies	79
3.6	Conclusion	80
Chapter 4	Intramembrane cavitation at the morphological scale	81
4.1	Abstract	82
4.2	Introduction	82
4.3	Methods	84
4.3.1	The NICE model	84
4.3.2	The SONIC model	85
4.3.3	A hybrid multi-compartmental, multi-layer electrical circuit	85
4.3.4	Myelinated and unmyelinated morphological axon models	88
4.3.5	Modeling of exogenous acoustic and electrical stimuli	90
4.3.6	Two-compartment SONIC benchmarks	91
4.4	Results	93
4.4.1	The SONIC paradigm enables accurate simulations in multi-compartmental axon models	93
4.4.2	Exogenous acoustic and electric sources produce normal field distributions along fibers	94
4.4.3	LIFUS modulates membrane capacitance to excite myelinated and unmyelinated axons	96
4.4.4	LIFUS can selectively recruit myelinated and unmyelinated axons	98
4.4.5	Resting membrane capacitance governs fiber excitability for long pulse durations	100
4.4.6	Pulsed LIFUS robustly modulates axon spiking activity	103
4.5	Discussion	105
4.5.1	Applicability of the SONIC paradigm in multi-compartmental models	106
4.5.2	Generalizability of the morphoSONIC framework	106
4.5.3	Comparison with empirical findings	107
4.5.4	Therapeutic implications	108
4.6	Conclusion	108
Chapter 5	Confrontation to the experimental setting	109
5.1	Abstract	110
5.2	Introduction	110

5.3	Results	111
5.3.1	Subthreshold responses to US stimulation.....	112
5.3.2	Spiking activity in response to US stimulation.....	114
5.3.3	Comparison between US- and EL-induced APs	116
5.4	Discussion.....	118
5.5	Materials and methods.....	120
5.5.1	Animals and preparation.....	120
5.5.2	Intracellular recordings.....	120
5.5.3	Ultrasound and electrical stimulation	121
5.5.4	Ultrasound calibration.....	121
5.5.5	Data analysis and statistics.....	122
5.6	Perspective: confrontation of model predictions to experimental data	122
5.6.1	Limitations of the experimental approach for model validation	122
5.6.2	Qualitative comparison: similarities and differences between modeling predictions and empirical data	123
5.6.3	Implications.....	124
Chapter 6	Discussion.....	125
6.1	Summary and discussion	125
6.1.1	Motivations for the initial choice of biophysical mechanism.....	125
6.1.2	Methodological achievement 1: substantial improvements of intramembrane cavitation models	125
6.1.3	Methodological achievement 2: expansion of model predictions to the morphological scale.....	126
6.1.4	Application: new predictions of LIFUS neuromodulatory effects on peripheral nerve fibers	126
6.1.5	Addressing the challenges identified in Chapter 1.....	127
6.2	Perspectives	127
6.2.1	Experimental validation and model refinement.....	127
6.2.2	Framework application to other neural targets.....	128
6.2.3	Towards multi-scale modeling.....	128
6.2.4	Towards hybrid, multi-physics modeling.....	129
6.2.5	Therapeutic perspectives	129
	Supplementary material for Chapter 5	130
	Bibliography	135
	Curriculum Vitae	149

List of Figures

- Figure 1. Schematic description of the resting bilayer sonophore structure.** (a) 3D view with the phospholipid head groups (red) and lipid chains (cyan), as well as the transmembrane proteins (green). (b). Transverse plane cross-section.17
- Figure 2. Schematic description of the perturbed bilayer sonophore structure.** (a) 3D view with the phospholipid head groups (red) and lipid chains (cyan), as well as the transmembrane proteins (green). (b). Transverse plane cross-section. 19
- Figure 3. Cross-sectional scheme illustrating the process of gas transport across the leaflet and radial diffusion into the fluid.** Arrows represent the unidirectional (blue) and radial (red) diffusion patterns. 22
- Figure 4. Typical behavior of the mechanical model.** Leaflet deflection, gas content, and pressures evolutions during the simulation of a sonophore with typical in-plane radius ($a = 32$ nm) with standard stimulation parameters ($F_{\text{drive}} = 500$ kHz, $A_{\text{drive}} = 0.5$ MPa). 39
- Figure 5. Impact of sonophore radius on cavitation dynamics.** (a) Leaflet deflection, gas content, and pressures evolutions during the simulation of a sonophore with small in-plane radius ($a = 15$ nm) and with standard stimulation parameters ($F_{\text{drive}} = 500$ kHz, $A_{\text{drive}} = 0.5$ MPa). (b) Idem, but with a large in-place radius ($a = 500$ nm). (c) Maximal membrane areal strain as a function of sonophore in-plane radius. 40
- Figure 6. Impact of sonophore tissue embedding on cavitation dynamics.** (a) Leaflet deflection, gas content, and pressures evolutions during the simulation of a sonophore (32nm in-plane radius) with small tissue embedding ($0.01 \mu\text{m}$), and with standard stimulation parameters ($F_{\text{drive}} = 500$ kHz, $A_{\text{drive}} = 0.5$ MPa). (b) Idem, but with a large tissue embedding ($100 \mu\text{m}$). (c) Maximal membrane areal strain as a function of sonophore tissue embedding.40
- Figure 7. Impact of stimulation parameters on cavitation amplitude.** Two-dimensional maps showing the maximal membrane areal strain during the cavitation of a sonophore (32 nm in-plane radius) as a function of acoustic frequency and amplitude. (a) Exposed sonophore. (b) Sonophore embedded in a $10 \mu\text{m}$ thick tissue layer. 41
- Figure 8. Hodgkin-Huxley formalism of a membrane equivalent electrical circuit with Sodium (Na), Potassium (K) and non-specific leakage (L) ionic conductances** (adapted from (Hodgkin and Huxley, 1952a)). 42
- Figure 9. Characteristic examples of point-neuron models using the Hodgkin-Huxley formalism.** (a) Unmyelinated peripheral axon responding to a very short intracellular current injection with a single action potential lasting. (b) Cortical regular spiking neuron responding to a sustained intracellular stimulus with a characteristic spike train. 44
- Figure 10. Relative variation of membrane capacitance as a function of leaflets deflection.**45
- Figure 11. Electrical pressure acting on the bilayer membrane as a function of charge density, for a sonophore at rest ($Z = 0$) and during an expansion phase ($Z = a$).** 47
- Figure 12. Typical response of a cortical regular spiking neuron to a continuous wave ultrasound stimulus (500 kHz, 50 kPa, 150 ms stimulus).** From top to bottom:

temporal profiles of acoustic pressure, membrane deflection, membrane capacitance, membrane potential and membrane charge density. Inset: zoom over a 4 μ s interval spanning two acoustic cycles..... 49

Figure 13. Dependency of the NICE model behavior of a cortical regular spiking neuron on continuous wave stimulation parameters (adapted from (Plaksin et al., 2014)). (a) Threshold acoustic intensity required to excite the neuron with a 30 ms stimulus, as a function of US frequency. (b, c) Threshold excitation intensity, and equivalent energy, as a function of stimulus duration ($f = 350$ kHz). (d) Number of detected spikes as a function of stimulus intensity and duration ($f = 350$ kHz). (e) Elicited firing rate as a function of stimulus intensity for various US frequencies from 250 kHz to 1 MHz. Response latency as a function of stimulus intensity for various US frequencies as in (e)..... 51

Figure 14. Comparison of NICE model predictions and *in vivo* brain stimulation measurements (King et al., 2013) (adapted from (Plaksin et al., 2014)). Success rates for eliciting motor responses versus US intensity at different frequencies (continuous stimulation for 40 000 acoustic cycles). Top: NICE model success rate predictions obtained by feeding the number of predicted spikes for a regular spiking (RS) neuron into a fitted sigmoid function. Bottom: success rate computed from measured hindlimb EMG activity upon sonication of the motor cortex in mice (experimental results from (King et al., 2013)). 52

Figure 15. Phase plane diagram of single-neuron responses predicted by the NICE model to varying US stimulation duty-cycle and intensity versus experimental cortical neuromodulation parameters (adapted from (Plaksin et al., 2016)). The phase diagram boundaries denote threshold intensities for US-mediated responses ($f = 0.69$ MHz, 500 ms stimulus) from excitatory regular spiking (RS, green dashed lines indicating 10 Hz and 1 kHz PRFs) and inhibitory low-threshold spiking interneurons (LTS, red dashed lines, changes only slightly for different PRFs, not shown). These boundaries separate the phase diagram into regions where either the inhibitory LTS neurons are activated alone (red, “suppression zone”) or the RS and the LTS neurons are jointly activated leading to net network stimulation (green, “activation zone”). The superposed bars indicate the experimental parameter ranges used in seven published cortical ultrasonic neuromodulation studies, color-coded according to the mediated responses: Ref. 1 ((King et al., 2013); bars with diagonal lines), Ref. 2 ((Yoo et al., 2011)), Ref. 3 ((Kim et al., 2015)), Ref. 4 ((Kim et al., 2012)), Ref. 5 ((Kim et al., 2014)), Ref. 6 ((King et al., 2014)), and Ref. 7 ((Tufail et al., 2011)). The excitation parameters reported for (King et al., 2013) were those that caused stimulation success rates significantly higher than their noise floor ($\approx 20\%$), with low-frequency CW intensities corrected for the expected formation of standing waves (Plaksin et al., 2014)..... 53

Figure 16. Description of the NICE electromechanical model. (a) Schematic representation of a bilayer sonophore structure (phospholipidic layers, inner cavity and surrounding transmembrane proteins) with the associated differential variables Z (apex deflection) and n_g (internal gas molar content). The local transmembrane potential V_m and electric pressure P_Q resulting from charge distributions on both sides of the membrane (green and red dots) are also indicated. (b) Electrical circuit representation of the local membrane dynamics, with the same transmembrane potential, a deflection-dependent capacitance C_m , and cell-type-specific Hodgkin-Huxley ionic conductances and reversal potentials. 58

Figure 17. Description of the model simplification and optimization steps. (a) Comparison of spatially integrated (green) and fitted approximation (dashed red) of intermolecular pressure profiles for a realistic range of deflections. (b) Explicit representation of the electrical system recasting, along with a comparison of the short-term evolution of the membrane potential (V_m) and charge density (Q_m) upon sonication (500 kHz, 100 kPa), showing remarkably different stiffness. (c) Schematic representation of the coarse-graining and precomputing pipeline. Mechanical simulations are run until periodic stabilization of Z and n_g , at which point the membrane capacitance C_m , transmembrane potential and voltage-gated rate constants are computed over the last acoustic cycle. The average value of V_m and rate constants are then stored into lookup tables. The process is repeated for various combinations of sonophore radii (a), US frequencies (f), acoustic pressure amplitudes (A) and membrane charge densities. (d) Schematic representation of the hybrid integration of the electrical system. Lookup tables are interpolated at a specific sonophore radius, US frequency and acoustic amplitude to yield 1D projected vectors of effective variables in the Q_m space, which are then used alternatively to interpolate effective variables during US-ON and US-OFF periods, respectively. 61

Figure 18. Schematic representation of the nanoscale multi-compartmental SONIC model. A bilayer sonophore of radius a (S , in light grey) is surrounded by a LIFUS-insensitive circular membrane patch (I , in dark grey) expanding between a and an outer radius $b = a/\sqrt{f_s}$, where f_s represents the sonophore coverage fraction of the total membrane area. Both sections are modeled electrically by voltage gated RC circuits, linked to ground in the extracellular medium, and connected to each other within a sub-membrane intracellular space of depth d_{eff} by a cylindrical resistor R_{SI} 64

Figure 19. Modulation of charge-dependent effective variables as a function of acoustic pressure amplitude, US frequency and intrinsic sonophore radius. Effective variables of an RS neuron are displayed as a function of membrane charge density, with a color code corresponding to the modulating variable at which they were derived (color bar depicted on top). The original, non-modulated variables (dashed black lines) are also depicted for comparison. (a) Dependence on acoustic pressure amplitude (32 nm radius sonophore, $f = 500$ kHz). (b) Dependence on US frequency (32 nm radius sonophore, $A = 50$ kPa). (b) Dependence on intrinsic sonophore radius ($f = 500$ kHz, $A = 50$ kPa). 66

Figure 20. Validation of the SONIC model against the detailed NICE model. Membrane charge density profiles from simulations with the detailed NICE model (light solid curves) and SONIC model (dark dashed curves) of different neurons under various LIFUS conditions are compared, along with derived spiking metrics (latency, firing rate and spike amplitude). (a) Top: comparison of charge density profiles of a RS neuron under CW sonication ($f = 500$ kHz) for sub-threshold ($A_T - 5$ kPa), threshold (A_T) and supra-threshold ($A_T + 20$ kPa) acoustic pressure amplitudes. Bottom: comparison of derived spiking metrics for varying supra-threshold pressure amplitudes. (b) Top: comparison of charge density profiles of a RS neuron under CW sonication at supra-threshold amplitude (threshold + 20 kPa) with $f = 20$ kHz and $f = 4$ MHz. Bottom: comparison of derived spiking metrics for varying carrier frequencies from 20 kHz to 4 MHz. (c) Top: comparison of charge density profiles of a RS neuron under CW sonication at supra-threshold amplitude (threshold + 20 kPa)

with 16 and 64 nm radius sonophores at $f = 500$ kHz. Bottom: comparison of derived spiking metrics for varying sonophore radii from 16 to 64 nm. (d) Top: comparison of charge density profiles of RS (blue) and LTS (red) neurons under pulsed-wave (PW) sonication ($f = 500$ kHz, $A = 100$ kPa, 100 Hz PRF) at 5% DC. Bottom: comparison of derived spiking metrics for varying duty cycles from 5 – 100%. (e) Top: comparison of charge density profiles of a LTS neuron under PW sonication ($f = 500$ kHz, $A = 100$ kPa, 5% DC) with PRF of 10 Hz, 100 Hz, 1 kHz and 10 kHz. Bottom: comparison of derived spiking metrics for varying PRF from 10 Hz to 10 kHz.⁶⁸

Figure 21. Quantification of the SONIC model acceleration. Comparison of computation times for 250 ms simulations under various LIFUS conditions, with the detailed NICE model (light gray) and SONIC model (dark gray, along with the fixed precomputation cost). (a) Comparison for CW simulations of the RS neuron at various sub- and supra-threshold acoustic amplitudes. The excitation threshold is also indicated (dashed vertical line). (b) Comparison for CW simulations of the RS neuron at various US frequencies with a supra-threshold amplitude (threshold + 20 kPa). (c) Comparison for CW simulations of the RS neuron with various sonophore radii, also at supra-threshold amplitude (threshold + 20 kPa). (d) Comparison for simulations of the RS (blue) and LTS (red) neurons ($f = 500$ kHz, $A = 100$ kPa, 100 Hz PRF) at various duty cycles. Dashed horizontal lines indicate characteristic durations. 70

Figure 22. Cell-type-specific LIFUS behavior maps. Two-dimensional behavior maps depicting the firing rate of RS and LTS neurons (32nm sonophore radius, 500 kHz US frequency) as a function of duty cycle and amplitude, for various PRF, along with threshold excitation amplitudes predicted from titration procedures (orange curves). Temporal profiles of membrane charge density (black) and effective membrane potential (gray) are also depicted for selected combinations of duty cycle and amplitude. (a) Behavior maps and selected profiles at 10 HZ PRF. (b) Maps and profiles at 100 Hz PRF. (c) Maps and profiles at 1 kHz PRF..... 72

Figure 23. Influence of sonophore radius and US frequency on excitation thresholds. Threshold excitation amplitude as a function of the duty cycle for an RS neuron (solid curves) and an LTS neuron (dashed curves), predicted through titration procedures. (a) Effect of sonophore radius ($f = 500$ kHz). (b) Effect of US frequency ($a = 32$ nm). 74

Figure 24. Distinct neuromodulatory effects of CW LIFUS ($f = 500$ kHz) on STN neurons at very low intensities, as predicted by the SONIC model. (a) Temporal evolution of firing rate during LIFUS, defined as in (Tarnaud et al., 2018a), for increasing acoustic amplitudes. (b) Neural responses elicited at three specific amplitudes showing the distinct modes of interaction. Corresponding spatial peak pulse averaged intensities, computed as in (Tarnaud et al., 2018a) but with $\rho_l = 1075$ kg·m⁻³, are shown for comparison. Electrical model parameters were taken from (Otsuka et al., 2004; Tarnaud et al., 2018a). 76

Figure 25. Effects of partial sonophore membrane coverage on neural responses. (a) Effective membrane potential (top) and charge density (bottom) of a RS neuron with 50% sonophore membrane coverage in response to CW sonication ($f = 500$ kHz, $A = 50$ kPa, 100 ms duration). Neural responses of a bilayer sonophore and its periphery computed with the nanoscale multi-compartmental SONIC model are depicted (solid dark and dashed light blue, respectively), as well the single response

obtained with a point-like SONIC model using a spatially averaged membrane capacitance (grey). (b) Threshold excitation amplitude as a function of sonophore membrane coverage, computed with both the point-like (grey) and multi-compartmental SONIC (dark blue) models, using titration procedures at $f = 500$ kHz (1 s stimulus).....77

Figure 26. Morphology, biophysics and incorporation of the SONIC paradigm in myelinated and unmyelinated axon models. (A) Schematic of the myelinated axon model morphology. (B) Electrical circuit representation of the membrane dynamics at the nodes of Ranvier. (C-D) Equivalent morphological and biophysical descriptions of the uniform unmyelinated axon. (E) Schematic diagram showing the incorporation of the SONIC paradigm into the axon models. 89

Figure 27. Evaluation of the SONIC paradigm accuracy in two-compartment benchmark models. (A) Schematic description of the two-compartment SONIC benchmark and associated divergence evaluation process. (B) Magnitude of the intra-cycle relative capacitance oscillation range as a function of stimulus frequency and pressure amplitude in myelinated and unmyelinated fibers, computed using axon-specific bilayer sonophore models at their respective resting charge density. White lines indicate cell-type-specific excitation threshold levels. (B) SONIC divergence (maximum RMSE between normalized charge density profiles resulting from SONIC and cycle-averaged NICE simulations) in a symmetric two-compartment passive model ($C_{m0} = 1 \mu\text{F}/\text{cm}^2$, $E_{\text{Leak}} = -70$ mV), as a function of the model's electrical time constants ($\tau_m = C_{m0}/g_{\text{Leak}}$, $\tau_{ax} = C_{m0}A_m/G_a$), for a typical US frequency (500 kHz) and sinusoidal oscillation drive ($\gamma = (1.2, 0.8)$). Acoustic periodicity, critical divergence level (1 mV), and fiber passive properties are indicated on the two-dimensional logarithmic color maps. Insets (i) and (ii) provide examples of NICE, cycle-averaged NICE, and SONIC charge density profiles for diverging conditions. Minimized maps evaluate SONIC divergence in the same model but for varying capacitance oscillation amplitudes and gradients, as well as varying US frequencies. (C) SONIC divergence in a two-compartment benchmark model of the myelinated axon for various combinations of oscillation pairs ($f = 500$ kHz, 1 ms stimulus). A critical divergence level (1 mV) is indicated on the color map. Insets (i-iii) provide examples of NICE, cycle-averaged NICE, and SONIC charge density profiles for various characteristic drive combinations. (D) Equivalent divergence evaluation in a two-compartment benchmark model of the unmyelinated axon (10 ms stimulus)..... 92

Figure 28. Qualitative nature of exogenous acoustic and electrical fields. (A) Normalized two-dimensional acoustic pressure amplitude distribution across the propagation plane computed upon sonication by a single-element planar transducer immersed in water-like medium, for various combinations of transducer radius and US frequency. A white line indicates the fiber's axis as considered in this work. (B) Normalized transverse pressure distribution measured at the transducer's focal distance, for the same combinations of transducer radius and US frequency. Dotted lines indicate FWHMs for each distribution. (C) FWHM of the pressure amplitude distribution along the fiber axis as a function of the transducer radius, for two characteristic US frequencies. (D) Normalized two-dimensional voltage distribution across a two-dimensional plane generated by a point-source electrode placed in a nerve-like anisotropic medium. A white line indicates the fiber's axis as

considered in this work. **(E)** FWHM of the extracellular voltage distribution along the fiber axis as a function of the electrode-fiber distance. 95

Figure 29. Typical responses of myelinated and unmyelinated axon models to a single US pulse. (A) Time profiles of effective membrane capacitance, effective membrane potential, and effective membrane charge density across compartments during a typical response of a myelinated axon to a 1 ms sonication (500 kHz frequency, 5 mm-wide Gaussian pressure distribution aligned on the fiber with a spatial peak of 120 kPa). **(B)** Equivalent time profiles during the typical response of an unmyelinated axon to a 10 ms sonication (identical pressure distribution as in **(A)**). **(C)** Quantification of the membrane and axial currents contributions to the first 5 mV of normalized charge build-up in the fiber central compartment. **(D)** Equivalent quantification for the response of the unmyelinated axon's central compartment. 97

Figure 30. Comparison of strength-duration curves of myelinated and unmyelinated axons upon electrical and ultrasonic stimulation. (A) SD curves of representative myelinated (10 μm diameter, in orange) and unmyelinated (0.8 μm diameter, in blue) axons, depicting the threshold absolute peak extracellular voltage required to elicit fiber excitation as a function of pulse duration, for a characteristic 5 mm wide Gaussian extracellular voltage distribution. Rheobase and chronaxie values of each curve are indicated, as well as distinct areas of fiber recruitment. **(B)** SD curves of representative myelinated and unmyelinated axons for Gaussian extracellular voltage distributions of varying widths (1 to 10 mm). Arrows indicate the translation of the chronaxie point in the SD space for increasing stimulus width. **(C)** SD curves both fiber types of upon stimulation with a characteristic voltage distribution, for varying fiber diameters within the physiological range of each population (myelinated: 5 to 20 μm , unmyelinated: 0.2 to 1.5 μm). Arrows indicate the translation of the chronaxie point in the SD space for increasing fiber diameter. **(D)** SD curves of representative myelinated and unmyelinated axons, depicting the threshold peak acoustic pressure amplitude required to elicit fiber excitation as a function of pulse duration, for a characteristic 5 mm wide Gaussian acoustic pressure distribution and US frequency ($f_{\text{US}} = 500 \text{ kHz}$), using typical values of sonophore radius ($a = 32 \text{ nm}$) and sonophore coverage fraction ($f_s = 80 \%$) in the model's compartments. SD curves using equivalent "node" models located under the stimulus peak are also indicated (light blue and orange curves), as well as rheobase and chronaxie values of each curve, and distinct areas of fiber recruitment. **(E)** SD curves of representative myelinated and unmyelinated axons with typical US frequency and sonophore parameters for Gaussian pressure distributions of varying widths (1 to 10 mm). **(F)** SD curves both fiber types with typical US frequency, pressure distribution and sonophore parameters, for varying fiber diameters within the physiological range of each population. **(G)** SD curves of equivalent "node" models of both fiber types with typical sonophore parameters and pressure distributions for varying US frequencies (20 kHz to 4 MHz). **(H)** SD curves of "node" models with typical pressure distribution, US frequency and sonophore coverage fraction for varying sonophore radii (16 to 64 nm). **(I)** SD curves of "node" models with typical pressure distribution, US frequency and sonophore radius, for varying sonophore coverage fractions (50 to 100 %). 99

Figure 31. Underlying mechanisms of distinct rheobase excitabilities in myelinated and unmyelinated axons. (A) Effective capacitance variations regulate sub-threshold charge build-ups. From left to right: LIFUS-triggered, exponentially converging

charge build-ups in myelinated and unmyelinated “node” models for various sub-threshold pressure amplitudes. Normalized steady-state charge build-ups for each “node” model as a function of sub-threshold pressure amplitude, computed from full membrane simulations (plain lines) and estimated from the sole relative variation in effective membrane capacitance (dashed lines, passive circuit approximation). Detailed intra-cycle oscillation profiles of membrane capacitance and membrane deflection for each fiber type at their respective threshold levels. **(B)** Charge-dependent electrical and molecular pressure regulate threshold sonophore kinematics. From left to right: detailed profiles of internal pressure forces regulating sonophore cavitation during an acoustic period, driven by cell-type-specific threshold acoustic pressures. Detailed profiles of electrical and molecular pressures in both fiber types along the physiological range of membrane deflection. **(C)** Schematic diagram showing the causal chain of influence by which resting membrane capacitance affects charge-dependent internal pressures, sonophore kinematics, effective capacitance variations, and ultimately rheobase excitability. 101

Figure 32. Modulation of spiking activity by pulsed sonication in myelinated and unmyelinated axons. **(A)** Average firing rate elicited in each axon type by a Gaussian acoustic pressure distribution covering one fifth of the fiber length, using default sonophore parameters ($a = 32\text{nm}$, $f_s = 80\%$) and US frequency ($f_{US} = 500\text{ kHz}$), for various pulse durations and pulse repetition frequencies. Dashed lines indicate half, one time and double of the stimulus rate. Detailed spatiotemporal profiles of membrane charge density are indicated for characteristic spiking regimes of each fiber type, along with detailed profiles of the stimulus spatial distribution (vertical) and temporal application (horizontal). **(B)** Average firing rate (normalized by pulse repetition frequency) elicited in each fiber type as a function of duty cycle and peak acoustic pressure amplitude for cell-type-specific pulse repetition frequencies yielding “robust” and “sensitive” spiking behaviors. Numbers on the color maps indicate characteristic regimes of normalized firing rate. 104

Figure 33. Experimental setup. a) Illustrative scheme of the setup. b) Leech dissection and ganglia chain exposition (1). On the top right corner, a detail of the extracted leech ganglion pinned onto the PDMS substrate (2). c) Focus on the Petri dish with a pinned ganglion (1) and the glass capillary containing the Ag/AgCl electrode for intracellular recording (2). d) The Petri dish with the pinned ganglion was positioned on top of the experimental setup (1). The setup included a US transducer (2) immersed in a tank (3) full of degassed deionized water used for US, and an electrophysiology setup. A micromanipulator (4) allows for fine positioning of the electrodes on ganglion surface. In this configuration two electrodes (5.1 - 5.2) are connected to the electrophysiology setup for recording. A light source (6) and an optical microscope (7) are used for cell identification and impalement. e) Temporal protocol of US: DC 5% (blue), T-on is 5 ms, T-off 95 ms; DC 50% (yellow), T-on 50 ms, T-off 50 ms; DC 100% (brown), T-on 100 ms. The tone burst duration is equal to T-on in case of pulsed stimulation and the pulse repetition period (PRP) is 100 ms; the stimulation duration (SD) is of 300 ms for the 3 temporal protocols. Each stimulation (SD 300 ms) is repeated 3 times during a recording session with an inter stimulation interval (ISI) of 20-30 s. In the inset, temporal evolution of US (violet); transducer central frequency is 490 kHz..... 112

Figure 34. US parameters and membrane depolarization. a) Definition of response and baseline interval for each DC; in case of 100% DC, baseline and response time interval is 300 ms; in case of 5% and 50% DC, baseline and response duration are equal to tone burst duration for each cycle. The membrane potential variation ΔV was defined as the difference between the membrane potential median value during stimulus onset (r_1 in the figure) and its median value during the preceding baseline (b_1 in the figure). b) Violin plot (Hintze and Nelson, 1998) of baseline variation, defined as the difference between membrane potential pre and post stimulus onset (median B_{i+1} - median B_i), for each pressure amplitude and DC (95 ms at DC 5 %, 50 ms at DC 50 %, 300 ms at DC 100 %). Asterisks indicate post-hoc significant inter-DC differences ($p < 0.05$). c) Membrane voltage variation over the three cycles at DC 5% and 50% for pressure 12kPa. d) Membrane potential variation for each pressure amplitude and DC. e) Median membrane voltage variation for each stimulation protocol setting. f) Stimulation intensity for each experimental protocol. g) Median membrane potential response as a function of the intensity. Color code in f) and g) indicates intensity binning: I_{spta} is binned into five groups: very low $\leq 0.5 \text{ mW/cm}^2 < \text{low} \leq 2.5 \text{ mW/cm}^2 < \text{medium} \leq 5 \text{ mW/cm}^2 < \text{high} \leq 10 \text{ mW/cm}^2 < \text{very high}$, with respectively 101, 110, 108, 97, 73 recorded traces.113

Figure 35. US parameters and firing activity. a) Example of N cell intracellular membrane potential (green) during US (red diamond) or EL (grey triangle) stimulations. Red line indicates US trigger. Black line indicates EL stimulation trigger. The response to EL stimuli is recorded to compare the spikes characteristics with the US induced and to verify cell health. A time interval of 20-30 s between consecutive stimulations allows the cell to recover. b) Zoom of the US trigger signal (red) and the EL triggered signal (black); recorded membrane potential (green). c) Success rate as a function of the intensity, binned into 5 groups. The considered spike detection time window for each stimulation lasted 400 ms from the stimulus onset (stimulus duration of 300 ms + 100 ms post stimulation). d) Distribution of latency as a function of DC of all US-triggered spikes. e) Distribution across neurons of intensity associated to the first response. Intensity ranges are defined as in Fig. 2f: very low $\leq 0.5 \text{ mW/cm}^2 < \text{low} \leq 2.5 \text{ mW/cm}^2 < \text{medium} \leq 5 \text{ mW/cm}^2 < \text{high} \leq 10 \text{ mW/cm}^2 < \text{very high}$115

Figure 36. AP features in US and EL stimulation. a) Shape of APs triggered by US (left 5 spikes) and EL (right 3 spikes) stimulation extracted from the trace in Fig. 3a. Left US plot shows definitions of amplitude (from peak to subsequent minimum value) and duration of early repolarization (width at half amplitude of declining phase). b) Left: median, interquartile range and dispersion of first spikes triggered by US (orange), following spikes triggered by USs (brown), the union of the two sets (red), and spike triggered by EL stimulation (grey). Right: comparison between the probability distributions of the durations of the different sets of spikes. Subplot in the center indicates significant differences between distributions. c) Analysis of the distributions of the amplitudes of the four spike categories defined in b). d) Analysis of the distributions of the amplitude/duration ratios of the four spike categories defined in b).117

Figure S1 (related to Figure 34). Estimation of observation time and membrane potential baseline variations. a) Analysis of the EL stimulations to estimate the probability of spike detection after the end of the stimulus; only few cells showed spikes during the considered post stimulation time interval (100 ms). The dotted line

corresponds to the end of EL trigger. Time measured from 100 ms after trigger end to preceding spike peak. b) Baseline variation on EL stimulation, defined as difference between membrane potential post and pre-current onset. A time window of 100 ms is considered for post and pre-stimulation baseline analysis. Membrane voltage after EL stimulation is lower on the considered observation window.130

Figure S2 (related to Figure 33). US calibration setup. a) left: calibration into the experimental setup; right: free field calibration setup. b) Scheme of the calibration measurement system. c) Detailed block representation of US/acquisition setup.131

Figure S3 (related to Figure 33). US calibration results. a) 2D spatial mapping of normalized peak-to-peak pressure produced by the transducer in free field. Transducer focus is at 140 mm. Asterisk indicates the distance between the transducer and target employed during experiments, i.e. 165 mm. b) On left, hydrophone root-mean-square pressure (P_{rms}) signal vs driving voltage; low pressure calibration of the transducer shows that pressure is linear with the input voltage. The signal measured in the experimental setup is attenuated with respect to the free field condition. On right, calculation of spatial-peak pulse-average intensity, I_{sppa} ; free field (blue), experimental setup (red). The measure has been conducted at 165 mm from transducer surface. c) Example of time variation of the pressure signal in free-field (blue) and experimental setup (red). It can be observed that the second is attenuated and a post stimulus onset effect is introduced by the experimental setup.132

Figure S4 (related to Figure 35c). Action potential success rate as a function of acoustic intensity (binned into 5 groups) and of US stimulus onset and offset. Blue: AP success rate during US stimulus (i.e., during a time window of 300ms following US stimulus onset). Red: AP success rate during a window of length equal to the stimulus duration (i.e., 300 ms) but preceding the stimulus onset. Yellow: AP success rate during a window of length equal to the stimulus duration (i.e., 300 ms) but following the stimulus offset.....133

Figure S5 (related to Figure 34 and Figure 35). Comparison between responses to US of P and N mechanoreceptors. a) Left: Same as Figure 2e for P cells stimulation. Empty square indicates that no cell responded to that particular parameters combination. Right: Figure 2e rescaled for clearer comparison. b) Comparison of average membrane potential deflection for P and N cells across stimulation intensities. c) Same as Figure 3c, displaying spike responses from P and N cells.134

Chapter 1 Introduction

1.1 The nervous system

The nervous system is at the core of human life. From its first appearance in early metazoans, this system has evolved into a gigantic, interconnected ensemble of cells that enables cognition, learning, behavior, and regulates all major processes in the human body.

The nervous system is made up of specialized cells – called neurons – that can receive, integrate and transmit information via specific connections called synapses. Neurons are described as *electrically excitable cells*, that is, they respond to changes in their surrounding electrical field by generating an electro-chemical pulse called *action potential*. This biological process relies on the maintenance of a voltage difference between their intracellular and extracellular environment, called *membrane potential*. A disruption of this membrane potential by a physiological or external agent triggers the transient opening of specific transmembrane proteins – called *ion channels* – allowing charged particles on either side of the membrane to move down their electrochemical gradient, and inducing a sudden rise in membrane potential followed by a repolarization. Once generated, the action potential propagates in a wave-like fashion along the neuron membrane with little / no attenuation, and can therefore travel across large distances ($d > 1$ m) at relatively high speeds (up to more than 100 m/s). Because of their efficient signaling mechanism, neurons have progressively evolved into an organized network – the nervous system – that constitutes the predominant communication system of the human body.

Anatomically speaking, the mammalian nervous system can be divided into two main parts: the central nervous system (CNS) comprises the brain and the spinal cord, and the peripheral nervous system (PNS) covers all the nerves and ganglia that project from central structures towards limbs and organs. Together, these two systems collaborate to regulate a wide range of biological functions. Motor pathways innervate muscles to enable the production of synchronized movements. Sensory pathways provide the necessary feedback that shapes our perceptions (vision, hearing, smell, taste and touch), and can also act as protective alarm systems (nociceptive pathway). Other areas of the cerebral cortex enable higher cognitive functions (reasoning, speaking and remembering amongst others), while the cerebellum shapes many of our emotions. Finally, the autonomic nervous system (ANS) – a specialized division of the PNS – innervates most of our internal organs in order to regulate their activity, including cardiac, respiratory, digestive and urinary functions, as well as sexual arousal.

Unfortunately, this well-oiled machinery sometimes fails to function properly. Neurodegenerative diseases, such as Alzheimer's disease, amyotrophic lateral sclerosis (ALS), Huntington's disease or Parkinson's disease to name but a few, induce a progressive degeneration of neurons that can alter a variety of cognitive and motor functions. Traumatic injuries such as stroke, traumatic brain injury (TBI) and spinal cord injury (SCI), damage nervous structures and / or disrupt neural communication pathways. Abnormal patterns of neuronal activity can induce neurological disorders such as epilepsy, but also have a role in a wide variety of other conditions such as chronic stress, diabetes, obesity, cardiovascular and pulmonary diseases. These disorders impair our ability to move, think, reason, feel, or more generally to "function" correctly, and can lead to life-threatening conditions. Moreover, because most of these disorders strike primarily in mid to late life, their incidence is expected to grow as the world's population ages.

Traditional therapeutic approaches to treat these conditions have historically involved the use of drugs and / or surgical interventions. Yet, despite undeniable efficacy, both of these approaches suffer from drawbacks and limitations. Drugs travel through the entire circulatory and often have limited specificity, leading to undesired side effects. Surgical interventions are highly invasive, often irreversible, and open the door to infections and inflammatory reactions. Hence, alternative approaches are highly desirable.

1.2 Neuromodulation

In order to tackle the issues raised above, the last decades have seen the development of alternative technologies aiming to dynamically interface with the nervous system and modulate neuronal activity in order to restore specific functions, while limiting invasiveness and associated risks. This general therapeutic approach, referred to as *neuromodulation*, finds its origins in the 1950s, with the advent of deep brain electrical stimulation (DBS) for treatment of chronic pain (Croft, 1952). It has since then branched into a number of declinations, which we will attempt to summarize here.

1.2.1 Traditional approaches

Historically, the central nervous system has been the primary target for neuromodulation, with DBS as main therapy. The development of modern DBS is attributed to Alim Benabid, who discovered that he could improve symptoms of Parkinson's disease by stimulating electrically the basal ganglia (Benabid et al., 1987). Since then, DBS has been used to treat obsessive compulsive disorder (Abelson et al., 2005) and Tourette's syndrome (Baldermann et al., 2016), and recent works suggest that DBS could be beneficial for many mental health conditions, such as schizophrenia and depression (Schlaepfer and Bewernick, 2013). In the last decades, electrical stimulation of the motor and sensory cortex through intra-cortical electrodes has also been investigated to restore the sense of touch in lower and upper limbs (Callier et al., 2020; Tomlinson and Miller, 2016).

In parallel, several research groups studying motor impairment disorders such as spinal cord injury (SCI) and stroke proposed that electrical stimulation of the PNS and muscles could restore the lost motor function (Bhadra and Peckham, 1997). Several studies have demonstrated the potential of intra-neural electrodes as well as multi-contact cuff electrodes to elicit stable, accurate and functional movement responses (Badia et al., 2011a; Wurth et al., 2017). Conversely, other groups have relied on the non-invasive stimulation of muscles – referred to as Functional Electrical Stimulation (FES) – to reliably induce movements (Crema et al., 2018; Sharif Razavian et al., 2018), although this technology is limited by the significant muscle fatigue it generates (Ibitoye et al., 2016).

Complementarily, electrical stimulation has also been used for the restoration of sensation in amputees and patients suffering from sensory deficits (Micera and Navarro, 2009). These approaches have been very successful to restore tactile sensations (Raspopovic et al., 2014), and recent efforts have been dedicated to the design of less invasive strategies and the encoding of an enriched, multi-modal sensory feedback in upper and lower limb amputees (D'Anna et al., 2019; Mendez et al., 2020; Petrini et al., 2019; Valle et al., 2018).

In parallel, several groups have investigated the potential of spinal cord stimulation (SCS) to restore motor and sensory functions, exploiting the ability to engage motor pathways pre-synaptically through the spinal circuitry in order to induce movements (Capogrosso et al., 2013). This approach has proved successful in restoring voluntary locomotion after SCI (Wagner et al., 2018), but can also enable specific upper limb movements in tetraplegic patients (Sharpe and Jackson, 2014).

Finally, the last few years have also seen the emergence of the concept of *bioelectronic medicine*, i.e. use of stimulating and sensing technologies targeting the autonomic nervous system to regulate biological processes and treat diseases. These technologies are expected to rely on miniature devices (so-called *electroceuticals*) that can use electrical, mechanical, or light stimulation to affect electrical signaling within the neural circuits that regulate the body's organs and functions (Famm et al., 2013). Such interfaces could target specific nerve fibers or brain circuits in order to treat a variety of conditions, such as epilepsy, chronic stress, diabetes, obesity, cardiovascular and pulmonary diseases, neurological and neuro-motor disorders, and pathologies resulting from chronic inflammation (e.g. rheumatoid arthritis) (Famm et al., 2013; Koopman et al., 2016). This highly promising, modern approach to medicine is currently the object of tremendous efforts to understand and map the neural circuits involved in different pathological pathways, and is likely to become a major growth industry in the decades to come.

Overall, most clinical neuromodulation therapies currently available make use of electrical stimulation technologies. Yet, despite their apparent maturity, these technologies are not perfect, as they often involve invasive and risky surgical procedures, as well as implanted devices that typically induce a foreign body response (FBR), thereby deteriorating the communication with neighboring neural structures over time, and the resulting treatment efficacy (Anderson, 2001; Badia et al., 2011b; Christensen et al., 2014; Leventhal et al., 2006; Wurth et al., 2017).

1.2.2 Modern approaches

In the last decades, several alternative technologies have emerged with the aim to overcome the drawbacks raised above. Some approaches aim at minimizing the bulkiness and tethering of stimulation devices to reduce their impact on biological tissue and ensure a better bio-integration. A notable effort in this direction is the development of miniature, wireless devices relying on piezoelectricity to generate or record local electric fields and therefore probe neural circuits (Johnson et al., 2018; Seo et al., 2013). However, those technologies still require much development before clinical use. Other approaches, such as transcranial magnetic stimulation (TMS) and transcranial direct current stimulation (tDCS), rely on the delivery of electromagnetic fields through the intact skull in order to modulate cortical activity (Klompai et al., 2015; Stagg and Nitsche, 2011), with existing clinical applications in the treatment of drug-resistant depression (Brunoni et al., 2016; Gaynes et al., 2014) as well as for rehabilitation after stroke (Dionísio et al., 2018). However, they suffer from limited spatial selectivity and cannot efficiently target deep brain regions. Notably, a recent technique involving temporally interfering electric fields has shown promise for the noninvasive modulation of deep neural circuits (Grossman et al., 2017), but uncertainties remain about its working principles and possible side effects. In contrast, techniques such as optogenetics (Boyden, 2011) and magneto-thermal neuromodulation (Chen et al., 2015), rely on the targeted genetic expression of transmembrane proteins to sensitize specific neurons to a new form of energy that can be delivered from a remote source without affecting surrounding tissue, thereby improving anatomical and functional selectivity. However, the intrinsic need for genetic manipulation is a major hurdle when it comes to the clinical adoption of these technologies.

In consequence, efforts are still ongoing to design an optimal neuromodulation technology that can elicit a precise, spatially and functionally selective modulation of neural activity, while limiting invasiveness and avoiding genetic manipulation.

1.3 Ultrasound neuromodulation

In the last decade, an increasing number of groups have started investigating the potential of *Low-Intensity Focused Ultrasound Stimulation* (LIFUS) as a noninvasive neuromodulation modality, following promising *in vitro* results (Tyler et al., 2008). In fact, acoustic energy entails many desirable physical properties that make it an optimal source of interaction with biological tissue, which are already exploited in the clinical setting for ablation therapies and diagnostic imaging (Escoffre and Bouakaz, 2016; Ghanouni et al., 2015; Hynynen et al., 2004). As such, it appears as an alternative stimulation modality that could potentially overcome the obstacles encountered by classical electrical stimulation.

Here, we will first describe the fundamental physical principles underlying the potential of ultrasound (US) for therapeutic applications, and provide an overview of past and present investigations that have exploited this form of energy to modulate neural activity.

1.3.1 The physics of ultrasound

1.3.1.1 Acoustic waves

Sound is defined as the mechanical disturbance of a medium such that small parts of that medium (i.e. particles) perform oscillatory movements. This disturbance process does not involve any mass transfer, and originates from a local change in the stress or pressure field within the medium. Mechanical energy is “embedded” in the medium in the form of elastic strains and vibrations of its constitutive particles, as they are displaced from their equilibrium position. Due to the medium’s elasticity, the displacement of a particle induces elastic forces that tend to drive the particle back to its initial position. Through this oscillation and the interaction between different particles, acoustic energy can propagate across the medium in the form of a wave, referred to as an *acoustic wave*. Therefore, sound requires a medium to travel (be it a gas, liquid, or solid) but cannot propagate in vacuum.

Acoustic waves propagate as a series of compressions and rarefactions of the medium, thereby dynamically modulating the local pressure at a frequency f , known as the *carrier frequency*. Waves with frequencies between 20 Hz and 20 kHz can be perceived by the human ear and are designated as (audible) sound, while those with higher frequencies are commonly referred to as *ultrasound* or *ultrasonic waves*.

Acoustic waves can also be classified according to the relative direction of particle displacement with respect to the direction of wave propagation. *Longitudinal waves* propagate with a particle motion that is parallel to the wave propagation direction, while *transverse* (or *shear*) *waves* travel with a particle displacement perpendicular to the wave propagation axis. Interestingly, longitudinal waves propagate extremely well through liquids and soft tissues (such as the brain, nerves and vessels), and are thus ideally suited for a wide range of biomedical applications. In contrast, standing waves are damped out rapidly soft tissues but propagate efficiently through hard tissue like bone, and must therefore be accounted for in applications involving penetration through the skull.

1.3.1.2 Propagation properties

Intensity, speed and wavelength. A traveling acoustic wave carries kinetic energy. This energy is commonly described in terms of intensity I , which is defined as the energy propagating through unit area per unit time, measured in W/m^2 . For a sinusoidal acoustic wave, that intensity is calculated as:

(1)

$$I = \frac{p^2}{2\rho c}$$

where p is the peak pressure amplitude (in Pa), ρ is the medium's density (in kg/m³) and c is the speed of sound in the medium. The latter is determined from the medium's density but also from its compressibility κ (i.e. the amount of volume change brought by a pressure variation):

(2)

$$c = \sqrt{\frac{1}{\kappa\rho}}$$

In other words, the more compressible and the denser the material, the slower acoustic waves propagate in it. Interestingly, soft biological tissues have densities and acoustic compressibilities very close to those of water, resulting in similar propagation speeds ($c \approx 1500$ m/s).

The oscillation frequency and propagation speed of an acoustic wave together determine its wavelength λ (in m), computed as:

(3)

$$\lambda = \frac{c}{f}$$

This wavelength describes the distance between two consecutive points of corresponding acoustic phase in the propagation medium. For a typical ultrasound frequency of 1 MHz and inside a water-like soft tissue, this acoustic wavelength is in the order of the millimeter.

Absorption and attenuation. As an acoustic wave propagates, some of its kinetic energy is “absorbed” by the medium and converted into thermal energy. This absorption process results from distinct mechanisms known as *viscous losses*, *heat conduction losses*, and *relaxation losses*, which will not be detailed here. Together, these effects contribute to acoustic attenuation, i.e. the exponential decrease of the acoustic pressure wave amplitude as it propagates through a medium.

Reflection, refraction, diffraction and scattering. As it reaches the interface between two media with different acoustic properties, an acoustic wave behaves similarly to a ray of light impinging on an optical discontinuity: some of the acoustic energy is reflected (*reflected wave*) at the interface and propagates back towards the “first” medium, while the remaining energy is transmitted through the acoustic barrier into the “second” medium (refracted wave). This refraction process is accompanied by a change in intensity and propagation direction of the wave that depend on the incident angle with respect to the interface, and from differences in acoustic properties of the two media. Additionally, as they impinge upon an interface with finite length or small openings, acoustic waves tend to diffract, i.e. bend around the barrier's edges and change their trajectories. The latter phenomenon is amplified when the acoustic wavelength approaches the order of magnitude of the barrier/opening dimensions.

Those principles do not only apply at well-defined acoustic barriers between two media, but also in inhomogeneous medium, i.e. medium that contains particles of differing acoustic properties. In that case, acoustic waves are also scattered, i.e. reflected in various directions of space or delayed in phase, as a result of the multiple acoustic discontinuities encountered along their progression. This phenomenon is used as a cornerstone mechanism in diagnostic ultrasound, where biological tissue can be imaged by processing the backscattering patterns of impinging acoustic waves.

Interference and standing waves. As two acoustic waves collide in space, they interact either constructively or destructively depending on their relative phases. *Constructive interference* occurs when the two waves are *in phase* and interact to enhance each other, resulting in a combined wave of higher

amplitude. Conversely, *destructive interference* occurs when two waves are *out of phase* and therefore cancel each other's energy.

A direct consequence of the interference phenomenon are *standing waves*. When a wave propagates through a confined medium, e.g., a medium surrounded by strong reflectors, it interferes with its own reflection. If the distance between the wave source and the reflector is a multiple of $\lambda/2$, this interference yields a motion pattern which appears spatially-still but with a temporally varying amplitude.

The focused ultrasound technology leverages many of the attracting physical properties of acoustic waves in order to control the delivery of mechanical energy at a precise spatial location in biological tissue (Ghanouni et al., 2015; Kyriakou, 2015). Specifically, by optimizing the geometry of the ultrasonic device, acoustic waves can be shaped into a concentric wave-front where each wave propagates efficiently through soft tissue and converges towards a common point where they can interact constructively, thereby concentrating acoustic energy inside a small focal volume, referred to as *acoustic focus*. Because it relies on the local positive interference of waves propagating in different directions, the size of this acoustic focus is on the order of magnitude of the acoustic wavelength, i.e. 100 μm to 1 mm for typical ultrasonic regimes used in neuromodulation applications (Rabut et al., 2020).

1.3.1.3 Physical effects

Acoustic waves interact with the medium in which they propagate through particle motion and pressure variations. This interaction yields a number of different physical effects, which are summarized below.

Thermal effects. Thermal effects are mostly related to the medium's temperature increase, due to the conversion of acoustic energy into heat, discussed above. They only occur at high acoustic intensities that are typically not used in ultrasound neuromodulation applications.

Acoustic radiation and acoustic streaming. At low oscillation amplitudes, both the acoustic pressure and the particle velocity of a wave can be assumed to follow a sinusoidal variation over time, meaning that changes induced during the compression phase reverse entirely during the rarefaction phase. However, at higher amplitudes, nonlinear acoustic effects induce an imbalance, where a higher positive pressure is observed during the compression phase than negative pressure during the rarefaction phase, thereby resulting in a net positive pressure over an acoustic cycle. This positive resultant, referred to as *radiation pressure*, tends to push the medium – or the interface between two media – along the direction of acoustic propagation, resulting in translational and / or angular displacements. Under a linearized regime, radiation force F_{rad} (in N/m^3) is calculated as:

(4)

$$F_{rad} = \frac{2\alpha I}{c}$$

where α is the medium's absorption coefficient (in Np/m). It follows that the amplitude of the radiation force is proportional to the intensity of the acoustic wave. More interestingly, it is also proportional to the absorption coefficient of the medium, a quantity known to increase with ultrasound frequency. Hence, radiation force is enhanced at higher frequencies.

Notably, in a fluid-like medium, this generated radiation force can also set the fluid into motion, a phenomenon referred to as *acoustic streaming*. This motion can be steady (*jet flow*) and/or circulatory (*vortex*), and can induce sufficient velocity gradients to perturb or damage the medium.

Acoustic cavitation. Cavitation occurs when a medium containing microscopic gaseous bodies (or *microbubbles*) is exposed to ultrasound. Upon perturbation by an oscillating acoustic pressure, the

gaseous bodies are entrained into a cyclic pattern of alternating expansions and contractions. During compression phases, the positive acoustic pressure exerts a force on the bubble shell that tends to “push it inwards” and compress its gaseous core, and the whole bubble contracts. Conversely, during rarefaction phases, the low pressure allows the bubble to “relax”, its gaseous core decompresses and the bubble expands in size. This cyclic process – referred to as *stable cavitation* – increases the local absorption of acoustic energy and can induce microstreaming in the surrounding fluid, thereby causing highly localized shear stresses that can lead to severe cell damage. Furthermore, because it generates viscous stresses in the medium, this process is enhanced at low ultrasonic frequencies ($f < 1$ MHz).

Stable cavitation, however, applies only for low-intensity acoustic waves and describes a periodic and sustainable microbubble oscillation. For high pressure amplitudes, microbubbles show larger expansions during the rarefaction cycle, but their compression is intrinsically limited by the presence of a gaseous core. As a result, the pressure response of the microbubble becomes highly nonlinear, and the bubble expands further in size with every rarefaction cycle by means of rectified diffusion, until the eventual fragmentation of the bubble shell and the bubble collapse. This phenomenon is called *transient* or *inertial cavitation*, can generate tremendous local increases in acoustic pressure and temperatures, but also produce shock waves and high-velocity liquid jets, all of which and can have dramatic effects on the surrounding medium / tissue.

Considering the fluid-like properties of biological tissue, all the above-mentioned physical effects can potentially occur upon application of an acoustic perturbation. In turn, all of those effects can give rise to a variety of destructive and non-destructive interactions with cells, and more specifically neurons, in order to induce physiological responses.

1.3.2 Ultrasound parameters

Before going more in depth, a precise terminology of the stimulation parameters used in ultrasound neuromodulation studies is desirable. US protocols are typically defined in a multi-layer fashion.

- At the fundamental layer (i.e. the shortest time scale), ultrasonic pulses consist of sinusoidal acoustic pressure waves with a carrier frequency (f) and a peak-to-peak pressure amplitude (p), often described by an equivalent spatial-peak pulse average intensity I_{sppa} .
- Those pulses are applied for a specific duration (pulse duration, or PD), and repeated at a given frequency (pulse-repetition frequency, or PRF) and with a given duty cycle ($DC = PD \cdot PRF$), thereby forming a pulse train, or *burst*, with a spatial-peak temporal average $I_{spta} = I_{sppa} \cdot DC$.
- Moving towards a larger time scale, such bursts can be repeated at a given frequency (burst-repetition frequency, or BRF), and again, a given duty cycle, for a total stimulus application duration that can vary from a few milliseconds to several minutes.

1.3.3 Neuromodulation by ultrasound: a review of the literature

Investigations on the effect of ultrasound on excitable tissues date back to the interwar period. However, little progress was made in the field for most of the 20th century. It is only recently that technological and scientific advancements have triggered a new wave of interest for this technology, focusing mainly on brain applications. Here, we review those pioneering investigations, as well as those carried out during the recent resurgence of the field.

1.3.3.1 Early investigations

The first evidence of the bioelectric effect of ultrasound on neural tissue dates back to 1929, when Harvey observed twitching of frog’s gastrocnemius muscle upon US irradiation of the sciatic nerve (Harvey, 1930). Later on, the Fry brothers carried out a series of pioneering investigations through the

1950s, and observed notably the reversible modulation of visually evoked potentials in cats upon US stimulation of brain areas (Fry et al., 1958).

During the 1970s and 1980s, most of the work in the field was performed in the Soviet Union by Gavrilov and his colleagues, who focused mainly on the effects of ultrasound stimulation on mechanoreceptors and auditory pathways in humans. They reported evoked tactile and hearing sensations, as well as heat and pain sensations when subjects were sonicated at high intensity (Foster and Wiederhold, 1978; Gavrilov et al., 1976, 1996; Tsirolnikov et al., 1988).

Parallel investigations focused on the overall effect of focused ultrasound on brain excitability, with the application of low intensity pulses focused on various cortical and thalamic regions of rats, rabbits and cats (Koroleva et al., 1986; Velling and Shklyaruk, 1988). Markedly, steady negative potential shifts, waves of spreading depression, changes in electrocorticogram amplitude, and modulation of electrostimulation thresholds were observed.

Throughout the second half of the 20th century, a few studies were also conducted on the effect of ultrasound on peripheral and central nerve fibers, using stimuli of medium to high intensity ($I_{\text{spta}} > 10 \text{ W/cm}^2$) and long sonication durations (seconds to minutes) (Bachtold et al., 1998; Lele, 1963; Mihran et al., 1990; Rinaldi et al., 1991; Takagi et al., 1960; Young and Henneman, 1961). While direct nerve excitation by ultrasound was not observed, acoustic waves were found to have a profound influence on the fibers' behavior, as they could modulate conduction speed, compound action potentials (CAP) amplitudes, and response latencies.

1.3.3.2 Recent resurgence and growing expansion

In the turn of the millennium, a few studies sparked a new interest in the field by showing that ultrasound, when delivered at low intensity, is able to directly elicit action potentials, as well as resulting synaptic activity, in hippocampal neurons cultures and *ex vivo* mice brains (Muratore et al., 2009; Tyler et al., 2008). These groundbreaking studies were followed by many *in vivo* investigations in anaesthetized rodent and rabbit models, studying the excitatory and inhibitory effects of US stimuli on various brain areas through different indicators such as muscle activity, evoked potentials or fMRI (Kim et al., 2012, 2015; King et al., 2013, 2014; Mehić et al., 2014; Min et al., 2011; Tufail et al., 2010; Yang et al., 2012; Yoo et al., 2011; Younan et al., 2013). These studies confirmed the ability of ultrasound to engage brain circuits and in particular motor pathways, by showing that the sonication of somato-motor cortical areas elicited motor responses in mice, rabbits and rats. More importantly, they explored a wide range of stimulation conditions in order to try and provide a better understanding of the interaction between the stimulus and the responses.

Overall, most investigations found a positive relation between the stimulus intensity and duration, and the excitatory response strength and likelihood. They also consistently suggested that a stimulation period of several tenths of milliseconds was needed to obtain a first response. Interestingly, studies using pulsed waves at different duty cycles found out that low duty factors yielded mostly inhibitory effects (suppression of visual and somatosensory evoked potentials) in rabbits, rats and humans (Kim et al., 2015; Legon et al., 2014; Yoo et al., 2011) while high duty values predominantly elicited excitatory effects (Kim et al., 2015). Finally, a majority of these studies emphasized the important influence of anesthesia levels on neural excitability, with light levels seemingly more suitable for eliciting excitation.

Notably, two recent studies on small animal models have demonstrated that LIFUS could also induce indirect neuromodulatory effects through an auditory pathway (Guo et al., 2018; Sato et al., 2018), and even more recently, such auditory confounds have also been reported in human studies (Braun et al., 2020; Sanguinetti et al., 2020), thereby raising questions about the selectivity of this stimulation

method. However, subsequent studies have reported LIFUS motor responses in chemically of genetically deafened animals (Mohammadjavadi et al., 2018), thereby confirming the direct neuromodulatory effects of LIFUS. In parallel, it was shown in humans that such confounds were primarily arising from the LIFUS signal envelope and could be effectively masked by the application of an auditory mask at the stimulus PRF. Altogether, these studies indicate that potential auditory side effects can be effectively circumvented if properly accounted for.

1.3.3.3 Translational studies

In a translational effort, LIFUS neuromodulatory effects in the brain have been further investigated in non-human primates (NHPs) and humans, using transcranial stimulation. The use of larger models (as compared to rabbits and rodents), combined with imaging technologies such as x-ray computed tomography (CT) and magnetic resonance imaging (MRI), allowed a targeted focusing of acoustic energy in order to study precise LIFUS effects in specific brain areas.

In NHPs, LIFUS applied to the frontal eye field could modulate the firing rate of single neurons, and as a result affect visual processings and decision behavior during visuo-motor decision tasks (Hameroff et al., 2013; Kubanek et al., 2020; Wattiez et al., 2017). When applied to the somatosensory cortex, it could modulate sensory networks observed by functional MRI (Yang et al., 2018). In humans, LIFUS directed to the somatosensory cortex was able to both modulate somatosensory evoked potentials (and the EEG dynamics) (Legon et al., 2014; Mueller et al., 2014) and directly stimulate the somatosensory region resulting in the generation of limb sensations (Lee et al., 2015a). Moreover, LIFUS directed at the frontal-temporal cortex could elicit non-specific mood effects (Deffieux et al., 2013). In all cases, effects were found to be very sensitive to the spatial focus of the ultrasound waves, confirming their local effect on neural structures.

In parallel, other groups have studied longer-lasting effects of LIFUS on brain structures, using sonication protocols lasting up to several minutes. In NHPs, stimulation of the amygdala and supplementary motor area induced significant changes in the connectivity pattern of targeted areas (observed by fMRI), enhancing their coupling with other brain regions and reducing their coupling with others (Folloni et al., 2019; Verhagen et al., 2019). Changes in functional connectivity have also been reported upon prolonged LIFUS application to the pre-frontal cortex in humans (Sanguinetti et al., 2020). Importantly, no significant side effects have been observed at the typical intensities used to elicit direct or long-term neuromodulatory effects (Gaur et al., 2020; Legon et al., 2020).

1.3.3.4 Investigations in the peripheral nervous system

In parallel to brain LIFUS investigations, several groups have studied the effects of ultrasound on peripheral circuits. Early investigations by the Fry brothers showed that the application of US could modulate the spiking activity of peripheral nerves (Fry and Fry, 1950). These findings have since then been confirmed by other studies (Colucci et al., 2009; Juan et al., 2014; Lee et al., 2015b; Lele, 1963; Mihran et al., 1990; Tsui et al., 2005), where ultrasound stimuli directly targeting the nerves affected conduction velocity, action potential shape, and overall spiking activity. However, *de novo* generation of action potentials was not observed, thereby raising concerns about the direct excitability of peripheral nerves by ultrasound.

However, two recent studies targeting peripheral nerves have reported direct excitatory effects. First, an *ex vivo* study on isolated crab leg nerve bundles – composed exclusively of unmyelinated fibers – reported that focused ultrasound stimulation (FUS) could directly elicit compound action potentials (Wright et al., 2015). Second, an *in vivo* study on mice reported that FUS targeted at the intact sciatic nerve could directly activate myelinated fibers to induce motor responses (Downs et al., 2018). Interestingly, both of these studies used very high acoustic intensities (pressures way over 1 MPa) in order

to elicit direct neuronal activity, i.e. more than one order of magnitude than typical excitation thresholds reported in the brain (King et al., 2013).

Overall, the pronounced differences in neuromodulatory effects observed between central and peripheral structures may point to distinct recruitment mechanisms, although it must be recalled that those structures are embedded in different anatomical environments that are targeted in distinct ways, which may explain some of those discrepancies.

1.3.4 Candidate mechanisms

Despite a decade of intense investigation and a growing collection of empirical observations, interrogations remain about the exact ways by which ultrasound interacts with neural structures in order to trigger spiking activity. This lack of precise characterization is primarily due to the number of physical effects that ultrasound exerts on biological tissue, but also to the variety of sub-cellular structures that may take part in the transduction of mechanical energy into an electrical response. Here, we will review the mechanistic hypotheses that have been proposed so far.

1.3.4.1 Ion channel mechanosensitivity

The main hypothesis advanced in the literature is that of ion channel mechanosensitivity, i.e. that ultrasound, by exerting stress on the surrounding tissue and the cell membrane, may cause the opening of ion channels to trigger the entry of cations and induce depolarizations (Tyler, 2011). Many *in vitro* studies have documented this behavior in specifically mechanosensitive channels (Ibsen et al., 2015; Prieto et al., 2017; Qiu et al., 2020), but also in voltage-gated ion channels that take part in the typical action potential machinery (Kubanek et al., 2016; Tyler et al., 2008). Very recently, an *in vitro* study has further characterized the role of these channels in regulating LIFUS excitation: it was reported that LIFUS directed at mouse primary cortical neurons induced the opening of specific mechanosensitive channels, prompting an inward calcium flow that, after intracellular amplification, could activate calcium-dependent sodium channels to induce action potentials (Yoo et al., 2020). These findings demonstrate that LIFUS-mediated neuromodulatory effects are, at least partially, attributable to the mechanosensitive nature of specific transmembrane ion channels. However, the diversity of identified responsive ion channels, as well as their heterogeneous expression across neural structures (Sukharev and Corey, 2004), hinders the formulation of a unifying theory that would clarify their interaction with ultrasound (i.e. which physical effect(s) of ultrasound these structures are sensitive to, and how this sensitivity might then depend on LIFUS parameters) in a quantitative manner.

1.3.4.2 Direct membrane effects

In parallel, alternative theories have also been advanced that focus on the direct interaction between ultrasound and the neuronal plasma membrane, building on a significant body of evidence describing the membrane conformational changes associated with action potentials (Abbott and Howarth, 1973; Inoue et al., 1973; Kobatake et al., 1971). Theoretical and empirical studies have shown that changes in membrane thickness (Heimburg and Jackson, 2005) and curvature (Petrov, 2002) can modulate the electrical state of the membrane (Prieto et al., 2013) in order to trigger action potentials that propagate as electromechanical waves. Notably, recent efforts have been pursued to model this electromechanical propagation in a quantitative manner (Chen et al., 2019), although it is not explicitly formulated how ultrasonic perturbations can involve the ion channels machinery. It has also been hypothesized that mechanical stresses, and the potential extracellular cavitation, induced by ultrasonic stimuli may induce the formation of physical pores in the plasma membrane, thereby providing an alternative way for ion entry and depolarization (Blackmore et al., 2019), although the specific involvement of such mechanisms with low-intensity ultrasound stimuli remains to be elucidated.

1.3.4.3 Intramembrane cavitation

Finally, it has been hypothesized that the local ultrasound pressure oscillation may induce the nucleation of small gaseous cavities within the membrane itself that, once formed, would undergo periodic deflections oscillations at the ultrasound frequency (Krasovitski et al., 2011). This process, referred to as *intramembrane cavitation*, could in turn induce high-frequency, large amplitude oscillations in membrane capacitance and membrane potential, thereby triggering depolarizing membrane currents that, once integrated over a sufficient time period, could give rise to action potentials (Plaksin et al., 2014). Notably, this hypothesis has been only advocated on a theoretical basis, and neither the mechanical oscillations of the membrane, nor the resulting large-amplitude oscillations of the membrane potential, have been directly observed experimentally (although the formation of intramembrane cavities is supported by *ex vivo* post-sonication observation in epidermal tissue (Krasovitski et al., 2011)).

This mechanistic hypothesis is portrayed by a *Neuronal Intramembrane Cavitation Excitation* (NICE) model that describes the entire process of energy transduction from an ultrasonic perturbation input (microsecond pressure oscillation) into an electrical response output (millisecond time course of the local membrane potential) in quantitative, mathematical terms. Moreover, the NICE model can explain multiple experimental observations:

- When applied to pyramidal cortical neurons, the NICE model predicts salient features of neuronal responses (latency, excitation thresholds, response strength) and of their dependency on LIFUS parameters (frequency, intensity, duration) that correlate with indirect empirical metrics of neuronal excitation upon sonication of the motor cortex area in mice (King et al., 2013).
- Furthermore, when expanded into minimalistic, yet functionally realistic thalamo-cortical neuronal networks, the NICE model predicts a LIFUS parameter dependent enhancement or suppression of cortical activity (due to the cell-type-specificity of ion channel populations) that is in good qualitative agreement with a large number of empirical observations in animal models and humans (Plaksin et al., 2016).

However, despite its enticing predictive power, the NICE model suffers from important limitations:

- This model approximates neurons as discrete points that lack a spatial representation. As such, it does not provide a complete picture of the intramembrane cavitation mechanism in morphologically realistic neuronal structures, and cannot address physiologically relevant questions, such as the influence of intracellular axial coupling and morphological inhomogeneity on neuronal responses, the spatiotemporal dynamics of those responses, and the impact of spatial features of the acoustic field on excitability (as is the case for electrical stimulation).
- The equations underlying the NICE model couple behavior across a wide range of time-scales and involve nonlinearities that make numerical integration a challenging and resource intensive task. Simulation of larger systems are typically unaffordable, and so is the exploration of a wide range of stimulation parameters.
- The rapid (ultrasonic frequency) transmembrane capacitance and associated transmembrane voltage oscillations result in dramatic fluctuations of the electrophysiological variables, such that their evolution cannot be studied and interpreted in terms and by means of classic electrophysiological approaches (channel dynamics, phase plots, bifurcation theory, etc.).
- On a practical level, solvers for the NICE model are custom-made (e.g., through Python or Matlab scripting) and their users cannot benefit from the large resources and infrastructure available, e.g., for a package like NEURON (Hines and Carnevale, 1997), for which large collections of neuron and network models, as well as high performance computing infrastructure and an important research community exist.

1.3.4.4 Summary and outlook

Each of the presented candidate mechanisms presents both promising aspects and associated drawbacks:

- Ion channel mechanosensitivity is supported by extensive empirical evidence but implies a wide landscape of interactions that have yet to be clarified and quantified.
- Direct interactions with the plasma membrane are supported by extensive evidence of its intrinsic mechano-electrical coupling and are supported by thermo-dynamical analyses, but do not specify a clear role for ion channels and may therefore provide an incomplete picture of the transduction chain.
- Intramembrane cavitation predicts both a physical and a biophysical mechanism in a quantitative manner, correlates extensively with high-level empirical data, but lacks direct experimental observation of the phenomenon.

Hence, the transduction of ultrasonic input into neural responses could stem from various candidate mechanisms involving several sub-cellular structures, the relevance of which is not yet fully established.

Notably, the different advanced mechanisms are also linked to different bioeffects of ultrasound. In particular, radiation-based mechanisms (such as stress-mediated mechanosensitivity and flexoelectricity) should be enhanced and therefore yield more prominent neuromodulatory effects at higher frequencies, which departs from the majority of empirical observations. Oppositely, cavitation-based mechanisms (such as sonoporation and intramembrane cavitation) should be stronger and yield more pronounced effects at lower frequencies, which is more in line with *in vivo* observations. Owing to these different sensitivities, systematic exploration of large parameter spaces represent a valuable approach to infer on the relevance of specific mechanisms (Menz et al., 2019), but this approach has remained largely unexploited.

1.4 Advantages and current limitations of LIFUS

At this stage, it appears evident that LIFUS offers a multiplicity of advantages as a stimulation and neuromodulation modality:

- First, it relies on acoustic waves that penetrate efficiently through biological tissue, propagate with a high degree of directionality, and can interact constructively in favorable conditions. This offers the ability to steer and focus acoustic energy around small focal volumes (literally the size of a grain of rice) virtually anywhere in the human body, including deep brain targets that are unreachable by analogous techniques (TMS, tDCS).
- Second, because those waves can also propagate through epidermal and bone-like tissue (e.g. the skull), LIFUS can be delivered noninvasively through an external device.
- Third, as it does not involve the application of electrical or magnetic fields, LIFUS constitutes the only form of non-ionizing energy that can be focused in deep tissues (Rabut et al., 2020).
- Fourth, it does not require the use of external chemical or genetic agents employed by other modern techniques such as optogenetics and magneto-thermal stimulation.
- Finally, because it interacts with neurons in a different manner than conventional electrical stimulation techniques, LIFUS may offer new types of anatomical, functional and cellular selectivity that have not been achieved so far.

However, it is also clear that several factors are still limiting the maturation of this technology:

- First, the lack of a comprehensive mechanistic understanding of LIFUS neuromodulatory effects, stemming from the variety of potential mechanisms and the difficulty to reproduce *in vivo* conditions in *in vitro* environments (Rabut et al., 2020).
- Second, remaining uncertainties regarding potential side effects and confounds, and how to effectively circumvent them.
- Third, significant disparities between the sensitivities of central and peripheral neural structures to LIFUS that still remain to be explained.
- Fourth, the tremendous variability of acoustic environments and stimulation parameters employed across studies, and the lack of systematic parameter space explorations allowing to establish clear relationships between these parameters and neuromodulatory outcomes.
- As a result of these limitations, the choice of sonication protocols – even in the most recent studies – is not mechanistically nor quantitatively informed, which is likely to affect the efficacy and specificity of induced effects.
- Finally, like all relatively new technologies, the long-term viability of LIFUS as a neuromodulation modality in chronic applications remains to be assessed.

Overall, these limitations emphasize the crucial need for predictive models to help designing stimulation devices and optimizing delivery protocols in order to achieve target and application specific neuromodulatory effects.

At the moment, the community is relying on modeling tools that predict acoustic propagation and energy deposition in complex animal and / or human anatomies (Neufeld et al., 2013; Treeby and Cox, 2010). These tools constitute a great support for experimenters, helping them to optimize their setup to reach a given neural target and quantify potential side effects such as diffraction and standing waves. However, while they can predict the focus of intervention, such models do not provide any insight on the resulting neuromodulatory effects in the targeted and surrounding areas. More specifically, they do not allow to answer essential questions:

- *Given the multiplicity of potential responsive elements in the cellular membrane and their heterogeneous expression across cell types, what sort of cell type specificity can be expected in LIFUS-evoked responses, and how does that specificity affect functional and behavioral outcomes?*
- *Within the cell itself, how does the morphological structure affect the location of excitation, the potential integration of the initiated response along a dendritic tree, and its propagation along axonal projections?*
- *In the case of highly connected neural circuits of the brain and spinal cord, how does the stimulation of a given area affect other, functionally and anatomically connected areas? How do these network effects scale over time?*
- *Can these specificities be exploited to induce new forms of neuromodulation?*

Hence, knowing *where*, *when*, and *in which quantity* the acoustic stimulus is delivered is not enough. In order to formulate reliable predictions, the dynamic effects of ultrasound on realistic neural structures *must* be considered. In this context, computational approaches constitute a great tool to drive research forward, as they allow to investigate LIFUS-neuron interactions within the frame of a specific mechanistic hypothesis, and, in some cases, can quantitatively relate the effects of LIFUS parameters on neuronal activity. Moreover, recent examples from other fields have demonstrated that such models, once embedded in the right computational pipeline, can provide valuable predictions of large scale functional and behavioral effects, and greatly accelerate the maturation of neuromodulation devices into the clinics (Wagner et al., 2018).

To date, the most significant effort in this direction was made by Plaksin et al. with the introduction of the NICE model, which showed great potential in predicting general trends of neuromodulatory effects in the brain. However, the limited morphological complexity of this model highlights one of the main challenges encountered when modeling ultrasound neuromodulatory effects: because LIFUS-neuron interactions are complex and involve multiple forms of energy, they cannot be captured by classical, highly abstracted neuronal representations used by electrophysiologists. Instead, alternative neuronal representations must be designed that account for this additional complexity. These considerations bring us to a central question that I will try to address in this work:

How can we efficiently model ultrasound neuromodulation across all relevant scales?

1.5 Objectives and outline of the thesis

In a will to answer the central question formulated above, this thesis focuses on the development of a computational framework to capture LIFUS neuromodulatory effects in morphologically-realistic neuronal representations, with a particular focus on peripheral nerve fibers. This general incentive can be subdivided into several objectives:

- Develop a computational neuron model that can formulate predictions of LIFUS neuromodulatory effects in an accurate, interpretable and cost-effective manner
- Develop a methodological and computational pipeline to expand this initial model into multi-compartmental neuronal representations, in order to provide refined predictions of LIFUS neuromodulatory effects in morphologically realistic structures.
- Exploit this framework to investigate the effects of LIFUS on peripheral nerve fibers, and identify the optimal sonication parameters required to obtain a reliable neuromodulation of these structures
- Confront the model predictions to empirical data in order to assess the physiological relevance of the energy transduction mechanism underlying the modeling developments

The pursuit of these objectives is organized as follows:

- Chapter 2 provides a detailed biophysical, mathematical and behavioral description of the intramembrane cavitation theory and the NICE model, which we use as a quantitative theoretical basis for the study of ultrasound neuromodulation. It also points out the intrinsic assumptions, predictive power, and numerical limitations of the NICE model.
- Chapter 3 presents our development of a *multi-Scale Optimized Neuronal Intramembrane Cavitation* (SONIC) model that alleviates the numerical limitations presented in Chapter 2 in order to enable more efficient simulations. Beyond algorithmic optimization, it also shows how this model introduces a more interpretable representation of the underlying mechano-electrical transduction problem, and facilitates its spatial expansion.
- Chapter 4 presents the development of morphoSONIC, a NEURON-based computational framework enabling a stable, accurate and efficient incorporation of the SONIC paradigm into

multi-compartmental neuron models. It also showcases the application of this framework to the study of intramembrane cavitation in morphologically realistic peripheral axons, yielding new predictions with exciting prospects for peripheral ultrasound neuromodulation.

- Chapter 5 presents the results of an experimental effort to elucidate the mechanisms of ultrasound neuromodulation in an *ex vivo* experimental setting. It also discusses the implications of those results regarding the physiological relevance of the intramembrane cavitation hypothesis.
- Finally, Chapter 6 discusses these methodological and experimental achievements, highlights their relevance for the field and suggests direction for future research.

Chapter 2 The Neuronal Intramembrane Cavitation (NICE) Model

The Neuronal Intramembrane Cavitation Excitation (NICE) model is an electromechanical model composed of two bi-directionally coupled dynamical systems. On the one hand, a mechanical model describes the periodic cavitation of nanoscale resonant phospholipidic structures located in the membrane of cells – so-called “bilayer sonophores” – at the ultrasound frequency. On the other hand, a Hodgkin-Huxley electrical model describes the progressive activation and inactivation of specific voltage-gated ion channels to generate membrane currents and induce a neuronal response. These two paradigms, although operating at different spatial and temporal scales, can be coupled under a specific set of assumptions, thereby providing a deterministic mechanistic hypothesis for ultrasound neuromodulatory effects. This chapter provides a detailed mathematical description of the mechanical and electrical parts of the NICE model, describing their core components and governing equations, but also highlighting the inherent assumptions taken throughout the model’s construction. A larger attention is given here to the mechanical part, which constitutes a relatively novel hypothesis.

2.1 Biomechanical part: the bilayer sonophore model

The bilayer sonophore model, introduced by (Krasovitski et al., 2011), formulates the hypothesis that the plasma membrane of cells can act as an acoustic resonator, and transform the acoustic pressure oscillation within the ultrasound range into nanometer scale membrane displacements. This model combines theories of bubble dynamics, viscoelasticity, gas diffusion and molecular interactions into a comprehensive set of equations, describing the periodic transverse deflections of the membrane sonophore structure and the associated variation in its internal gas content. It forms the mechanical part of the NICE model.

2.1.1 Steady-state system

2.1.1.1 Geometry

Consider a flat round patch of bilayer lipid membrane with diameter $2a$, surrounded by a constraining circle of transmembrane proteins (**Figure 1**). This patch is composed of two monolayer leaflets considered as viscoelastic solids, each with a thickness δ_0 and an exposed surface area $S_0 = \pi a^2$. The gap Δ between the two monolayers creates an inter-leaflet space filled with gas (standard air composition, i.e. 79% N_2 and 21% O_2), filling a volume $V_0 = \pi \Delta a^2$. The extracellular and intracellular spaces lying on either side of the bilayer are both considered as an incompressible Newtonian fluid saturated with air. Altogether, these three components form the so-called *bilayer sonophore* (BLS), i.e. the fundamental resonating structure at the core of the intramembrane cavitation theory. Thanks to its cylindrical symmetry, this three-dimensional structure can be projected onto a two-dimensional (r, z) coordinate system, where r and z respectively denote the *in-plane* and *transverse* directions with respect to the membrane plane.

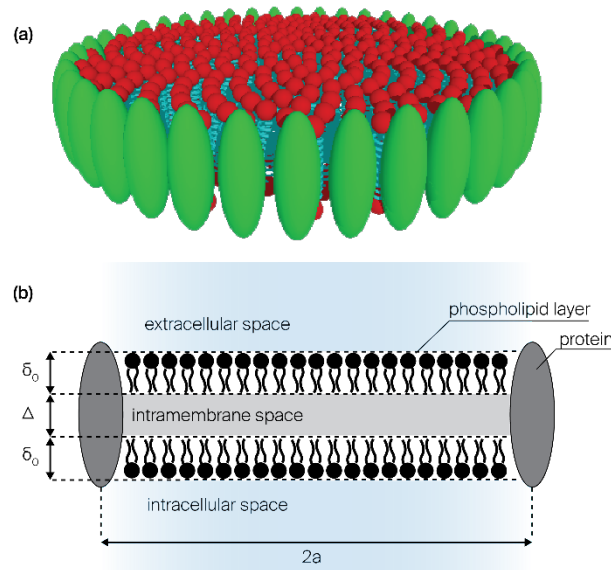


Figure 1. Schematic description of the resting bilayer sonophore structure. (a) 3D view with the phospholipid head groups (red) and lipid chains (cyan), as well as the transmembrane proteins (green). (b). Transverse plane cross-section.

2.1.1.2 Forces

The steady-state configuration of the bilayer sonophore results from the balance between three pressure forces acting on the leaflets: the static hydrostatic pressure in the surrounding fluid P_0 , the gas pressure in the inter-leaflet space P_G , the intermolecular force per area between the leaflets P_M . Cylindrical symmetry implies that each of these forces acts on both leaflets with equal amplitude but opposite directions.

Gaseous and hydrostatic pressures. The hydrostatic and gas pressures P_0 and P_G apply normally to the leaflet surface but in opposite directions (pointing inward and outward the bilayer respectively). Neglecting the effects of pressure accumulation with depth in the infinite fluid, the hydrostatic pressure P_0 is space-invariant. Moreover, assuming that the extracellular and intracellular fluids are saturated with air, the leaflet permeability to gas allows the static pressures on both sides of the leaflet to equalize, hence for the initial steady-state system $P_G = P_0$. Hence, the initial gas molar content in the inter-leaflet space can be computed as:

(5)

$$n_{g,0} = \frac{P_0 V_0}{R_g T}$$

where R_g and T denote the universal gas constant (in $\text{Pa}\cdot\text{m}^3\cdot\text{mol}^{-1}\cdot\text{K}^{-1}$) and the absolute temperature (in K) respectively.

Intermolecular attraction/repulsion pressure. The intermolecular pressure P_M results from close-range, complex molecular interactions between the amphiphilic molecules of the two phospholipid layers of the membrane. Multiple types of interactions do exist at such atomic scales, each of them being either of attractive or repulsive nature. While molecular attraction can be mostly explained by *Van der Waals* forces, repulsion effects arise from several types of entropic forces (e.g. undulation, peristaltic, protrusion,...) that are hardly distinguishable. However, all these forces exhibit similar dependencies on the inverse of the interaction distance, raised to some specific power (Israelachvili, 1992). Therefore, rather than trying to interpret molecular interaction as the explicit sum of a given set of forces, it is defined by a generic *Lennard-Jones* expression that expresses the local intermolecular

pressure as the net difference between a repulsive and an attractive term, both depending on molecular distance:

$$p_M(d) = \underbrace{\frac{c_1}{d^m}}_{\text{repulsion}} - \underbrace{\frac{c_2}{d^n}}_{\text{attraction}} \quad (6)$$

In this expression c_1 and c_2 are constants, d denotes the local distance between the two layers, and m and n are repulsion and attraction exponents respectively. Geometrically speaking, the steady-state configuration implies the assumption of a uniform inter-leaflet gap across the BLS structure, and thus a spatially constant intermolecular pressure. Moreover, this constant pressure must be null in order to ensure equilibrium of the unperturbed system. Therefore at $d = \Delta$ we must have:

$$\frac{c_1}{\Delta^m} = \frac{c_2}{\Delta^n} = p_\Delta \quad (7)$$

and the generic expression for the local intermolecular pressure can be rewritten as:

$$p_M(d) = p_\Delta \left[\left(\frac{\Delta}{d} \right)^m - \left(\frac{\Delta}{d} \right)^n \right] \quad (8)$$

2.1.2 Perturbation

Upon application of an external acoustic perturbation P_A , the equilibrium of the bilayer patch is disrupted. We consider here the case of a rarefactional acoustic pressure ($P_A < 0$) applied to the surrounding fluid far away from the bubble and thus adding up to the fluid static pressure P_0 . This negative pressure causes the leaflets to pull apart in a symmetric way.

2.1.2.1 Geometry

As the leaflets reach for a new equilibrium, they deform to acquire a *dome*-like shape (**Figure 2**). We denote by $z(r)$ the local deviation of each leaflet from its initial position (along the transverse axis) at a distance r from the center of the constraining ring. Considering the circular anchoring of the BLS structure, the maximal transversal displacement Z of each leaflet at a given time must occur at the center of the constraining ring ($r = 0$).

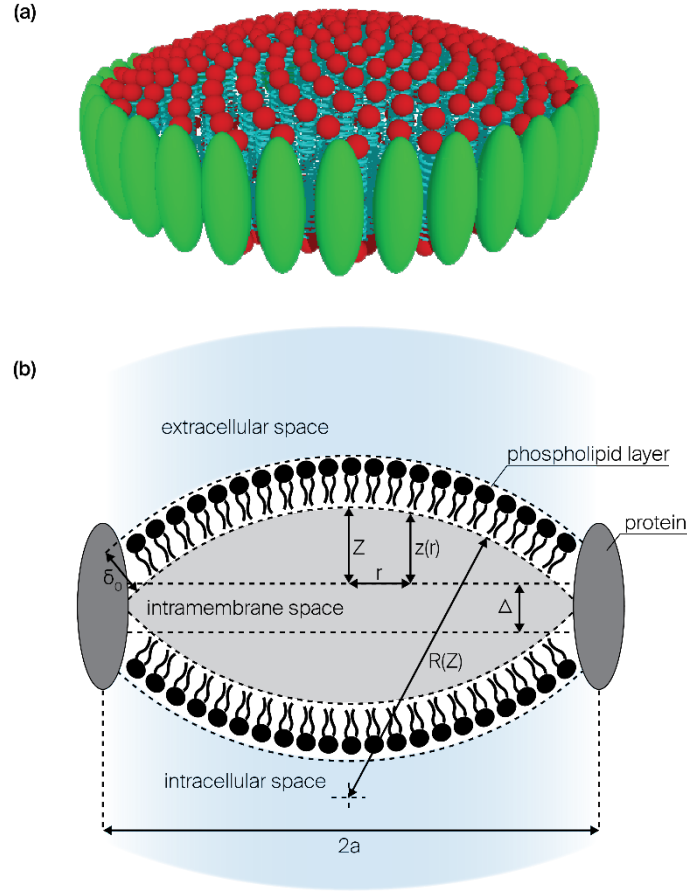


Figure 2. Schematic description of the perturbed bilayer sonophore structure. (a) 3D view with the phospholipid head groups (red) and lipid chains (cyan), as well as the transmembrane proteins (green). (b). Transverse plane cross-section.

Furthermore, it is assumed that the curvature of the deformed leaflet is constant across its entire surface, or in other words that the deformation of the leaflet exhibits spherical symmetry. With this in mind, the radius of curvature R of the upper leaflet is easily derived from the geometry of the system:

(9)

$$R = \frac{a^2 + Z^2}{2Z}$$

It is worth noting that equation (9) defines the curvature radius as a *signed measure*, i.e. R will take negative values for negative deflections. On a more quantitative prospect, minimal curvature radius amplitude is reached at $Z = \pm a$, at which point $R = a$. Constant curvature also permits to define the local deviation $z(r)$ from the system's geometry:

(10)

$$z(r) = \text{sign}(Z) \left(\sqrt{R^2 - r^2} - |R| + |Z| \right)$$

Notice that just as the apex deflection and the curvature radius, z is also defined as a signed measure in order to reflect both positive and negative local deflections. Furthermore, the exposed surface of the curved leaflet equals:

(11)

$$S = \pi(a^2 + Z^2)$$

and the inter-leaflet space expands to a volume that is the sum of a cylinder and two spherical caps:

(12)

$$V = \pi\Delta a^2 \left[1 + \frac{Z}{3\Delta} \left(3 + \frac{Z^2}{a^2} \right) \right]$$

2.1.2.2 Modified intermolecular pressure.

In this new configuration, the attraction/repulsion forces do not add out anymore, since the inter-leaflet gap varies along the membrane plane. At a distance r from the center of the structure, the local leaflet deviation $z(r)$ implies a local inter-leaflet gap $d(r) = 2z(r) + \Delta$. Using this new metric, local intermolecular pressure can be redefined as:

(13)

$$p_M(r) = p_\Delta \left[\left(\frac{\Delta}{2z(r) + \Delta} \right)^m - \left(\frac{\Delta}{2z(r) + \Delta} \right)^n \right]$$

Obviously, the amplitude of the local intermolecular pressures will vary across the perturbed BLS structure. Therefore, an average intermolecular pressure felt across one leaflet is obtained by integration of the local force per unit area over the entire leaflet surface:

(14)

$$P_M = \frac{1}{S} \int_0^a \int_0^{2\pi} p_M(r) r dr d\theta = \frac{2}{a^2 + Z^2} \int_0^a p_M(r) r dr$$

In order to quantify the displacement of the system for a given perturbation, two situations will be evaluated, for small and large deviations from the equilibrium. The mechanical response of the leaflets and the liquid around them voluntarily neglected in the former case (*quasi-steady* system), while it must be considered the latter case (*dynamical* system).

2.1.3 Quasi-steady system

In this section, we consider the case of a small deviation of the dome center from its planar position ($|Z| \leq Z_{min}$), and evaluate the new magnitude of the forces applied on the system.

2.1.3.1 Polytopic gas expansion

In a quasi-steady system, it is assumed that for a small enough deviation of the leaflet from equilibrium, the resulting imbalance is not large enough to generate a diffusion of gas across the leaflet. Hence, the gas inside the membrane experiences an polytopic expansion to fill the greater volume between the leaflets, thereby reducing the internal pressure. Considering a small change in volume, the gas expansion is considered as an isotherm transformation ($PV = \text{constant}$), hence the new internal pressure can be written as:

(15)

$$P_G = P_{G,0} \frac{V_0}{V} = \frac{P_{G,0}}{1 + \frac{Z}{3\Delta} \left(3 + \frac{Z^2}{a^2} \right)}$$

2.1.3.2 Transcendental equation

Altogether, the force balance equation of the quasi-steady system is expressed as:

(16)

$$P_M + P_G - P_0 - P_A = 0$$

Owing to the inherent simplifications of the quasi-steady system, equation (16) does not contain any derivative term with respect to time. Therefore, solving the quasi-steady system simply comes down to finding the unique value of Z that cancels the left-hand side of the equation (termed as the *quasi-steady total pressure*, $P_{tot,qs}$), for a given external acoustic perturbation P_A . However since the variable Z is found both inside and outside an integral form, equation (16) is *transcendental* and does not bear any algebraic solution. Hence it must be solved with numerical methods.

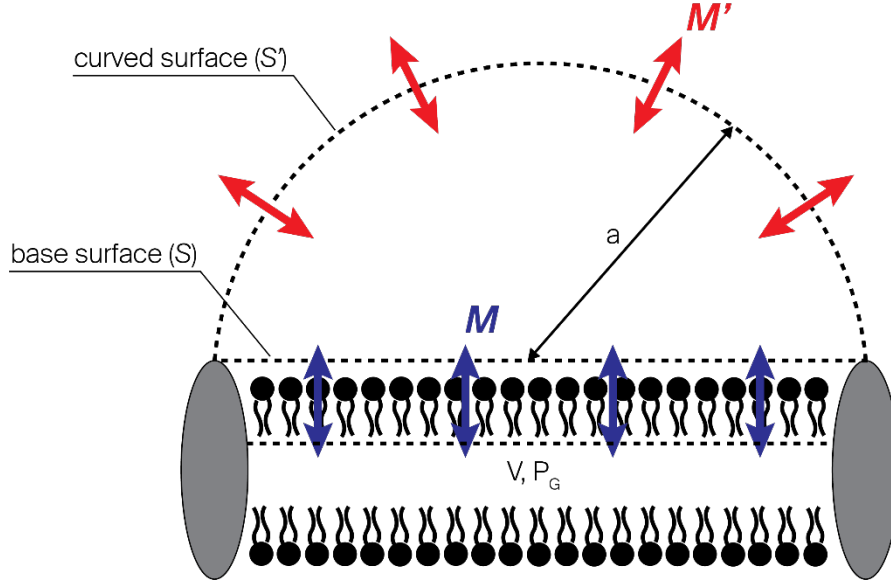
2.1.4 Dynamical system

In this section, we consider a situation of large deviation of the dome center from its planar position ($|Z| > Z_{min}$). In this case, the diffusion of gas across each monolayer, as well as the mechanical response of the corresponding leaflet and surrounding liquid, are too important to be neglected: they must be taken into account in the force balance equation.

2.1.4.1 Gas transport across the leaflet

As the leaflet deviation becomes significant and generates an important imbalance in the static pressures on both sides of the leaflets, the resulting transport of gas across monolayers must be considered. To do so, the curvature and thickness of the monolayers are neglected: each leaflet is considered as a flat disk with radius a , fixed on an infinite impermeable plane along the membrane. We consider here two cases of gas transport across leaflet, namely *radial diffusion* in semi-infinite space and *one-dimensional diffusion* through a membrane of fixed thickness, each associated with different assumptions. In both cases, equations are derived while considering the diffusion of gas from the inter-leaflet space to the surrounding fluid, thereby reducing the internal gas pressure P_G . Nonetheless, it is worth noting that the equations are valid for a diffusion in both directions.

Radial diffusion in semi-infinite space. In this first case, assumption is made that the gas diffuses across the leaflet perpendicularly to its surface, and then radially once in the fluid. In this system, diffusion through the leaflet membrane is considered to be significantly faster than in the fluid, which allows to greatly simplify the diffusive system by considering that the *fast* membrane diffusion dynamics fully complies with the *limiting* diffusion dynamics in the fluid. Therefore, gas transport across the membrane is solely governed by equations of gas diffusion in the surrounding fluid.



The transition from a unidirectional to a radial motion is handled by considering a hemisphere of radius a placed on the leaflet disk. Let us define M and M' as the total flux of gas diffusing across the base (S) and the curved (S') surfaces of the hemisphere, respectively. The former flux can be related to the number of gas molecules (expressed in *mol*) living the inter-leaflet space:

(17)

$$M = -\frac{dn_g}{dt}$$

while the latter is simply derived from Fick's first law of diffusion. In a spherically symmetric system, the radial diffusion flux density $J(r)$ at a distance r from the source (approximated by the center of the disk in our case) is defined as:

(18)

$$J(r) = -D_{gl} \frac{\partial C_G}{\partial r}$$

where D_{gl} is the diffusion coefficient of gas in fluid assumed as constant, and $C_G(r)$ is the local gas concentration in the fluid. Hence, the total flux of gas diffusing through S' is simply:

(19)

$$M' = S'J(a) = -S'D_{gl} \left(\frac{\partial C_G}{\partial r} \right)_{r=a}$$

In the above-defined system, the hemisphere volume formally represents the physical space needed to transit from unidirectional to spherical diffusion. For simplification purposes, we can consider this transition as an instantaneous process, by virtually reducing the volume of the hemisphere to zero. As a consequence, we neglect the surface expansion from S to S' and consider the fluxes M and M' as equivalent:

(20)

$$\begin{cases} S = S' \\ M = M' \end{cases}$$

Therefore, recalling equations (17) and (19) we have:

(21)

$$\frac{dn_g}{dt} = SD_{gl} \left(\frac{\partial C_G}{\partial r} \right)_{r=a}$$

Concretely, equation (21) states that the rate of change of the gas molar content in the inter-leaflet space is proportional to the gas concentration gradient in the fluid at a specific radial distance a from the source. This concentration gradient remains to be formulated.

The diffusion of the dissolved gas in the fluid is controlled by Fick's second law:

(22)

$$\frac{\partial C_G}{\partial t} = D_{gl} \nabla^2 C_G$$

where ∇^2 denotes the laplacian operator, and C_G is function of both space and time. In the present system, we consider purely radial diffusion in a fluid region bounded internally by a sphere of radius a . Therefore, equation (22) is expressed in spherical coordinates:

(23)

$$\frac{\partial C_G}{\partial t} = D_{gl} \left(\frac{\partial^2 C_G}{\partial r^2} + \frac{2}{r} \frac{\partial C_G}{\partial r} \right)$$

and evaluated for $r \geq a$. In order to provide a unique solution to this second-order partial differential equation, initial and boundary conditions must be provided. Therefore, it is assumed that the initial gas concentration at $t = 0$ is constant across the fluid:

(24)

$$C_G(r, 0) = C_0; \quad r > a$$

Moreover, we suppose that the concentration at the internal surface is maintained constant:

(25)

$$C_G(a, t) = C_s \quad t > 0$$

Considering such conditions, the problem can be solved using Laplace transformation with the introduction of a new variable $u = C_G r$ (Crank, 2009), and the solution takes the form:

(26)

$$\frac{C_G(r, t) - C_0}{C_s - C_0} = \frac{a}{r} \operatorname{erfc} \left(\frac{r - a}{2\sqrt{D_{gl}t}} \right)$$

where *erfc* is the *complement error function*. The formulation of the concentration gradient follows from (26) by simple derivation:

(27)

$$\frac{\partial C_G}{\partial r} = -\frac{a}{r}(C_s - C_0) \left[\frac{1}{r} \operatorname{erfc} \left(\frac{r-a}{2\sqrt{D_{gl}t}} \right) + \frac{1}{\sqrt{\pi D_{gl}t}} e^{-\left(\frac{r-a}{2\sqrt{D_{gl}t}}\right)^2} \right]$$

Finally, evaluating (24) at $r = a$ and inserting into equation (18) yields:

(28)

$$\frac{dn_g}{dt} = SD_{gl}(C_0 - C_s) \left[\frac{1}{a} + \frac{1}{\sqrt{\pi D_{gl}t}} \right]$$

The term C_s of equation (28) deserves particular attention: assuming an instantaneous transition from unidirectional to spherical diffusion, the internal boundary of the problem also happens to be the interface between the gas and fluid layers. At this interface, Henry's law states that the amount of gas going into solution is proportional to the internal gas pressure:

(29)

$$C_s = \frac{P_G}{k_H} \quad t > 0$$

where k_H is *Henry's constant*, and the internal pressure P_G can be expressed in terms of the gas molar content n_g :

(30)

$$P_G = \frac{n_g R_g T}{V}$$

Considering the total rate of change across the two leaflets, we have:

(31)

$$\frac{dn_g}{dt} = 2SD_{gl} \left(C_0 - \frac{P_G}{k_H} \right) \left[\frac{1}{a} + \frac{1}{\sqrt{\pi D_{gl}t}} \right]$$

One-dimensional steady-state diffusion through the membrane. In this second case, assumption is made of a uniform gas concentration in the surrounding fluid, i.e. that $C_G(t) = C_0$ at all times and points. Due to this steady-state configuration, the distribution of gas concentration in the fluid can be neglected to focus on its unidirectional diffusion across a membrane layer of finite thickness ξ , representing the leaflet. Thanks to the assumption formulated above, both C_s and C_0 can be considered as constant for a small enough time interval. After some time, a steady-state is reached in which the concentration remains constant at all points of the membrane. Assuming that this steady-state is instantaneously reached, the diffusion equation in one dimension across the leaflet then reduces to:

(32)

$$\frac{dC_G}{dx} = \text{constant}$$

where x is the direction of diffusion. Integrating with the boundary conditions at both surfaces we get:

(33)

$$\frac{C_G - C_S}{C_0 - C_S} = \frac{x}{\xi}$$

Hence, the rate of change of internal gas molar content simply equals the total flux of gas diffusing through the leaflet of surface S . Considering the total rate of change across the two leaflets, we have:

(34)

$$\frac{dn_g}{dt} = 2SD_{gl} \frac{dC_G}{dx} = \frac{2SD_{gl}}{\xi} \left(C_0 - \frac{P_G}{k_H} \right)$$

2.1.4.2 Rayleigh-Plesset dynamics

Let us now focus on the dynamics of the leaflets and the surrounding fluid as the BLS structure experiences compression or expansion. To do so, we consider a control volume $V_{control}$ that consists of a thin lamina (spherical shell section) containing a small portion of a leaflet as well as the adjacent gas and fluid layers. The geometry of the perturbed BLS implies that the leaflet exhibits constant curvature inside this small volume. We can thus define $V_{control}$ to exhibit the same curvature as the radius, thereby yielding a spherically symmetric local system, for all deflection amplitudes. Assuming that this spherical symmetry can be applied to the *entire* leaflet (including its leaflet extremities), the dynamics of the system can be expressed by the same radial differential equations that are used to characterize bubble expansion and collapse. For intuitive purposes, we can thus imagine the curved upper leaflet to be part of the boundary layer of a spherical bubble of radius R filled with gas and immersed in a fluid, subject to *Rayleigh-Plesset* like dynamics as described in (Church, 1995). An important difference with the aforementioned work should nonetheless be mentioned: since the position of the upper leaflet extremities is fixed due to membrane anchoring, the center of the equivalent bubble necessarily moves in space as the upper leaflet deflection changes, in order to ensure spherical symmetry at all times.

We start by defining a standard (r, θ, ϕ) spherical coordinate system where r represents the radial distance from the center of the cavity (i.e. the equivalent bubble in our case), and θ and ϕ specify the polar and azimuthal angles respectively. In order to study the mechanical behaviour of both the spherical leaflet and the liquid around it, we define τ_S and τ_L as their respective stress tensors. As for the dynamics, $u(r, t)$ denotes the radial velocity of a material element (leaflet or surrounding fluid) at a given distance $r \geq R(t)$.

Considering both the leaflets and surrounding fluid as incompressible materials, conservation of mass is applied. Since the system is spherically symmetric, the inverse-square law requires that $u(r, t)$ must be inversely proportional to the square of the distance from the center of the cavity (Brennen, 1995). Therefore, letting $F(t)$ be some function of time:

(35)

$$u(r, t) = \frac{F(t)}{r^2}$$

Assuming zero mass transport at the gas-leaflet interface ($r = R$), the radial velocity U at this radial distance equals the velocity of the cavity's boundary. Considering our system, this velocity is defined as the rate of change of the upper leaflet deflection with time, i.e. $U(t) = dZ/dt$. It is worth noting that this definition of interface velocity differs from the standard *Rayleigh-Plesset* problem, where it is

described as dR/dt . This difference arises from the fact that the cavity center does not remain fixed in space in our system. Therefore we have:

(36)

$$U(t) = \frac{dZ}{dt} = \frac{F(t)}{R^2}$$

Hence we can derive a generic expression for the radial velocity:

(37)

$$u(r, t) = \frac{R^2}{r^2} U(t)$$

We notice that u is a function of 2 variables: r and t . In order to avoid any confusion, we recall here that the distance r is not bound to the position of any physical element, contrarily to R . Therefore, the latter variable depends on time whereas the former does not. We can thus compute the partial derivatives of u :

(38)

$$\begin{cases} \frac{\partial u}{\partial t} = \frac{2R(t)}{r^2} \frac{dR}{dt} U(t) + \frac{R^2(t)}{r^2} \dot{U}(t) \\ \frac{\partial u}{\partial r} = -\frac{2R^2(t)}{r^3} U(t) \end{cases}$$

Following from equation (9), the variation of the curvature radius with time can be expressed in terms of the boundary velocity:

(39)

$$\frac{dR}{dt} = \frac{dR}{dZ} \frac{dZ}{dt} = \frac{Z^2(t) - a^2}{2Z^2(t)} U(t) = \left(1 - \frac{R(t)}{Z(t)}\right) U(t)$$

and the time derivative of u can be rewritten as:

(40)

$$\frac{\partial u}{\partial t} = \frac{2R(t)}{r^2} \left(1 - \frac{R(t)}{Z(t)}\right) U^2(t) + \frac{R^2(t)}{r^2} \dot{U}(t)$$

Hence, the *material derivative* of u (i.e. the rate of change of the velocity of a point particle as it moves about in space) can be expressed in spherical coordinates as the sum of a *time derivative* and an *advective* term:

(41)

$$\frac{Du}{Dt} = \frac{\partial u}{\partial t} + u \frac{\partial u}{\partial r} = \frac{2R \left(1 - \frac{R}{Z}\right) U^2 + R^2 \dot{U}}{r^2} - \frac{2R^4 U^2}{r^5}$$

where Z , R and U are obviously functions of time. Here the time derivative term represents the local variation of the radial velocity at a given point in space, while the advective term denotes the change in velocity when traveling along r . The latter is at the very origin of the nonlinearity of the system.

Conservation of radial momentum. With these definitions in mind, the governing equation of the system can be derived. Considering the conservation of radial momentum inside an infinitely small volume inside the leaflet (or the surrounding fluid), we apply the differential form of the Navier-Stokes equation in spherical coordinates:

(42)

$$\rho \left(\frac{\partial u}{\partial t} + u \frac{\partial u}{\partial r} \right) = -\frac{\partial P}{\partial r} + \frac{1}{r^2} \frac{\partial}{\partial r} (r^2 \tau_{rr}) - \frac{\tau_{\theta\theta} + \tau_{\phi\phi}}{r}$$

This equation basically states that the rate of change of the momentum of a point particle in the material results from a force that can be divided in two terms (Landau et al., 2011). First, a pressure term $-\partial P/\partial r$ representing the pressure gradient force acting per unit volume of the material. Second, a stress term (rest of the right-hand side) that denotes shear forces acting inside the material due to its viscosity (and, for leaflet, elasticity) attempting to bring the volume shape back into its equilibrium state. Although initially derived for fluids, equation (42) is also valid for viscoelastic solids, and is therefore applied to the leaflet.

Because the trace of the stress tensor τ is zero for both Newtonian fluids and viscoelastic solids (Landau et al., 2011), we have $\tau_{rr} = -(\tau_{\theta\theta} + \tau_{\phi\phi})$. Also, we can compute the partial derivative of the $r^2 \tau_{rr}$ term:

(43)

$$\frac{\partial}{\partial r} (r^2 \tau_{rr}) = 2r \tau_{rr} + r^2 \frac{\partial \tau_{rr}}{\partial r}$$

Hence equation (42) can be simplified as:

(44)

$$\rho \left(\frac{\partial u}{\partial t} + u \frac{\partial u}{\partial r} \right) = -\frac{\partial P}{\partial r} + \frac{\partial \tau_{rr}}{\partial r} + 3 \frac{\tau_{rr}}{r}$$

Integration with a solid surface layer. Considering a $[r_1, r_2]$ radial interval of homogeneous material (constant density), integration of equation (44) yields:

(45)

$$\begin{aligned} U^2 \left[2R \left(1 - \frac{R}{Z} \right) \left(\frac{\rho}{r_1} - \frac{\rho}{r_2} \right) + \frac{1}{2} R^4 \left(\frac{\rho}{r_2^4} - \frac{\rho}{r_1^4} \right) \right] + \dot{U} R^2 \left[\frac{\rho}{r_1} - \frac{\rho}{r_2} \right] \\ = P(r_1) - P(r_2) + \tau_{rr}(r_2) - \tau_{rr}(r_1) + 3 \int_{r_1}^{r_2} \frac{\tau_{rr}}{r} dr \end{aligned}$$

In order to characterize the global motion of our system, integration is performed in two separate intervals, namely from R to $R_* = R + \delta_0$ using the parameters appropriate for the leaflet, and from R_* to ∞ with those appropriate for the surrounding fluid. Summing up the two left-hand side terms yields an expression representing the time rate of change of the radial momentum carried by the entire system (leaflet and surrounding fluid):

(46)

$$\begin{aligned}
 I_1 &= \int_R^{R_*} \rho \left(\frac{\partial u}{\partial t} + u \frac{\partial u}{\partial r} \right) dr + \int_{R_*}^{\infty} \rho \left(\frac{\partial u}{\partial t} + u \frac{\partial u}{\partial r} \right) dr \\
 &= \left[2R \left(1 - \frac{R}{Z} \right) U^2 + R^2 \dot{U} \right] \left(\frac{\rho_S}{R} + \frac{\rho_L}{R_*} - \frac{\rho_S}{R_*} \right) - \frac{1}{2} R^4 U^2 \left(\frac{\rho_S}{R^4} + \frac{\rho_L}{R_*^4} - \frac{\rho_S}{R_*^4} \right) \\
 &= U^2 \left[2R \left(1 - \frac{R}{Z} \right) \left(\frac{\rho_S}{R} + \frac{\rho_L}{R_*} - \frac{\rho_S}{R_*} \right) - \frac{1}{2} R^4 \left(\frac{\rho_S}{R^4} + \frac{\rho_L}{R_*^4} - \frac{\rho_S}{R_*^4} \right) \right] + \dot{U} R^2 \left(\frac{\rho_S}{R} + \frac{\rho_L}{R_*} - \frac{\rho_S}{R_*} \right) \\
 &= U^2 \left[2 \left(1 - \frac{R}{Z} \right) \left(\frac{\rho_S}{R} + (\rho_L - \rho_S) \frac{R}{R_*} \right) - \frac{1}{2} \left(\rho_S + (\rho_L - \rho_S) \frac{R^4}{R_*^4} \right) \right] + \dot{U} R \left[\rho_S + (\rho_L - \rho_S) \frac{R}{R_*} \right] \\
 &= U^2 \left[\left(\frac{3}{2} - \frac{2R}{Z} \right) \rho_S + 2(\rho_L - \rho_S) \frac{R}{R_*} \left(1 - \frac{R}{Z} - \frac{1}{4} \frac{R^3}{R_*^3} \right) \right] + \dot{U} R \left[\rho_S + (\rho_L - \rho_S) \frac{R}{R_*} \right] \\
 &= U^2 \left[\left(\frac{3}{2} - \frac{2R}{Z} \right) \rho_S + (\rho_L - \rho_S) \frac{2 \left(1 - \frac{R}{Z} \right) R_*^3 - R^3}{2R_*^3} \right] + \dot{U} R \left[\rho_S + (\rho_L - \rho_S) \frac{R}{R_*} \right] \\
 &= \rho_S U^2 \left[\frac{3}{2} - \frac{2R}{Z} + \left(\frac{\rho_L - \rho_S}{\rho_S} \right) \frac{2 \left(1 - \frac{R}{Z} \right) R_*^3 - R^3}{2R_*^3} \right] + \rho_S R \dot{U} \left[1 + \left(\frac{\rho_L - \rho_S}{\rho_S} \right) \frac{R}{R_*} \right]
 \end{aligned}$$

while the addition of the right-hand side terms gives the sum of all pressure and shear forces acting on the system:

(47)

$$\begin{aligned}
 I_2 &= \int_R^{R_*} \left(-\frac{\partial P}{\partial t} + \frac{\partial \tau_{rr}}{\partial r} + 3 \frac{\tau_{rr}}{r} \right) dr + \int_{R_*}^{\infty} \left(-\frac{\partial P}{\partial t} + \frac{\partial \tau_{rr}}{\partial r} + 3 \frac{\tau_{rr}}{r} \right) dr \\
 &= P_S(R, t) - P_S(R_*, t) + P_L(R_*, t) - P_L(\infty, t) + \tau_{S,rr}(R_*, t) - \tau_{S,rr}(R, t) - \tau_{L,rr}(R_*, t) \\
 &\quad + 3 \int_{R(t)}^{R_*(t)} \frac{\tau_{S,rr}}{r} dr + 3 \int_{R_*(t)}^{\infty} \frac{\tau_{L,rr}}{r} dr
 \end{aligned}$$

Boundary conditions. We now consider more closely the two interfaces of the system, where conservation of momentum can also be applied. At the interface between the gas and the leaflet, two external forces act normally to the surface: the internal gas pressure P_G and the average intermolecular force per unit area P_M . Hence since the system global constraint must be conserved we have:

(48)

$$\underbrace{P_S(R) - \tau_{S,rr}(R)}_{\text{leaflet side}} = \underbrace{P_G + P_M}_{\text{cavity side}}$$

As for the interface between the leaflet and the surrounding fluid, we have:

(49)

$$\underbrace{P_S(R_*) - \tau_{S,rr}(R_*)}_{\text{leaflet side}} = \underbrace{P_L(R_*) - \tau_{L,rr}(R_*)}_{\text{fluid side}}$$

It is worth noting here that all terms in equations (48) and (49) depend on time. We also notice that the contribution of surface tension effects to the global constraint is neglected in both equations.

In the case of a dynamical system, the consideration of the mechanical response implies that fluid pressure cannot be considered uniform in space anymore. Particularly, the fluid pressure applying locally at the interface with the leaflet $P_L(R_*, t)$ is greatly influenced by the dynamics of the system. Oppositely, the fluid pressure far from the cavity $P_L(\infty, t)$ is not influenced by the system and thus remains unchanged, i.e. $P_L(\infty, t) = P_0 + P_A(t)$. Using these boundary conditions, equation (47) can be simplified:

(50)

$$I_2 = P_G + P_M - P_0 - P_A + 3 \int_R^{R_*} \frac{\tau_{S,rr}}{r} dr + 3 \int_{R_*}^{\infty} \frac{\tau_{L,rr}}{r} dr$$

We can already note that in the current system where positive transverse direction is pointing outward the BLS structure, the definition of pressures implies that P_G and P_M drive a positive momentum rate while P_0 and P_A act for a negative momentum rate. Let us now focus on the definition of the radial stresses τ_{rr} for the two layers of interest in our system.

Viscous stresses. For the Newtonian surrounding fluid, the radial stress only depends on the dynamic viscosity μ_L and simply evaluates as:

(51)

$$\tau_{L,rr} = 2\mu_L \frac{\partial u}{\partial r}$$

Hence, the integral term of the fluid radial stress in equation (50) equals:

(52)

$$3 \int_{R_*(t)}^{\infty} \frac{\tau_{L,rr}}{r} dr = -12\mu_L R^2 U \int_{R_*}^{\infty} \frac{dr}{r^4} = -4\mu_L \frac{R^2}{R_*^3} U$$

Since the leaflet layer exhibits a viscoelastic behaviour, its radial stress entails both a viscous and an elastic contribution. The former simply takes the form:

(53)

$$\tau_{S,rr,viscous} = 2\mu_S \frac{\partial u}{\partial r}$$

where μ_S is the monolayer leaflet dynamic viscosity. The viscous part of the leaflet stress integral term in equation (50) thus equals:

(54)

$$3 \int_R^{R_*} \frac{\tau_{S,rr,viscous}}{r} dr = -12\mu_S R^2 U \int_R^{R_*} \frac{dr}{r^4} = -4\mu_S U \left(\frac{R_*^3 - R^3}{RR_*^3} \right)$$

Hence, while shear stresses denote the local viscous constraints applying to the material, their integration yield terms that represent global viscous constraints applying on the entire fluid and leaflet layers. Since these constraints are expressed in Pascals, we will refer to them as *equivalent viscous pressures*, respectively P_{VS} and P_{VL} for the leaflet and fluid layers. The term "pressure" is used here for convenience, however to avoid confusion it must be recalled that such viscous stresses do not bear

the same physical meaning than regular isotropic pressures, since they depend on the velocity of the system. Nevertheless, we can define such viscous pressures as:

(55)

$$\begin{cases} P_{VS} = -4\mu_S U \left(\frac{R_*^3 - R^3}{RR_*^3} \right) \\ P_{VL} = -4\mu_L \frac{R^2}{R_*^3} U \end{cases}$$

These terms denote the resistance of the system to gradual deformation by shear stress, and therefore act against motion regardless of the dynamics of the leaflet. Mathematically speaking, P_{VS} and P_{VL} are negative when the sonopohre cavity is expanding ($U > 0$), and they are positive during compressive phases ($U < 0$).

Elastic stress. The latter, elastic contribution of the stretched layer is obtained differently. First, since $\tau_{S,rr,elastic}$ is expressed in N/m², dividing by r and integrating over a radial distance (as in equation (50)) will yield a term also expressed in N/m² representing the global elastic constraint applied on the leaflet. Just as for the viscous terms, we refer to this constraint as an *equivalent elastic tension pressure*, noted P_E , for consistency with other terms. Rather than integrating the local elastic stress to evaluate this constraint, a model of linear elasticity is applied: P_E is expressed in terms of a circumferential tension per unit length, noted T_E , divided by the leaflet curvature ($C = 1/R$). Thus we have:

(56)

$$3 \int_R^{R_*} \frac{\tau_{S,rr,elastic}}{r} dr = P_E = -\frac{T_E}{R}$$

The use of a linear elasticity model implies that we neglect the effects of leaflet bending and consider that the tension T_E only arises from an increase in the leaflet surface area, or *areal strain*, noted ϵ_A . The amount of tension developed for a given areal strain is expressed as:

(57)

$$T_E = k_A \epsilon_A = k_A \frac{S - S_0}{S_0}$$

where k_A denotes the *area compression modulus*. Since lipid monolayers are essentially two dimensional structures, k_A is typically defined only within the leaflet plane. Intuitively, one might expect that this modulus would vary linearly with the layer thickness as it would for a thin plate of isotropic material. In fact this is not the case and k_A is only weakly dependent on bilayer thickness. The reason for this is that the lipids in a fluid bilayer rearrange easily so, unlike a bulk material where the resistance to expansion comes from intermolecular bonds, the resistance to expansion in a bilayer is a result of the extra hydrophobic area exposed to water upon pulling the lipids apart (Boal, 2012). Therefore, k_A is not estimated from bulk parameters but rather measured experimentally. With this in mind, the equivalent elastic tension pressure can be expressed as:

(58)

$$P_E = -\frac{k_A}{R} \frac{S - S_0}{S_0} = -\frac{2k_A Z^3}{a^2(a^2 + Z^2)}$$

The minus sign in equations (56) and (58) is introduced for physical soundness, since the elastic tension pressure, by definition, acts against deflection to bring the leaflet back to its unstretched position, and must therefore be negative.

Using the boundary conditions and newly defined pressure terms, we can assemble the governing equation of the dynamical bilayer sonophore system:

$$\begin{aligned} & \rho_S U^2 \left[\frac{3}{2} - \frac{2R}{Z} + \left(\frac{\rho_L - \rho_S}{\rho_S} \right) \frac{2 \left(1 - \frac{R}{Z} \right) R_*^3 - R^3}{2R_*^3} \right] + \rho_S R \dot{U} \left[1 + \left(\frac{\rho_L - \rho_S}{\rho_S} \right) \frac{R}{R_*} \right] \\ & = P_G + P_M - P_0 - P_A + P_E + P_{VS} + P_{VL} \end{aligned} \quad (59)$$

Density considerations. Considering a configuration in which the BLS is part of the thin membrane of a nerve cell, further simplifications can be made. In fact, we can assign the densities of the leaflet and fluid media to those of a phospholipid-cholesterol mixture at 20°C (1.01 g/cm³, (Johnson and Buttress, 1973)) and human nerve tissue (1.075 g/cm³, (IT'IS Foundation, 2015)), respectively. Given such similar values, the system is simplified by stating that $\rho_S = \rho_L$. By doing so, we neglect the effects of the density difference between the leaflet and fluid layers on their mechanical response, and equation (59) becomes:

$$\rho_L U^2 \left[\frac{3}{2} - \frac{2R}{Z} \right] + \rho_L R \dot{U} = P_G + P_M - P_0 - P_A + P_E + P_{VS} + P_{VL} \quad (60)$$

Nonlinearity. The first term of (60) introduces a nonlinearity in the equation. This inertial term is directly proportional to the square of leaflet radial velocity. Particular attention must be paid here to the multiplying factor of the square leaflet velocity, as this term differs by a factor $f = 1 - 4R/3Z$ from the one obtained by (Krasovitski et al., 2011) whose publication was taken as reference for the present work. For the sake of consistency though, it is chosen to use the same simplification in this study. Therefore, equation (60) becomes:

$$\frac{3}{2} \rho_L U^2 + \rho_L R \dot{U} = P_G + P_M - P_0 - P_A + P_E + P_{VS} + P_{VL} \quad (61)$$

Leaflet thickness approximation. At this point, assumption is made that the instantaneous curvature radius of the leaflet is significantly greater than its thickness, i.e. $R \gg \delta_0$. Consequently, a few simplifications can be made. First, the leaflet thickness can be neglected when considering the viscous response of the fluid. In mathematical terms, this can be viewed as a change in the integration interval of the fluid viscous stress, from $[R_*, \infty[$ to $[R, \infty[$. Therefore, the fluid viscous pressure is approximated by:

$$P_{VL} \simeq - \frac{4\mu_L U}{R} \quad (62)$$

As for the viscous response of the leaflet, the layer thickness is obviously of critical importance and therefore cannot be neglected. In fact, we can see in equation (55) that the leaflet viscous pressure is proportional to the difference between R_*^3 and R^3 . Hence, let us derive a simplified expression for this

difference that accounts for the leaflet thickness. Considering δ_0 as a variable and letting R be fixed, we define the function $f(\delta_0) = R_*^3(\delta_0) = (R + \delta_0)^3$. For an infinitely thin layer, we can thus derive a first-order Taylor polynomial approximation of f around zero:

(63)

$$f(\delta_0) \simeq f(0) + \delta_0 f'(0) = R^3 + 3R^2\delta_0$$

Using this approximation, the difference between the inner and outer radii can be written as:

(64)

$$R_*^3 - R^3 = 3R^2\delta_0$$

However, since the denominator of the leaflet viscous pressure term does not represent a direct measure of this "difference", the leaflet thickness is neglected therein by approximating that $R_*^3 = R^3$. Combining these two assumptions, P_{VS} can be approximated as:

(65)

$$P_{VS} \simeq -\frac{12\mu_s\delta_0 U}{R^2}$$

Negative deflections. The equations of the dynamical system have been derived under the inherent assumption of a negative (rarefactional) acoustic perturbation that caused a outward deflection of the leaflets ($Z > 0$). Since ultrasound perturbations consist of a sign-changing sinusoidal pressure wave, we also need to consider the case of a positive acoustic pressure causing a thinning of the inter-leaflet space ($Z < 0$). In this configuration, the intuitive representation of the BLS structure as a gas-filled bubble immersed in an infinite fluid does not hold anymore. Nonetheless the system is still spherically symmetry, therefore it is assumed that equation (61) can apply to the negative deflection range owing to some modifications.

Two points are worth addressing here. As previously mentioned, the leaflet curvature is a signed measure and in the case of $Z < 0$ it must be negative. Moreover, the deflection velocity U still points outward the BLS structure in this new configuration. Therefore, a positive velocity depicts a leaflet whose deflection decreases in amplitude, coming back to its equilibrium state. Oppositely, a negative velocity corresponds to a leaflet whose negative deflection is gaining in amplitude.

With this mind, the static pressure terms (P_M , P_G , P_0 and P_A) have the exact same meaning and must therefore have the same influence on the rate of momentum of the system. In order to act against the leaflet negative deflection, the elastic tension pressure must this time be positive. In fact, P_E is by definition of opposite sign to that of the curvature radius, and will therefore be positive for $Z < 0$. Finally, in order to act against leaflet motion, viscous pressures must be positive for $U < 0$ and negative for $U > 0$. In order to satisfy this criterion, the fluid viscous pressure is redefined as:

(66)

$$P_{VL} = -\frac{4\mu_L U}{|R|}$$

Finally, since the leaflet apex acceleration \dot{U} is also points outwards the BLS structure, it must be defined such that a positive resultant pressure (right-hand side of equation (61)) drives an increase in deflection velocity. In order to fulfill this condition for both positive and negative deflections, equation (61) is divided by $\rho_L R$ and the curvature radius dividing the right-hand side of the new equation is

considered in absolute value. Recalling that $U = dZ/dt$, we thus drive a final form of the bilayer sonophore dynamical system governing equation:

(67)

$$\frac{d^2Z}{dt^2} = -\frac{3}{2R} \left(\frac{dZ}{dt} \right)^2 + \frac{1}{\rho_L |R|} [P_G + P_M - P_0 - P_A + P_E + P_{VS} + P_{VL}]$$

This second-order differential equation states that the leaflet apex acceleration \ddot{U} is the sum of a *pressure-driven acceleration* (right-hand side) and a *nonlinear acceleration* ($-3U^2/2R$). The latter term - as currently defined - is of opposite sign to that of Z regardless of the deflection dynamics (i.e. the sign of U) and therefore tends to bring the system back to its equilibrium, flat configuration at all times. Finally, it is worth noting because of its nonlinearity, equation (67) does not bear any analytical solution, and will be solved by numerical integration methods.

2.1.4.3 Embedding in cellular tissue

So far we have “naively” considered the environment surrounding the BLS structure as a simple viscous fluid, in order to derive a system’s governing equations similar to that of Rayleigh-Plesset for a spherical bubble. While this assumption can be reasonable for cells directly interfacing a fluidic medium (e.g. endothelial cells at the free surface of capillary lumen), it is far from realistic for membranes of most cells lying deep in cellular tissue, particularly neurons. As mentioned in (Krasovitski et al., 2011), when the membrane is within or between cells, the periodic expansion of the outward leaflet in the bilayer sonophore is associated with pushing and stretching of nearby cellular structures, and that additional resistance substantially limits the leaflet expansion amplitude. This effect is incorporated into the model as an additional *tissue membrane* of thickness d_{tissue} made of a linear viscoelastic isotropic continuum, connected in parallel to the BLS moving leaflet. Here again, bending effects are neglected and a linear elasticity model is used that defines the amount of tension developed to be proportional to the areal strain of the layer. However, given the 3-dimensional nature of the surrounding cellular tissue, its areal expansion modulus should increase linearly with the layer thickness. Assuming a purely *deviatoric* stress (i.e. a stress that distorts the cellular layer without inducing any change in volume), the strain to stress ratio of an infinitesimally thin tissue lamina is defined as $2\tilde{G}$, where \tilde{G} is the *dynamic shear modulus* of the tissue ((Reismann and Pawlik, 1991), p. 132). Considering the apparent thickness of the layer, we obtain $k_{A,tissue} = 2\tilde{G}d_{tissue}$.

Due to its viscoelastic nature, cellular tissue subject to mechanical tension is characterized by a inherent relaxation time (during which the stress progressively decays to zero as the network relaxes), which implies that its effective shear modulus is time-dependent ((Boal, 2012), section 6.5.2). Under vibratory conditions such as the ones induced by the moving leaflet, this modulus is more easily expressed as a complex number in the frequency domain:

(68)

$$\tilde{G}(\omega) = G_s(\omega) + jG_l(\omega)$$

Here ω is the angular vibration frequency, and G_s and G_l respectively denote the *shear storage* and *shear loss* moduli. The real part is a measure of the elastic energy stored and retrieved from the system, while the imaginary part represents the amount of energy dissipated as heat (i.e. the viscous portion) ((Boal, 2012), section 6.5.2). While both moduli are frequency dependent, rheology experiments on smooth muscle cells (Fabry et al., 2001) predict that (1) the shear loss modulus is expected to dominate at high frequencies ($f > 300$ Hz), and (2) G_l is almost linearly dependent on the frequency in the ultrasonic range. Hence, we will assume here that $\tilde{G} \simeq G_l \propto f$. As a further

simplification, strain variations along the layer transverse direction (due to bending) are neglected, such that the tissue is assumed to experience the exact same areal expansion as the moving leaflet. Consequently, the viscoelastic tension per unit length developing in the tissue layer can be expressed as:

(69)

$$T_{tissue} = k_{A,tissue}\epsilon_A = 2G_l(\omega)d_{tissue}\epsilon_A$$

This tension is then added to that of the leaflet, yielding the following total elastic tension:

(70)

$$T_E = (k_A + k_{A,tissue})\epsilon_A$$

2.1.5 Assumptions

In order to obtain a model that is both mathematically valid and of reasonable complexity, several assumptions and simplifications have been made regarding the geometry, the applied forces and the dynamical behaviour of the system. This section is an attempt to clearly formulate them, and to provide justifications when possible.

BLS structure. First of all, the bilayer sonophore structure is approximated as a disk-shaped surface with continuous mechanical anchoring at the radial extremities of both layers. While this structured, circular organization can seem unrealistic, analogous distribution patterns are in fact observed in real cell membranes as shown in (Lillemeier et al., 2006). Moreover, the spatial extent of a single bilayer sonophore structure is assumed to be small compared to the acoustic wavelength, so that the acoustic pressure can be considered spatially uniform at a given time. On a more mechanical aspect, the effects of leaflet bending upon compression/expansion of the BLS structure, including surface tension, are neglected. This is a misrepresentation of reality since biological membranes are found to have a bending resistance ((Boal, 2012), section 7.4), however it is supposed here that its influence is negligible compared to the one arising from leaflet elastic tension. Furthermore, the model assumes that spatially uniform condition exist inside the BLS cavity. While this seems reasonable in terms of gas pressure, it is not true for intermolecular forces who vary locally with the inter-leaflet gap and could therefore greatly influence the pressure balance, especially for short inter-leaflet distances. Finally, perhaps the most impacting assumption is that of *spherical symmetry*, assumed at all times in order to derive the system's equations. While it can be argued that the range of leaflet deflections considered in this model will not produce a high global curvature, tremendous fluctuations can occur locally, particularly at the leaflet extremities. In fact, it seems difficult to imagine a perturbed leaflet that would conform to a perfect spherical shape, given the anchoring constraints brought by the transmembrane proteins. However, accounting for such local variations would greatly complicate the problem by introducing some spherical harmonics in the dynamics of the system, and are therefore neglected here.

Surrounding media. As a first and practical approximation, no difference is made between the cytoplasmic and extracellular sides of the bilayer sonophore structure, both considered as uniform fluid-like media with identical properties (i.e. density and viscosity), expanding to infinity. These two assumptions (symmetry and infinite limits) greatly simplify the initial system and allow to derive a governing equation (equation (67)) in the first place. In a second phase, an additional layer of viscoelastic cellular tissue is added in parallel to the moving leaflet, in order to represent the mechanical resistance of the surrounding environment (and possibly also the intracellular cytoplasm) to deformation. Although this addition to the model somehow corrects the first assumption, the amplitude of the new pressure term greatly depends on the arbitrary choice of effective tissue

thickness. In addition, this geometric parameter is expected to vary substantially depending on the embedding level of the cells of interest. On a different aspect, it is worth noting that gravitational forces are neglected thereby yielding a constant fluid static pressure.

Homogeneous density. Beyond the approximations made on individual components of the bilayer sonophore structure, further simplification of the system is made by neglecting the density difference between the membrane monolayers and the surrounding media.

Quasi-steady approximation. The quasi-steady system governed by equation (16) is obtained by neglecting the mechanical response of the leaflet and surrounding fluid. That is, both layers are regarded as inertia-free components that do not bear any disinclination to move. Consequently, their behaviour is totally determined by the quasi-steady balance equation. While this simplified system does not apply for large leaflet deflections and deflection velocities, it allows to solve the initial impact of an acoustic perturbation on resting bilayer sonophore structure ($Z = 0$) for which the more general governing equation fails numerically.

Leaflet thickness. In order to simplify the governing equation, the viscous pressure terms were corrected by either neglecting the leaflet thickness or approximating it with a first-order Taylor polynomial. While questions can be raised about the strategy of applying different treatments for a single simplification, the underlying assumption that $R \gg \delta_0$ is reasonable. In fact, a typical circular patch of proteins is about 50-100 nm in diameter (Lillemeier et al., 2006), and the corresponding sonophore radius is thus more than one order of magnitude greater than the monolayer thickness ($\delta_0 = 2 \text{ nm}$).

Nonlinear term. As previously mentioned, the full derivation of the system's governing equation in section 2.4.2 revealed that the nonlinear term differed by a factor $f = 1 - 4R/3Z$ compared to that of the established bilayer sonophore governing equation ((Krasovitski et al., 2011), supplementary material), adapted from the Rayleigh-Plesset equation of a standard gas bubble with an elastic surface layer (Church, 1995). In such a system, the bubble center is considered fixed in space and the velocity at the interface is simply dR/dt . In the bilayer sonophore system however, the structure is not anchored at the virtual center of the bubble but rather on a ring in its periphery. This constraint imposes to compute the interface velocity from the leaflet deflection Z (the fixed frame metrics in this system), as dZ/dt . Therefore, the term dR/dt becomes an indirect measure of the interface velocity, differing by a factor $1 - R/Z$, as shown in equation (39). This change then propagates through the derivation process up to equation (60), where the factor becomes $1 - 4R/3Z$. Hence, it seems that the BLS equation of (Krasovitski et al., 2011) was directly derived from the final equation of (Church, 1995), thereby explaining the absence of the multiplying factor. For the sake of consistency with reference studies, it is chosen here to ignore this factor, although it could potentially have a significant influence on the dynamics of the system that should be further investigated.

2.1.6 Parameters

Most parameters used in this study are taken directly from the two works of reference on intramembrane cavitation by Krasovitski (Krasovitski et al., 2011) and Plaksin (Plaksin et al., 2014). It should be mentioned here that these two modeling studies were designed to study the behaviour of different tissues for different experimental conditions, namely epithelium at room temperature (around 20 – 25°C) for the former and brain tissue at physiological conditions (36°C) for the latter. Therefore, some parameters of the model differ notably between the two studies, especially those that are temperature-sensitive. Consequently, a detailed explanation of the choice of each parameter is provided in this section for clarification purposes.

First, since the long-term purpose of this analysis is to study the behaviour of peripheral neural tissue exposed to ultrasound, the system's temperature is set to the same physiological conditions as in (Plaksin et al., 2014), i.e. 36°C (or 309.15 K). The static pressure term P_0 is defined as the standard sea level atmospheric pressure (neglecting hydrostatic effects), and R_g as the universal gas constant ((Wong, 1977), p. 203).

Leaflet parameters. Equation (13) provides a generic expression of local intermolecular pressure with unresolved parameters. These are determined by fitting the intermolecular model to empirical data for repulsion/attraction forces between amphiphilic bilayers (Helm et al., 1989; Israelachvili, 1992) (assuming they are the same as between two leaflets of the same membrane), while imposing a few conditions in order to reduce the number of degrees of freedom. While these conditions are not specifically detailed in (Krasovitski et al., 2011), it is supposed that the authors chose to arbitrarily set the pressure coefficient p_Δ and inter-leaflet gap Δ to 10^5 Pa and 1.4 nm respectively, and then used least-square fitting on a distance shifted-dataset of ((Helm et al., 1989), fig. 4) to determine the repulsion and attraction coefficients as $m = 5$ and $n = 3.3$. Given the lack of details on the imposed conditions and fitting methods, as well as the sparse literature on the subject, it is chosen to use the same parameter values in this work in order to ensure, if not absolute physical validity, consistency with reference studies. As for the thickness of the leaflet itself, it is defined as the approximate length of a hydrocarbon chain in a single membrane layer ((Boal, 2012), p. 246).

Fluid density. The density of the surrounding medium is set to the physiological value of 1075 kg/m^3 reported for human nerve tissue, while its dynamic viscosity is approximated as that of water at 36°C, i.e. $7 \cdot 10^{-4} \text{ Pa}\cdot\text{s}$ (IT'IS Foundation, 2015), which is the value used in (Plaksin et al., 2014).

Viscosities. Given the sparse literature on cell membrane viscosity measurements, the authors of (Krasovitski et al., 2011) and (Plaksin et al., 2014) guessed that a membrane leaflet possesses similar viscous properties as standard oils, with a temperature dependent dynamic viscosity in the order of $[10^{-2} - 10^{-1}] \text{ Pa}\cdot\text{s}$. For consistency, they fixed a ratio of $\mu_s/\mu_L = 50$ in both studies. The same strategy is applied here, with $\mu_s = 0.035 \text{ Pa}\cdot\text{s}$ as in (Plaksin et al., 2014).

Gas concentration and Henry's constant. The initial gas concentration (C_0) and Henry's constant (k_H) are two intricately linked parameters, whose dependency arises from the steady-state definition. Such a system is characterized by the equalization of static pressures ($P_G = P_0$), but also by the absence of gas flux across the leaflet ($\dot{n}_g(t) = 0$, i.e. $C_s = C_0$). Recalling that the surface concentration C_s is directly linked to the inner gas pressure by Henry's constant (cf. equation (29)), it follows that the product $C_0 k_H$ must necessarily equal the static pressure P_0 . Considering the solubilization of air in water in this case, Henry's constant exhibits a strong temperature dependency. It is easily computed at 25 °C from the weighted values of the gas species composing the mixture (Sander, 2015). However at 36°C very few (if any) direct measures of k_H are available in the literature. Hence, the authors of (Plaksin et al., 2014) seem to have used solubility values of oxygen and nitrogen in pure water around 309 K (Geng and Duan, 2010; Sun et al., 2001) in order to compute a resulting gas concentration in water of 0.62 mol/m^3 at that temperature. Using this as a reference for C_0 , Henry's constant is then derived as $k_H = 1.613 \cdot 10^5 \text{ Pa}\cdot\text{m}^3\cdot\text{mol}^{-1}$. Interestingly, the authors of (Plaksin et al., 2014) found a slightly different value for Henry's constant ($k_H = 1.63 \cdot 10^5 \text{ Pa}\cdot\text{m}^3\cdot\text{mol}^{-1}$). Nevertheless, the values computed here are used in this study.

Diffusion coefficient. The diffusion coefficient of gas in the surrounding fluid D_{gl} also varies between the two reference studies due to the temperature difference. Using the diffusion coefficient of air in water as a reference, a linear interpolation from the table of (Wise and Houghton, 1966) gives values of $2.85 \cdot 10^{-9}$ and $3.68 \cdot 10^{-9} \text{ m}^2\cdot\text{s}^{-1}$ for 25 and 36°C respectively. Pairwise comparison shows that these

values are significantly higher than those used in the two reference studies, which might have underestimated the diffusion coefficients. Consequently, a value of $D_{gl} = 3.68 \cdot 10^{-9} \text{ m}^2 \cdot \text{s}^{-1}$ is used in this work. As for the thickness of the boundary layer for gas transport across the leaflet, no direct measurement can be found in the literature therefore it is chosen to use the same value that was guessed by the authors in (Plaksin et al., 2014), i.e. $\xi = 0.5 \text{ nm}$. It is worth noting that this value is four times smaller than the actual leaflet thickness used in the geometric model, hence the authors have likely considered that the gas transport boundary layer was only constituted by a small fraction of the transverse phospholipid structure (probably the more spatially constrained hydrophilic part).

Membrane elastic modulus. As mentioned in (Krasovitski et al., 2011), the area compression modulus of the leaflet can take a wide range of values. In fact, when not subject to high tensile stresses lipid membranes strongly undulate under thermal fluctuations (Sens and Safran, 1998). Therefore, stretching the leaflet primarily flattens it, overcoming its bending resistance k_{bend} , before actually inducing an increase in area per molecule and acting against its stretching resistance $k_{stretch}$. Experimental measures reveal that for bilayer membranes, k_{bend} takes significantly lower values (around 0.08 N/m (Phillips et al., 2009)) than $k_{stretch}$ (mean value of 0.24 N/m measured on lipid diOPC bilayers through micropipette pressurization techniques (Rawicz et al., 2000)). Therefore k_A is set to 0.24 N/m in the present work, in order to account for both bending and stretching stiffness, under the notable assumption that monolayers and bilayers possess similar stretching properties. Interestingly, while this value is also mentioned in the supplementary material of (Krasovitski et al., 2011), this reference chose a significantly lower range of compression moduli for its simulations (0.03 – 0.12). However, a modulus of 0.24 N/m is also used in (Plaksin et al., 2014).

Tissue elastic modulus. As previously mentioned, the shear loss modulus G_l of the tissue layer is assumed to depend linearly on f for sufficiently high frequencies, based on observations from (Fabry et al., 2001). However, neither the authors of (Fabry et al., 2001) or (Krasovitski et al., 2011) provide an explicit coefficient, and the depicted modulus profile depicted on (Fabry et al., 2001) (fig. 2) does not allow to perform accurate linear regression over the high frequency range ($f > 100 \text{ kHz}$) since the dataset only spans part of the audible range ($f < 1 \text{ kHz}$). Nevertheless, a linear regression was approximated between two characteristic points arbitrarily chosen in the (x, y) logarithmic grid. The proportionality constant $\alpha = G_l/f$ was computed as 7.56 Pa.s.

Sonophore dimensions. Lastly, the in-plane radius of the BLS structure (i.e. the radius of the leaflet boundary), despite being subject to tremendous variation according to TEM measurements on T-cells (Lillemeier et al., 2006) was set to 32 nm in (Plaksin et al., 2014). This value was derived from the average distance between neighboring proteins in native oocytes ($\bar{d} = 53 \text{ nm}$) (Pralle, 1998), although differences might exist with the membrane organization of neuronal structures (particularly nodes of Ranvier in myelinated axons). Also, the derivation of sonophore radius was defined by the authors of (Plaksin et al., 2014) as *half of the unit cell's diagonal* assuming a rectangular grid geometry. While this assumption seems reasonable, applying this rule yields to a different value of BLS radius ($a = 0.5\sqrt{\bar{d}} = 37.5 \text{ nm}$) than the one they reported. Nonetheless, the BLS radius is also primarily set to $a = 32 \text{ nm}$ in this study for consistency with (Plaksin et al., 2014). The influence of this parameter on the system, shown in (Krasovitski et al., 2011), should nonetheless be kept in mind during further investigations.

A detailed list of the biomechanical parameters used in the present study is detailed in **Table 1**, along with the source from which it was taken or derived.

Parameter	Symbol	Value	Unit	Source
Temperature	T	309.15	K	(Plaksin et al., 2014)
Universal gas constant	R_g	8.314	$\text{Pa} \cdot \text{m}^3 \cdot \text{mol}^{-1} \cdot \text{K}^{-1}$	(Wong, 1977)
Thickness of the leaflet	δ_0	2	nm	(Boal, 2012; Krasovitski et al., 2011)

Gap between the two leaflets at equilibrium	Δ	1.4	nm	(Krasovitski et al., 2011)
Attraction/repulsion pressure coefficient	p_A	10^5	Pa	
Exponent in the repulsion term	m	5	-	
Exponent in the attraction term	m	3.3	-	
Density of the surrounding fluid	ρ_L	1075	kg·m ⁻³	(IT'IS Foundation, 2015)
Dynamic viscosity of the surrounding fluid	μ_L	$7 \cdot 10^{-4}$	Pa·s	(IT'IS Foundation, 2015; Plaksin et al., 2014)
Dynamic viscosity of the leaflet	μ_s	0.035	Pa·s	(Plaksin et al., 2014)
Area compression modulus of the leaflet	k_A	0.24	N/m	(Krasovitski et al., 2011; Phillips et al., 2009; Rawicz et al., 2000)
Tissue layer shear loss modulus coefficient	α	7.56	Pa·s	(Fabry et al., 2001)
Initial gas molar concentration in fluid	C_0	0.62	mol·m ⁻³	(Boal, 2012; Geng and Duan, 2010; Sun et al., 2001)
Henry's constant	k_H	$1.613 \cdot 10^5$	Pa·m ³ ·mol ⁻¹	
Static pressure in the surrounding fluid	P_0	10^5	Pa	(Wong, 1977)
Diffusion coefficient of gas in fluid	D_{gl}	$3.68 \cdot 10^{-9}$	m ² ·s ⁻¹	(Wise and Houghton, 1966)
Boundary layer thickness for gas transport	ξ	0.5	nm	(Plaksin et al., 2014)

Table 1: Summary of the biomechanical parameters of the model (symbol, value, unit and source) used in this work.

2.1.7 Numerical resolution

Simulating the model comes down to computing the temporal evolution of the anti-symmetric leaflet apex deflection in the sonophore structure, given an acoustic perturbation of specific amplitude and frequency. For this purpose, *quasi-steady* and *dynamical* systems have been defined for mutually exclusive deflection ranges, each one associated with a governing equation that can be solved numerically. With this in mind, the resolution procedure should consist of a hybrid iterative algorithm alternating between the two governing equations in order to compute the leaflet deflection vector for a given set of temporal samples.

That being said, it is worth recalling that the *quasi-steady* system bears assumptions that are highly questionable from a biomechanical standpoint. Therefore, one can question the need to use this simplified system in the first place: why not just use the more comprehensive, *dynamical* system for all conditions? The answer is that this dynamical system, defined under the assumption of spherical symmetry, is not adapted to model the dynamics of a flat sonophore structure. In fact, this geometric configuration implies an infinite leaflet curvature radius that necessarily restricts the leaflet acceleration components to zero (cf. equation (67)). This restriction is of particular concern for any system initially at steady-state ($Z = 0$, $U = 0$): the application of an external acoustic perturbation, despite producing a net resultant pressure on the leaflet, would not produce any acceleration, and therefore no kinematic change on the BLS structure. Any other case would however result in leaflet motion, either via its intrinsic velocity ($U \neq 0$) or because of the net acceleration generated by the system imbalance ($Z \neq 0$).

Considering this problematic, it is chosen to restrict the *quasi-steady* deflection range to its minimum by setting $Z_{min} = 0$. By applying this criterion, the *quasi-steady* system should theoretically be used only once, for the first time step following stimulation offset, in order to give the system some momentum. After that, the more comprehensive *dynamical* system is used. In parallel, the evolution of the gas molar content inside the sonophore cavity is calculated using the *one-dimensional steady-state* diffusion model for its simplicity and computational speed, as well as for consistency with the more recent reference for the NICE model (Plaksin et al., 2014).

2.1.8 Dynamical behavior

2.1.8.1 Typical behavior

We first provide a qualitative description the model behavior under “typical” conditions, that is, the cavitation of a typical sonophore structure (32 nm in-plane radius, no additional tissue layer), upon perturbation by a sinusoidal acoustic pressure wave of frequency $F_{drive} = 500$ kHz and amplitude $A_{drive} = 0.5$ MPa (Figure 4). Rarefactional periods induce a rather smooth sonophore expansion that

coincides with an increase the leaflets elastic tension and triggers gas transport into the cavity. As the acoustic pressure decreases in magnitude, the sonophore progressively falls back towards its equilibrium position, triggering an opposite gas flux towards the surrounding fluids. It is worth noting that the expansion apex, as well as the maximal gas accumulation, coincide with the time of peak rarefactional acoustic pressure. By contrast, intervals of positive pressure induce a limited and vibratory sonophore compression (resulting from the highly nonlinear increase in repulsive molecular pressure forces) and virtually no gas transport across the membrane.

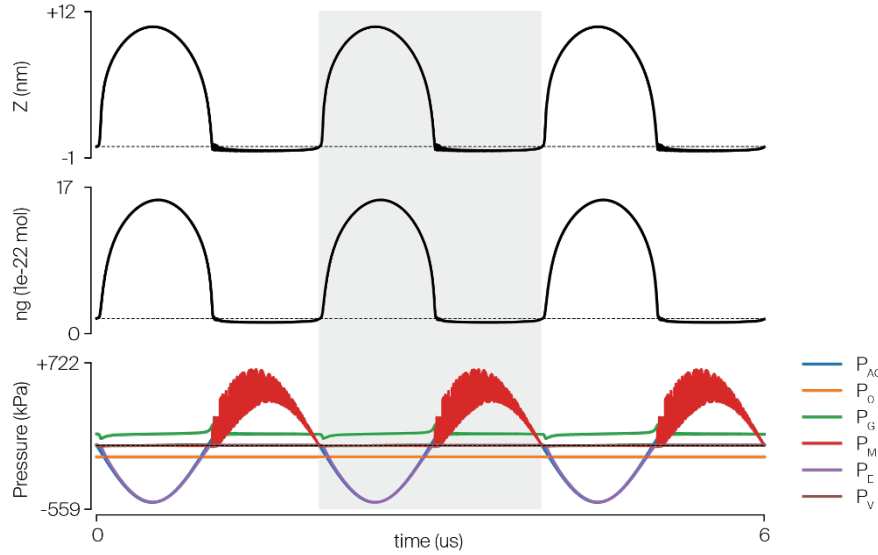


Figure 4. Typical behavior of the mechanical model. Leaflet deflection, gas content, and pressures evolutions during the simulation of a sonophore with typical in-plane radius ($a = 32$ nm) with standard stimulation parameters ($F_{\text{drive}} = 500$ kHz, $A_{\text{drive}} = 0.5$ MPa).

2.1.8.2 Influence of sonophore dimensions

Among all the parameters defining the mechanical model, the sonophore in-plane radius is probably one of those subject to the largest variations, as mentioned in section 2.1.6. Hence, we study here the influence of this parameter on the dynamics and amplitude of intramembrane cavitation.

Expectedly, narrow sonophore structures ($a = 15$ nm, **Figure 5a**) show a smaller cavitation amplitude compared to the typical sonophore. Moreover, high-frequency oscillations in the deflection profile observed during compressed phases are greatly reduced. Wide sonophore structures ($a = 500$ nm, **Figure 5b**) show a greater cavitation amplitude than that of a “typical” sonophore, and more strikingly, vibratory dynamics is also observed during expansion phases as a result of the larger system inertia. Due to this highly sensitive dynamics and intrinsic inertia, the wider structure takes a few cycles to reach a periodically stable behavior. Overall, cavitation amplitude and resulting maximal membrane areal strain during rarefactional periods both increase with the sonophore radius (**Figure 5c**).

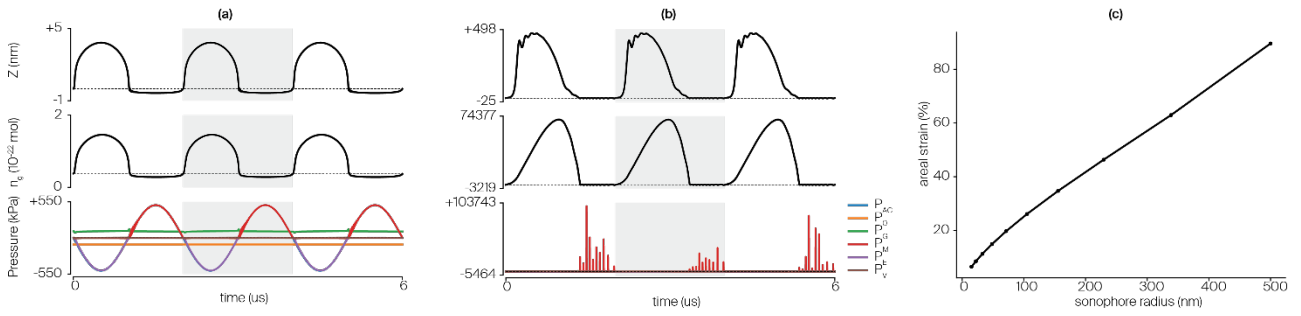


Figure 5. Impact of sonophore radius on cavitation dynamics. (a) Leaflet deflection, gas content, and pressures evolutions during the simulation of a sonophore with small in-plane radius ($a = 15$ nm) and with standard stimulation parameters ($F_{\text{drive}} = 500$ kHz, $A_{\text{drive}} = 0.5$ MPa). (b) Idem, but with a large in-plane radius ($a = 500$ nm). (c) Maximal membrane areal strain as a function of sonophore in-plane radius.

2.1.8.3 Influence of tissue embedding

Just like the diameter of the BLS structure, the extent of surrounding tissue embedding the resonating plasma membrane is also subject to tremendous variation, depending on the location of the target nervous cell in the body. Hence, it is also of crucial importance to understand the impact of the surrounding tissue embedding the cell on the cavitation dynamics.

As anticipated, structures with a limited amount of tissue embedding show a highly similar cavitation dynamics as an exposed sonophore (Figure 6a). By contrast, deeply embedded sonophores show a great reduction in cavitation amplitude caused by the increase in elastic tension (Figure 6b). Overall, the maximal areal strain caused by intramembrane cavitation shows an inverse dependency on the tissue embedding depth, where layers thicker than a few microns prevent any significant membrane deflection during rarefaction periods (Figure 6c).

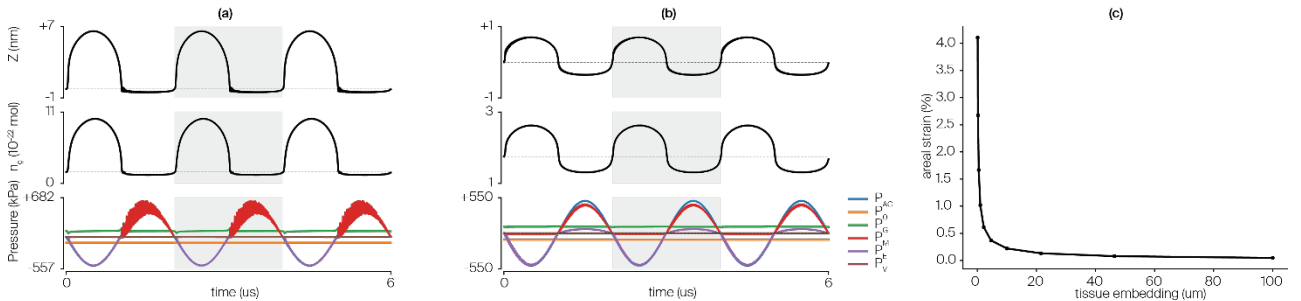


Figure 6. Impact of sonophore tissue embedding on cavitation dynamics. (a) Leaflet deflection, gas content, and pressures evolutions during the simulation of a sonophore (32 nm in-plane radius) with small tissue embedding (0.01 μm), and with standard stimulation parameters ($F_{\text{drive}} = 500$ kHz, $A_{\text{drive}} = 0.5$ MPa). (b) Idem, but with a large tissue embedding (100 μm). (c) Maximal membrane areal strain as a function of sonophore tissue embedding.

2.1.8.4 Impact of stimulation parameters

The previous analyses assessed the sensitivity of the system to anatomical parameters over which we have no control. We will now investigate the influence of stimulation parameters on the cavitation dynamics, which is a much more exciting prospect given the fact that these parameters can be tuned in order to elicit the mechanoelectrical response of interest.

Simulations in an exposed sonophore show that cavitation magnitude increases monotonically with pressure amplitude (with a sharp increase around 20 kPa) and show almost no dependency on stimulation frequency over the 20 kHz – 4 MHz range (Figure 7a). By contrast, embedded sonophores show much smaller cavitation amplitudes and a more pronounced dependency on stimulus periodicity: indeed, the frequency-dependency of the tissue elastic modulus generates a higher resistance to motion – and thus smaller cavitation amplitudes – at higher frequencies (Figure 7b).

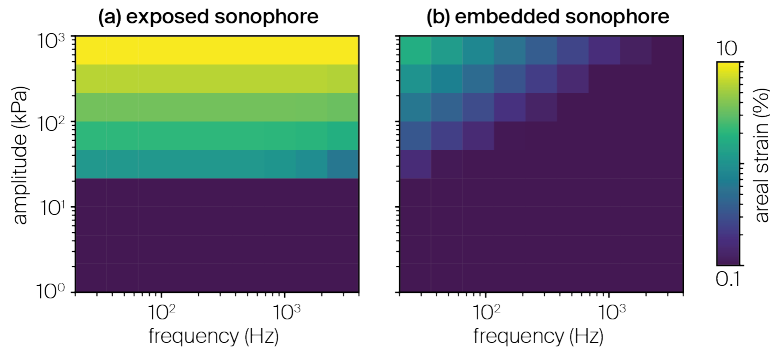


Figure 7. Impact of stimulation parameters on cavitation amplitude. Two-dimensional maps showing the maximal membrane areal strain during the cavitation of a sonophore (32 nm in-plane radius) as a function of acoustic frequency and amplitude. (a) Exposed sonophore. (b) Sonophore embedded in a 10 μm thick tissue layer.

2.1.9 Numerical stiffness and computational cost

Beyond informing on the model's dynamical behavior, the profiles displayed in section 2.1.8 emphasize the important numerical stiffness of the bilayer sonophore model. In fact, the presence of highly nonlinear internal components influencing the pressure balance (in particular molecular forces) induces the generation of vibratory resonance in the resulting kinematic output at frequencies much higher than the fundamental ultrasonic frequency. As a result of this system stiffness, numerical integration must be carried out with costly integration procedures (implicit, multi-step, variable order solvers (Hindmarsh, 1983; Petzold, 1983)) and to use many time steps per acoustic period (1000 in our implementation) to ensure stable integration of intra-cycle system oscillations. Consequently, simulating the model's oscillatory dynamics over just a few cycles (i.e. a few microseconds) already results in significant computation times (in the order of seconds). Considering the fact that this mechanical model is to be coupled with an electrical counterpart and simulated over hundreds of milliseconds, that intrinsic stiffness represents a significant limitation.

2.1.10 Conclusions

The bilayer sonophore biomechanical model describes the periodic antiphase deflections of the membrane phospholipidic leaflets upon perturbation by a sinusoidal acoustic pressure in the ultrasonic range. The construction of this model involves specific assumptions about the structure homogeneity and spherical symmetry, as well as mathematical simplifications (Taylor expansion, neglecting nonlinear acceleration term) that permit the derivation of a solvable differential system. Moreover, many of its constituent parameters entail an intrinsic uncertainty due to the lack of physical characterization of the considered phenomenon. Nevertheless, the model predicts clear trends on the impact of structure dimensions, anatomical embedding and stimulation parameters on the resulting sonophore cavitation dynamics.

2.2 Electrical part: the Hodgkin-Huxley formalism

The Hodgkin-Huxley formalism represents a foundational biophysical model describing the nonlinear electrical behaviour of the neuron membrane, allowing it to generate action potentials. It was famously introduced in the 1950s by Alan Hodgkin and Andrew Huxley, in a series of historic papers describing voltage-clamp experiments on the unmyelinated axon of the giant squid *Loligo* (Hodgkin and Huxley, 1952a, 1952d, 1952c, 1952b; Hodgkin et al., 1952). This work was awarded the Nobel Prize in Physiology in 1963, and has since then been employed to model the membrane dynamics of a variety of neuron types, in both the peripheral (Frankenhaeuser and Huxley, 1964; McIntyre et al., 2002) and central (Pospischil et al., 2008) nervous system. It forms the electrical part of the NICE model.

2.2.1 Membrane equivalent electrical circuit

The Hodgkin-Huxley formalism models the neuronal membrane with an equivalent electrical circuit combining capacitive and resistive elements in parallel (Hodgkin and Huxley, 1952a).

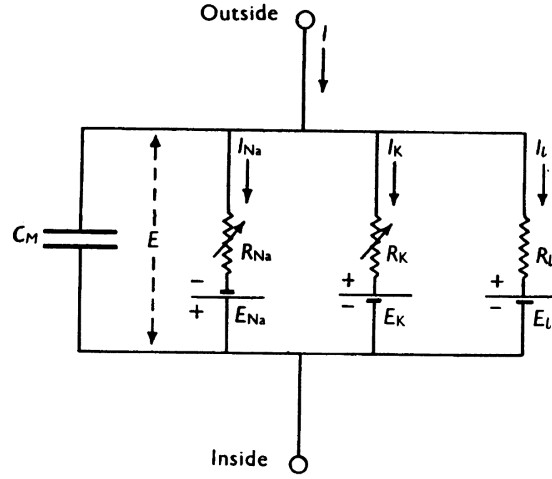


Figure 8. Hodgkin-Huxley formalism of a membrane equivalent electrical circuit with Sodium (Na), Potassium (K) and non-specific leakage (L) ionic conductances (adapted from (Hodgkin and Huxley, 1952a)).

In this circuit, the capacitance C_m represents the ability of the membrane to be polarized by the accumulation of charged particles (i.e. ions) of opposite signs on either side of its very thin layer, yielding a capacitive current I_c . Transverse conductances (g_x) represent the permeability of specific populations of constituent ion channels, allowing ions to flow across the membrane, driven by the difference between the membrane potential V_m and their respective reversal potential (E_x , determined for each ion mix from the Nernst equation). The total current through the membrane is then given by the sum of capacitive and ionic terms:

(71)

$$I_{tot} = I_c + I_{ion} = C_m \frac{dV_m}{dt} + \sum_i g_i (V_m - E_i)$$

2.2.2 Ionic conductances

Just like in the original formalism, most Hodgkin-Huxley models include voltage-gated conductances for Sodium and Potassium currents that regulate the action potential dynamics, as well as a non-specific “leakage” conductance to account for the passive component of the membrane response. However, other types of conductances (e.g. Calcium, Chloride) can also be found in specific cell types.

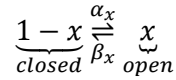
Non-leakage ionic conductances are typically modeled as a maximal conductance (relating to the number of specific ion channels present in the cell membrane) regulated by the product of one or multiple gating variables x_i , representing the probability of constitutive elements of the channels (called “gates”) to be in an open permissive state, raised to a specific power (i.e. the number of each gating element):

(72)

$$g_x = \overline{g}_x \cdot \prod_i x_i^{y_i}$$

Sodium conductances are typically represented by 2 gating variables (m^*h formalism) to account for inactivation mechanisms, while potassium conductance only requires a single variable (n^* formalism). The evolution of each gating variable is described by a two-state kinetic scheme, where transitions between the open state (x) and the closed state ($1 - x$) are governed by specific voltage-dependent activation and inactivation rate constants (α_x and β_x , respectively):

(73)



Under this formalism, the evolution of the gating variable is given by:

(74)

$$\frac{dx}{dt} = \alpha_x(V_m) \cdot (1 - x) - \beta_x(V_m) \cdot x$$

An equivalent paradigm exists that models the gating variable evolution as a function of a steady state probability ($x_\infty = \frac{\alpha_x}{\alpha_x + \beta_x}$) and a time constant ($\tau_x = \frac{1}{\alpha_x + \beta_x}$):

(75)

$$\frac{dx}{dt} = \frac{x_\infty(V_m) - x}{\tau_x(V_m)}$$

2.2.3 Dynamical behavior

The Hodgkin-Huxley formalism is, by definition, a way of representing the electrical behavior of neuronal membranes using a particular set of constitutive elements and associated differential equations. That is, there is not *one* Hodgkin-Huxley model, but rather a *collection* of them, derived across neuron types and species, and each associated with a specific set ionic currents and gating parameters. Hence, to give a good appreciation of the versatility of this formalism, we present here two examples HH-type models representing two neurons with fundamentally different function roles, and that are used in subsequent chapters of this work:

- The original Hodgkin-Huxley model derived for unmyelinated peripheral axons (Hodgkin and Huxley, 1952a), characterized by a fast action potential dynamics allowing to efficiently transmit information over large distances (**Figure 9a**)
- A more recently derived regular spiking model for pyramidal neurons of the mammalian cortex (Pospischil et al., 2008), with a slower action potential dynamics with allowing to integrate complex dendritic inputs into a “meaningful” electrical information (**Figure 9b**)

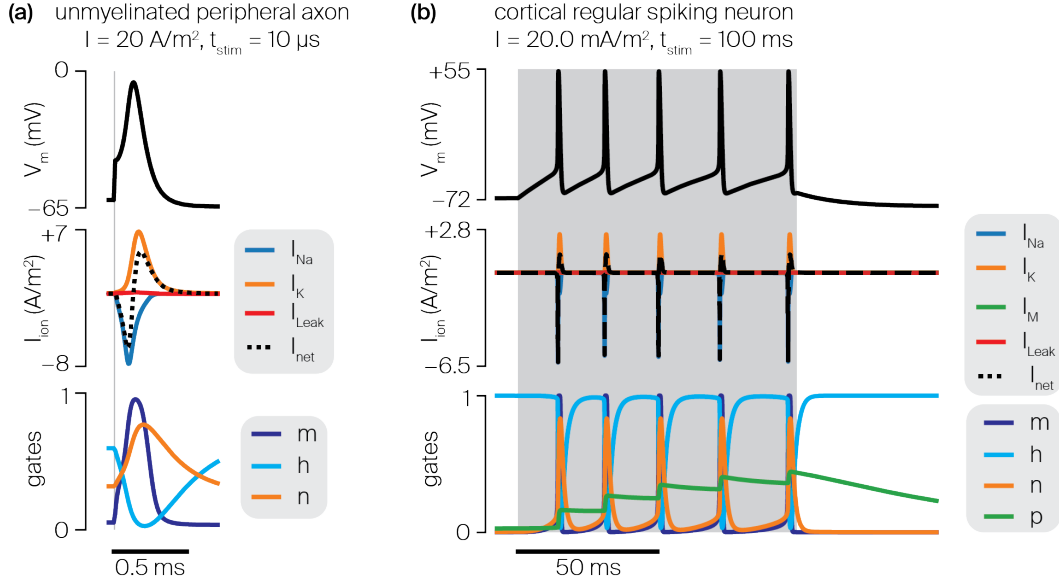


Figure 9. Characteristic examples of point-neuron models using the Hodgkin-Huxley formalism. (a) Unmyelinated peripheral axon responding to a very short intracellular current injection with a single action potential lasting. (b) Cortical regular spiking neuron responding to a sustained intracellular stimulus with a characteristic spike train.

2.3 Bi-directional coupling

In sections 2.1 and 2.2, we introduced the two core components of the NICE model, namely a universal mechanical model of intramembrane cavitation, and a cell-type-specific electrical model of membrane dynamics. Here, we describe how these two models are connected together by a bi-directional piezoelectric effect to yield a dynamical system that transforms acoustic stimuli into electrical responses.

The mechano-electrical transduction is obtained by direct piezoelectric effect: the periodic deflections of the sonophore leaflets induce dynamic changes in the local membrane thickness, which in turn affect the cell membrane capacitance (Gross et al., 2011) and the resulting membrane potential. Reversibly, electro-mechanical transduction is caused by the intrinsic polarity of neuronal membranes where the attraction between charged particles on either side of the bilayer generates an electrical pressure that perturbs the cavitation kinetics.

2.3.1 Mechano-electrical coupling

Given its dielectric properties and plane-like conformation, the cell membrane can be reasonably approximated as a parallel-plate capacitor composed of two monolayer leaflets acting as electrical “plates”. A generic formula for this type of capacitor is given by:

(76)

$$C = \frac{\epsilon_0 \epsilon_r A}{d}$$

Where C is the capacitance, ϵ_0 is the permittivity of space (dielectric constant) and ϵ_r the relative permittivity of the dielectric material, A is its surface area and d the separation distance between the two parallel plates (Giancoli, 2008). Considering the inter-leaflet gap Δ (defined in section 2.1.1.1) as the plate separation distance, the resting membrane capacitance per unit area thus equals:

(77)

$$C_{m0} = \frac{\epsilon_0 \epsilon_r}{\Delta}$$

However, upon perturbation by an acoustic pressure, the sonophore periodic deflections affect the inter-leaflet gap ($d(r) = 2z(r) + \Delta$, see section 2.1.2.1) and the resulting local membrane capacitance:

(78)

$$C_m(r) = \frac{\epsilon_0 \epsilon_r}{2z(r) + \Delta} = C_{m0} \frac{\Delta}{2z(r) + \Delta}$$

Integrating equation (78) over the entire sonophore surface area, we obtain an average value for the sonophore membrane capacitance as a function of the leaflet apex deflection:

(79)

$$C_m(Z) = \frac{1}{\pi a^2} \int_0^a \int_0^{2\pi} C_{m0} \frac{\Delta}{2z(r) + \Delta} r dr d\theta = C_{m0} \frac{\Delta}{a^2} \left[Z + \frac{a^2 - Z^2 - Z \cdot \Delta}{2Z} \ln \left(\frac{2Z + \Delta}{\Delta} \right) \right]$$

Figure 10 depicts the profile the relative average sonophore capacitance as a function of apex leaflet deflection. Notably, capacitance decreases towards zero as the sonophore expands, and increases above its resting value as the sonophore compresses (which is in accordance with equation (76)). Moreover, equation (79) ensures that $C_m(Z = 0) = C_{m0}$.

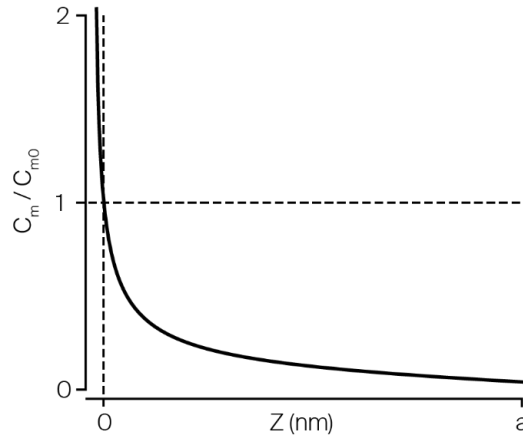


Figure 10. Relative variation of membrane capacitance as a function of leaflets deflection.

2.3.2 Electro-mechanical coupling

2.3.2.1 Electrical pressure

Due to their intrinsic polarity, neuronal membranes accumulate charged particles of opposite signs on either side of the bilayer, thereby creating an electric force that attracts the two leaflets towards each other. Here again, the magnitude of this force can be derived by considering the cell membrane as a parallel plate capacitor, with the two leaflets acting as individual electrode plates and separated by a distance Δ .

Because the leaflets separation is very small compared to their in-plane surface, the capacitor's electric field can be regarded as homogenous and normal to the membrane plane. In that case, the field intensity inside the membrane E_m receives equal contributions from both sides ($E_m = E^+ + E^-$; $E^+ =$

E^-). Moreover, its magnitude is given by the potential difference between the electrodes (i.e. the transmembrane voltage V_m in this case), divided by the separation distance between the plates:

(80)

$$E_m = \frac{V_m}{\Delta}$$

The force acting on each plate is then proportional to the charge it stores and to the component of the electric field produced by the *other* plate:

(81)

$$F_Q = QE^+ = Q \frac{V_m}{2\Delta}$$

Dividing equation (81) by the membrane surface area, we obtain a formula for the “electrical pressure” exerted on the membrane:

(82)

$$P_Q = \frac{Q_m V_m}{2\Delta}$$

where Q_m is the membrane charge density (in nC/cm²). By definition, this variable is the product of resting transmembrane potential and membrane capacitance:

(83)

$$Q_m = C_m V_m$$

Inserting equations (77) and (83) into equation (82), we thus obtain the formula for the electrical pressure on the resting neuronal membrane:

(84)

$$P_{Q0} = \frac{Q_m^2}{2\epsilon_0 \epsilon_r}$$

Now, as the sonophore is deformed by the acoustic perturbation, the same electrical force is applied over a larger surface area. Hence, equation (84) must be adapted to account for this relative change, in order to yield a deflection and charge dependent formula for the electric pressure:

(85)

$$P_Q(Z, Q_m) = \frac{S_0}{S} P_{Q0} = \frac{a^2}{Z^2 + a^2} \cdot \frac{Q_m^2}{2\epsilon_0 \cdot \epsilon_r}$$

Figure 11 depicts the profile electrical pressure as a function of membrane charge density, for two different deflection states: a sonophore at rest ($Z = 0$) and during a significant expansion phase ($Z = a$). In both cases, electrical pressure increases with the square of membrane charge density. The inverse dependency on leaflets deflection is also observable, yielding larger pressures for small / no deflection.

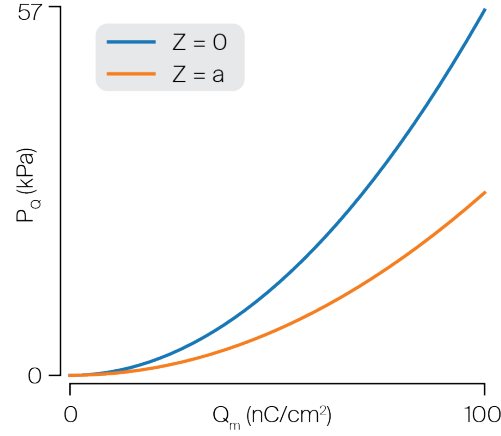


Figure 11. Electrical pressure acting on the bilayer membrane as a function of charge density, for a sonophore at rest ($Z = 0$) and during an expansion phase ($Z = a$).

Note that when considering electrical pressure in the pressure balance that regulates the sonophore cavitation dynamics, a preceding minus sign is added for consistency with other constraining forces.

2.3.2.2 Modified molecular pressure

We saw in section 2.1.1.2 that the steady-state equilibrium of the sonophore results from the balance of gaseous, hydrostatic and molecular pressure forces summing up to yield a zero resultant pressure. More specifically, gas transport through the leaflets ensures that $P_G = P_0$, and molecular pressure is intrinsically defined to cancel out at $Z = 0$ (see equation (13)). In the case of neurons however, the polarized nature of the resting membrane introduces a non-negligible electrical pressure, and yielding a modified condition for the mechanical steady-state:

(86)

$$P_G - P_0 + P_M - P_Q = 0$$

Obviously, gas equilibration still applies in this cases, and equation (86) can thus be reduced to:

(87)

$$P_M(Z = 0) = P_Q(Z = 0, Q_{m0})$$

Notably, with the traditional definition of molecular pressure, equation (87) has no solution if $Q_{m0} \neq 0$. Hence, to maintain a stable equilibrium for a charged membrane, a modified expression of local inter-molecular pressure is defined here as:

(88)

$$p_M(r) = p_\Delta \left[\left(\frac{\Delta^*}{2z(r) + \Delta} \right)^m - \left(\frac{\Delta^*}{2z(r) + \Delta} \right)^n \right]$$

where Δ is the inter-leaflet gap for a membrane at resting charge density, and Δ^* the same inter-leaflet gap in the absence of charges, determined numerically to satisfy equation (87).

2.3.3 Dimensional considerations

At this stage, it appears important to consider the scales involved in this bidirectional coupling. The Hodgkin-Huxley formalism provides a deterministic, macroscopic approximation of the gating dynamics of large ion channels populations over micro or millimeter scale membrane areas (Catterall et al.,

2012). That approximation becomes invalid for problems of smaller dimensions – such as a nanometer-scale sonophore and its direct vicinity – where the stochastic gating dynamics of individual ion channels plays a very significant role (Chow and White, 1996; Faisal et al., 2005; Fink and Noble, 2009). This spatial discrepancy is resolved in the NICE model by considering a large scale mechano-electrical transduction, i.e. that resulting from the synchronized cavitation of a population of sonophores over a membrane area sufficiently large that its electrical dynamics can be captured by a macroscopic approximation. That is, the sonophore population is modeled as a density mechanism – akin to the mathematical representation of ion channels populations – and membrane capacitance is calculated as a weighted mean of the resting and dynamic capacitances:

(89)

$$C_m = C_m(t)f_s + C_{m0}(1 - f_s)$$

where f_s is the active area fraction), influencing an equipotential membrane patch.

2.3.4 Differential system

The construction of the NICE model relies on the bidirectional coupling of two dynamical systems, each described by a system a governing differential equations (equations (34) and (67) for the mechanical part, and equations (71) and (74) for the electrical part). Therefore, a naïve approach to its numerical resolution would be to simply couple these two systems under a single differential scheme, accounting for a time-varying capacitance, as well as the electrical and modified molecular pressures. However, one must remember that the definition of the capacitive current in the classical Hodgkin-Huxley formalism is made under the assumption of constant membrane capacitance. With the introduction of a time-varying capacitance, this current becomes:

(90)

$$I_C = \frac{d(C_m V_m)}{dt} = C_m \frac{dV_m}{dt} + V_m \frac{dC_m}{dt}$$

and equation (71) must be adapted accordingly. Altogether, the governing differential system of the NICE model becomes:

(91)

$$\left\{ \begin{array}{l} \frac{d^2 Z}{dt^2} = -\frac{3}{2R} \left(\frac{dZ}{dt} \right)^2 + \frac{1}{\rho_L |R|} [P_G + P_M^* - P_0 - P_A + P_E + P_{VS} + P_{VL} - P_Q] \\ \frac{dn_g}{dt} = \frac{2SD_{gl}}{\xi} \left(C_g - \frac{P_G}{k_H} \right) \\ \frac{dV_m}{dt} = -\frac{1}{C_m} \left[V_m \frac{dC_m}{dt} + \sum_i g_i \cdot (V_m - E_i) \right] \\ \frac{dx}{dt} = \begin{cases} \alpha_x(V_m) \cdot (1 - x) - \beta_x(V_m) \cdot x \\ \frac{x_\infty(V_m) - x}{\tau_x(V_m)} \end{cases} \quad \text{for } x \text{ in } \{m, h, n, \dots\} \end{array} \right.$$

where P_M^* is the modified molecular pressure.

2.4 Dynamical behavior

Having established the governing equations of the NICE model, we can now focus on its dynamical behavior.

2.4.1 Typical behavior

We present here a typical example of the predicted response of a cortical regular spiking neuron to an acoustic stimulus ($f = 500$ kHz, $A = 50$ kPa, **Figure 12**).

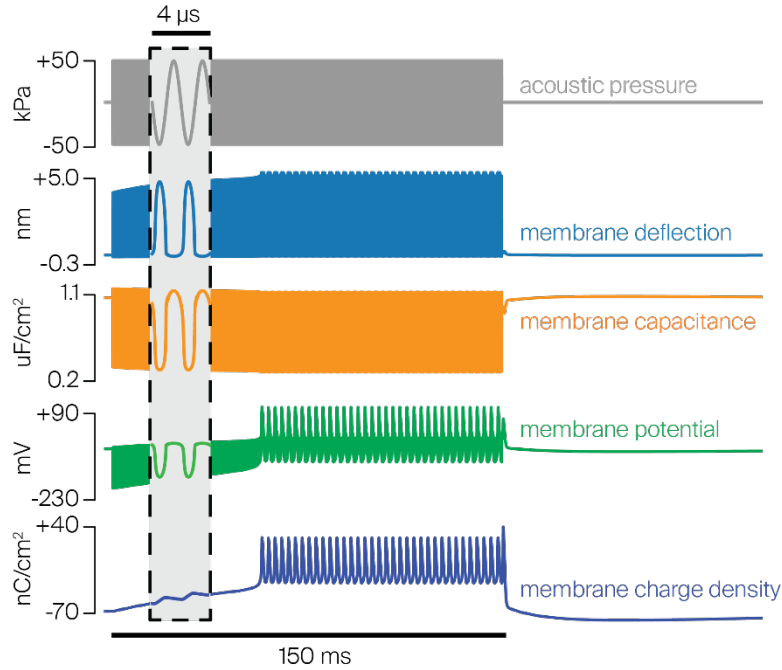


Figure 12. Typical response of a cortical regular spiking neuron to a continuous wave ultrasound stimulus (500 kHz, 50 kPa, 150 ms stimulus). From top to bottom: temporal profiles of acoustic pressure, membrane deflection, membrane capacitance, membrane potential and membrane charge density. Inset: zoom over a 4 μ s interval spanning two acoustic cycles.

This mechano-electrical response can be broken down into separate phases, occurring across a broad range of time scales:

- Upon stimulation onset, the sinusoidal acoustic pressure wave generates alternating expansions and compressions of the sonophore and the ultrasound frequency. Note that expansion is loosely limited by elastic tension, while compression is strongly restricted by repulsive molecular forces, which creates an asymmetric deflection profile (see section 2.1.8.1).
- This intramembrane cavitation induces local, periodic oscillations in membrane capacitance, which also shows a significant asymmetry (C_m decreases down to 30% of its resting value during expansion phases, and increases only by 10% during compression phases).
- Asymmetric capacitance oscillations cause large-amplitude oscillations of the local transmembrane ($V_m = Q_m/C_m$) potential that manifest as a large hyperpolarization (down to -200 mV) during expansion phases, and a slight depolarization during compression phases.
- Large hyperpolarizations trigger depolarizing leakage currents ($I_L = g_L(V_m - E_L)$) that aim to bring the transmembrane potential back towards its resting value. In doing so, they induce an incremental raise in the membrane charge density. This process is reversed during compression phases, where slight depolarizations induce hyperpolarizing leakage currents. However, the significant asymmetry of voltage deviations during these two half-cycles induces an imbalance in leakage currents towards depolarization, thereby causing a net increase in charge density over an acoustic period.

- Eventually, this imbalance perpetuates over consecutive acoustic cycles, and induces a progressive increase in charge density until the neuron's spiking threshold is met and the action potential machinery (Sodium and Potassium channels) kicks off.
- The high frequency, large amplitude modulation of the membrane potential affects the gating kinetics of voltage-gated ion channels, thereby producing a high frequency spike train.
- The stimulus offset causes a quasi-instantaneous mechanical stabilization of the membrane. Under the absence of a mechanical drive, the neuron stops firing and the membrane progressively falls back to its resting electrical state.

2.4.2 Dependency on stimulus parameters

The NICE model predicts that the progressive integration of asymmetric, microsecond-scale mechanical membrane oscillations induces a slow-scale depolarization towards the spiking threshold and eventually, a sustained firing activity. The efficiency of this mechano-electrical transduction directly depends on the amplitude of the predicted intramembrane cavitation. Therefore, the dependency of the NICE model on sonication parameters can be intuitively deduced from the behavior of the sole mechanical model, described in section 2.1.8.4. A summary of its main dependencies is provided here, taken from the original paper describing the NICE model (Plaksin et al., 2014), where acoustic intensity is defined as $I = \frac{P_{Ac}^2}{2\rho c}$, with ρ and c the medium's density and speed of sound, respectively.

- Excitation thresholds increase slightly with US frequency within the 0.2 – 2 MHz range, and then more sharply above 2 MHz, as a result of the increased viscoelastic resistance to motion that limits sonophore expansion (**Figure 13a**).
- Excitation thresholds decrease with increasing stimulus durations, since a longer stimulus integration requires less charge increase per cycle to reach the same spiking threshold (**Figure 13b**).
- For this specific neuron, stimulus durations of about 45 ms yield an optimal trade-off between low acoustic intensity and short stimulus duration, resulting in a minimum stimulation energy to reach the spiking threshold (**Figure 13c**).
- Following an initial build-up phase, the neuron enters a non-adaptive tonic firing regime (number of spikes increases linearly with stimulus duration), whose rate increases with the stimulus intensity (**Figure 13d-e**).
- Increasing stimulus intensities amplify cavitation amplitude and yield more asymmetric deflection profiles that elicit more charge increase per acoustic cycle. This enhanced mechano-electrical transduction accelerates depolarization and thus decreases response latency (**Figure 13f**).

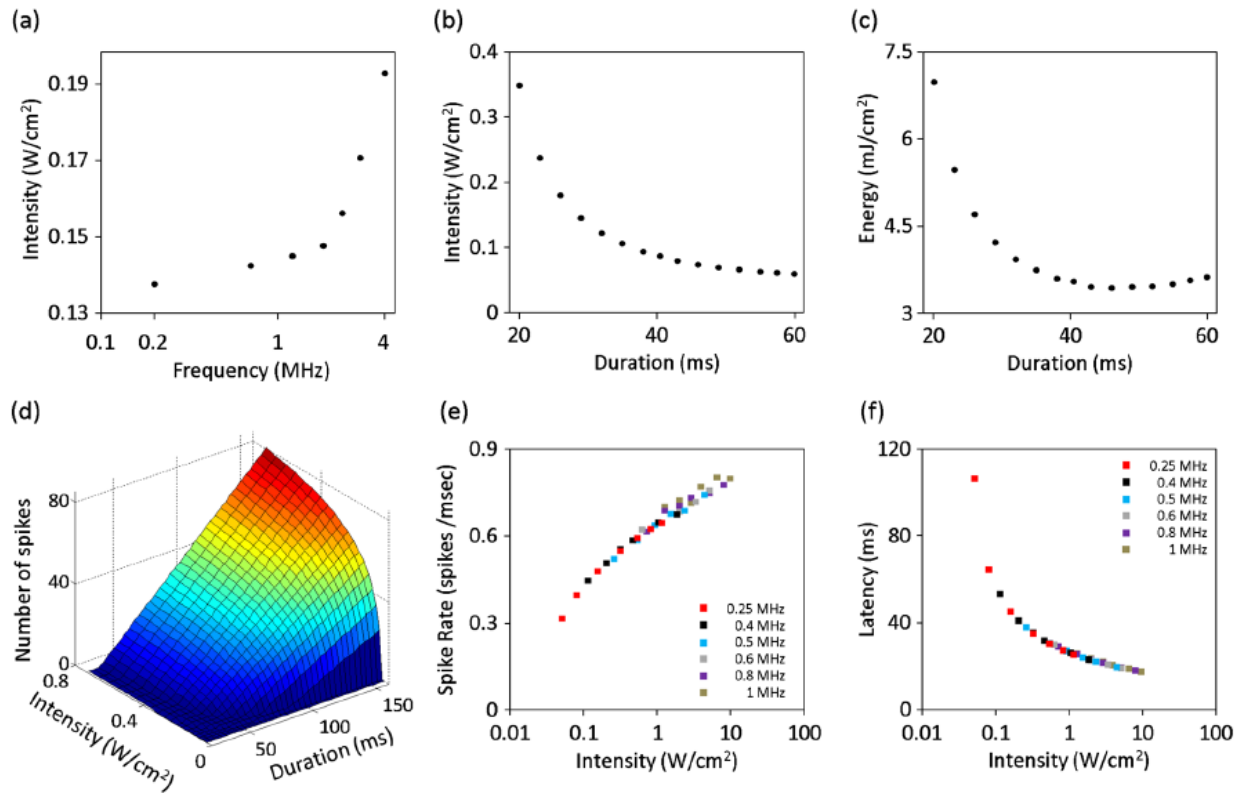


Figure 13. Dependency of the NICE model behavior of a cortical regular spiking neuron on continuous wave stimulation parameters (adapted from (Plaksin et al., 2014)). (a) Threshold acoustic intensity required to excite the neuron with a 30 ms stimulus, as a function of US frequency. (b, c) Threshold excitation intensity, and equivalent energy, as a function of stimulus duration ($f = 350$ kHz). (d) Number of detected spikes as a function of stimulus intensity and duration ($f = 350$ kHz). (e) Elicited firing rate as a function of stimulus intensity for various US frequencies from 250 kHz to 1 MHz. Response latency as a function of stimulus intensity for various US frequencies as in (e).

2.5 Predictive power

As stated in chapter 1, one of the – if not the biggest – incentives for the use of the NICE model resides in its predictive power.

At the single neuron level, the NICE model predicts that continuous-waves LIFUS entrains cortical regular spiking neurons into a tonic firing regime – after some latency period – where the number of spikes increases with duration. Given the lack of availability of direct neuronal recordings upon sonication at the time of their investigation, Plaksin et al. opted to compare their modeling predictions to a higher-level recording metrics: the success rate of motor responses elicited by LIFUS directed at the motor cortical area of mice (King et al., 2013). To this end, they fitted a sigmoidal function of only two parameters (determined from a Buckingham-Pi dimensional analysis (Buckingham, 1914; Plaksin et al., 2014)) linking the number of spikes predicted by the NICE model to the experimental success rate (**Figure 14**). The resulting predictions in motor response likelihood offered a very interesting level of qualitative agreement with experimental results, over a wide range of ultrasound frequencies (spanning the sub-MHz range) and pressure amplitudes.

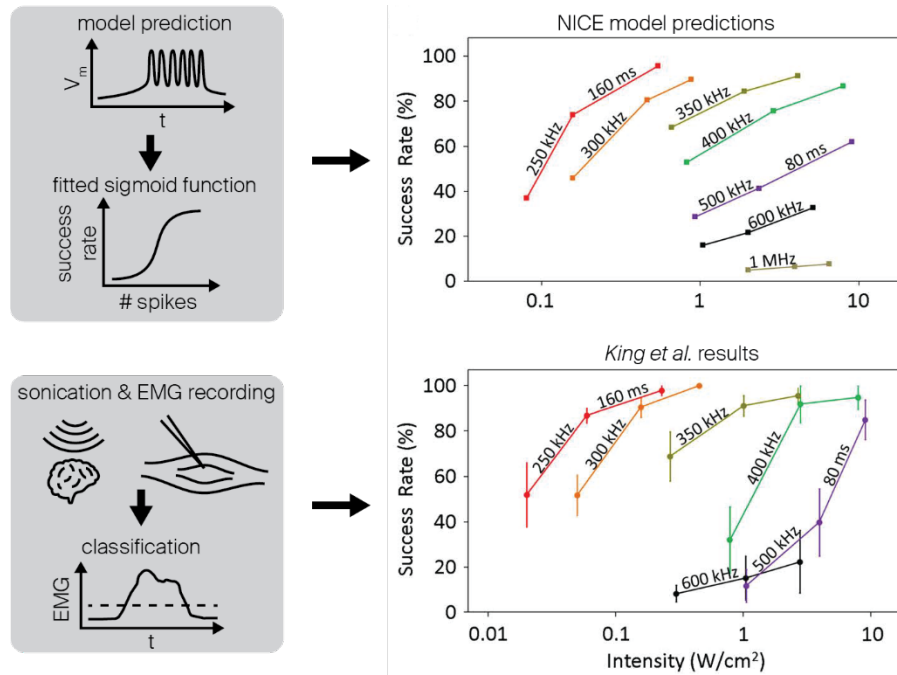


Figure 14. Comparison of NICE model predictions and *in vivo* brain stimulation measurements (King et al., 2013) (adapted from (Plaksin et al., 2014)). Success rates for eliciting motor responses versus US intensity at different frequencies (continuous stimulation for 40 000 acoustic cycles). Top: NICE model success rate predictions obtained by feeding the number of predicted spikes for a regular spiking (RS) neuron into a fitted sigmoid function. Bottom: success rate computed from measured hindlimb EMG activity upon sonication of the motor cortex in mice (experimental results from (King et al., 2013)).

Note that the larger success rates observed here at lower frequencies do not come from a higher efficacy *per se*, but rather from the fact that stimulus durations were set to a fixed number of acoustic cycles ($n = 40\,000$) thereby yielding longer stimuli at lower frequencies. Nonetheless, those results do make sense in the context of the NICE model where the number the spikes is predicted to increase linearly with stimulus duration.

Later on, Plaksin et al. refined those predictions by considering a larger, heterogeneous population of cortical neurons arranged into minimalistic, yet functionally-realistic spiking network model composed of one type of excitatory neuron (RS) and two types of inhibitory neurons: fast spiking (FS) and low-threshold spiking (LTS) (Vierling-Claassen et al., 2010). By simulating this network upon sonication, they found that different combinations of stimulus amplitude and duty cycle could entrain (cortical activation) or silence (cortical suppression), by acting differently on specific ion channels present in the different neurons. More importantly, simulations revealed a clear bifurcation between these two sub-regions of the parameter space, where and identified activation and suppression regions agreed remarkably well with an extensive body of empirical observations in animal models and humans (Plaksin et al., 2016) (Figure 15).

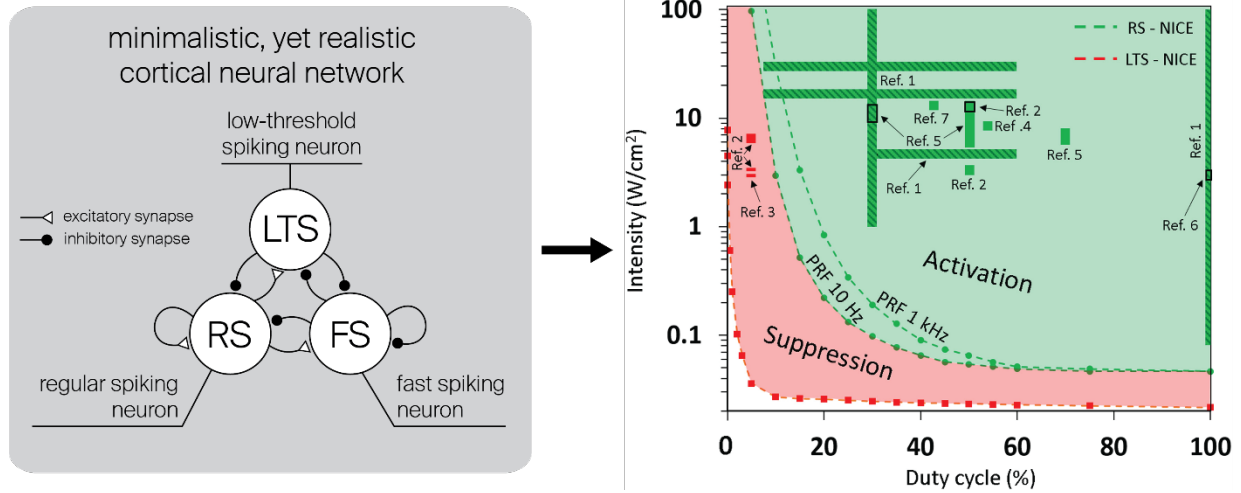


Figure 15. Phase plane diagram of single-neuron responses predicted by the NICE model to varying US stimulation duty-cycle and intensity versus experimental cortical neuromodulation parameters (adapted from (Plaksin et al., 2016)). The phase diagram boundaries denote threshold intensities for US-mediated responses ($f = 0.69$ MHz, 500 ms stimulus) from excitatory regular spiking (RS, green dashed lines indicating 10 Hz and 1 kHz PRFs) and inhibitory low-threshold spiking interneurons (LTS, red dashed lines, changes only slightly for different PRFs, not shown). These boundaries separate the phase diagram into regions where either the inhibitory LTS neurons are activated alone (red, “suppression zone”) or the RS and the LTS neurons are jointly activated leading to net network stimulation (green, “activation zone”). The superposed bars indicate the experimental parameter ranges used in seven published cortical ultrasonic neuromodulation studies, color-coded according to the mediated responses: Ref. 1 ((King et al., 2013); bars with diagonal lines), Ref. 2 (Yoo et al., 2011)), Ref. 3 ((Kim et al., 2015)), Ref. 4 ((Kim et al., 2012)), Ref. 5 ((Kim et al., 2014)), Ref. 6 ((King et al., 2014)), and Ref. 7 ((Tufail et al., 2011)). The excitation parameters reported for (King et al., 2013) were those that caused stimulation success rates significantly higher than their noise floor ($\approx 20\%$), with low-frequency CW intensities corrected for the expected formation of standing waves (Plaksin et al., 2014).

2.6 Conclusions

The electromechanical NICE model formulates quantitative predictions on how the plasma membrane can progressively transform acoustic perturbations into electrical responses and neuronal spiking activity. To this aim, it relies on the bidirectional coupling of two dynamical systems evolving at different time scales, where microsecond mechanical oscillations of the plasma membrane affect the millisecond development of a neuronal electrical response, and vice-versa. Although purely theoretical and despite a lack of validation at the cellular level, the NICE model can explain a number of features of high-level LIFUS neuromodulatory effects (latency, threshold) obtained in the brain across the literature, making it an attractive target for the development of modeling frameworks.

However, the intimate electromechanical coupling of this model also produces a very stiff differential system in which detailed intra-cycle (i.e. sub- μ s) variations must be integrated to compute the neuronal response of interest (typically over tens / hundreds of ms), resulting in a tremendous computational burden (several days to run a single simulation on a traditional laptop). This intrinsic burden limits the ability to scan efficiently of the stimulation and physiological parameter space, but also to scale up modeling predictions towards clinically relevant scales.

Chapter 3 The multi-Scale Optimized Intramembrane Cavitation (SONIC) model

Chapter 2 describes the internal components, parameters, governing equations and typical behavior of the NICE model, as well as its dependency on stimulation parameters. It also emphasizes that the model entails a significant numerical stiffness that hinders both its efficiency of use and the reliability of its predictions.

This chapter presents a strategy based on temporal multiscaling to drastically reduce the numerical stiffness of the NICE model, allowing the exploration of dense, multi-dimensional parameter spaces, and facilitating its expansion towards the morphological scale. This effective variant, called the multi-Scale Optimized Neuronal Intramembrane Cavitation (SONIC) model, is the first original contribution presented in this thesis.

The contents of this chapter are adapted from the manuscript **Lemaire, T.**, Neufeld, E., Kuster, N., and Micera, S., “Understanding ultrasound neuromodulation using a computationally efficient and interpretable model of intramembrane cavitation” published in Journal of Neural Engineering, 16, 046007 (2019).

Personal contributions as first author: conceptualized the study, implemented the model, performed the simulations, analyzed the results, prepared the figures and wrote the manuscript.

Understanding ultrasound neuromodulation using a computationally efficient and interpretable model of intramembrane cavitation

Théo Lemaire¹, Esra Neufeld², Niels Kuster^{2,3}, and Silvestro Micera^{1,4}

¹Translational Neural Engineering Laboratory, Center for Neuroprosthetics and Institute of Bioengineering, School of Engineering, École Polytechnique Fédérale de Lausanne (EPFL), Lausanne, Switzerland

²Foundation for Research on Information Technologies in Society (IT²S), Zurich, Switzerland

³Department of Information Technology and Electrical Engineering, Swiss Federal Institute of Technology (ETH), Zurich, Zurich, Switzerland

⁴The Biorobotics Institute, Scuola Superiore Sant'Anna (SSSA), Pisa, Italy

3.1 Abstract

Objective. Low-intensity focused ultrasound stimulation (LIFUS) emerges as an attracting technology for noninvasive modulation of neural circuits, yet the underlying action mechanisms remain unclear. The neuronal intramembrane cavitation excitation (NICE) model suggests that LIFUS excites neurons through a complex interplay between microsecond-scale mechanical oscillations of so-called sonophores in the plasma membrane and the development of a millisecond-scale electrical response. This model predicts cell-type-specific responses that correlate indirectly with experimental data, but it is computationally expensive and difficult to interpret, which hinders its potential validation. Here, we introduce a multi-Scale Optimized Neuronal Intramembrane Cavitation (SONIC) model to achieve fast, accurate simulations and confer interpretability in terms of effective electrical response. **Approach.** The NICE system is recast in terms of smoothly evolving differential variables affected by cycle averaged internal variables that are a function of sonophore size and charge density, stimulus frequency and pressure amplitude. Problem separation allows to precompute lookup tables for these functions, which are interpolated at runtime to compute coarse-grained, electrophysiologically interpretable and spatially distributed predictions of neural responses. **Main Results.** The SONIC model accelerates computation by more than three orders of magnitude, accurately captures millisecond-scale electrical responses of various cortical and thalamic neurons and offers an increased interpretability to the effects of ultrasonic stimuli in terms of effective membrane dynamics. Using this model, we explain how different spiking behaviors can be achieved in cortical neurons by varying LIFUS parameters, and interpret predictions of spike amplitude and firing rate in light of the effective electrical system. We demonstrate the substantial influence of sonophore size on excitation thresholds, and use a nanoscale spatially extended SONIC model to suggest that partial sonophore membrane coverage has a limited impact on neuronal excitability. **Significance.** By providing an electrophysiologically interpretable description, the SONIC model clarifies cell-type-specific LIFUS neuromodulation according to the intramembrane cavitation hypothesis.

3.2 Introduction

Ultrasound (US)-based therapeutic applications, such as diagnostic imaging and thermal ablation therapies, are now widely accepted in the clinical field (Escoffre and Bouakaz, 2016; Kyriakou et al., 2014). Low-intensity focused ultrasound stimulation (LIFUS), employing the same technology but with different sonication parameters (carrier frequency, peak pressure amplitude, duration, pulse repetition frequency, and duty cycle), has recently emerged as a very compelling modality for neuromodulation therapies. Owing to their mechanical nature, US waves can be accurately directed through biological tissue, offering the ability to concentrate the acoustic energy to a deep focal spot (Ghanouni et al., 2015; Kyriakou et al., 2014). Moreover, numerous experiments on both animal models and humans

have demonstrated that transcranial LIFUS is able to either excite, inhibit, or modulate the electrical activity of neurons in the central nervous system (CNS) (Deffieux et al., 2013; Kim et al., 2015; King et al., 2013; Legon et al., 2014; Mueller et al., 2014; Tyler et al., 2008; Younan et al., 2013). Furthermore, exhaustive explorations of different sonication parameters on the motor cortex of mice have shown that stronger stimulus intensities and durations increase the probability of a motor response without affecting the duration or strength of the response, thereby suggesting a threshold excitation mechanism associated with the US intensity (King et al., 2013). LIFUS could therefore trigger a local and controllable neuromodulatory effect on various neural targets, using a distant and possibly noninvasive sonication device. However, in order for LIFUS to become a reliable neuromodulation technology, we must elucidate the fundamental mechanism(s) by which US waves interact with neural tissue at the cellular scale, how these mechanisms may vary across neural structures and how optimal sonication parameters change with it.

Several theories have emerged to try to decipher this interaction. Among them, the neuronal intramembrane cavitation excitation (NICE) model (Plaksin et al., 2014) hypothesizes that incoming US waves induce the cavitation of specific nanometer-scale phospholipidic structures (so-called “bilayer sonophores”) within plasma membranes. This model provides quantitative predictions of cell-type-specific neural responses upon US exposure that result in excitation or inhibition of cortical networks depending on LIFUS parameters (Plaksin et al., 2016). These predictions agree with the results of numerous *in vitro* experiments and *in vivo* studies sonicating the CNS of various animal models (Kim et al., 2012, 2014, 2015; King et al., 2013; Tufail et al., 2011; Yoo et al., 2011). Yet, the model is purely theoretical and built around the intramembrane cavitation hypothesis, whose direct mechanical and electrical manifestations have yet to be observed experimentally. Moreover, the intrinsic electromechanical coupling of the model entails important computational limitations. From an algorithmic standpoint, the explicit modeling of mechanical membrane oscillations with microsecond-scale periodicity results in a very stiff differential system that severely hinders numerical integration. From an analysis standpoint, the bidirectional coupling between mechanical and electrical variables evolving at different time scales produces a singular electrical response that can be difficult to interpret under the classical frame of neural dynamics. These limitations have so far prevented systematic, large-scale explorations of the LIFUS parameter space with the NICE electromechanical model, and its efficient integration in realistic applications involving the simultaneous solving of coupled differential systems, such as multi-compartmental morphological models and neuron population models.

In this study, we present a coarse-grained variant of the NICE electromechanical model – the so-called multi-Scale Optimized Neuronal Intramembrane Cavitation (SONIC) model – that allows the interpretation of the millisecond-scale dynamics of neural responses upon US exposure in terms of effective membrane dynamics. We show that the SONIC model can provide accurate predictions of cell-type-specific neural responses with respect to the detailed NICE model, while significantly decreasing computation times. We then exploit the SONIC model to explore systematically the dense, multidimensional LIFUS parameter space, and analyze responses of different neuron types with an advanced electrophysiological understanding. Finally, we use a nanoscale spatially extended SONIC model to study the impact of partial sonophore coverage on predicted neural responses and expected excitability.

3.3 Methods

3.3.1 The NICE electromechanical model

The NICE electromechanical model (Krasovitski et al., 2011; Plaksin et al., 2014, 2016) is a mathematical model consisting of a system of first- and second-order differential equations describing the dynamic

mechanical and electrical behavior of a bilayer sonophore that cavitates upon sonication while being anchored by surrounding transmembrane proteins (Figure 16(a)).

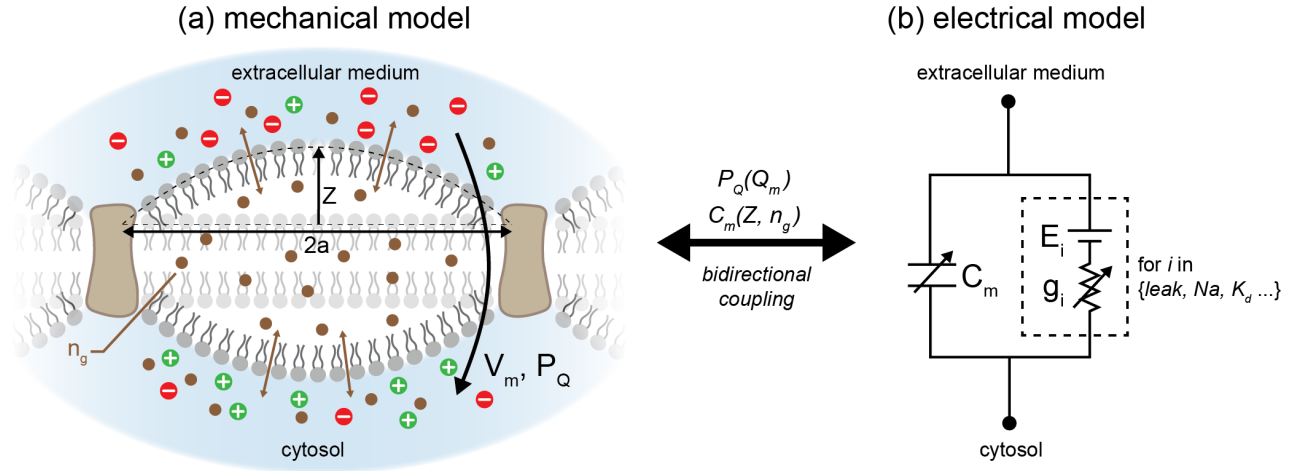


Figure 16. Description of the NICE electromechanical model. (a) Schematic representation of a bilayer sonophore structure (phospholipidic layers, inner cavity and surrounding transmembrane proteins) with the associated differential variables Z (apex deflection) and n_g (internal gas molar content). The local transmembrane potential V_m and electric pressure P_Q resulting from charge distributions on both sides of the membrane (green and red dots) are also indicated. (b) Electrical circuit representation of the local membrane dynamics, with the same transmembrane potential, a deflection-dependent capacitance C_m , and cell-type-specific Hodgkin-Huxley ionic conductances and reversal potentials.

3.3.1.1 NICE mechanical model

The mechanical part of the NICE electromechanical model predicts that incoming US waves generate a dynamic pressure imbalance that drives alternating expansions and compressions of sonophore structures, to oscillate at the US frequency. This cyclic behavior is captured by a second-order partial differential equation (akin to the Rayleigh-Plessey equation of bubble cavitation (Plesset, 1949)) describing the antiphase apex deflection Z of the sonophore inner and outer leaflets, and a first-order equation describing the variation of internal gas content n_g :

(92)

$$\begin{aligned} \frac{d^2 Z}{dt^2} &= -\frac{3}{2R(Z)} \left(\frac{dZ}{dt} \right)^2 \\ &\quad + \frac{1}{\rho_l \cdot |R(Z)|} \left[P_A + P_S(Z) + P_{VS} \left(\frac{dZ}{dt} \right) - P_0 + P_{VL} \left(\frac{dZ}{dt} \right) + P_M(Z) + P_G(Z, n_g) \right. \\ &\quad \left. + P_Q(Z, Q_m) \right] \\ \frac{dn_g}{dt} &= \frac{2S(Z) \cdot D_{gl}}{\xi} \left(C_g - \frac{P_G(Z)}{k_H} \right) \end{aligned}$$

where $R(Z)$ and $S(Z)$ represent the curvature radius and surface area of a sonophore leaflet and Q_m the local membrane charge density around the sonophore (for a definition of all other parameters see Table 2). Ultimately, the normal acceleration of a leaflet apex depends on the resultant of the applied acoustic pressure P_A , the constant hydrostatic pressure P_0 around the membrane, and several intrinsic pressure forces, defined as in (Krasovitski et al., 2011; Plaksin et al., 2014):

- the elastic membrane tension pressure developed in the two leaflets: $P_S(Z) = -\frac{k_S}{R(Z)} \frac{(S(Z) - S_0)}{S_0}$
- the viscous pressure developing in the leaflets: $P_{VS} \left(\frac{dZ}{dt} \right) = -12 \frac{\mu_S \cdot \delta_0}{R^2(Z)} \frac{dZ}{dt}$

- the viscous pressure in the extra-membrane medium: $P_{VL} \left(\frac{dZ}{dt} \right) = -4 \frac{\mu_l}{|R(Z)|} \frac{dZ}{dt}$
- the intermolecular pressure between leaflets: $P_M(Z) = \frac{1}{S(Z)} \int_0^{2\pi} \int_0^a A_r \cdot (\gamma^x - \gamma^y) dr d\theta$ with $\gamma = \frac{\Delta^*}{2z(r) + \Delta(Q_{m0})}$
- the internal gas pressure in the cavity: $P_G(Z, n_g) = \frac{n_g \cdot R_g \cdot T}{V(Z)}$
- the electric pressure exerted on the sonophore by charges on either side of its membrane:

$$P_Q(Z, Q_m) = -\frac{S_0}{S} \frac{Q_m^2}{2\epsilon_0 \cdot \epsilon_r}$$

Here, S_0 represents the leaflet surface area at rest, $V(Z)$ the sonophore volume, r the in-plane distance from the sonophore center, $z(r)$ the local deflection at this distance, and $\Delta(Q_{m0})$ the charge-dependent gap between the two leaflets of the sonophore when the neuron is at rest (computed by canceling out P_M and P_Q at $Z = 0$).

Parameter	Symbol	Unit	Value	Source(s)
Sonophore radius (default value)	a	nm	32.0	(Plaksin et al., 2014)
Temperature	T	K	309.15	(Pospischil et al., 2008)
Universal gas constant	R_g	$\text{Pa} \cdot \text{m}^3 \cdot \text{mol}^{-1} \cdot \text{K}^{-1}$	8.314	(Wong, 1977)
Thickness of the leaflet	δ_0	nm	2.0	(Boal, 2012; Krasovitski et al., 2011)
Gap between the two leaflets on an uncharged membrane	Δ^*	nm	1.4	(Krasovitski et al., 2011)
Intermolecular pressure coefficient	A_r	Pa	10^5	
Exponent in the intermolecular repulsion term	x	-	5.0	
Exponent in the intermolecular attraction term	y	-	3.3	
Density of the extramembrane medium	ρ_l	$\text{kg} \cdot \text{m}^{-3}$	1075	(IT'IS Foundation, 2015)
Dynamic viscosity of the extramembrane medium	μ_l	$\text{Pa} \cdot \text{s}$	$7 \cdot 10^{-4}$	(Plaksin et al., 2014)
Dynamic viscosity of the leaflet	μ_s	$\text{Pa} \cdot \text{s}$	0.035	
Area compression modulus of the bilayer membrane	k_s	$\text{N} \cdot \text{m}^{-1}$	0.24	(Krasovitski et al., 2011; Phillips et al., 2009; Rawicz et al., 2000)
Gas concentration in the extra-membrane medium	C_g	$\text{mol} \cdot \text{m}^{-3}$	0.62	(Geng and Duan, 2010; Plaksin et al., 2014; Sun et al., 2001)
Henry's constant	k_H	$\text{Pa} \cdot \text{m}^3 \cdot \text{mol}^{-1}$	$1.613 \cdot 10^5$	
Hydrostatic pressure in the extra-membrane medium	P_0	Pa	10^5	(Wong, 1977)
Diffusion coefficient of air in the extra-membrane medium	D_{gl}	$\text{m}^2 \cdot \text{s}^{-1}$	$3.68 \cdot 10^{-9}$	(Wise and Houghton, 1966)
Effective thickness of boundary layer between extramembrane medium and intramembrane space for gas transport	ξ	nm	0.5	(Plaksin et al., 2014)
Vacuum permittivity	ϵ_0	$\text{F} \cdot \text{m}^{-1}$	$8.854 \cdot 10^{-12}$	(Mohr et al., 2008)
Relative permittivity of the intramembrane cavity	ϵ_r	-	1	(Plaksin et al., 2014)
Resting membrane capacitance	C_{m0}	$\mu\text{F} \cdot \text{cm}^{-2}$	1.0	(Pospischil et al., 2008)

Table 2. Parameters of the NICE mechanical model.

3.3.1.2 NICE electrical model.

The electrical part of the NICE electromechanical model predicts that the alternating expansions and compressions of a cavitating sonophore induce local, periodic oscillations in the plasma membrane capacitance (given by $C_m(Z) = \frac{C_{m0}\Delta}{a^2} \left[Z + \frac{a^2 - Z^2 - Z \cdot \Delta}{2Z} \ln \left(\frac{2Z + \Delta}{\Delta} \right) \right]$ as in (Plaksin et al., 2014)), which in turn cause large-amplitude oscillations of the transmembrane potential V_m near the resonating structure. The detailed effects of such voltage variations on neuronal excitation are cell-type-specific and captured by a modified Hodgkin-Huxley differential system (Figure 16(b)), where the evolution of the local membrane potential V_m depends not only on the contribution of several ionic currents with specific

conductances g_i and reversal potentials E_i , but also on a so-called capacitive displacement current ($I_C = V_m \frac{dC_m}{dt}$) originating from the capacitance oscillations:

(93)

$$\begin{aligned} \frac{dV_m}{dt} &= -\frac{1}{C_m} \left[V_m \frac{dC_m}{dt} + \sum_i g_i \cdot (V_m - E_i) \right] \\ \frac{dx}{dt} &= \begin{cases} \alpha_x(V_m) \cdot (1 - x) - \beta_x(V_m) \cdot x \\ \frac{x_\infty(V_m) - x}{\tau_x(V_m)} \end{cases} \end{aligned}$$

In this system, non-leakage ionic conductances are regulated by the product of one or multiple gating variables x , whose evolution is regulated by specific voltage-dependent activation and inactivation rate constants (α_x and β_x , respectively), or by a steady state probability x_∞ and a time constant τ_x (also both voltage-dependent). Sodium (m and h) and delayed rectifier potassium (n) currents gating variables have been defined with the former paradigm (Pospischil et al., 2008), while that of slow non-inactivating (p) and calcium (s and u) currents are defined with the latter one (Plaksin et al., 2016; Pospischil et al., 2008).

It should be noted that the electric pressure term P_Q depends directly on the membrane charge density, and therefore varies over the course of neural activation. As a result, the mechanical and electrical differential systems are bidirectionally coupled.

3.3.2 A multi-Scale Optimized Neuronal Intramembrane Cavitation (SONIC) model

The NICE mechanical model (described in (Plaksin et al., 2014)) and the Hodgkin-Huxley models of cortical regular spiking (RS), fast spiking, low-threshold spiking (LTS), thalamic reticular, and thalamo-cortical neurons (described in (Plaksin et al., 2016)), as well as Subthalamic Nucleus (STN) neurons (described in (Otsuka et al., 2004; Tarnaud et al., 2018a)) have been implemented in Python 3.6 and coupled together, using identical equations and parameters as in the references. Model equations are solved here with the `odeint` function from the `scipy.integrate` Python library (<http://www.scipy.org>) that uses a fixed step, variable order solver automatically selecting between nonstiff (Adams) and stiff (BDF) methods based on dynamic monitoring of the integrated system (Hindmarsh, 1983; Petzold, 1983). Numerical simulation of a RS neuron with typical sonophore in-plane radius (32 nm) and LIFUS parameters (500 kHz carrier frequency, 100 kPa pressure amplitude) reveals the extreme stiffness of the differential system. In consequence, the algorithm requires to use many time steps per acoustic period (1000 in our implementation) to ensure stable integration of intra-cycle system oscillations, and results in tremendous computation times ($\gg 1$ day for a 150 ms CW stimulus). Therefore, we introduce here multiple optimization steps to reduce the computational cost of the algorithm.

3.3.2.1 Lennard-Jones approximation of intermolecular pressure.

Profiled simulations of the mechanical model in isolation reveal that the spatial integration of intermolecular pressure P_M is by far the longest internal computation at each iteration. However, despite its complexity, this integrated pressure term depends solely on leaflet deflection and the nature of its profile is similar to that of its local counterpart. Therefore, a precomputing step is defined wherein a

Lennard-Jones expression of the form $\widetilde{P}_M(Z) = \widetilde{A}_r \left[\left(\frac{\widetilde{A}^*}{2Z + \Delta(Q_m)} \right)^{\widetilde{x}} - \left(\frac{\widetilde{A}^*}{2Z + \Delta(Q_m)} \right)^{\widetilde{y}} \right]$ is fitted to the integrated profile and then used as a new predictor of intermolecular pressure during the iterative numerical resolution (Figure 17(a)). This simplification allows to reduce computation times by more than one

order of magnitude, without significantly affecting the resulting deflection profiles (RMSE = 0.8% of cavitation extent over one acoustic period for typical simulation conditions mentioned above).

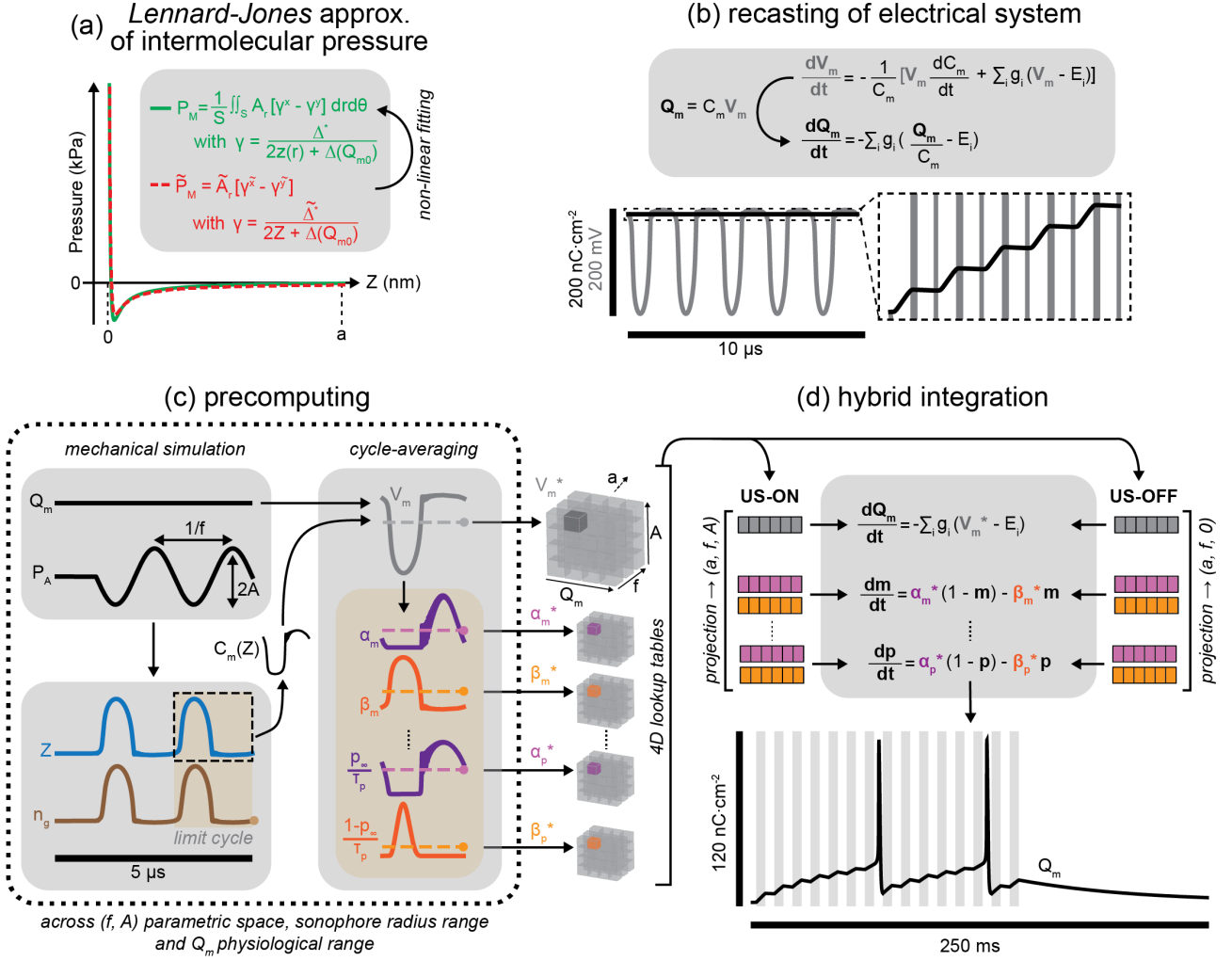


Figure 17. Description of the model simplification and optimization steps. (a) Comparison of spatially integrated (green) and fitted approximation (dashed red) of intermolecular pressure profiles for a realistic range of deflections. (b) Explicit representation of the electrical system recasting, along with a comparison of the short-term evolution of the membrane potential (V_m) and charge density (Q_m) upon sonication (500 kHz, 100 kPa), showing remarkably different stiffness. (c) Schematic representation of the coarse-graining and precomputing pipeline. Mechanical simulations are run until periodic stabilization of Z and n_g , at which point the membrane capacitance C_m , transmembrane potential and voltage-gated rate constants are computed over the last acoustic cycle. The average value of V_m and rate constants are then stored into lookup tables. The process is repeated for various combinations of sonophore radii (a), US frequencies (f), acoustic pressure amplitudes (A) and membrane charge densities. (d) Schematic representation of the hybrid integration of the electrical system. Lookup tables are interpolated at a specific sonophore radius, US frequency and acoustic amplitude to yield 1D projected vectors of effective variables in the Q_m space, which are then used alternatively to interpolate effective variables during US-ON and US-OFF periods, respectively.

3.3.2.2 Recasting of the electrical system.

Simulations of the detailed NICE electromechanical model predict that while the local membrane potential of a cavitating sonophore undergoes large-amplitude oscillations, the membrane charge density and the ion channel gating variables around that structure evolve much more smoothly over the course of neural activation (Plaksin et al., 2014) and Figure 17(b)). Therefore, the distinct electrical system is first recast as function of charge (using the transformation $Q_m = C_m \bullet V_m$), thereby removing the capacitive displacement current term and yielding a new scheme composed only of smooth differential variables:

(94)

$$\begin{aligned} \frac{dQ_m}{dt} &= - \left[\sum_i g_i \cdot \left(\frac{Q_m}{C_m} - E_i \right) \right] \\ \frac{dx}{dt} &= \begin{cases} \alpha_x \left(\frac{Q_m}{C_m} \right) \cdot (1 - x) - \beta_x \left(\frac{Q_m}{C_m} \right) \cdot x \\ \frac{x_\infty \left(\frac{Q_m}{C_m} \right) - x}{\tau_x \left(\frac{Q_m}{C_m} \right)} \end{cases} \end{aligned}$$

As Q_m/C_m is still rapidly oscillating, the evolution of electrical differential variables during US-ON periods is then expressed as a function of “effective” internal variables (using this time the rate constants formulation for all gates, with $\alpha_x = x_\infty/\tau_x$ and $\beta_x = 1/\tau_x - \alpha_x$), obtained by averaging their rapid oscillatory part over an acoustic period T . This is only possible because the differential variables evolve smoothly and allows to capture the millisecond-scale system evolution without explicitly resolving intra-cycle oscillations:

(95)

$$\begin{aligned} \left(\frac{dQ_m}{dt} \right)^* &= - \sum_i g_i \cdot \left(\frac{\int_0^T \frac{Q_m}{C_m(Z)} dt}{\frac{T}{V_m^*}} - E_i \right) \\ \left(\frac{dx}{dt} \right)^* &= \frac{\int_0^T \alpha_x \left(\frac{Q_m}{C_m(Z)} \right) dt}{\frac{T}{\alpha_x^*}} \cdot (1 - x) - \frac{\int_0^T \beta_x \left(\frac{Q_m}{C_m(Z)} \right) dt}{\frac{T}{\beta_x^*}} \cdot x \end{aligned}$$

We shall refer to V_m^* as the effective membrane potential and to α_x^* and β_x^* as effective rate constants.

3.3.2.3 Precomputation and hybrid integration of effective solutions.

As they depend directly on the sonophore deflection profile and thus indirectly on the sonophore geometry, LIFUS parameters and electromechanical coupling, effective variables are precomputed for various combinations of sonophore radii (a), US frequencies (f), acoustic peak pressure amplitudes (A) and membrane charge densities – covering the LIFUS parametric space, sonophore geometrical range and membrane physiological range – and then stored in 4D lookup tables to be linearly interpolated at runtime (Figure 17(c)). For each combination, a short simulation of the mechanical system is performed until a limit cycle is reached (detected by thresholding the root mean square error between two consecutive cycles of both Z and n_g), and effective variables are then computed over the last acoustic cycle. The required granularity of lookup tables was determined by visually inspecting the nonlinearity of effective variables along each dimension. Lookups are computed here for 3 characteristic sonophore radii (16, 32 and 64 nm), 7 carrier frequencies (20, 100 and 500 kHz, 1, 2, 3 and 4 MHz), pressure amplitudes including 0 Pa and 50 logarithmically distributed values between 0.1 and 600 kPa, and cell-type-specific ranges of physiologically realistic, linearly distributed charge densities (from $V_{m0} \cdot C_{m0} - 25$ to 50 nC/cm² with a 1 nC/cm² step).

Effective solutions are computed by interpolating effective variables at (a, f, A) and $(a, f, 0)$ to yield 1D projected vectors in the Q_m space, which are then used to interpolate effective variables and solve equation (95) during US-ON and US-OFF periods, respectively (Figure 17(d)). The same *odeint* solver as for the detailed NICE model is used, however the absence of rapid oscillations allows to use a constant time step far greater than a typical acoustic period ($dt = 50 \mu s$).

For the sake of simplicity, this new model variant involving electrical system recasting and coarse-graining, precomputation of effective variables and hybrid numerical integration using lookup interpolation tables will be referred to as SONIC model later on.

3.3.3 Comprehensive characterization of neural responses

3.3.3.1 Spike detection and derived metrics.

Incident neural spikes are detected on charge density profiles as local maxima using prominence thresholding, and neighboring local minima are used to define the spike boundaries. Spike amplitude is defined as the smallest differential between the local maximum and the neighboring local minima. Latency is defined as the delay between the stimulus onset and the occurrence of the first spike, and firing rate as the average of reciprocals of inter-spike intervals, accounting only for spikes occurring during the stimulus interval.

3.3.3.2 Systematic exploration of the LIFUS parameter space.

A typical LIFUS protocol comprises five distinct stimulation parameters: US frequency, acoustic peak pressure amplitude, pulse repetition frequency (PRF), duty cycle (DC), and duration, all of which substantially affect the mechanical and electrical response of a neuron. The latter also depends heavily on the cell-type-specific ion channel population and on the acoustic properties of the immediate anatomical environment. Hence, LIFUS optimization is a complex problem that requires the exhaustive characterization of the effects of multiple, possibly co-dependent, parameters over a high-dimensional space – a challenge that goes far beyond what is experimentally feasible. In this context, computational models can constitute a powerful tool to study the effect of a specific set of parameters in an isolated manner, provided they can be used efficiently.

The NICE electromechanical model predicts that cell-type-specific sensitivities to LIFUS can be classified into two main categories, depending on the presence or absence of a voltage-gated depolarization current active at sub-threshold charge levels (Plaksin et al., 2016). Therefore, the parameter space is systematically explored for RS and LTS neurons – that provide a typical use case for each category – by varying the following stimulation parameters: sonophore radius (5 logarithmically distributed values from 16 to 64 nm), US frequency (500 kHz and 4 MHz), acoustic peak pressure amplitude (30 logarithmically distributed values from 10 to 600 kPa), PRF (10, 100 and 1000 Hz) and duty cycle (1 to 100% with a 1% step). Stimulus duration is fixed to 1 s in order to analyze all relevant features of neural responses (excitation thresholds, firing rate adaptation, bursting behaviors, etc.). Two-dimensional behavior maps are then produced by plotting firing rates of resulting responses as a function of duty cycle and pressure amplitude, since neural activation across cell types is found to be mostly sensitive to these parameters, presumably along with the sonophore radius.

3.3.4 A multi-compartmental SONIC model to study spatially-distributed nanoscale interactions

Because it is recast as a differential system akin to the familiar Hodgkin-Huxley formulation, the SONIC model can be easily extended into multiple spatial compartments. Considering the inherent assumptions of the intramembrane cavitation theory, the first (most evident) expansion scale to consider is that of the sonophore itself, in interaction with its direct surroundings. Therefore, a nanoscale multi-compartmental SONIC model is developed to study the impact of that interaction on the local neural response. It consists of two radially symmetric membrane sections (Figure 18): a bilayer sonophore (compartment S) of radius a , surrounded by a LIFUS-insensitive circular membrane patch (compartment I) expanding from a to an outer radius b . The ratio of sonophore membrane area (πa^2) divided by the total membrane area (πb^2) is designated as the sonophore coverage fraction ($f_s = a^2/b^2$). Compartments S and I are modeled electrically by voltage gated RC circuits, representing the local effective

transmembrane dynamics of an RS neuron in the LIFUS-modulated sonophore region and the LIFUS-insensitive surrounding membrane. Both compartments are linked to ground in the extracellular medium, and connected to each other within a sub-membrane intracellular space of depth d_{eff} by a cylindrical resistor R_{SI} . The resistor value is approximated by considering an element that spans between the middle radial coordinates of compartments S and I, such that $R_{SI} = \int_{\frac{a}{2}}^{\frac{a+b}{2}} \frac{\rho}{2\pi \cdot d_{eff} \cdot r} dr = \frac{\rho}{2\pi \cdot d_{eff}} \ln\left(\frac{a+b}{a}\right)$, where the cytoplasmic resistivity ρ is set to the typical value of $100 \Omega \cdot \text{cm}$ (McNeal, 1976). Finally, d_{eff} is arbitrarily set to 100 nm, i.e. within the order of magnitude of a typical sonophore diameter.

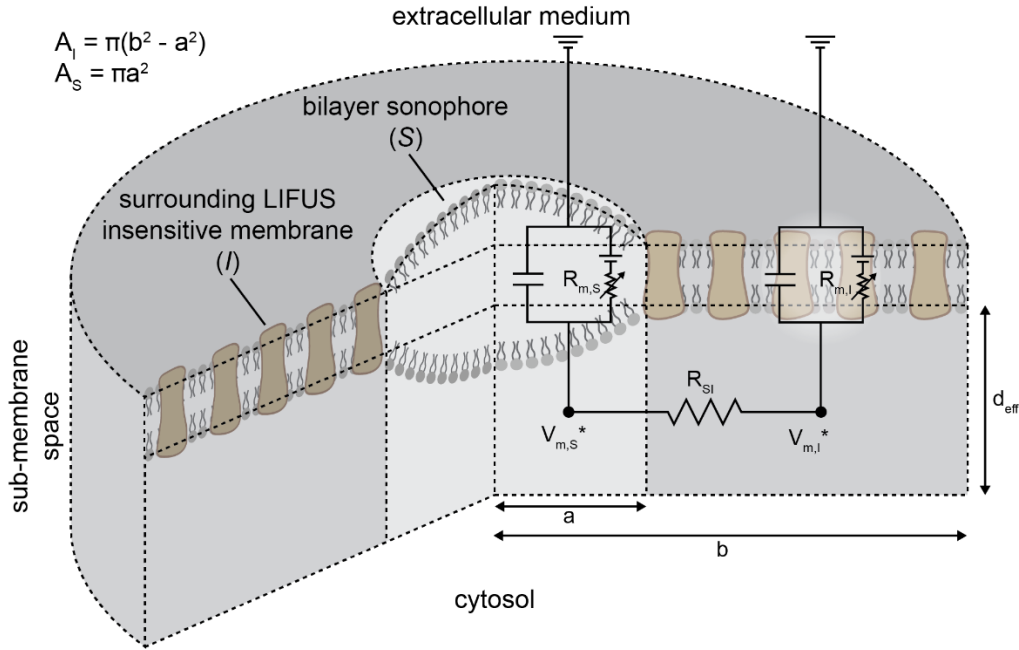


Figure 18. Schematic representation of the nanoscale multi-compartmental SONIC model. A bilayer sonophore of radius a (S, in light grey) is surrounded by a LIFUS-insensitive circular membrane patch (I, in dark grey) expanding between a and an outer radius $b = a/\sqrt{f_s}$, where f_s represents the sonophore coverage fraction of the total membrane area. Both sections are modeled electrically by voltage gated RC circuits, linked to ground in the extracellular medium, and connected to each other within a sub-membrane intracellular space of depth d_{eff} by a cylindrical resistor R_{SI} .

In this cylindrically geometric model, the effective variation of membrane charge density in each compartment results from (1) transmembrane currents triggered by the local effective membrane potential variations, and (2) effective intracellular currents between the two compartments as a result of differences in local effective membrane potential: $I_{SI}^* = \frac{1}{T} \int_0^T \frac{V_{mS} - V_{mI}}{R_{SI}} dt = \frac{V_{mS}^* - V_{mI}^*}{R_{SI}}$. It results in the following equations:

(96)

$$\begin{aligned} \left(\frac{dQ_{mS}}{dt}\right)^* &= \frac{1}{\pi a^2} \cdot \frac{V_{mI}^* - V_{mS}^*}{R_{SI}} - \sum_i g_i \cdot (V_{mS}^* - E_i) \\ \left(\frac{dQ_{mI}}{dt}\right)^* &= \frac{1}{\pi(b^2 - a^2)} \cdot \frac{V_{mS}^* - V_{mI}^*}{R_{SI}} - \sum_i g_i \cdot (V_{mI}^* - E_i) \end{aligned}$$

where local ionic conductances are regulated by independent sets of gating variables defined as in equation (95).

This multi-compartmental model has been implemented *NEURON* (Hines and Carnevale, 1997), by using the precomputed lookup tables from an RS neuron (see Figure 17) to compute membrane currents, and a custom intracellular connection scheme explicitly casted in terms of V_m^* to compute intracellular currents.

The hypothesis of a unique, transmembrane potential variation across the entire membrane patch is also considered. This hypothesis was previously assessed with a point-like NICE model by only considering an attenuated version of the membrane capacitance oscillations resulting from the cavitating sonophore ($C_m(t) = f_s \cdot C_{mS}(t) + (1 - f_s) \cdot C_{m0}$), thereby reducing the variation range of the transmembrane potential (Plaksin et al., 2016). Here, a point-like SONIC model is developed in parallel that uses lookup tables derived from mechanical simulations with this spatially averaged capacitance.

3.4 Results

3.4.1 LIFUS-dependent effective variables

In this section, effective profiles of membrane capacitance, membrane potential and ion channels rate constants of an RS neuron are interpolated from the corresponding pre-computed lookup tables (see section 3.3.2.3 and Figure 17(c)) at various acoustic amplitudes, US frequencies, and sonophore radii, and evaluated as a function of membrane charge density.

3.4.1.1 Effective membrane potential and rate constants are significantly amplified as a function of acoustic pressure amplitude.

In the absence of acoustic perturbation, the mechanical state of the sonophore is solely dependent on gas content and charge density. As the latter increases in magnitude, augmentation of the electrical pressure compresses the sonophore and increases its membrane capacitance. As a result, the profile of the unperturbed effective membrane potential $V_m^* = Q_m/C_m$ is an odd function of Q_m that deviates slightly from linearity (Figure 19(a)). For small acoustic perturbations ($A < 50$ kPa), the amplitude of intra-cycle oscillations is still heavily dependent on the electrical pressure. Hence, the sonophore expansions and the resulting capacitance drops throughout acoustic cycles are considerably reduced as the magnitude of membrane charge density increases. Thus, the effective membrane capacitance $C_m^* = \left[\frac{1}{T} \int_0^T \frac{dt}{C_m(Z)} \right]^{-1}$ displays an inverse bell-shaped profile as a function of charge, and the resulting effective membrane potential, despite conserving its odd symmetry, is amplified at intermediate values of $|Q_m|$ before converging asymptotically towards its unperturbed counterpart as charge magnitude is further increased. Larger acoustic perturbations ($A > 50$ kPa) induce greater sonophore expansions and capacitance drops within intra-cycle oscillations, during which the influence of the electrical pressure is heavily reduced. This means that the C_m^* profile is shifted towards lower values and exhibits little dependency on the charge density within the physiological range. Consequently, the V_m^* charge profile is amplified and transitions towards another quasi-linear regime. This amplification generates larger deviations from reversal potentials, and thus stronger ionic currents.

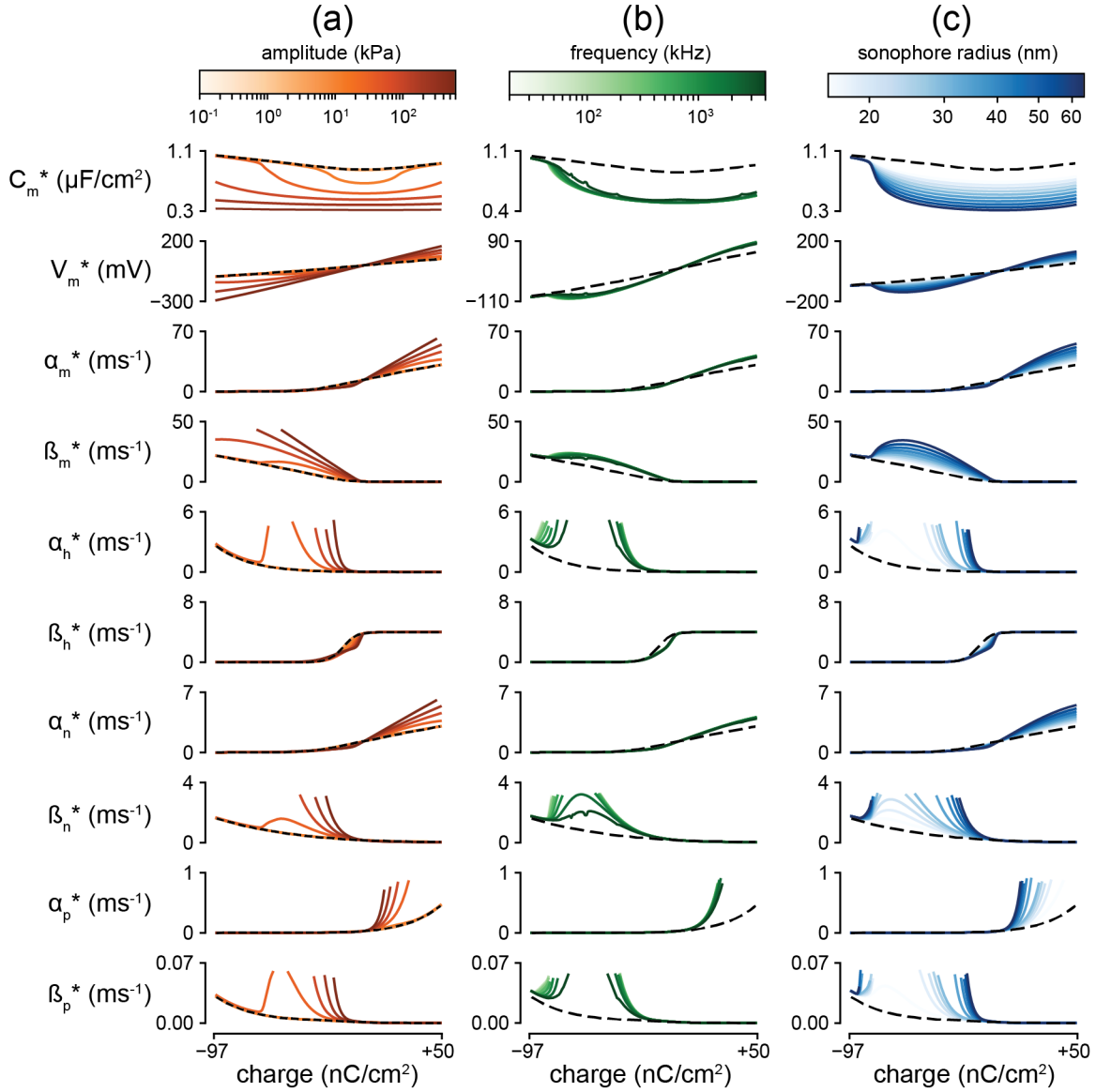


Figure 19. Modulation of charge-dependent effective variables as a function of acoustic pressure amplitude, US frequency and intrinsic sonophore radius. Effective variables of an RS neuron are displayed as a function of membrane charge density, with a color code corresponding to the modulating variable at which they were derived (color bar depicted on top). The original, non-modulated variables (dashed black lines) are also depicted for comparison. (a) Dependence on acoustic pressure amplitude (32 nm radius sonophore, $f = 500$ kHz). (b) Dependence on US frequency (32 nm radius sonophore, $A = 50$ kPa). (c) Dependence on intrinsic sonophore radius ($f = 500$ kHz, $A = 50$ kPa).

As voltage-gated rate constants are nonlinear functions of the membrane potential, their effective counterparts cannot be derived directly from V_m^* and must be explicitly computed. For small acoustic perturbations, they also deviate from their original counterpart at intermediate charge values and re-converge asymptotic towards it as we reach the borders of the physiological range. For large acoustic perturbations, all profiles are widely amplified around one extremity of the range due to their exponential nature, with the exception of the sigmoidal β_h profile. In particular, α_m^* and α_n^* are amplified for positive charge values which corresponds to faster openings of the sodium m-gate and potassium n-gate during action potentials. Hence, increasing acoustic amplitude also amplifies rate constants, which is likely to trigger faster gating variations.

3.4.1.2 Effective variables are significantly amplified as a function of the sonophore radius.

For intermediate values of acoustic pressure amplitude (here 50 kPa), varying the sonophore radius within a realistic range around its default value ($16 < a < 64$ nm) produces significant changes in the

effective variables profiles (Figure 19(b)). Expectedly, larger sonophores yield more pronounced sonophore expansions (as shown in (Krasovitski et al., 2011)) and related capacitance drops, thereby amplifying the effective membrane potential profile in a charge-symmetric manner, as obtained when increasing acoustic amplitude. It results in a similar amplification of all effective rate constants. Oppositely, smaller sonophores have narrower periodic expansions, which limits the amplification of effective variables. The consequences of the dependence of effective variables on sonophore radius in terms of neuronal excitability are discussed in section 3.4.5.1.

3.4.2 Model validation

In this section, we evaluate the ability of the SONIC model to accurately reproduce membrane charge density profiles generated with the detailed NICE model (based on the charge-casted NICE electro-mechanical model described in equations (92) and (94)) for a variety of LIFUS conditions. For cases requiring the identification of sub- and supra-threshold regimes, a binary search to find the excitation threshold amplitude was conducted with the SONIC model and the appropriate neuron type, US frequency, and sonophore radius.

3.4.2.1 The model accurately captures predicted cell-type-specific excitation thresholds and responses to CW stimuli.

Under typical continuous-wave (CW) LIFUS conditions ($f = 500$ kHz, 150 ms stimulus), the SONIC model accurately captures both passive responses of an RS neuron at sub-threshold amplitudes, and non-adaptive high-frequency tonic spike trains elicited at supra-threshold amplitudes (Figure 20(a), top). In the latter regime, amplitude-dependent variations in response latency, firing rate, and spike amplitude within the tonic train are picked up with a remarkable accuracy up to 600 kPa (Figure 20(a), bottom), a value far exceeding the pressure amplitudes used in recent neuromodulation studies on the CNS (Kubaneck, 2018). However, the model fails to capture the exact threshold amplitude at which the neuron transitions from a passive response to an active spiking behavior: integration with the detailed NICE model does not yield excitation at the threshold amplitude determined with the SONIC model (Figure 20(a), top). It can be assumed that this arises from the high nonlinearity of the effective membrane potential at low acoustic pressure amplitudes and negative charge densities (Figure 19(a)), yielding inaccurate linear interpolations during the build-up phase.

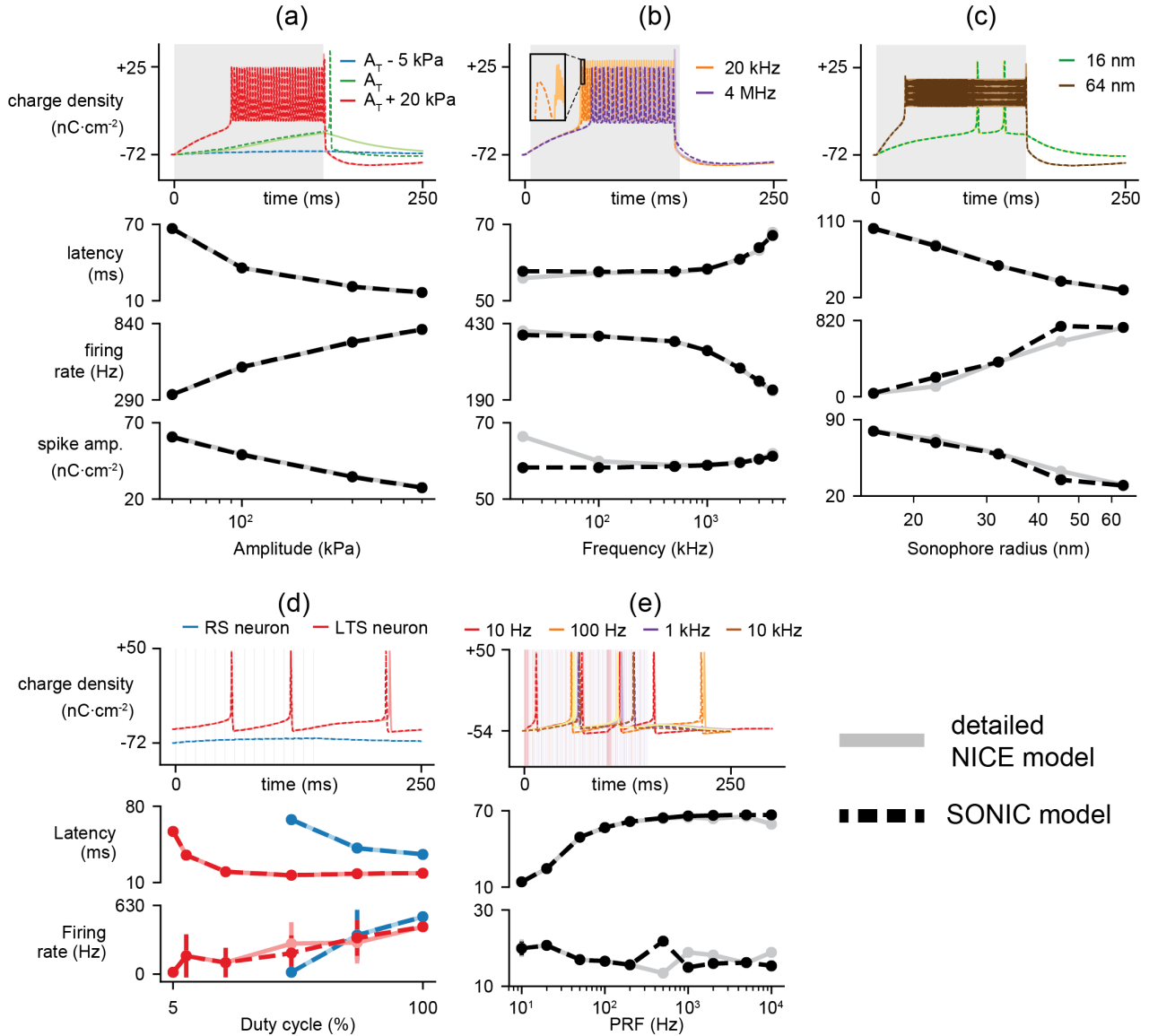


Figure 20. Validation of the SONIC model against the detailed NICE model. Membrane charge density profiles from simulations with the detailed NICE model (light solid curves) and SONIC model (dark dashed curves) of different neurons under various LIFUS conditions are compared, along with derived spiking metrics (latency, firing rate and spike amplitude). (a) Top: comparison of charge density profiles of a RS neuron under CW sonication ($f = 500$ kHz) for sub-threshold ($A_T - 5$ kPa), threshold (A_T) and supra-threshold ($A_T + 20$ kPa) acoustic pressure amplitudes. Bottom: comparison of derived spiking metrics for varying supra-threshold pressure amplitudes. (b) Top: comparison of charge density profiles of a RS neuron under CW sonication at supra-threshold amplitude (threshold + 20 kPa) with $f = 20$ kHz and $f = 4$ MHz. Bottom: comparison of derived spiking metrics for varying carrier frequencies from 20 kHz to 4 MHz. (c) Top: comparison of charge density profiles of a RS neuron under CW sonication at supra-threshold amplitude (threshold + 20 kPa) with 16 and 64 nm radius sonophores at $f = 500$ kHz. Bottom: comparison of derived spiking metrics for varying sonophore radii from 16 to 64 nm. (d) Top: comparison of charge density profiles of RS (blue) and LTS (red) neurons under pulsed-wave (PW) sonication ($f = 500$ kHz, $A = 100$ kPa, 100 Hz PRF) at 5% DC. Bottom: comparison of derived spiking metrics for varying duty cycles from 5 - 100%. (e) Top: comparison of charge density profiles of a LTS neuron under PW sonication ($f = 500$ kHz, $A = 100$ kPa, 5% DC) with PRF of 10 Hz, 100 Hz, 1 kHz and 10 kHz. Bottom: comparison of derived spiking metrics for varying PRF from 10 Hz to 10 kHz.

The model accuracy for supra-threshold amplitudes is conserved as the carrier frequency increases up to several MHz (Figure 20(b), top). However, significant differences in spike amplitude (and to a lesser extent in latency and firing rate) appear as the frequency approaches the lower bound of the US domain (Figure 20(b), bottom). In fact, at such low frequencies, the order-of-magnitude of the intra-cycle oscillations dynamics approaches that of the gating kinetics of sodium and potassium ion channels, thereby inducing large intra-cycle gating variations that modulate the membrane charge density at the US frequency and cause considerable oscillations in the detailed solution (Figure 20(b), inset).

As can be expected, these oscillations are absent from the effective solution because of the intrinsic cycle-averaging strategy of the SONIC model, but the resulting spiking behavior stays qualitatively correct. This intra-cycle interference (and the resulting divergence) vanishes at frequencies higher than 100 kHz. This supra-threshold accuracy is also conserved for the sonophore radii bounding the lookup interval (16 and 64 nm): the larger radius yields similar reductions in latency and spike amplitude and increases in firing rate, and vice-versa (Figure 20(c), top). Interestingly, simulations of the SONIC model at intermediate radii that are not present in the lookup tables yield identical latencies than those obtained with the detailed NICE model, but higher firing rates and spike amplitudes (Figure 20(c), bottom). This inaccuracy suggests that while the effective membrane potential governing the initial charge build-up exhibits a rather linear dependency on the sonophore radius, effective rate constants depend nonlinearly on this variable, hence a higher resolution of the lookup tables in this dimension would be needed to produce quantitatively identical results. Nonetheless, spiking patterns stay qualitatively similar. Thus, the SONIC model can estimate cell-type-specific threshold excitation amplitudes with a precision in the order of kPa, and accurately captures the amplitude, frequency and sonophore radius dependencies of neural responses to CW stimuli. Note that these observations translate to other neuron types since they all share the same mode of interaction with CW stimuli (data not shown), except for the STN neuron type which was validated separately (see section 3.5.1.3).

3.4.2.2 The model accurately captures predicted cell-type-specific responses to PW stimuli.

Under typical PW stimulation conditions ($f = 500$ kHz, $A = 100$ kPa, 100 Hz PRF), the SONIC model accurately captures cell-type-specific, DC-dependent changes in latency and firing rate of RS and LTS neurons, which are good representatives of the two main types of sensitivities to pulsed LIFUS protocols according to predictions from the NICE model (Plaksin et al., 2016). In particular, at very low duty cycles, both the passive response of a RS neuron and the sparse firing of a LTS neuron are accurately reproduced (Figure 20(d), top). In the latter case, a minor divergence is initiated and amplified during US-OFF periods, which is likely due to the great sensitivity of the charge-casted system to initial conditions of early depolarization phases as well as intrinsic differences in the computation of membrane capacitance between the NICE and SONIC models. This divergence is also found for the RS neuron that starts firing at 50% DC and yields small inaccuracies in the reported firing rates (Figure 20(d), bottom), despite producing very similar spiking behaviors. The SONIC model accuracy is mostly preserved throughout variations in PRF for a LTS neuron at 5% DC (Figure 20(e)), with two notable exceptions around 1 kHz and at 10 kHz. In the former case, the model inaccuracy is probably due to a particular pulse-spike synchronization that amplifies divergence of the effective solution – **in fact**, a slight divergence in the charge build-up phase can shift spike occurrence by one or several pulses, thereby offsetting the entire downstream response dynamics. In the latter case, however, divergence likely arises from the increasing number of ON-OFF transitions and the decrease of pulse duration down to the order of magnitude of the integration time step of the SONIC model, limiting the number of iterations per pulse and thereby the accuracy of the effective solution. Thus, the SONIC model accurately captures the duty cycle and PRF dependencies of cell-type-specific neural responses to PW stimuli, relevant to different gating mechanisms.

3.4.3 The SONIC model boosts algorithmic efficiency by at least 3 orders of magnitude

The algorithmic acceleration provided by the presented SONIC model is assessed by comparing computation times of SONIC simulations with that of detailed NICE simulations, performed on the same computer (24-core, 2.1 GHz clock rate server, 126 GB RAM, Ubuntu 16.04.3 operating system).

For typical CW stimulation parameters ($f = 500$ kHz), the detailed solution of the NICE model is computed in approx. 1 day, while the effective solution of the SONIC model is solved in less than 1 min. (Figure 21(a)), which corresponds to a gain in efficiency of more than 3 orders of magnitude.

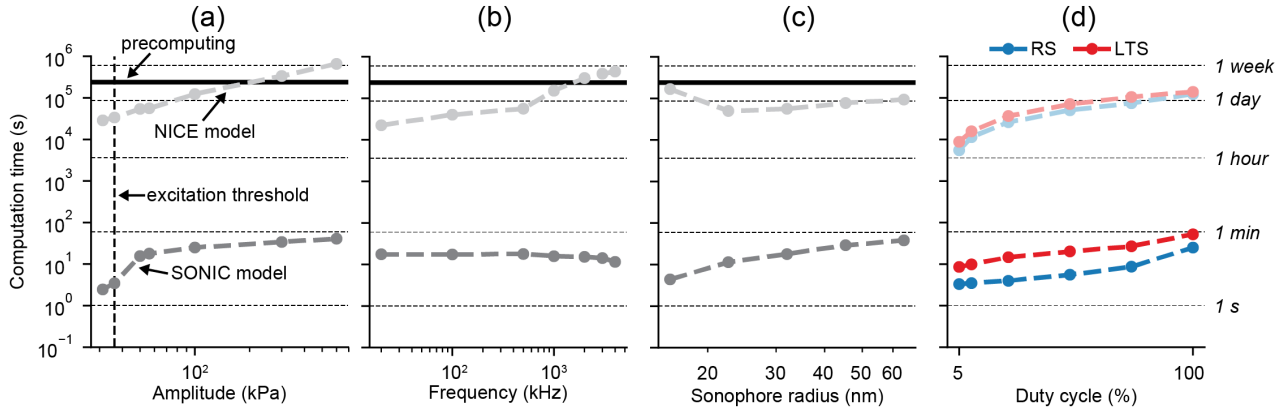


Figure 21. Quantification of the SONIC model acceleration. Comparison of computation times for 250 ms simulations under various LIFUS conditions, with the detailed NICE model (light gray) and SONIC model (dark gray, along with the fixed precomputation cost). (a) Comparison for CW simulations of the RS neuron at various sub- and supra-threshold acoustic amplitudes. The excitation threshold is also indicated (dashed vertical line). (b) Comparison for CW simulations of the RS neuron at various US frequencies with a supra-threshold amplitude (threshold + 20 kPa). (c) Comparison for CW simulations of the RS neuron with various sonophore radii, also at supra-threshold amplitude (threshold + 20 kPa). (d) Comparison for simulations of the RS (blue) and LTS (red) neurons ($f = 500$ kHz, $A = 100$ kPa, 100 Hz PRF) at various duty cycles. Dashed horizontal lines indicate characteristic durations.

The computation times of SONIC simulations show a significant increase between the sub- and supra-threshold regimes. This illustrates the stiffer differential system resulting from an active electrical response, as the employed LSODA solver uses an adaptive integration scheme that takes an increasing number of internal steps at each iteration as the system stiffness augments. Conversely, the computation times of NICE simulations augment linearly with acoustic amplitude and do not exhibit a sharp transition between those two regimes, as the full electromechanical model possesses a huge intrinsic stiffness that is hardly affected by the presence of an active electrical response, but rather by the increase in magnitude of intra-cycle oscillations.

Expectedly, computation times of the NICE model increase as the stimulus carrier frequency increases, owing to the algorithm's frequency-dependent integration time step, while those of the SONIC model do not exhibit any dependency on that parameter (Figure 21(b)). The NICE model takes longer to compute supra-threshold simulations for very small sonophore radii – which could indicate an increase in the system's nonlinearity for such small structures – and is otherwise rather constant across values of a . Conversely, the SONIC model takes longer to compute supra-threshold simulations (threshold + 20 kPa, where the threshold is determined for each value of a by a titration procedure) as the sonophore radius increases. This results from the greater sensitivity of larger sonophores to pressure amplitude, meaning that responses in the supra-threshold range transition faster towards tonic, high-frequency firing (see Figure 20(c)), which produces stiffer differential systems 20 kPa above the excitation threshold.

For PW stimuli, NICE computation times increase as the stimulus duty cycle increases, for both actively and passively responding neurons (Figure 21(d)), as a result of the longer LIFUS-ON total duration. SONIC computation times show less sensitivity to that parameter, but more intra-neuron variability: computation times for the actively responding LTS neuron are on average twice that of the RS neuron that is less activated, thereby confirming the influence of electrical variables on the effective system's stiffness.

Overall, the gain in algorithmic efficiency provided by the SONIC model must be mitigated as it comes with an initial cost: the time required to inform the lookup tables necessary to run SONIC simulations is in the order of 2-3 days. However, this precomputation cost is fixed and can be significantly decreased by a trivial parallelization, which is impossible with the detailed NICE model.

3.4.4 Cell-type-specific excitability and spiking activity depends on multiple LIFUS parameters

The different sensitivities of the RS and LTS neurons to LIFUS have been previously characterized in (Plaksin et al., 2016). This section aims at providing an interpretation of their respective recruitment mechanisms, based on the newly introduced effective membrane dynamics, and at using behavior maps to establish detailed trends of their firing behavior in different regions of the parameter space. It should be noted that a typical behavior map (i.e., 3000 simulations, see Methods section) was generated here in about 30 hours, a process that would have taken more than 10 years with the detailed NICE model.

3.4.4.1 Regular spiking neurons are recruited by leakage currents above a critical ultrasonic dose.

In the sub-threshold state where the membrane charge density is below the neuron's spiking threshold Q_T , LIFUS-ON periods of sufficient intensity trigger a strong effective hyperpolarization of several tens of millivolts that closes all voltage-gated ion channels, but also triggers a depolarizing leakage current (proportional to the difference $V_m^* - E_{leak}$) that increases the membrane charge density (Figure 22(a), insets i-ii). At each pulse offset, the sudden mechanical stabilization of the membrane prompts an effective depolarization that crosses the leakage reversal potential and brings the membrane potential above its pre-pulse level, yet remaining in the sub-threshold state. Hence, the leakage current changes polarity and the charge density decreases. As a result, the net charge variation over a PRI depends on the combination of pressure amplitude and duty cycle (referred to as US dose) that determines the magnitude and duration of LIFUS-ON effective depolarization, and is positive for US doses above a certain threshold. As the charge density progressively approaches Q_T , effective hyperpolarizations and depolarizations are shifted towards higher potential values, which diminishes the imbalance between the LIFUS-ON and LIFUS-OFF charge variations, ultimately reducing the net charge increase per PRI. Above a critical US dose, the imbalance stays positive as the charge crosses Q_T , at which point the sodium channels begin to open and drive further charge increase.

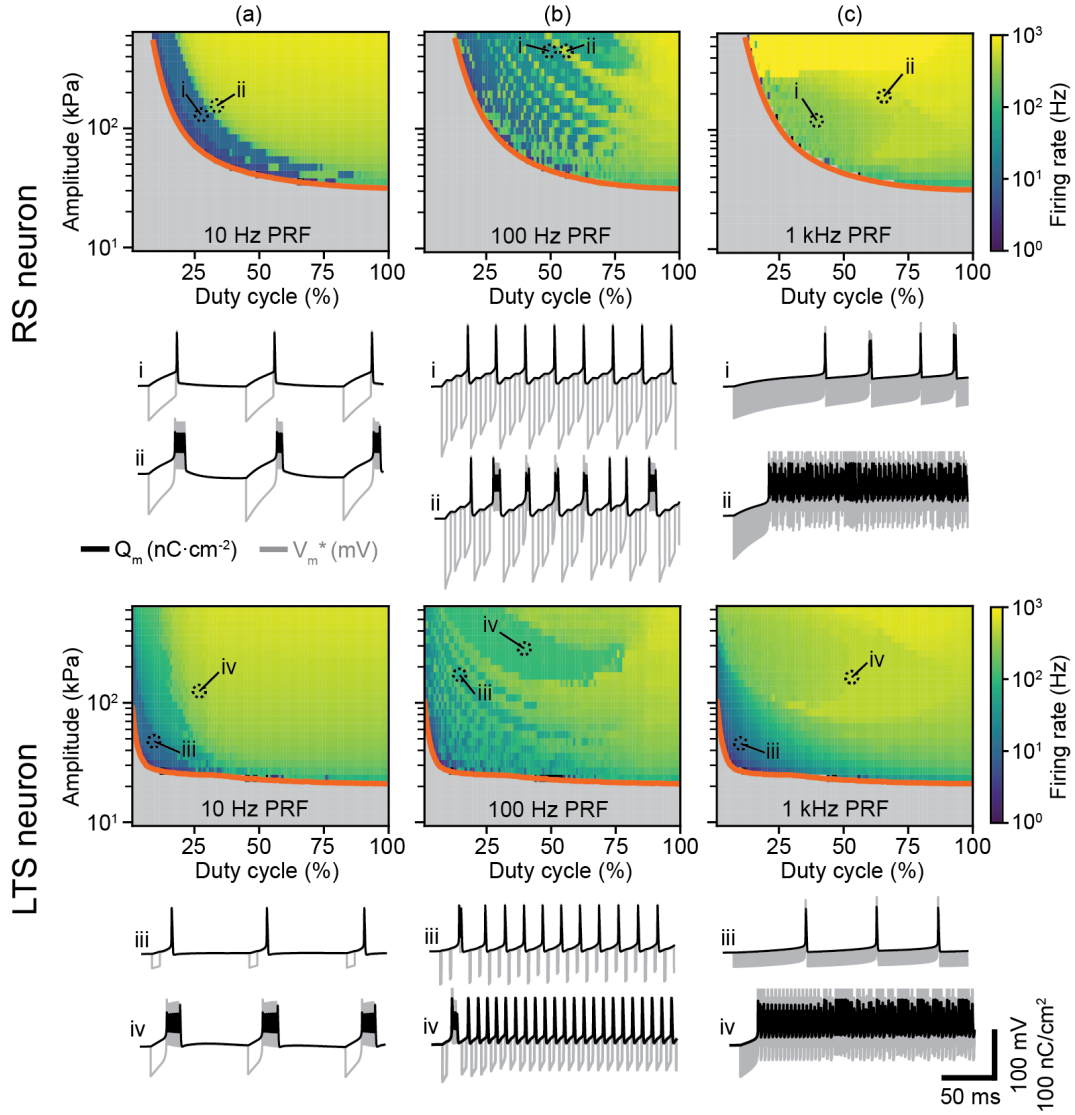


Figure 22. Cell-type-specific LIFUS behavior maps. Two-dimensional behavior maps depicting the firing rate of RS and LTS neurons (32nm sonophore radius, 500 kHz US frequency) as a function of duty cycle and amplitude, for various PRF, along with threshold excitation amplitudes predicted from titration procedures (orange curves). Temporal profiles of membrane charge density (black) and effective membrane potential (gray) are also depicted for selected combinations of duty cycle and amplitude. (a) Behavior maps and selected profiles at 10 HZ PRF. (b) Maps and profiles at 100 Hz PRF. (c) Maps and profiles at 1 kHz PRF.

3.4.4.2 Low-threshold spiking neurons can be recruited at lower ultrasonic doses thanks to calcium currents.

The LTS neuron is intrinsically easier to bring to a supra-threshold state due to its higher resting potential, and is thus generally activated at lower amplitudes than the RS neuron (Figure 22, bottom maps). Moreover, in the sub-threshold state, the sudden effective depolarization at pulse offsets triggers the transient opening of intrinsic low-threshold calcium voltage-gated channels during LIFUS-OFF periods, producing a depolarizing current that can overcome the effect of the hyperpolarizing leakage current and drive further depolarization of the membrane towards Q_T . As a result, the LTS neuron can be excited at far lower duty cycles than the RS neuron with sub-MPa amplitudes (Figure 22(a), inset iii).

3.4.4.3 Cortical neurons can be entrained into different spiking behaviors depending on PRF values.

When a regular or low-threshold spiking neuron reaches the supra-threshold state ($Q_m > Q_T$), the effective gating kinetics of sodium and potassium channels during LIFUS-ON periods trigger a high-frequency, non-adaptive train of action potentials with a high spiking frequency ($\gg 100$ Hz) and reduced spike amplitude ($\ll 70$ nC/cm²), as seen in Figure 20(a-c). During LIFUS-OFF periods, the system's behavior mainly depends on its electrical state at the preceding pulse offset: a decreasing membrane charge at the transition tends to induce repolarization, whereas an increasing membrane charge triggers further depolarization towards an action potential of "standard" amplitude through the traditional (i.e., unmodulated) membrane dynamics of the neuron.

For low PRFs allowing complete membrane repolarization between consecutive pulses, both neurons exhibit a similar, typical behavior (Figure 22(a)): US doses just above their respective excitation threshold see each pulse trigger exactly one spike (insets i and iii), whereas at higher doses each pulse necessarily triggers a burst of spikes (insets ii and iv). Notice that the transition between those spiking patterns is sharper for the RS neuron.

At intermediate PRFs that induce an accumulative depolarization effect between consecutive pulses, both neurons exhibit more complex spiking patterns (Figure 22(b)). Just above the excitation threshold, a large number of pulses is required to trigger a single spike. This number decreases as the US dose is increased. For particular US doses, the rate of sub-threshold charge increase is such that after multiple preceding pulses, the neuron's excitation threshold is reached exactly at the time of a pulse onset, such that a burst of spikes can be fired within the pulse, enriching the firing rate spectrum with a high-frequency component. Interestingly, because the RS neuron's leakage-driven sub-threshold build-up is quasi-linear, it synchronizes its bursting activity with a multiple of the PRI (referred to as nPRI-locked bursting) in a robust manner throughout the stimulus (Figure 22(b), inset ii). Moreover, this behavior is achieved at specific combinations of duty cycle and pressure amplitude seen as distinct stripes of higher firing rate on the behavior map, corresponding to different multiples of the PRI, and surrounded by regions of cyclic spiking activity (Figure 22(b), insets i and ii). This clustered pattern of nPRI-locked bursting cannot be obtained for the LTS neuron, because of the nonlinear influence of the T-type calcium current on the sub-threshold charge build-up. However, as the latter current enhances sensitivity to LIFUS, the LTS neuron can synchronize its spiking activity with the stimulus by firing exactly one spike for each pulse at high US doses (Figure 22(b), inset iv). This behavior (referred to as PRI-locked spiking) is seen over a large region of the considered amplitude-DC space, (which suggests that it could be reliably elicited), something that is not obtained with the RS neuron for the range of considered acoustic amplitudes. When further raising the acoustic dose, both neuron types fire a burst of spikes at each pulse.

At high PRF for which PRI is in the order of magnitude of spike duration, synchronization phenomena do not occur and both neurons show less regular responses (Figure 22(c)). At low US doses slightly above their respective excitation threshold, both neuron fire sparse spikes at a variable rate (Figure 22(c), insets i and iii). At higher US doses, this high-frequency pulsing protocol tends to constrain the membrane charge density to a supra-threshold regime and yields very high firing rates for both neurons (Figure 22(c), insets ii and iv), similar to those obtained by continuous stimulation.

3.4.5 Excitation thresholds are sensitive to LIFUS parameters and sonophore geometry

Visual inspection of effective variables reveals the significant influence of both US frequency and sonophore radius on a neuron's effective electrical system (Figure 19(b-c)), and ultimately on its electrical response. Hence, this section analyzes the influence of these two parameters on excitation thresholds, assessed using titration procedures.

3.4.5.1 Neuronal excitability shows substantial sensitivity to the sonophore radius.

For an RS neuron, augmenting the sonophore radius to twice its reference value (64 nm) induces larger cavitation that amplifies the effective membrane potential (Figure 19(c)) and the resulting leakage-driven sub-threshold depolarization, thereby shifting the excitation threshold significantly towards lower US doses (Figure 23(a), solid curves). This decrease is particularly important at low duty cycles (e.g., > 3-fold decrease from 180 to 45 kPa at 20% DC). Oppositely, diminishing the sonophore radius to half its reference value (16 nm) induces a tremendous increase in threshold amplitudes. Again, this augmentation is particularly marked at low duty cycles (e.g., > 5-fold increase from 110 to 600 kPa at 25% DC, below which it becomes impossible to excite the neuron with amplitudes in our lookup range). However, the augmentation is also substantial at high duty cycles (e.g., from 30 to 65 kPa at 100% DC).

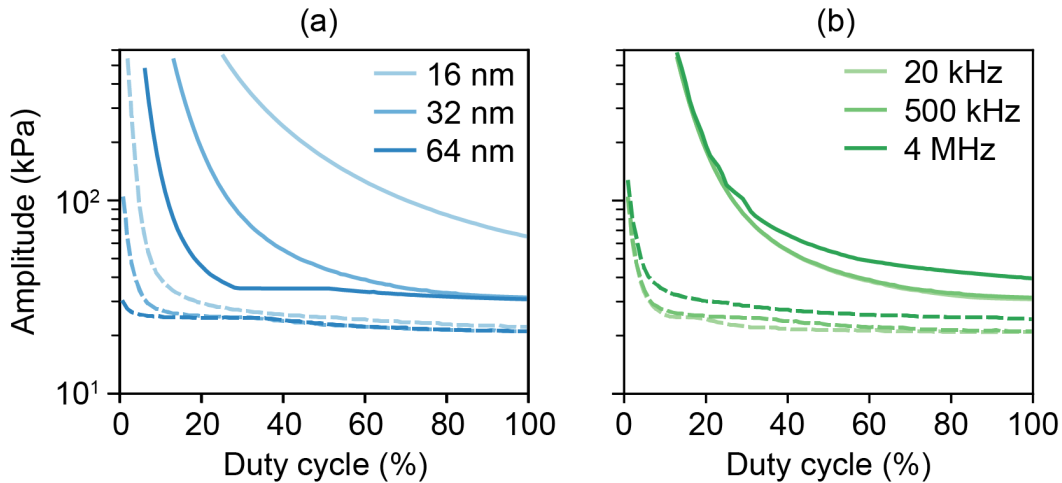


Figure 23. Influence of sonophore radius and US frequency on excitation thresholds. Threshold excitation amplitude as a function of the duty cycle for an RS neuron (solid curves) and an LTS neuron (dashed curves), predicted through titration procedures. (a) Effect of sonophore radius ($f = 500$ kHz). (b) Effect of US frequency ($a = 32$ nm).

The effects are smaller on an LTS neuron (Figure 23(a), dashed curves): doubling or halving the sonophore radius respectively shift the excitation threshold towards lower or higher US doses for small duty cycles (below 20% DC). For larger duty cycles, the neuron's excitability is very robust to changes in sonophore extent (less than 5 kPa variation across the 3 conditions).

3.4.5.2 US frequencies above 1 MHz reduce neuronal excitability.

As anticipated from Figure 19(b), sub-MHz variations of the US frequency do not induce significant changes in the threshold excitation profiles of both neurons (Figure 23(b)). However, increasing the frequency up to 4 MHz induces stronger viscous stresses that limit the amplification of the effective membrane potential (Figure 19(b)) and the resulting leakage-driven sub-threshold depolarization, thereby shifting the excitation threshold towards slightly higher US doses. This effect is only relevant on large sonophores (here 32 and 64 nm radius) experiencing higher viscous stresses during cavitation. It is also more prominent in RS neurons than in LTS neurons, as the latter cell type is more dependent on LIFUS-ON periods to reach its spiking threshold.

3.5 Discussion

3.5.1 Interpretability of the SONIC model

3.5.1.1 The SONIC model provides interpretability to the LIFUS-modulated spiking dynamics of cortical neurons.

The high degree of similarity between detailed and effective solutions of the NICE and SONIC electromechanical models, respectively, reveals that membrane charge density and ion channels gating variations during a LIFUS neural response can be expressed as a function of “effective” membrane potential and rate constants, averaged over acoustic cycles. These effective variables all exhibit a dependency on Q_m in the absence of acoustic perturbation, and they are amplified upon sonication to an extent that depends on acoustic pressure amplitude, US frequency and sonophore membrane span.

The amplification of effective variables explains key features of the specific dynamics observed in both cortical RS and LTS neurons during LIFUS-ON periods (Figure 20(a-c)). 1) Given that sodium and potassium have reversal potentials of opposite signs (50 and -90 mV, respectively), V_m^* amplification primarily increases the deviation from E_{Na} and thus the magnitude of the depolarizing sodium current when $Q_m < 0$, and deviation from E_K and the magnitude of the hyperpolarizing potassium current when $Q_m > 0$. This sign-dependent, ion-specific current amplification limits the charge density variation range, ultimately reducing the amplitude of the depolarization and hyperpolarization peaks reached during action potential trains. 2) The amplification of (i) α_m^* and α_h^* for positive charge densities and (ii) β_m^* and β_h^* for negative charge densities accelerate the opening and closing of the sodium and potassium activation gates during action potentials, further enhancing their temporal dynamics. 3) α_h^* amplification triggers faster reactivation of the sodium h -gate upon repolarization, which effectively eliminates recovery periods between spikes, thereby considerably increasing the firing frequency to a rate far superior to what can be evoked with electrical stimulation. 4) α_p^* amplification accelerates the p -gate opening upon occurrence of the first spike, yielding a very fast firing rate adaptation within the first few spike intervals, and is therefore responsible for the non-adaptive nature of LIFUS-triggered spike trains. Hence, the SONIC model provides interpretability to the high-frequency and non-adaptive nature of spike trains in cortical RS and LTS neurons upon CW LIFUS.

3.5.1.2 The SONIC model captures complex trends of LIFUS responses depending on multiple parameters.

Due to its associated computational burden, the NICE model only allows for sparse explorations of the LIFUS parameter space. While such explorations can reveal crucial information (e.g. cell-type-specific, DC-dependent excitation thresholds obtained by titration procedures), denser explorations such as the ones performed in this study allow to capture finer trends in neural responses, and to assess the influence of parameters such as the PRF on those trends. Here, we showed that low PRFs can entrain both neuron types into regular firing behaviors, transitioning from isolated spikes to cyclic bursting at the PRF as US doses are increased. Higher PRFs yield more complex behaviors, from dose-specific synchronization phenomena at 100 Hz to a more continuous interaction at 1 kHz.

3.5.1.3 The SONIC model captures subtle neuromodulatory effects over narrow regions of the LIFUS space.

Interestingly, a recent computational study of the NICE model for STN neurons suggests that CW LIFUS can also induce other, subtle neuromodulatory effects on these spontaneously firing neurons (Tarnaud et al., 2018a). Markedly, the authors predict that increasing levels of US doses successively elicit (1) steady increase in the firing rate of the neuron above its physiological baseline, (2) further increase of the firing rate with significant spike-frequency and spike-amplitude adaptation, and (3) generation of silenced plateau potentials after a transient period of adaptation. While those transitions

between qualitatively distinct modes of LIFUS-neuron interaction occur over a narrow range of low acoustic amplitudes ($A < 25$ kPa), they are remarkably captured by the SONIC model (Figure 24).

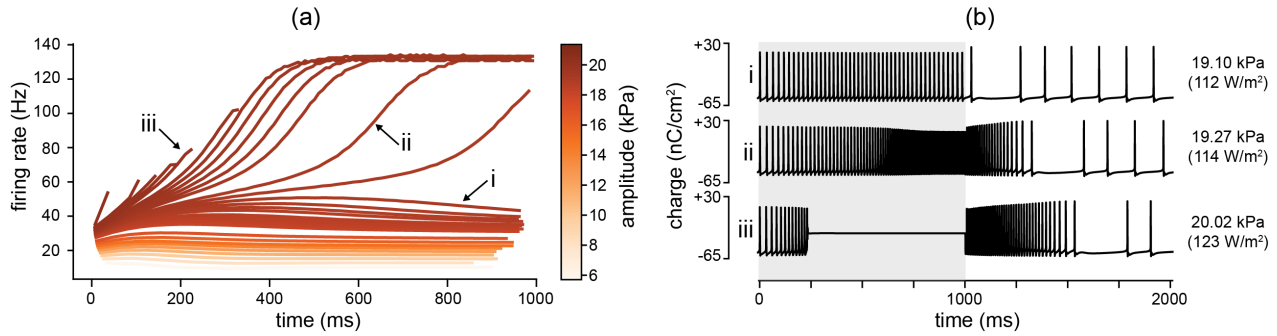


Figure 24. Distinct neuromodulatory effects of CW LIFUS ($f = 500$ kHz) on STN neurons at very low intensities, as predicted by the SONIC model. (a) Temporal evolution of firing rate during LIFUS, defined as in (Tarnaud et al., 2018a), for increasing acoustic amplitudes. (b) Neural responses elicited at three specific amplitudes showing the distinct modes of interaction. Corresponding spatial peak pulse averaged intensities, computed as in (Tarnaud et al., 2018a) but with $\rho = 1075$ kg·m⁻³, are shown for comparison. Electrical model parameters were taken from (Otsuka et al., 2004; Tarnaud et al., 2018a).

3.5.2 Effects of partial sonophore membrane coverage on neural responses

Sonophore membrane coverage is a key parameter of the NICE model likely to vary across a wide range of possible values. The influence of this parameter was previously assessed using a point-like NICE model with spatially-averaged capacitance, i.e. assuming that neural response is only sensitive to the spatial average of membrane potential variations. Here, instead, we assess the influence of partial sonophore membrane coverage using a nanoscale multi-compartmental SONIC model (see section 3.3.4) that considers the spatial co-distribution of sonophores with ion channels, as well as the effects of local intracellular currents, on an RS neuron's response.

For typical CW LIFUS parameters ($f = 500$ kHz, $A = 50$ kPa, 100 ms duration) and with 50% membrane coverage, the stimulus onset creates an instantaneous effective capacitance drop and hyperpolarization of the local sonophore membrane potential (Figure 25(a)). This creates an effective voltage imbalance with the unaffected surroundings, which drives significant intracellular currents. As these currents rapidly equilibrate the effective membrane potential across the 2 compartments, they also drive fast and significant changes in membrane charge density, increasing Q_m locally around the sonophore and decreasing it in the periphery. During the stimulus, the sonophore mechanical resonance induces leakage membrane currents that progressively increase the membrane charge density locally, but also in the periphery through the action of intracellular currents that equilibrate effective membrane potentials. After approximately 40 ms, Q_m around the sonophore eventually reaches the threshold value that drives the opening of local voltage-gated ion channels and triggers a spike train. As intracellular currents still maintain the V_m^* spatial equilibrium, Q_m is also reached in the surrounding membrane where voltage-gated ion channels also open. Both compartments then fire synchronized spike trains but with different Q_m variation ranges, since their effective electrical systems are not identically modulated by the stimulus. As the sonication stops, the sonophore membrane capacitance instantaneously returns to its resting value, which synchronizes charge density across the entire membrane patch.

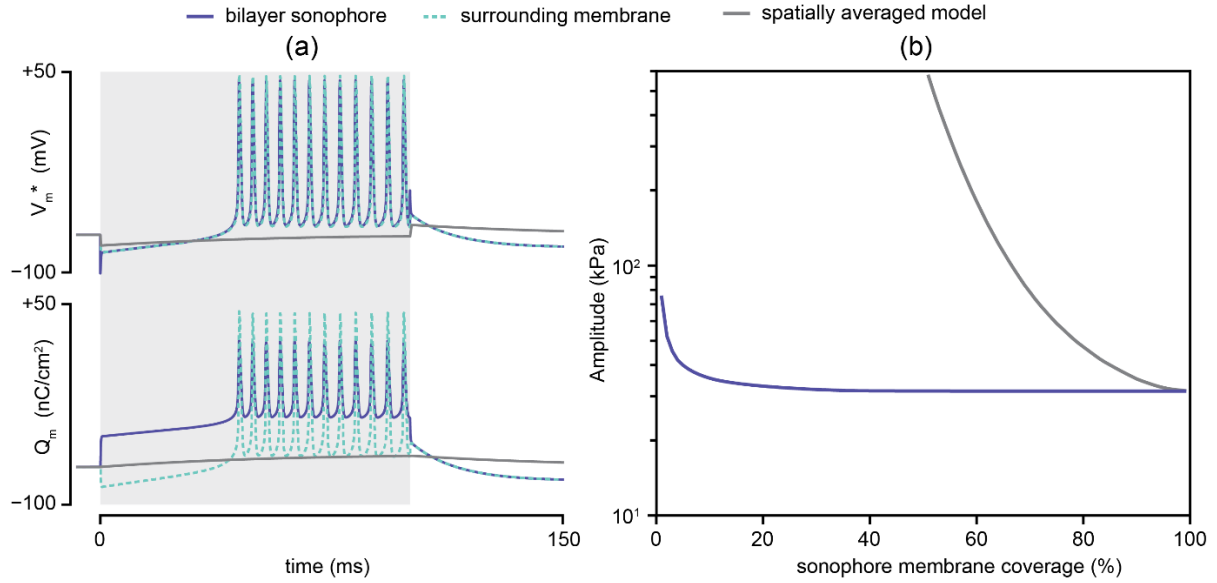


Figure 25. Effects of partial sonophore membrane coverage on neural responses. (a) Effective membrane potential (top) and charge density (bottom) of a RS neuron with 50% sonophore membrane coverage in response to CW sonication ($f = 500$ kHz, $A = 50$ kPa, 100 ms duration). Neural responses of a bilayer sonophore and its periphery computed with the nanoscale multi-compartmental SONIC model are depicted (solid dark and dashed light blue, respectively), as well the single response obtained with a point-like SONIC model using a spatially averaged membrane capacitance (grey). (b) Threshold excitation amplitude as a function of sonophore membrane coverage, computed with both the point-like (grey) and multi-compartmental SONIC (dark blue) models, using titration procedures at $f = 500$ kHz (1 s stimulus).

This model involves several simplifications. First, it assumes that ion channels are present in the direct vicinity of a sonophore structure and respond to local changes in membrane potential, regardless of the global membrane fraction covered by such structures. Second, it assumes that these ion channels (in particular leakage channels) are present in sufficient number to drive a local depolarization up to the spiking threshold that may excite an entire neuron. Third, it neglects other intracellular driving forces that may be relevant at this nanometer scale, including the intracellular diffusion of ion particles following their concentration gradient. Fourth, it only consists of two compartments without further spatial discretization, and may therefore fail to capture the effects of a more continuous interaction between a sonophore and its surroundings. Fifth, it includes arbitrary choices such as the simplistic assumption of cylindrical symmetry, the value of effective sub-membrane depth and that of the intracellular resistor. Nevertheless, this model suggests that local depolarization around a sonophore generates intracellular currents that predominate overwhelmingly over membrane currents to synchronize the membrane electrical state in a very robust manner, unaffected by changes in key model parameters. In fact, while the choice of effective sub-membrane depth in this multi-compartmental model is indeed arbitrary, a sensitivity analysis shows that a decrease by several orders of magnitude below the nanometer range would be required in order to start observing desynchronized responses.

Critically, the point-like SONIC model considering a spatially-averaged potential across the entire membrane patch (see section 3.3.4) only predicts a sub-threshold response for identical parameters.

3.5.3 Influence of sonophore size and density on neural excitability

Simulations of the NICE model in reference studies (Plaksin et al., 2014, 2016) were all performed by assuming a constant sonophore radius of 32 nm – a value derived from the averaged distance between neighboring proteins in native oocytes (Pralle, 1998). While the order of magnitude of this parameter can be deemed reasonable, it is likely to vary significantly across organisms, cell types, and morphological sections of a given cell. Moreover, it is shown here that this parameter affects both the gating dynamics and the threshold excitation amplitudes of our neuron models, and is thus likely to

play a key role in the excitability of most neuron types. In particular, it might shift the region of cortical suppression predicted in (Plaksin et al., 2016) to smaller or higher US doses.

Sonophore membrane coverage is another key variable likely to vary across a wide range of possible values. However, past simulations were mostly performed assuming 100% coverage, which is arguably unrealistic. The effect of partial coverage on neural response was only assessed for a single value of 75%, with a pressure amplitude far above the neuron's excitation threshold (Plaksin et al., 2016), using a point-like NICE model with a spatially-averaged capacitance. With this model, membrane charge density can only be brought above the spiking threshold by the progressive action of transmembrane depolarizing currents which, for an RS neuron under CW sonication, directly depend on the amplitude of LIFUS-triggered effective capacitance drop. As the sonophore membrane coverage decreases, the spatially-averaged drop is substantially dampened. This attenuates the effective variables of the electrical system, which raises excitation thresholds (Figure 25(b)). Under this paradigm, neuronal excitability is very sensitive to the density of sonophores: 75% coverage is enough to double the threshold excitation amplitude, and below 50% no pressure amplitude within the considered LIFUS range is able to excite the neuron.

The nanoscale multi-compartmental SONIC model – that considers spatially distributed voltage variations and ion channels gating – reveals an additional mechanism by which Q_m can be raised locally towards the spiking threshold. In fact, upon stimulus offset, the effective sonophore hyperpolarization generates local intracellular currents converging from the surrounding, unaffected membrane region that induce a rapid and substantial rise in the sonophore membrane charge density (Figure 25(a)). This effect is amplified for small fractions of sonophore coverage as the predominance of the unaffected membrane drives stronger intracellular currents towards the sonophore. However, this predominance also hinders the subsequent progressive charge increase once V_m^* has reached a spatial equilibrium. Nevertheless, this additional mechanism contributes to maintaining a very robust neuronal excitability as sonophore densities decreases (Figure 25(b)): excitation threshold amplitudes are hardly affected above 10%, and even a coverage fraction as low as 1% raises the threshold excitation amplitude by less than a factor 3.

The predicted effects of partial sonophore coverage on neural excitability are highly dependent on inherent model assumptions. The point-like SONIC model, considering spatially-averaged US effects on the membrane, predicts that neuronal excitability is very sensitive to that parameter, and that low sonophore densities ($f_s < 50\%$) may prevent the recruitment of cortical neurons with typical LIFUS protocols. Conversely, the multi-compartmental SONIC model developed here, considering spatially-distributed US effects on the membrane, predicts that the US excitability of cortical neurons is very robust to partial sonophore membrane coverage. More generally, the predictions of the latter model seem to agree with the experimental observation that US neuromodulation can be found in a diverse range of neural targets, despite important variabilities in their membrane structure. This observation suggests that the acoustic impact is likely to mechanistically interact with localized features of the structure (the sonophores in the case of the intramembrane cavitation hypothesis).

3.5.4 Relevance for experimental validation

Despite predicting LIFUS parameter-dependent trends of neural activation and inhibition that match with indirect responses (e.g. hindlimb motor activity, mesoscale cortical activity) observed experimentally (Plaksin et al., 2014, 2016), one major limitation of the NICE electromechanical model is the lack of direct experimental validation at the cellular level, and in particular, direct observation of intramembrane cavitation, given the nanometer-scale extent of the hypothesized bilayer sonophores. Recording local oscillations in membrane thickness or transmembrane potential might be elusive, as this would require a sensing technology of high spatial (< 100 nm) and temporal (< 1 μ s) resolution with

enough sensitivity to detect thickness variations of a few nanometers. However, the predicted dependency of excitation thresholds, response latencies, neural firing rates and spike amplitudes on LIFUS parameters are testable features that could (1) provide indirect validation of the NICE electromechanical hypothesis and (2) constrain specific model parameters with significant associated variability, such as the sonophore radius and density. In this context, our SONIC model defines effective membrane dynamics as a more interpretable frame of reference, supporting the design of such validation experiments and providing additional insight on how exactly LIFUS modulates ion channel gating dynamics.

3.5.5 Generalizability and integration

The presented coarse-graining approach can be adapted to any neuron model with conductance-based membrane dynamics, provided that response time constants of its constituent voltage-gated ion channels are in the millisecond range. The translation into effective channel models could be further simplified by neglecting the small-scale changes in deflection profiles across different neuron types, and thus deriving cell-type-specific effective variables from a single precomputed table of mechanical deflections. Moreover, while we focused here on single neuron characterization, SONIC models of several neuron types could easily be coupled together with synaptic connections in order to design realistic, yet computationally efficient representations of cortical and/or peripheral neural networks responding to LIFUS. These network models could be used to increase our understanding of the influence of different LIFUS parameters on large-scale neural response as in (Plaksin et al., 2016). Alternatively, they could guide the design of studies on the causal role of certain brain regions in specific behaviors and behavioral disorders, as LIFUS currently emerges as very compelling technology for causal brain mapping (Kubanek, 2018).

3.5.6 Advantage over other simplification strategies

The authors of the NICE electromechanical model have already proposed approaches to tackle the computational inefficiency of the original differential system (equations (92) and (93)), and speed up the numerical integration of solutions. A hybrid resolution scheme was developed that takes advantage of the weak influence of the electrical system on the mechanical one: the full electromechanical system is periodically integrated (every 500 μ s) for a few acoustic cycles until quasi-static (oscillatory) stabilization of the mechanical variables, which are then assumed to remain unchanged for the rest of the 500 μ s interval, allowing to integrate a simplified system with reduced stiffness for a large portion of the solution (Plaksin et al., 2014). A later simplification was devised that represents the oscillations of sonophore membrane capacitance by a simple sinusoid at the US frequency, thereby dispensing from integrating the mechanical part of the model (Plaksin et al., 2016). However, as both simplifications explicitly model the high-frequency, large-amplitude oscillations of the transmembrane potential, their integration time step must stay significantly smaller than the acoustic period to ensure convergence, which represents a strongly limiting factor for algorithmic optimization. Conversely, the time step used in our SONIC model is completely independent from the stimulus frequency, and only limited by the order of magnitude of the response time constants of constituent ion channels (as well as the PRI). Moreover, despite yielding excitation profiles that are qualitatively similar to that of the detailed NICE model, the sinusoidal capacitance-driven model does not properly capture the asymmetry of capacitance oscillations that dictates the dynamics of the initial charge build-up phase during CW stimulation; therefore, it cannot provide an accurate estimate of the response latency and excitation threshold for such protocols. On the other hand, our SONIC model considers this asymmetry during the precomputation of lookup tables, and can therefore reliably predict these excitation metrics. Obviously, this precomputation step is time consuming but it stays within the same order of magnitude as that required to run a single simulation of the detailed model. Moreover, it is a

fixed cost, meaning one precomputation then allows to explore the entire parameter space. Furthermore, PRF and duty cycle do not need to be considered at this stage, which reduces the problem dimensionality. Finally, as it consists of a high number of small, independent mechanical simulations, precomputation can be easily optimized by parallelization (in fact, on our 24-core server, the parallelized process only takes 2 to 3 hours per neuron type).

3.6 Conclusion

In this study, we derived an effective coarse-grained variant of the NICE electromechanical model that greatly accelerates numerical simulations while preserving the accuracy of computed solutions and offering electrophysiological interpretability. This so-called SONIC model was used to explore systematically the LIFUS parametric space and establish cell-type-specific behavior maps, by recasting LIFUS responses under the frame of an “effective” neural dynamics. We also expanded the SONIC model into a nanoscale multi-compartmental representation to study the impact of the electrical interactions between LIFUS receptive sub-cellular structures and their surroundings on the neural response. In ongoing work, we are conducting sonication experiments on isolated leech ganglia and analyzing the electrical responses of specific neurons to LIFUS with intracellular recordings, in order to verify the trends in effective spiking dynamics suggested by the model and provide indirect validation and quantification of the intramembrane cavitation mechanism. We are also expanding the SONIC model into cell-morphological neuron representations in order to study the effects of LIFUS on different neural structures in a more realistic manner.

Chapter 4 Intramembrane cavitation at the morphological scale

Chapter 3 presents an effective variant of the NICE model – called SONIC – that allows to compute neuronal responses to acoustic perturbations as a function of a pre-computed, cycle-averaged impact of the mechanical oscillations on the electrical system. This model accelerates model simulations while maintaining numerical accuracy, and therefore allows to explore dense parametric spaces in a time-efficient manner. Moreover, through charge-casting and temporal multi-scaling, the SONIC paradigm isolates a smoothly-evolving electrical system that is readily available for spatial expansion.

This chapter introduces a set of mathematical and computational tools that together enable the incorporation of the SONIC paradigm into multi-compartmental neuron models, and therefore to study intramembrane cavitation at the morphological scale. It is built on a modified electrical cable representation of neurons that ensures numerical accuracy and stability, and that can be readily applied to a variety of neuron models. A demonstrative application of this framework to morphologically realistic models of peripheral axons is presented, revealing that myelinated and unmyelinated axons are expected to respond with different sensitivities to ultrasound stimuli, and that this difference can be exploited for various therapeutic applications. This morphological expansion framework – called morphoSONIC – and the model predictions on ultrasound neuromodulatory effects in peripheral axons, both constitute original contributions presented in this thesis.

The contents of this chapter are adapted from the manuscript **Lemaire, T.**, Vicari E., Neufeld, E., Kuster, N., and Micera, S., “MorphoSONIC: a morphologically realistic intramembrane cavitation model reveals fiber specific recruitment by ultrasound”, currently under review.

Personal contributions as first author: conceptualized the study, implemented the model, performed the simulations, analyzed the results, prepared the figures and wrote the manuscript.

MorphoSONIC: a morphologically realistic intramembrane cavitation model reveals fiber specific recruitment by ultrasound

Théo Lemaire^{1*}, Elena Vicari^{1,2}, Esra Neufeld³, Niels Kuster^{3,4} and Silvestro Micera^{1,2}

¹Translational Neural Engineering Laboratory, Center for Neuroprosthetics and Institute of Bioengineering, School of Engineering, École Polytechnique Fédérale de Lausanne (EPFL), Lausanne, Switzerland

²The Biorobotics Institute, Scuola Superiore Sant'Anna (SSSA), Pisa, Italy

³Foundation for Research on Information Technologies in Society (IT²S), Zurich, Switzerland

⁴Department of Information Technology and Electrical Engineering, Swiss Federal Institute of Technology (ETH) Zurich, Zurich, Switzerland

4.1 Abstract

Objective. Low-Intensity Focused Ultrasound Stimulation (LIFUS) is emerging as a promising technology for the remote modulation of neuronal activity, but an incomplete mechanistic characterization hinders its clinical maturation. Intramembrane cavitation has been proposed as a candidate mechanism, but it has only been studied in single or two-compartment computational neuron models. Here, we present a computational framework to investigate this mechanism in multi-compartmental, morphologically realistic neuron models, and use it to study ultrasound neuromodulation of peripheral nerve fibers. **Approach.** We recast NEURON's internal cable representation to enable the simulation of multi-compartment models with temporally and spatially varying membrane capacitance. This allowed to seamlessly incorporate the multi-Scale Optimized Neuronal Intramembrane Cavitation (SONIC) paradigm across an arbitrary number of connected compartments, while simultaneously ensuring numerical stability and accuracy. Within this framework, we then implemented single-cable models of myelinated and unmyelinated peripheral axons in order to compute their response to spatially-varying pressure fields. **Main results.** Our findings show that LIFUS offers distinct parametric subspaces to selectively recruit myelinated and/or unmyelinated axons by leveraging fiber-specific differences in membrane electromechanical coupling. This fiber-specific activation is conserved across a wide range of acoustic field distributions and consistently explains recent empirical findings. Moreover, LIFUS can modulate the spiking activity of both fiber types over physiologically relevant regimes and within safe exposure limits. **Significance.** These findings suggest that LIFUS can preferentially target nociceptive and sensory fibers, opening up new opportunities for peripheral therapeutic applications currently not addressable by electric stimulation. More generally, our framework can be readily applied to other neural targets in order to investigate electrophysiologically relevant LIFUS neuromodulatory effects and guide the development of application-specific LIFUS protocols.

4.2 Introduction

Ultrasound (US)-based approaches have been increasingly adopted over the past decades for a variety of noninvasive therapeutic interventions (Escoffre and Bouakaz, 2016). These therapies rely on the mechanical nature of acoustic waves that propagate efficiently through biological tissue and can be accurately steered to concentrate mechanical energy within small volumes ($\sim\text{mm}^3$) around deep anatomical targets. In recent years, several *in vitro* and *in vivo* studies have shown that such acoustic waves can also be used to reversibly modulate the activity of various neural targets with remarkable spatial accuracy (Blackmore et al., 2019). These findings have propelled the development of low-intensity focused ultrasound stimulation (LIFUS) as a novel technology to achieve noninvasive, selective and reversible neuromodulation of virtually any neural structure.

Yet, despite a decade of intense investigation, several open issues have impeded the development of LIFUS as a clinically relevant technology. The variety of known physical effects of acoustic waves in biological tissue implies a wide range of possibilities for how neurons may translate mechanical energy into electrical responses, including membrane piezoelectricity (Heimburg and Jackson, 2005), flexoelectricity (Petrov, 2002) and mechanosensitive channels activation (Tyler, 2011). At the same time, distinguishing these candidate mechanisms in experimental settings and establishing their predominance over the multi-dimensional LIFUS parameter space remains a challenge. Consequently, it is difficult to provide a mechanistic perspective that would clarify and guide the heterogeneous and sometimes conflicting collection of neuromodulatory effects (excitatory and inhibitory, short and long term, localized and large-scale, reversible and permanent) obtained across animal models, neural targets, and experimental designs.

In light of these challenges, computational approaches have become helpful tools to increase the understanding of LIFUS-neuron interactions, as they allow a specific candidate mechanism to be examined. A significant effort made by Plaksin et al., who introduced the *Neuronal Intramembrane Cavitation Excitation* (NICE) model, described a candidate mechanism in which LIFUS induces the cavitation of specific phospholipidic structures (so-called bilayer sonophores), thereby dynamically altering membrane capacitance and triggering action potentials. This model predicts cell-type-specific LIFUS responses of cortical and thalamic neurons (Plaksin et al., 2016) that correlate indirectly with a range of empirical results obtained in the central nervous system (CNS) (Kim et al., 2012; King et al., 2013; Tufail et al., 2011; Yoo et al., 2011).

The NICE model, however, entails a significant numerical stiffness that has so far limited its applications to point-neuron studies (Plaksin et al., 2014, 2016; Tarnaud et al., 2018a) that could not address physiologically relevant questions, such as the influence of intracellular axial coupling and morphological inhomogeneity on neuronal responses, the spatiotemporal dynamics of those responses, and the impact of spatial features of the acoustic field on excitability (as is the case for electrical stimulation). Hence, a multi-compartmental model of intramembrane cavitation incorporating morphological details would be highly beneficial to increase our understanding of LIFUS neuromodulation by intramembrane cavitation in a more realistic setting.

In a recent study, we developed a *multi-Scale Optimized Neuronal Intramembrane Cavitation* (SONIC) model that alleviates the numerical stiffness of the NICE model by integrating the coarse-grained evolution of effective electrical variables as a function of a pre-computed, cycle-averaged impact of the oscillatory mechanical system (Lemaire et al., 2019), thereby drastically reducing computational costs while maintaining numerical accuracy. Building on this effective paradigm, we present *morphoSONIC*, a novel framework to simulate intramembrane cavitation into morphologically realistic neuron models. This framework leverages the optimized modeling and numerical integration pipelines of the NEURON simulation environment (Hines and Carnevale, 1997), and provides an alternative implementation of its internal cable representation as a hybrid (charge and voltage casted) electrical circuit that is numerically compatible with the SONIC model.

Specifically, we exploit this framework to investigate the mechanisms of ultrasonic neuromodulation in myelinated and unmyelinated peripheral fibers, using previously validated single-cable axon models (Reilly et al., 1985; Sundt et al., 2015). First, we provide an in-depth analysis of predicted LIFUS neuronal responses and recruitment mechanisms in both fiber types. Second, we characterize their LIFUS excitability by evaluating strength-duration (SD) “signatures” across a wide range of model and stimulation parameters and compare those signatures to those traditionally obtained with electrical stimulation. Third, we identify key morphological features underlying the distinct LIFUS sensitivities of myelinated and unmyelinated axons. Finally, we analyze cell-type-specific neuronal responses upon

repeated acoustic exposure and identify pulsing protocols yielding a robust modulation of spiking activity.

4.3 Methods

4.3.1 The NICE model

The NICE electromechanical model developed by Plaksin et al. (Plaksin et al., 2014) provides a mathematical formulation of the intramembrane cavitation hypothesis. Mechanically, the periodic cavitation of a single bilayer sonophore is described by two differential variables: the deflection of a leaflet apex from its resting position in the transmembrane plane (Z) and the internal gas content in the sonophore cavity (n_g). The resting leaflet position results from a pressure balance between several static pressure forces, namely the elastic tension developing in the leaflets (P_S), attractive and repulsive intermolecular forces between leaflets (P_M), internal gas pressure in the sonophore cavity (P_G), the electrical pressure resulting from the membrane polarity (P_Q), and a constant hydrostatic term (P_0). Upon perturbation by a time-varying acoustic pressure $P_A(t)$, the dynamic pressure imbalance drives a normal acceleration that deforms the leaflets in antiphase, generates viscous forces in the membrane (P_{VS}) and surrounding medium (P_{VL}), and triggers gas transport across the cavity. These oscillatory dynamics are captured by the following differential system (all pressure terms and parameters are defined in (Lemaire et al., 2019)):

(97)

$$\begin{aligned} \frac{d^2 Z}{dt^2} &= \frac{-3}{2R(Z)} \left(\frac{dZ}{dt} \right)^2 \\ &\quad + \frac{1}{\rho_l \cdot |R(Z)|} \left[P_A(t) + P_S(Z) + P_{VS} \left(\frac{dZ}{dt} \right) - P_0 + P_{VL} \left(\frac{dZ}{dt} \right) + P_M(Z) + P_G(Z, n_g) \right. \\ &\quad \left. + P_Q(Z, Q_m) \right] \\ \frac{dn_g}{dt} &= \frac{2S(Z) \cdot D_{gl}}{\xi} \left(C_g - \frac{P_G(Z)}{k_H} \right) \end{aligned}$$

Electrically, the development of an electrical response across the membrane is captured by a modified Hodgkin-Huxley differential system, describing the evolution of the membrane charge density (Q_m) as the negative sum of voltage-dependent ionic currents with specific conductances g_i and reversal potentials E_i . In this system, time-varying ionic conductances are the product of one or multiple gating variables (x , with $x \in \{m, h, n, p, \dots\}$), whose evolution is regulated either by a voltage-dependent activation and inactivation rate constants (α_x and β_x , respectively) or by a steady state probability x_∞ and a time constant τ_x (also both voltage-dependent), yielding the following system (note that charge-casting was introduced in (Lemaire et al., 2019)):

(98)

$$\begin{aligned} \frac{dQ_m}{dt} &= - \left[\sum_i g_i \cdot \left(\frac{Q_m}{C_m} - E_i \right) \right] \\ \frac{dx}{dt} &= \begin{cases} \alpha_x \left(\frac{Q_m}{C_m} \right) \cdot (1 - x) - \beta_x \left(\frac{Q_m}{C_m} \right) \cdot x \\ \frac{x_\infty \left(\frac{Q_m}{C_m} \right) - x}{\tau_x \left(\frac{Q_m}{C_m} \right)} \end{cases} \end{aligned}$$

The coupling between these two systems is modelled by a bi-directional piezoelectric effect. Mechano-electrical transduction results from the periodic deflections of the sonophore leaflets, inducing high frequency oscillations in the local membrane capacitance (given by $C_m(t) = \frac{C_{m0}\Delta}{a^2} \left[Z(t) + \frac{a^2 - Z(t)^2 - Z(t) \cdot \Delta}{2Z(t)} \ln \left(\frac{2Z(t) + \Delta}{\Delta} \right) \right]$, as in (Plaksin et al., 2014)). Considering a larger, macroscale portion of membrane area, local fluctuations of membrane capacitance around individual sonophores influence the spatial average of membrane capacitance, calculated as a weighted mean of the resting and dynamic capacitances ($C_m = C_m(t)f_s + C_{m0}(1 - f_s)$, where f_s is the sonophore membrane coverage fraction). This global fluctuation then causes large-amplitude oscillations of the transmembrane potential in the compartment of interest ($V_m = Q_m/C_m$ in equation (98)). Reversibly, electro-mechanical transduction results from progressive changes in the membrane electrical polarity that dynamically modify the electrical pressure exerted on the sonophore leaflets and the resulting pressure balance (P_Q in equation (97)), thereby influencing the sonophore cavitation dynamics.

4.3.2 The SONIC model

The SONIC model (Lemaire et al., 2019) uses temporal multiscaling to separate the two relevant time scales of the NICE model, namely microsecond-scale mechanical oscillations and millisecond-scale development of neuronal responses. It is based on the observation that ion channel gates – whose time constants are typically in the millisecond range – do not follow large-amplitude, high-frequency variations of transmembrane potential observed in the NICE model, but rather adapt to the temporal average of voltage oscillations over an acoustic cycle. As a result, the evolution of membrane charge density and ion channels gating variables can be expressed as a function of an effective membrane potential (V_m^*) and effective activation and inactivation rate constants (α_x^* and β_x^* , respectively, for each gating variable x), representing the average value of their original, voltage-dependent counterparts (V_m , α_x and β_x , respectively) over an acoustic cycle:

(99)

$$\begin{aligned} \frac{dQ_m}{dt} &= - \sum_{ion} g_{ion} \cdot (V_m^* - E_{ion}) \\ \frac{dx}{dt} &= \alpha_x^* \cdot (1 - x) - \beta_x^* \cdot x \end{aligned}$$

The SONIC model uses a sequential approach to compute electrical responses of a given neuron type to various LIFUS stimuli. First, a parallelized precomputation step is performed (once per neuron type) in which the mechanical system (equation (97)) is simulated for various combinations of sonophore radii (a), US frequencies (f_{US}), acoustic peak pressure amplitudes (A_{US}), and membrane charge densities, covering the LIFUS parametric space, sonophore geometrical range and membrane physiological range. Each simulation is run until a limit cycle is detected, at which point, the profile of oscillating membrane capacitance over the last acoustic cycle is extracted, dampened for a range of sonophore membrane coverage fractions, and used to compute effective variables stored in multi-dimensional lookup tables. Second, the electrical response of the neuron to a given LIFUS stimulus is rapidly computed at runtime by interpolating effective variables at (a, f_s, f_{US}, A_{US}) and $(a, f_s, f_{US}, 0)$ to yield 1D projected vectors in the Q_m space, which are then used to interpolate effective variables and solve equation (98) during US-ON and US-OFF periods, respectively.

4.3.3 A hybrid multi-compartmental, multi-layer electrical circuit

In its most basic form, the multi-compartmental expansion of point-neuron NICE / SONIC models requires the addition of axial current terms contributing to the evolution of charge density in each

compartment (see (Lemaire et al., 2019), equation 5). However, that formulation only considers intracellular axial coupling, and is therefore not adapted to “double-cable” models that account for both intra and extracellular longitudinal coupling. More importantly, the use of explicit current terms representing axial coupling is prone to yielding numerical instabilities in the presence of tightly connected sections or abrupt changes in voltage gradients. Hence, in this study, we derived a hybrid multi-compartmental multi-layer electrical circuit that is applicable to both myelinated and unmyelinated structures with temporally and spatially varying membrane capacitances, and compatible with reference numerical integration schemes and simulation environments.

The circuit model is composed of multiple longitudinal compartments, each represented by a pair of intracellular and extracellular voltage nodes (V_i and V_x , respectively) on either side of the plasma membrane with time-varying capacitance $C_m(t)$. The voltage difference across the plasma membrane $V_m^* = V_i - V_x$ influences the opening and closing of distinct ion channels, ultimately giving rise to a net membrane ionic current I_{ion} . On the extracellular side, a transverse resistor-capacitor (RC) circuit of conductance g_x and capacitance C_x represents the myelin membrane and connects the extracellular node to the extracellular driving voltage E_x , which is usually grounded but can also have a value imposed by an external electrical field. Longitudinally, neighboring nodes are connected intracellularly and extracellularly by axial conductors (G_a and G_p , respectively). All variables and parameters of the circuit are described in **Table 3**.

Parameter / Variable	Symbol	Unit
Intracellular voltage	V_i	mV
Extracellular voltage	V_x	mV
Transmembrane voltage	V_m	mV
Transmembrane charge density	Q_m	nC/cm ²
Extracellular driving voltage	Φ_e	mV
Membrane capacitance	C_m	μF/cm ²
Intracellular stimulation current	I_s	mA/cm ²
Net transmembrane ionic current	I_{ion}	mA/cm ²
Intracellular axial conductance	G_a	S
Capacitance of surrounding extracellular membrane (e.g. myelin)	C_x	μF/cm ²
Transverse conductance of surrounding extracellular membrane (e.g. myelin)	g_x	S/cm ²
Extracellular axial conductance (e.g. periaxonal space)	G_p	S
Membrane area of the compartment	A_m	cm ²

Table 3. Parameters and variables of the hybrid multi-compartmental, multi-layer electrical circuit.

For any compartment k connected to a set of neighboring compartments, the application of Kirchhoff’s law at the corresponding intracellular and extracellular nodes yields the following current balance equations:

$$\begin{aligned}
 C_m^k \frac{dV_m^k}{dt} + V_m^k \frac{dC_m^k}{dt} + I_{ion}^k &= I_s^k + \frac{1}{A_m^k} \underbrace{\sum_j G_a^{kj} (V_i^j - V_i^k)}_{\text{intracellular axial current}} \\
 C_x^k \frac{dV_x^k}{dt} + g_x^k (V_x^k - \phi_e^k) &= C_m^k \frac{dV_m^k}{dt} + I_{ion}^k + \frac{1}{A_m^k} \underbrace{\sum_j G_p^{kj} (V_x^j - V_x^k)}_{\text{periaxonal axial current}}
 \end{aligned}
 \tag{100}$$

Using $V_i = V_m + V_x$, and re-arranging the terms, we find:

(101)

$$\begin{aligned} C_m^k \frac{dV_m^k}{dt} + V_m^k \frac{dC_m^k}{dt} + \frac{1}{A_m^k} \sum_j G_a^{kj} (V_m^k - V_m^j) + \frac{1}{A_m^k} \sum_j G_a^{kj} (V_x^k - V_x^j) &= I_s^k - I_{ion}^k \\ C_x^k \frac{dV_x^k}{dt} - \left(C_m^k \frac{dV_m^k}{dt} + V_m^k \frac{dC_m^k}{dt} \right) + g_x^k V_x^k + \frac{1}{A_m^k} \sum_j G_p^{kj} (V_x^k - V_x^j) &= I_{ion}^k + g_x^k \phi_e^k \end{aligned}$$

By substituting transmembrane voltage for transmembrane charge density ($Q_m(t) = C_m(t) \cdot V_m(t)$); $\frac{dQ_m}{dt} = C_m \frac{dV_m}{dt} + V_m \frac{dC_m}{dt}$, and defining $I_e^k = g_x^k \phi_e^k$ as the extracellular driving current, we obtain:

(102)

$$\begin{aligned} \frac{dQ_m^k}{dt} + \frac{1}{A_m^k} \sum_j G_a^{kj} \left(\frac{Q_m^k}{C_m^k} - \frac{Q_m^j}{C_m^j} \right) + \frac{1}{A_m^k} \sum_j G_a^{kj} (V_x^k - V_x^j) &= I_s^k - I_{ion}^k \\ C_x^k \frac{dV_x^k}{dt} - \frac{dQ_m^k}{dt} + g_x^k V_x^k + \frac{1}{A_m^k} \sum_j G_p^{kj} (V_x^k - V_x^j) &= I_{ion}^k + I_e^k \end{aligned}$$

By applying the above equations to a model of n compartments connected in series, we obtain a hybrid charge-voltage partial differential equation system of size $2n$ that can be described as:

(103)

$$C \frac{dy}{dt} + G(t) \cdot y(t) = I(t)$$

where:

- y is a hybrid vector of transmembrane charge density and extracellular voltage, and dy/dt its temporal derivative;
- C is a constant matrix composed of both capacitance terms (multiplying voltage elements of dy/dt) and “identity” terms (multiplying charge elements of dy/dt);
- $G(t)$ is a time-varying matrix composed of both conductance terms (multiplying voltage elements of y) and “frequency” terms (conductance by capacitance ratios in MHz, multiplying charge elements of y); and
- $I(t)$ is a time-varying vector of stimulation and membrane currents

This matrix formulation allows for the use of implicit methods to solve the differential equation problem, thus providing an enhanced stability over explicit schemes.

Moreover, by mapping the first n elements of the y vector to transmembrane charge density nodes and the following n elements to extracellular voltage nodes, we can describe the C , G and I terms of the system as combinations of block matrices and vectors, i.e.:

(104)

$$C = \begin{bmatrix} I_n & 0 \\ -I_n & [C_x] \end{bmatrix}, G(t) = \begin{bmatrix} \begin{bmatrix} G_a \\ A_m \cdot C_m(t) \end{bmatrix} & \begin{bmatrix} G_a \\ A_m \end{bmatrix} \\ 0 & [g_x] + \begin{bmatrix} G_p \\ A_m \end{bmatrix} \end{bmatrix}, I(t) = \begin{bmatrix} [I_s(t)] - [I_{ion}(t)] \\ [I_{ion}(t)] + [I_e(t)] \end{bmatrix},$$

where:

- I_n is an n -by- n identity matrix;
- $[C_x]$ is an n -by- n diagonal matrix of transverse extracellular membrane (e.g. myelin) capacitance;
- $\left[\frac{G_a}{A_m}\right]$ and $\left[\frac{G_p}{A_m}\right]$ are n -by- n tridiagonal matrices of intracellular and extracellular axial conductance, respectively, where each row is normalized by the corresponding node's membrane area;
- $\left[\frac{G_a}{A_m \cdot C_m(t)}\right]$ is an n -by- n tridiagonal matrix of intracellular axial conductance where each row is normalized by corresponding node's membrane area and each column is dynamically normalized by the time-varying membrane capacitance of the corresponding node;
- $[g_x]$ is an n -by- n diagonal matrix of transverse extracellular membrane (e.g. myelin) conductance; and
- $[I_s(t)]$, $[I_{ion}(t)]$ and $[I_e(t)]$ are n -sized, time-varying vectors of intracellular stimulation currents, transmembrane ionic currents and extracellular driving currents, respectively.

We implemented this hybrid system in NEURON (Hines and Carnevale, 1997), a reference computational environment for neuronal simulations that uses a very similar matrix formulation to enable numerical integration by implicit schemes. However, since that environment is not designed for models of varying capacitance or for hybrid charge-voltage casting, we employed three main adaptation strategies. First, a unit capacitance was set to all membrane mechanisms, thereby implicitly setting the I_n upper block matrix and effectively transforming NEURON's internal variable v as an alias to transmembrane charge density. Second, pressure amplitude and charge density dependent lookup tables of effective SONIC terms (transmembrane potential and ion channels rate constants obtained from original SONIC lookup tables (Lemaire et al., 2019)) were dynamically inserted into these mechanisms to compute the evolution of voltage, ion channels states and ionic currents via bilinear interpolation (thereby implicitly setting the I_{ion} upper block vector). Third, a "Linear Mechanism" object was implemented that defines alternative C' , G' and I' terms to complete the hybrid circuit setup once the model's compartments and their connections are defined:

(105)

$$C' = \begin{bmatrix} 0 & 0 \\ 0 & [C_x] \end{bmatrix}, G'(t) = \begin{bmatrix} \left[\frac{G_a}{A_m \cdot C_m(t)}\right] & \left[\frac{G_a}{A_m}\right] \\ \left[\frac{G_a}{A_m \cdot C_m(t)}\right] & \left[\frac{G_a}{A_m}\right] + [g_x] + \left[\frac{G_p}{A_m}\right] \end{bmatrix}, I'(t) = \begin{bmatrix} 0 \\ [I_e(t)] + I_s(t) \end{bmatrix}.$$

It should be noted that the terms $-I_n$ and $[I_{ion}(t)]$ in the lower block are replaced by equivalent axial conduction and intracellular stimulation current terms (using the equality of the upper block) to remove the need to access the net membrane current (a hidden NEURON variable). Numerical integration is then carried out by NEURON's embedded general sparse matrix solver (a differential-algebraic solver with a preconditioned Krylov method from the SUNDIALS package (Hindmarsh et al., 2005)) using a variable time step with a pure absolute error tolerance criterion ($\epsilon = 10^{-3}$), while dynamically updating C_m -dependent terms in the G' matrix throughout the simulation. Compared to previous approaches using explicit axial current terms (Lemaire et al., 2019), this implicit integration scheme offers increased numerical stability.

4.3.4 Myelinated and unmyelinated morphological axon models

Peripheral nerve fibers represent privileged, accessible neuromodulation targets, for which multiple studies have demonstrated the paramount influence of cellular morphology on the resulting excitability by electrical fields (McNeal, 1976; Rattay, 1986). As such, they are natural candidates for the study

of LIFUS effects in morphologically realistic models. To this aim, we used single-cable axonal representations allowing for a numerically valid incorporation of the SONIC paradigm while maintaining a certain level of morphological realism.

Our myelinated axon model was based on the spatially-extended nonlinear node (SENN) model developed by Reilly et al. (Reilly et al., 1985). This model represents myelinated axons as a set of nodes with active membrane dynamics based on the Frankenhaeuser-Huxley equations for a *Xenopus* Ranvier node (Frankenhaeuser and Huxley, 1964) including fast sodium (I_{Na}), delayed-rectifier potassium (I_{Kd}), non-specific delayed (I_p) and non-specific leakage (I_{Leak}) currents, connected by intracellular resistors representing the myelinated internodes (**Figure 26A-B**). This representation omits specific features of myelinated axons (namely transmembrane internodal dynamics and extracellular longitudinal coupling), but it incorporates enough morphological complexity to provide quantitatively accurate predictions of their excitability by electrical fields. In fact, it represents a standardized model for electromagnetic exposure safety assessment (Reilly, 2011). Our unmyelinated axon model was based on the work of Sundt et al. (Sundt et al., 2015), representing the continuous unmyelinated neurite as a set of nodes containing fast Sodium (I_{Na}), delayed-rectifier Potassium (I_{Kd}), and leakage (I_{Leak}) membrane currents, also connected by intracellular resistors (**Figure 26C-D**).

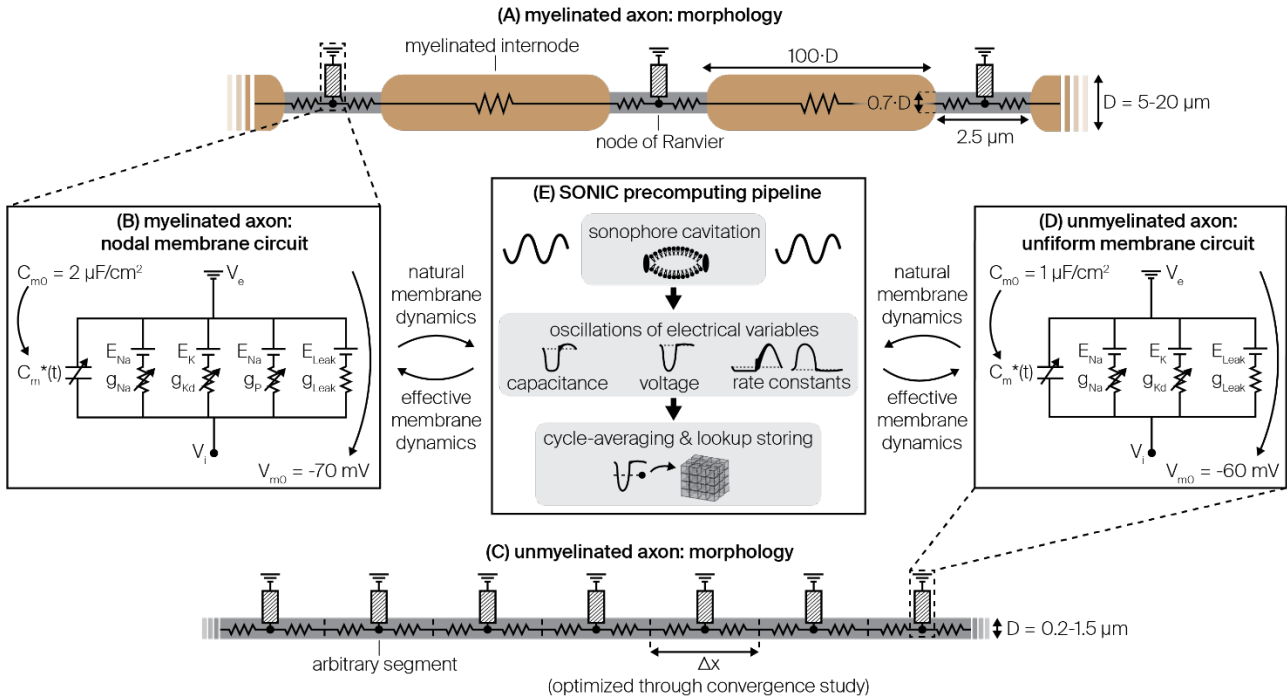


Figure 26. Morphology, biophysics and incorporation of the SONIC paradigm in myelinated and unmyelinated axon models. (A) Schematic of the myelinated axon model morphology. (B) Electrical circuit representation of the membrane dynamics at the nodes of Ranvier. (C-D) Equivalent morphological and biophysical descriptions of the uniform unmyelinated axon. (E) Schematic diagram showing the incorporation of the SONIC paradigm into the axon models.

The selected axon models were validated numerically by verifying specific physiological features (spike amplitude, conduction velocity, threshold excitation current for various pulse widths) against the reference literature (Reilly et al., 1985; Sundt et al., 2015), using NEURON's native voltage-based connection scheme with constant membrane capacitance. For the unmyelinated model, a convergence study was carried out to determine the optimal spatial discretization. Unmyelinated compartments were progressively and uniformly shortened from 1 mm to 5 μm, and an optimal segment length was defined as the maximal length for which all physiological features were within 5% of their converging values (obtained for the shortest segment length). As the optimum segment length exhibited a clear dependency on fiber diameter, we performed a piecewise linear fit within the 0.5 – 1.5 μm range to

obtain a fiber diameter-dependent formulation: $L_{opt} = \min(16.4 \mu\text{m}^{-1} \cdot D_{fiber} + 9.1 \mu\text{m}; 22 \mu\text{m})$. Finally, we validated our hybrid circuit implementation by comparing direct voltage traces, as well as physiological features, to those obtained with the “native” implementation.

Membrane equations of both models were adapted to 36°C by applying a Q_{10} correction with a factor of 3 (as in (Sundt et al., 2015)), and lookup tables of SONIC effective variables were generated for the membrane circuits of both models to enable their simulation upon acoustic perturbations (Figure 26E).

Beyond the differences in morphologies and ion channel populations, the two models have different resting membrane capacitances ($C_{m0}^{SENN} = 2 \mu\text{F}/\text{cm}^2$, $C_{m0}^{Sundt} = 1 \mu\text{F}/\text{cm}^2$), thereby implying variations in their charge density by a factor of 2 for identical voltages. Therefore, to allow for an unbiased comparison of electrical responses across the two models, charge-density based criteria and derived outputs were divided by the resting capacitance of the associated model, referred to as the “normalized charge density” (in mV).

4.3.5 Modeling of exogenous acoustic and electrical stimuli

In order to evaluate the effect of exogenous electrical and ultrasonic stimulation on isolated fibers, we modeled the propagation of both electrical and acoustic fields from a realistic remote excitation source to the target through a homogenous intraneural medium. To this end, we considered a 3-dimensional (x, y, z) coordinate system in which the fiber was aligned on the x axis and centered at the origin.

For ultrasonic stimulation, we considered a single-element planar acoustic transducer with a center in the xz plane and a normal vector along the z -axis, and a homogenous, water-like propagation medium (density $\rho = 1000 \text{ kg}/\text{m}^3$, speed of sound $c = 1500 \text{ m}/\text{s}$). We modeled acoustic distribution in the xz propagation plane using the Distributed Point Source Method (DPSM) (Yanagita et al., 2009), which provides accurate approximations of the Rayleigh-Sommerfeld integral (RSI) in homogenous medium. That is, assuming a uniform particle velocity normal to the transducer surface of amplitude v_0 , the acoustic peak pressure amplitude at each field point (x, z) for an acoustic frequency f can be computed as:

(106)

$$P_{ac}(x, z) = \left\| -j f \rho v_0 \iint_S \frac{e^{jk_f d}}{d} dS \right\|,$$

where j is the unit imaginary number, $k_f = 2\pi f/c$ is the wave number, and $d = \sqrt{(x - x_{as})^2 + (z - z_{as})^2 + y_{as}^2}$ is the distance between the field point and a surface element dS . We numerically approximated this integral as the sum of individual contributions of a finite set of M uniformly distributed point sources – each associated with a surface area ΔS – arranged in a concentric fashion on the transducer surface:

(107)

$$P_{ac}(x, z) = \left\| -j f \rho v_0 \Delta S \sum_{i=1}^M \frac{e^{jk_f d_i}}{d_i} \right\|.$$

Here again, we performed a sensitivity analysis to determine the optimal density of point sources required to achieve a good prediction accuracy. Starting with a low source density (10 samples / mm^2),

the predicted pressure distribution along the central z axis was evaluated against the corresponding closed form RSI solution ($P(z) = \rho c v_0 \left[e^{jk_f z} - e^{jk_f \sqrt{z^2 + r^2}} \right]$, with r the transducer radius), and source density was increased until the variation of the root mean square error (RMSE) fell below a threshold value (10 kPa). We then selected the minimal value satisfying that criterion over a wide frequency range (500 kHz – 5 MHz), yielding an optimal density of 217 samples / mm².

Finally, we evaluated pressure distributions along the transverse x axis at the acoustic focal distance (calculated as $z_f = \frac{fr^2}{c} - \frac{c}{4f}$) for each combination of transducer radius and US frequency.

For electrical stimulation, we considered a point source electrode located in the xz plane and an anisotropic conductivity tensor characteristic of the mammalian endoneurium (longitudinal resistivity $\rho_x = 175 \Omega \cdot \text{cm}$, transverse resistivity $\rho_{yz} = 1211 \Omega \cdot \text{cm}$) (Ranck and Bement, 1965). Extracellular potentials at each field point (x, z) were computed with the formula:

$$\phi_e(x, z) = \frac{I}{4\pi \sqrt{\frac{(x_0 - x)^2}{\rho_{yz}^2} + \frac{z_0^2}{\rho_x \cdot \rho_{yz}}}}, \quad (108)$$

where I is the injected current and (x_0, z_0) are the electrode coordinates, and equivalent sets of intracellular currents were used to simulate the influence of the extracellular electric field, as in (McIntyre et al., 2002).

Note that equations (107) and (108) provide closed-form expressions to predict the qualitative nature of ultrasonic and electric field distributions along a fiber, thereby allowing general trends about the impact of those distributions on axon excitability to be established. However, they only consider propagation within a homogeneous medium, which is a limitation.

4.3.6 Two-compartment SONIC benchmarks

A recent study has shown that in multi-compartmental structures, the presence of large axial currents could introduce significant intra-cycle charge redistribution mechanisms, thereby inducing a significant divergence of the SONIC paradigm (Tarnaud et al., 2020). Thus, we aimed to establish the conditions of this divergence and whether it applies to the models of this study. To this end, we designed two-compartment benchmark models of intramembrane cavitation in which mechanical perturbation is modeled as a pure sinusoidal oscillation of membrane capacitance around its resting value with a specific amplitude in each compartment ($C_m^k(t) = C_{m0} (1 + \frac{\gamma_k}{2} \sin(2\pi f_{US} t))$, with k being the compartment index and γ_k the relative oscillation range, **Figure 27A**). This simplified perturbation produces neuronal responses in cortical models that are qualitatively comparable to those obtained with a detailed intramembrane cavitation model ((Plaksin et al., 2016), Fig. 9) and therefore facilitates the assessment of SONIC accuracy in the presence of a high-frequency, spatially-varying acoustic perturbation – arising either from pressure amplitude gradients or variations in sonophore coverage – without requiring the tedious integration of the mechanical model. For each tested condition, SONIC accuracy was assessed by (i) simulating the benchmark under the NICE and SONIC paradigms using frequency-dependent time steps ($dt_{\text{SONIC}} = 1 / f_{US}$, $dt_{\text{NICE}} = 0.01 / f_{US}$), (ii) cycle-averaging the NICE simulation output and (iii) computing the maximal RMSE (ϵ_{max} , in mV) between normalized charge density profiles of the SONIC solution and the cycle-averaged NICE solution.

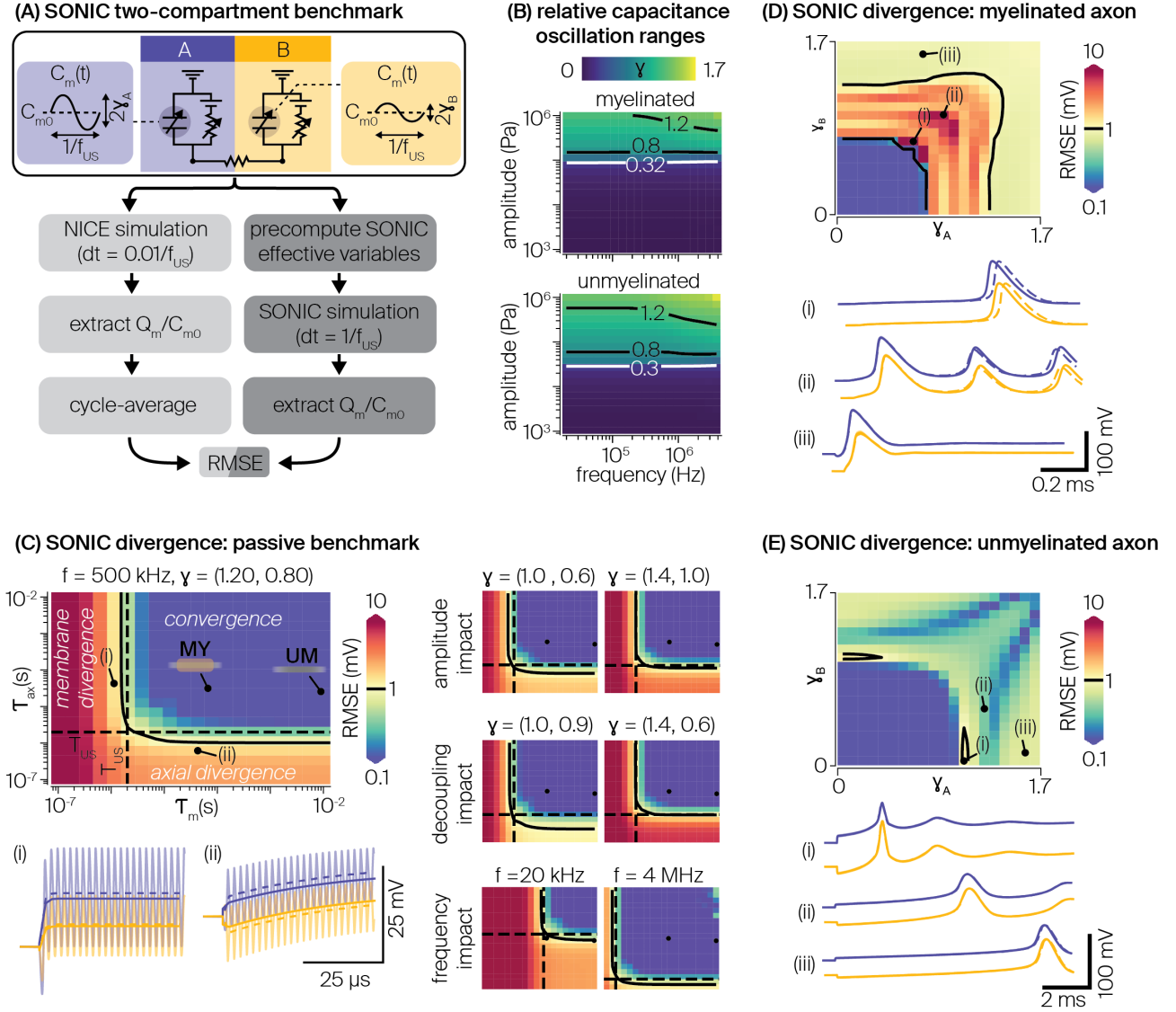


Figure 27. Evaluation of the SONIC paradigm accuracy in two-compartment benchmark models. (A) Schematic description of the two-compartment SONIC benchmark and associated divergence evaluation process. (B) Magnitude of the intra-cycle relative capacitance oscillation range as a function of stimulus frequency and pressure amplitude in myelinated and unmyelinated fibers, computed using axon-specific bilayer sonophore models at their respective resting charge density. White lines indicate cell-type-specific excitation threshold levels. (B) SONIC divergence (maximum RMSE between normalized charge density profiles resulting from SONIC and cycle-averaged NICE simulations) in a symmetric two-compartment passive model ($C_{m0} = 1 \mu\text{F}/\text{cm}^2$, $E_{\text{Leak}} = -70 \text{ mV}$), as a function of the model's electrical time constants ($\tau_m = C_{m0}/g_{\text{Leak}}$, $\tau_{ax} = C_{m0}A_m/G_a$), for a typical US frequency (500 kHz) and sinusoidal oscillation drive ($\gamma = (1.2, 0.8)$). Acoustic periodicity, critical divergence level (1 mV), and fiber passive properties are indicated on the two-dimensional logarithmic color maps. Insets (i) and (ii) provide examples of NICE, cycle-averaged NICE, and SONIC charge density profiles for diverging conditions. Minimized maps evaluate SONIC divergence in the same model but for varying capacitance oscillation amplitudes and gradients, as well as varying US frequencies. (C) SONIC divergence in a two-compartment benchmark model of the myelinated axon for various combinations of oscillation pairs ($f = 500 \text{ kHz}$, 1 ms stimulus). A critical divergence level (1 mV) is indicated on the color map. Insets (i-iii) provide examples of NICE, cycle-averaged NICE, and SONIC charge density profiles for various characteristic drive combinations. (D) Equivalent divergence evaluation in a two-compartment benchmark model of the unmyelinated axon (10 ms stimulus).

We first designed a generic benchmark composed of two passive compartments with identical geometries and passive membrane properties ($C_{m0} = 1 \mu\text{F}/\text{cm}^2$, $V_{m0} = E_{\text{Leak}} = -70 \text{ mV}$). Membrane and axial conductances were mapped to equivalent time constants ($\tau_m = C_{m0}/g_{\text{Leak}}$ and $\tau_{ax} = C_{m0}A_m/G_a$, respectively), and simulation durations were fixed to five times the longest time constant in order to ensure steady-state convergence, while ensuring at least 10 acoustic cycles. Then, we designed axon-specific benchmarks composed of two identical compartments with axon-specific

morphological properties and full membrane dynamics of each fiber type. Physiologically relevant simulation durations known to elicit spiking activity in each model (1 ms and 10 ms for the myelinated and unmyelinated cases, respectively) were used.

4.4 Results

4.4.1 The SONIC paradigm enables accurate simulations in multi-compartmental axon models.

We used two-compartment benchmarks to evaluate the accuracy of the SONIC paradigm in spatially-extended representations. These benchmarks used a simplified capacitance sinusoidal drive that can be intuitively mapped to original sonication parameters: for both axon models, relative capacitance oscillation ranges increased monotonically with acoustic pressure and showed little modulation by US frequency over the 20 kHz – 4 MHz range (**Figure 27B**), with rheobase excitation thresholds occurring around $\gamma = 0.3$ for the central, most-exposed node (see **Figure 31**).

First, we investigated the influence of model and stimulus properties on the accuracy of the SONIC paradigm in predicting sub-threshold depolarization – a critical aspect of neuronal responses – using a passive benchmark model (see Methods). We evaluated SONIC divergence for various combinations of model membrane and axial time constants, providing quantitative estimates of the time taken by leakage and axial currents to respond to variations in transmembrane and longitudinal intracellular voltage gradients, respectively.

For a typical driving frequency (500 kHz) and supra-threshold oscillation ranges ($\gamma = [1.2, 0.8]$), the divergence of the SONIC paradigm showed a rather symmetrical dependency on both axial and membrane conductances (**Figure 27C**). Strong electrical conductances (i.e., short time constants) increase the sensitivity of the electrical system to the oscillatory mechanical drive to a point that currents instantaneously “convert” part of the capacitive displacement energy into fast-charge redistribution during an acoustic period, thereby impacting the net charge variation over that period. We can differentiate two distinct mechanisms of intra-cycle charge redistribution. On the one hand, leakage currents opposing intra-cycle deviations from reversal potentials create a transmembrane charge redistribution that reduces the net charge increase at each cycle, hindering the slow scale charge build-up in each compartment (**Figure 27C**, inset (i)). On the other hand, intracellular currents opposing intra-cycle voltage gradients create an axial charge redistribution across the two compartments that reduces the net charge gradient achieved over a cycle, ultimately limiting the magnitude of effective charge density gradients over time (**Figure 27C**, inset (ii)). Neither of these redistribution mechanisms were captured by the SONIC paradigm, which resulted in a divergent sub-space ($\epsilon_{max} > 1$ mV) for strong enough conductances. Conversely, weaker conductances (i.e. larger time constants) ensured minimal intra-cycle charge redistribution and outlined a sub-space of SONIC convergence ($\epsilon_{max} < 1$ mV). A clear bifurcation between these two sub-spaces emerged as the membrane and / or axial time constant approached the order of magnitude of the acoustic period.

Interestingly, the accuracy of the SONIC paradigm also depended on intrinsic stimulus features. On the one hand, both stronger amplitudes and larger gradients of capacitance oscillations amplified intra-cycle charge redistributions (and SONIC divergence) within the divergence sub-space, but they did not significantly affect the bifurcation time constant. Whereas, increasing oscillation frequencies expanded the convergence sub-space to shorter time constants, but did not significantly affect the magnitude of SONIC divergence within the divergence sub-space. Together, these findings suggested that the critical condition for SONIC convergence is that the model’s time constants should be longer than the drive periodicity ($\{\tau_m, \tau_{ax}\} > 1/f_{US}$). The passive properties of both axon models used in this study satisfied this criterion, except at very low drive frequencies ($f = 20$ kHz).

Second, we investigated the applicability of the SONIC paradigm for the particular axon models used in this study. For this, we used two-compartment models with axon-specific morphological properties and full membrane dynamics, and evaluated SONIC divergence across a symmetric two-dimensional space of capacitance oscillation pairs with a drive frequency of 500 kHz.

As expected, limited drive oscillation amplitudes triggered passive build-ups in charge density in both models that were accurately captured by the SONIC paradigm (**Figure 27D-E**). As the capacitance oscillation amplitude reached a critical threshold in one compartment ($y_{thr} = 0.7$ and 0.9 for myelinated and unmyelinated benchmarks, respectively), both models then transitioned towards an active response. A few regions of SONIC inaccuracy appeared in the myelinated case around the transition threshold, where the timing of the action potential (AP) generation was especially sensitive to the sub-threshold build-up dynamics and therefore tended to amplify subtle differences in initial build-ups between the two paradigms (**Figure 27D**, insets (i)-(ii)). However, those differences vanished at higher oscillation amplitudes which elicited a more robust spiking dynamics (faster build-up, reduced post-spike oscillations) (**Figure 27D**, inset (iii)). It is also worth noting that SONIC inaccuracies were restricted to very few combinations of capacitance oscillation amplitudes, which corresponded to a narrow range of stimulus amplitudes. In the unmyelinated case, the slower intrinsic membrane dynamics and limited axial coupling enabled a robust SONIC accuracy across the entire explored oscillation range (**Figure 27E**, insets (i)-(iii)).

Taken together, these findings suggested that the SONIC model can provide accurate predictions of neuronal responses in single cable peripheral axon models across the entire LIFUS parameter space with the exception of very low US frequencies ($f < 100$ kHz) and can thus be reliably applied to investigate intramembrane cavitation in those models.

4.4.2 Exogenous acoustic and electric sources produce normal field distributions along fibers

The simulation of spatially extended morphological models by artificial exogenous fields traditionally requires the spatial distribution of a perturbation variable across the model's compartments to be solved. Thus, we aimed to analyze the nature of acoustic pressure and extracellular voltage distributions obtained from simplified, yet realistic configurations.

First, we used the distributed point source method (DPSM, see Methods) to predict acoustic propagation from a single element planar transducer in a water-like medium (Yanagita et al., 2009). Normalized pressure distributions in the propagation plane showed a high degree of directionality, with significant amplitudes concentrating along the main lobe normal to the transducer surface (**Figure 28A**). Both larger transducer diameters and higher frequencies induced a more pronounced near-field effect and shifted the focal distance further away from the source. At their respective focal distance, all configurations produced Gaussian-like pressure distributions along the transverse axis (**Figure 28B**), as confirmed by D'Agostino and Pearson's statistical normality test on all distributions. Moreover, the full width at half maximum (FWHM) of these distributions increased linearly with the transducer radius and showed little modulation by US frequency (**Figure 28C**).

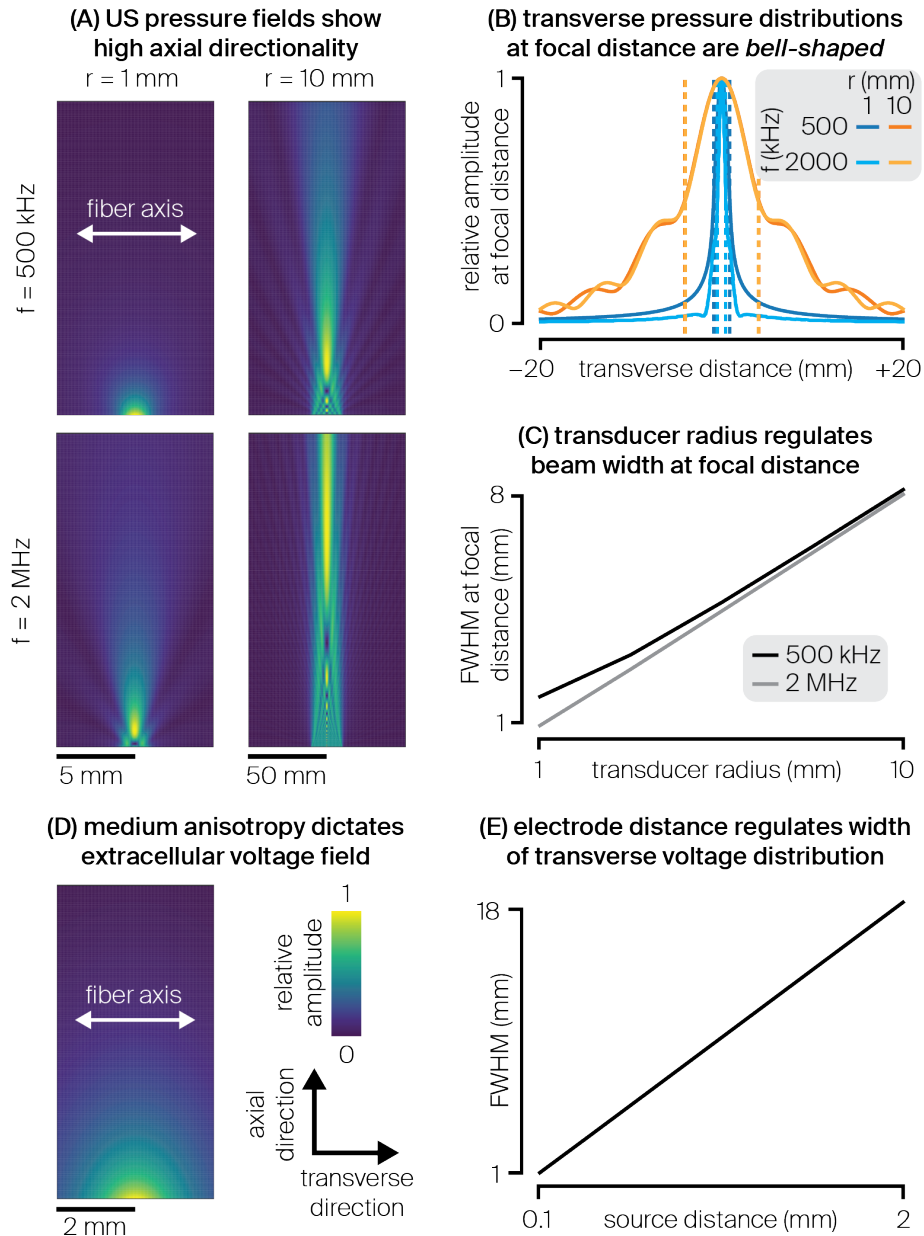


Figure 28. Qualitative nature of exogenous acoustic and electrical fields. (A) Normalized two-dimensional acoustic pressure amplitude distribution across the propagation plane computed upon sonication by a single-element planar transducer immersed in water-like medium, for various combinations of transducer radius and US frequency. A white line indicates the fiber's axis as considered in this work. (B) Normalized transverse pressure distribution measured at the transducer's focal distance, for the same combinations of transducer radius and US frequency. Dotted lines indicate FWHMs for each distribution. (C) FWHM of the pressure amplitude distribution along the fiber axis as a function of the transducer radius, for two characteristic US frequencies. (D) Normalized two-dimensional voltage distribution across a two-dimensional plane generated by a point-source electrode placed in a nerve-like anisotropic medium. A white line indicates the fiber's axis as considered in this work. (E) FWHM of the extracellular voltage distribution along the fiber axis as a function of the electrode-fiber distance.

Second, used a point-source electrode approximation (see Methods) to predict extracellular voltage fields in a nerve-like environment (Ranck and Bement, 1965). Resulting distributions also showed some degree of directionality due to the medium anisotropic properties (Figure 28D). Distributions were somewhat simpler than for the acoustics case, with voltage amplitude decreasing as a function of distance from the electrode as a result of the increasing resistive path. Nevertheless, voltage distributions along the transverse axis were also “Gaussian-like”, and their width linearly increased as a function of the distance from the electrode (Figure 28E).

These results obtained using realistic propagation models show that both ultrasonic and electrical sources produce normal distributions of the perturbation variable along the fiber's longitudinal axis, and that the “width” of those distributions can be controlled with a single parameter (transducer radius and electrode distance, respectively). Therefore, to assess the impact of stimulus spatial distribution on fiber excitability in a controlled manner and allow a direct comparison across the two simulation modalities, we sampled exogenous fields directly from Gaussian distributions of varying widths and amplitudes for the study of single, isolated fibers. In the following, the FWHM of the field distribution is referred to as the stimulus “beam width”.

4.4.3 LIFUS modulates membrane capacitance to excite myelinated and unmyelinated axons

In this section, we describe “typical” predicted responses of myelinated and unmyelinated axons to ultrasound stimulation. We selected standard axon models using representative diameters for each axon population (10 μm and 0.8 μm for myelinated and unmyelinated fibers, respectively), and assumed a uniform sonophore depiction across the model non-insulated compartments (i.e. Sundt unmyelinated membrane and SENN Ranvier nodes). We chose a typical sonophore radius ($a = 32 \text{ nm}$) used in previous studies (Lemaire et al., 2019; Plaksin et al., 2014, 2016) and a physiologically plausible sonophore coverage fraction ($f_s = 80\%$) falling within a range of conserved excitability in cortical point-neuron models (see (Lemaire et al., 2019), Fig. 10). Importantly, those parameters were chosen ad-hoc, without re-tuning or post-hoc adjustments. We also considered “standard” acoustic perturbations, using a typical US frequency (500 kHz) and sampling acoustic pressures stemming from a 5 mm-wide Gaussian distribution (i.e. qualitatively equivalent to the distribution generated by a 10 mm diameter single-element planar transducer at focal distance at this frequency) with a peak amplitude of 120 kPa (i.e. significantly above excitation thresholds of both axons). Finally, we examined responses to pulse durations for which the rheobase regime is approached for each fiber type (1 ms and 10 ms for the myelinated and unmyelinated fibers, respectively, see next section). To better identify mechanisms of axonal recruitment by US pulses, we quantified the time required to reach a normalized charge build-up of 5 mV in the central compartment for each response and computed the contribution of each individual current to this initial build-up.

For both models, the sonication pulse onset generated instantaneous drops in effective membrane capacitance in the axon compartments, whose magnitude increased with the amplitude of the local acoustic pressure, thereby amplifying the absolute value of transmembrane voltage and inducing hyperpolarization (**Figure 29A-B**). Due to the Gaussian distribution of acoustic pressure along the axon, central compartments experienced a stronger hyperpolarization than peripheral ones, which introduced a longitudinal gradient in transmembrane voltage along the fiber.

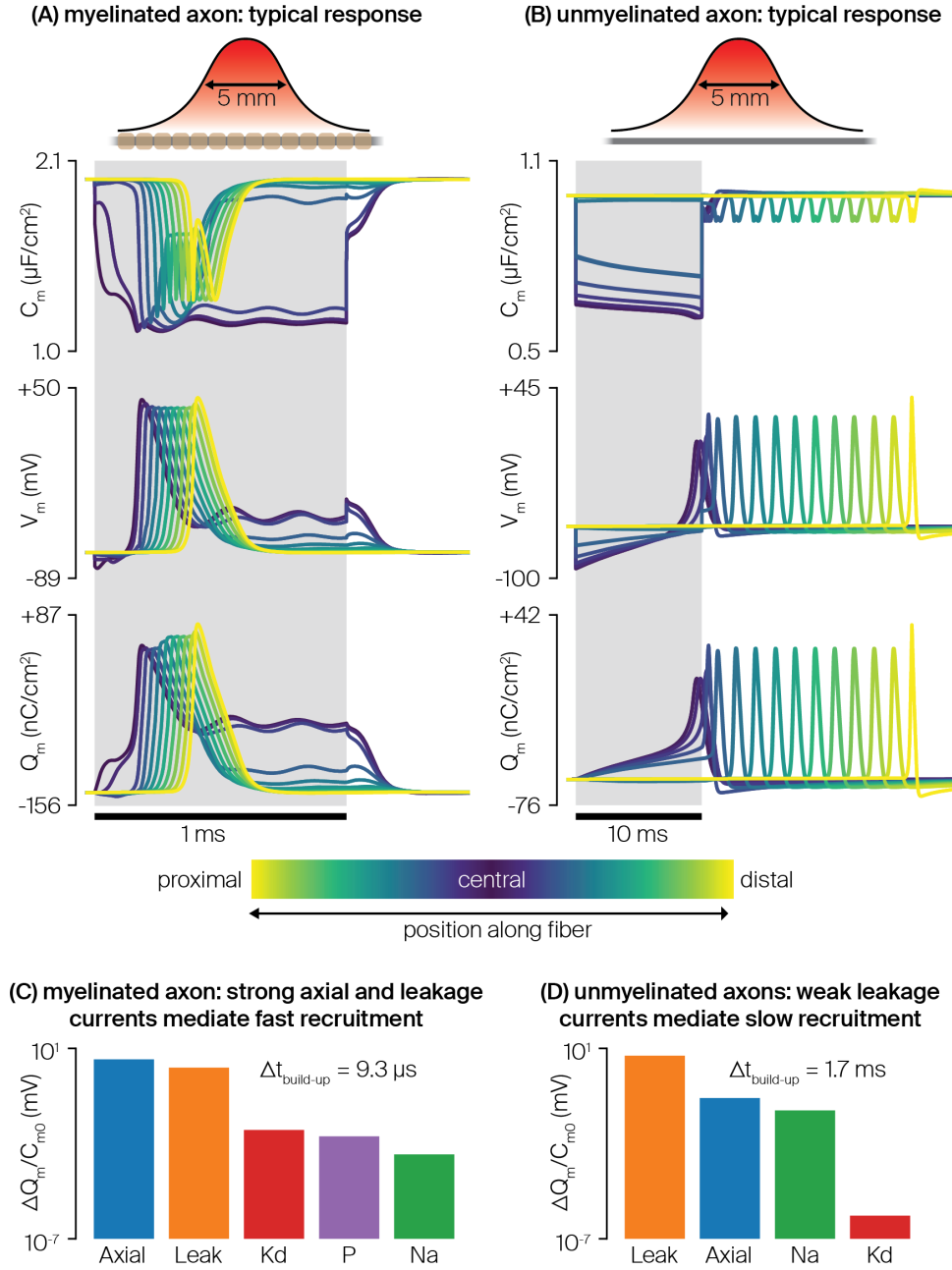


Figure 29. Typical responses of myelinated and unmyelinated axon models to a single US pulse. **(A)** Time profiles of effective membrane capacitance, effective membrane potential, and effective membrane charge across compartments during a typical response of a myelinated axon to a 1 ms sonication (500 kHz frequency, 5 mm-wide Gaussian pressure distribution aligned on the fiber with a spatial peak of 120 kPa). **(B)** Equivalent time profiles during the typical response of an unmyelinated axon to a 10 ms sonication (identical pressure distribution as in **(A)**). **(C)** Quantification of the membrane and axial currents contributions to the first 5 mV of normalized charge build-up in the fiber central compartment. **(D)** Equivalent quantification for the response of the unmyelinated axon's central compartment.

At the central compartment where hyperpolarization is the largest, leakage currents arose to bring transmembrane voltage towards the leakage reversal potential, thereby inducing a build-up in local charge density. The considerably higher density of leakage channels in the Ranvier node compared to the unmyelinated membrane ($g_{\text{leak}}^{\text{SENN}} \approx 300 g_{\text{leak}}^{\text{Sumdt}}$) induced much larger leakage currents (**Figure 29C-D**). Moreover, significant axial currents also arose in the myelinated axon, driven by large voltage gradients between the central and neighboring Ranvier nodes. Together, these two depolarizing currents yielded a much faster membrane charge build-up in the myelinated axon, yielding shorter response latencies. These differences are reflected in the times required to achieve a normalized

charge build-up of 5 mV in the central compartment (9 μ s and 1.7 ms for myelinated and unmyelinated fibers, respectively).

For a long enough sonication, membrane charge density increased until a spiking threshold was reached, prompting the opening of Sodium ion channels and thereby triggering an AP in the central compartment that started travelling bi-directionally towards the axon extremities. As expected, both axons exhibited marked differences in conduction velocities: fast saltatory conduction in the large diameter myelinated axon allowed the AP to reach the extremities of the axon in less than 1 ms, whereas that process took more than 10 ms in the slowly conducting unmyelinated axon. As the sonication outlasted the AP duration in the myelinated axon, affected nodes transitioned into a “plateau potential” regime (stabilization of membrane charge density around a depolarized value).

Finally, the sonication offset removed the mechanical membrane perturbation, and effective membrane capacitances instantaneously reverted to their resting values, triggering a rapid reduction in transmembrane voltage magnitudes. The myelinated axon then simply repolarized back to its equipotential resting state, while the AP propagated towards peripheral extremities in the unmyelinated axon.

The effect of electro-mechanical coupling was visible across neuronal responses. During the sub-threshold charge build-up, the decrease in electrical pressure (a constraining force on the bilayer sonophore, proportional to Q_m^2) amplified membrane deflections, which further reduced the effective membrane capacitance (an effect more pronounced on the myelinated axon). In addition, the propagating spike induced a wave of time-varying electrical pressure that also modulated the effective membrane capacitance.

4.4.4 LIFUS can selectively recruit myelinated and unmyelinated axons

In the previous section, we showed that ultrasonic axon recruitment requires the membrane charge density to be brought locally above a spiking threshold to engage voltage-gated channels. Yet, the underlying mechanisms eliciting this charge build-up differ significantly from those of electrical stimulation (McNeal, 1976; Rattay, 1986). Therefore, we aimed to determine if the two stimulation modalities could produce distinct excitability patterns. To this end, we computed excitation thresholds for various pulse durations ranging from 10 μ s to 1 s (using binary search procedures) to construct strength-duration (SD) curves.

First, we evaluated the excitability of representative myelinated and unmyelinated axons (10 μ m and 0.8 μ m diameters, respectively) with a typical stimulus width (5 mm). With electrical stimulation, threshold peak extracellular voltages required to elicit a travelling AP decreased with increasing pulse duration, and then reached an asymptotical (so-called “rheobase”) regime for long enough pulses (**Figure 30A**). In line with previous modeling studies (Lubba et al., 2019; Tarnaud et al., 2018b), excitation thresholds for the myelinated axon were lower than those of the unmyelinated axon over the entire range of pulse durations. This result can be explained by two main factors. For short pulses where the speed of the depolarization predominantly determines when / if the spiking threshold is reached, myelinated axons can be recruited because of short membrane time constants, whereas unmyelinated axons fail to respond fast enough. Conversely, for long pulses approaching the rheobase regime, transient features become less critical and longitudinal gradients of the applied extracellular voltage become the main determinant of axonal excitability (Warman et al., 1992). Here again, myelinated axons are easier to recruit because of their insulated internodes that effectively discretize the voltage field at sparsely distributed Ranvier nodes, thereby producing stronger longitudinal gradients at the central node than those encountered across the continuous membrane of unmyelinated axons. With ultrasonic stimulation, threshold peak acoustic pressure amplitudes required for excitation also decreased

with increasing pulse durations and reached a rheobase regime for long enough pulses (**Figure 30B**). Similarly as with electrical stimulation, short membrane and axial time constants conferred a low response latency to myelinated axons (see **Figure 29**), thereby allowing excitation by short ultrasonic pulses to which unmyelinated axons failed to respond. Surprisingly however, for longer pulse durations ($PD \geq 10\text{ ms}$), the SONIC paradigm predicted lower excitation thresholds in unmyelinated axons than in myelinated axons.

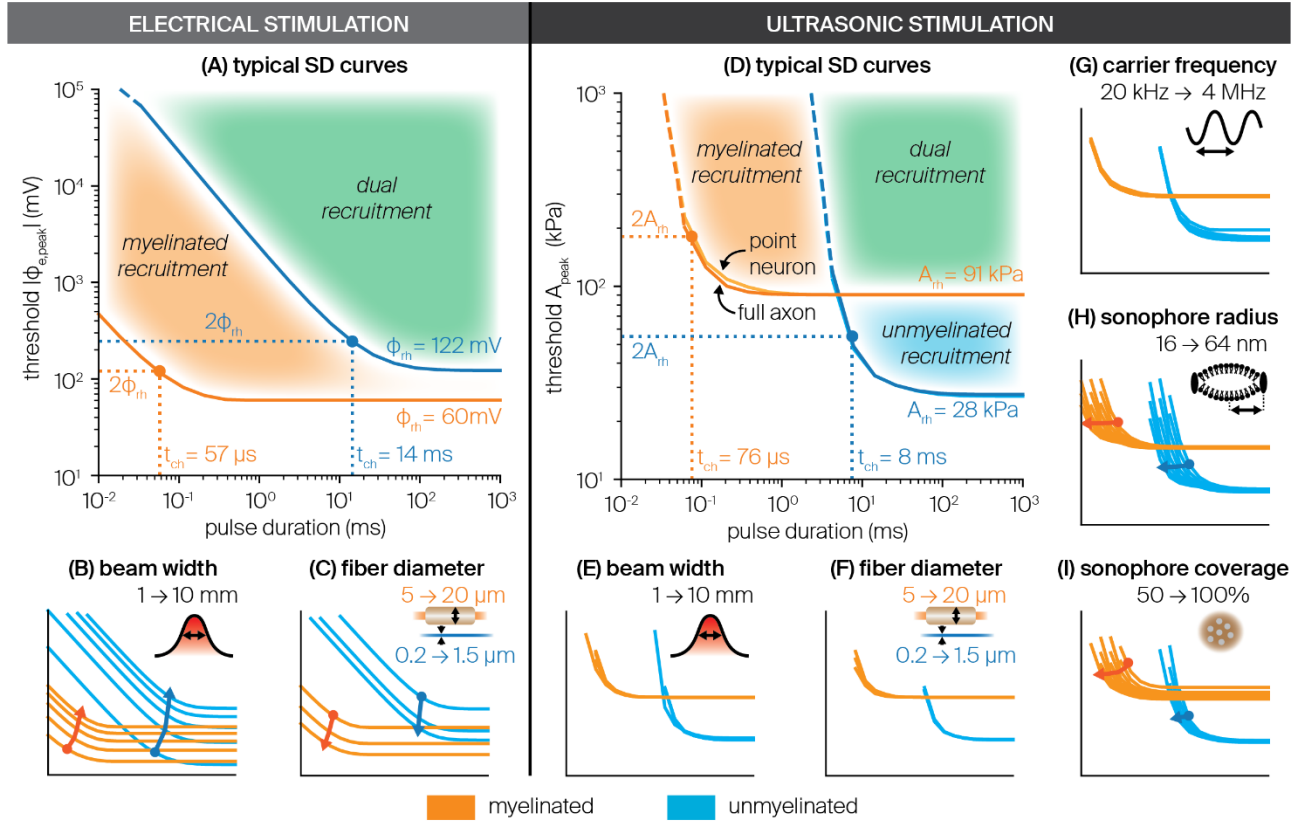


Figure 30. Comparison of strength-duration curves of myelinated and unmyelinated axons upon electrical and ultrasonic stimulation. (A) SD curves of representative myelinated (10 μm diameter, in orange) and unmyelinated (0.8 μm diameter, in blue) axons, depicting the threshold absolute peak extracellular voltage required to elicit fiber excitation as a function of pulse duration, for a characteristic 5 mm wide Gaussian extracellular voltage distribution. Rheobase and chronaxie values of each curve are indicated, as well as distinct areas of fiber recruitment. (B) SD curves of representative myelinated and unmyelinated axons for Gaussian extracellular voltage distributions of varying widths (1 to 10 mm). Arrows indicate the translation of the chronaxie point in the SD space for increasing stimulus width. (C) SD curves both fiber types of upon stimulation with a characteristic voltage distribution, for varying fiber diameters within the physiological range of each population (myelinated: 5 to 20 μm , unmyelinated: 0.2 to 1.5 μm). Arrows indicate the translation of the chronaxie point in the SD space for increasing fiber diameter. (D) SD curves of representative myelinated and unmyelinated axons, depicting the threshold peak acoustic pressure amplitude required to elicit fiber excitation as a function of pulse duration, for a characteristic 5 mm wide Gaussian acoustic pressure distribution and US frequency ($f_{\text{US}} = 500\text{ kHz}$), using typical values of sonophore radius ($a = 32\text{ nm}$) and sonophore coverage fraction ($f_s = 80\%$) in the model's compartments. SD curves using equivalent "node" models located under the stimulus peak are also indicated (light blue and orange curves), as well as rheobase and chronaxie values of each curve, and distinct areas of fiber recruitment. (E) SD curves of representative myelinated and unmyelinated axons with typical US frequency and sonophore parameters for Gaussian pressure distributions of varying widths (1 to 10 mm). (F) SD curves both fiber types with typical US frequency, pressure distribution and sonophore parameters, for varying fiber diameters within the physiological range of each population. (G) SD curves of equivalent "node" models of both fiber types with typical sonophore parameters and pressure distributions for varying US frequencies (20 kHz to 4 MHz). (H) SD curves of "node" models with typical pressure distribution, US frequency and sonophore coverage fraction for varying sonophore radii (16 to 64 nm). (I) SD curves of "node" models with typical pressure distribution, US frequency and sonophore radius, for varying sonophore coverage fractions (50 to 100 %).

Second, we characterized the impact of stimulus beam width and fiber diameter on excitability by systematically exploring relevant parameter ranges and using the "chronaxie point" (i.e. the pulse duration at which the threshold is twice the rheobase, see **Figure 30A-B**) as a reference point to measure

the rigid translation of SD curves in the (pulse duration – stimulus amplitude) space. With electrical stimulation, narrowing stimulus beam widths enhanced excitability of myelinated and unmyelinated axons by producing stronger longitudinal gradients in extracellular voltage (**Figure 30C**). These stronger gradients primarily translated SD curves towards lower thresholds, but they also slightly diminished chronaxie durations. Very narrow beams produced an inversion of rheobase values, and unmyelinated axons became easier to recruit with long enough pulses. In a mirroring manner, increasing fiber diameters also enhanced excitability in both axon types (**Figure 30D**) as a result of (i) a larger intracellular conductance amplifying depolarization in response to a given extracellular voltage gradient, and (ii) in myelinated axons, an increased internodal spacing ($L = 100D_{fiber}$) that further amplifies longitudinal gradients between consecutive Ranvier nodes. Again, both of these effects induced considerable shifts of SD curves towards lower thresholds and slightly reduced chronaxie durations in both axon types. Conversely, with ultrasonic stimulation, SD curves were remarkably consistent across a range of stimulus beam widths, as well as across the physiological range of fiber diameters of both populations, with only very slight variations in the chronaxie point and no clear trend emerging (**Figure 30E-F**).

The relatively low sensitivity of ultrasonic excitation thresholds to stimulus beam width and fiber diameter suggest that excitability patterns are primarily dictated by the magnitude of the peak acoustic pressure along the axon, rather than by the beam shape or the axial properties of the axon. To verify that hypothesis, we carried out the same excitability analysis in point-neuron models representing isolated neuronal compartments of the two axon models, namely a SENN Ranvier node and a Sundt unmyelinated segment, referred to as “node” models. We found almost identical SD curves between the node and full axon models (**Figure 30D**), thereby confirming that excitation is primarily mediated by the localized action of acoustic pressure on the cellular membrane. At first glance, these results seem to challenge the observation that axial currents contribute significantly to the initial charge build-up at the central node of myelinated axons upon sonication (**Figure 29**), and may therefore indicate the presence of a sharp transition in the mechanical response of the membrane to intensifying acoustic fields, bringing axons from passive to active responses within narrow amplitude ranges. Nevertheless, these results suggest that LIFUS-triggered excitation is primarily a local phenomenon – at least in these models – that can be accurately predicted without considering extended morphological details.

Given the high accuracy of node models in predicting cell-type-specific excitation thresholds, we leveraged their computational efficiency to explore the impact of acoustic frequency, sonophore size and sonophore coverage on neuronal excitability. In line with previous modeling results in CNS neurons (Lemaire et al., 2019; Plaksin et al., 2014) we found that US frequency does not significantly affect excitation thresholds apart from a slight increase above 1 MHz due to higher viscous stresses limiting sonophore cavitation (**Figure 30G**). Moreover, increasing sonophore radii induced mainly a “horizontal” shift of excitability towards shorter durations (**Figure 30H**), while increasing sonophore coverage fractions reduced both threshold baselines and chronaxie durations (**Figure 30I**).

4.4.5 Resting membrane capacitance governs fiber excitability for long pulse durations

Strength-duration analyses revealed that unmyelinated axons exhibited lower excitation thresholds for long ultrasonic pulses, a trend robust to variations in model and stimulus parameters. Thus, we aimed to investigate the underlying mechanisms supporting this enhanced excitability using cell-type-specific node models, which proved to be appropriate benchmark tools to study ultrasonic neuronal recruitment (**Figure 30**).

For sub-threshold acoustic amplitudes and rheobase pulse durations, both the myelinated and the unmyelinated nodes responded to sonication with a build-up in charge density towards a more depolarized steady state (**Figure 31A**). Increasing the acoustic amplitude enhanced the magnitude of this build-up until the node's spiking threshold was reached and an AP was fired. Interestingly, the exponential convergence of sub-threshold charge build-ups indicated that they were mostly mediated by passive currents, and could therefore be approximated by a simple RC membrane circuit with a single leakage conductance. Under this approximation, the steady-state charge build-up is proportional to the variation of effective membrane capacitance ($C_m^* = \left[\frac{1}{T_{US}} \int_t^{t+T_{US}} \frac{dt}{C_m(Z(t))} \right]^{-1}$) from its resting value:

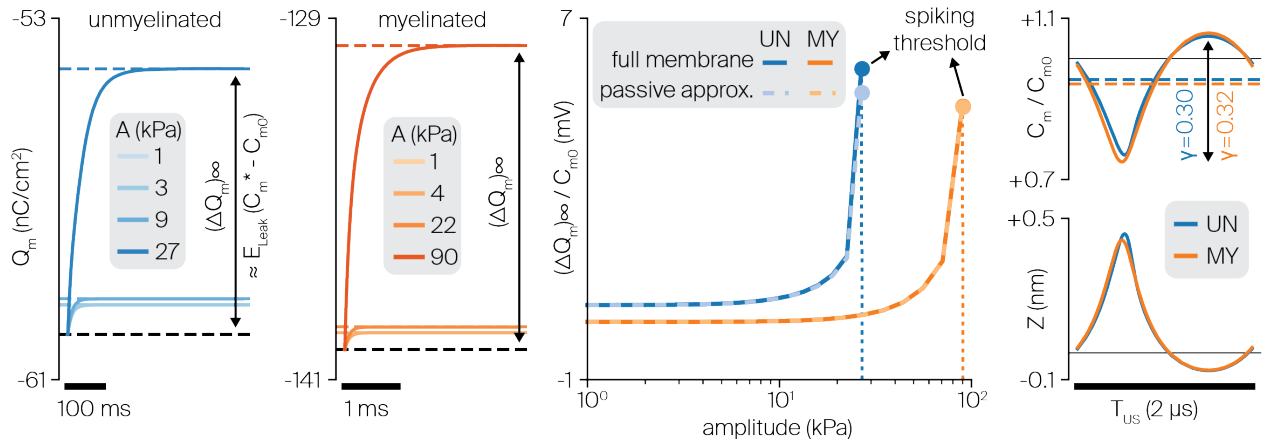
(109)

$$\left(\frac{dQ_m}{dt} \right)_{\text{sub-threshold}} \approx -g_{\text{Leak}}(V_m^* - E_{\text{Leak}})$$

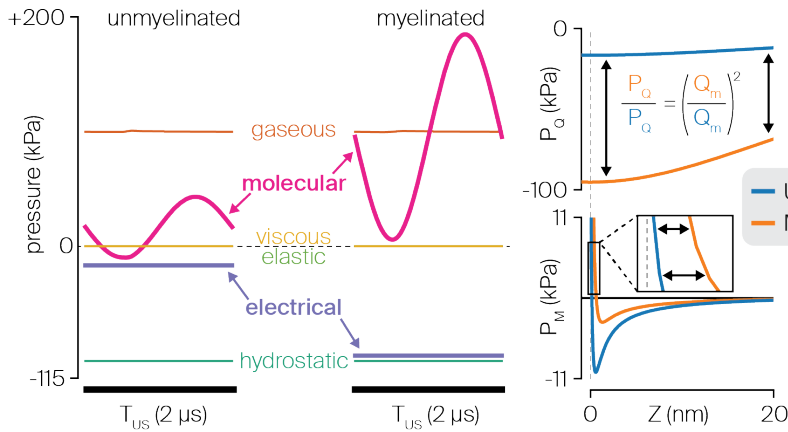
$$(\Delta Q_m)_{\infty} \approx (C_m^* - C_{m0})E_{\text{Leak}}.$$

For both cell types, the passive circuit approximation can accurately predict the magnitude of steady-state charge build-up across a cell-type-specific range of sub-threshold acoustic amplitudes. This high prediction accuracy confirms that sub-threshold dynamics is almost entirely governed by the drop in effective capacitance.

(A) effective capacitance drop regulates leakage-driven sub-threshold charge build up



(B) charge-dependent internal pressures regulate sonophore kinematics at threshold levels



(C) resting membrane capacitance explains cell-type-specific rheobase excitability

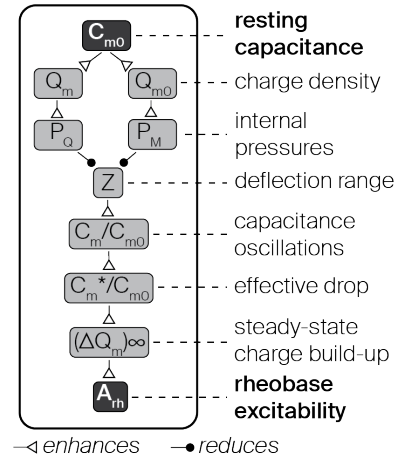


Figure 31. Underlying mechanisms of distinct rheobase excitabilities in myelinated and unmyelinated axons. (A) Effective capacitance variations regulate sub-threshold charge build-ups. From left to right: LIFUS-triggered, exponentially converging charge build-ups in myelinated and unmyelinated “node” models for various sub-threshold pressure amplitudes. Normalized

steady-state charge build-ups for each “node” model as a function of sub-threshold pressure amplitude, computed from full membrane simulations (plain lines) and estimated from the sole relative variation in effective membrane capacitance (dashed lines, passive circuit approximation). Detailed intra-cycle oscillation profiles of membrane capacitance and membrane deflection for each fiber type at their respective threshold levels. **(B)** Charge-dependent electrical and molecular pressure regulate threshold sonophore kinematics. From left to right: detailed profiles of internal pressure forces regulating sonophore cavitation during an acoustic period, driven by cell-type-specific threshold acoustic pressures. Detailed profiles of electrical and molecular pressures in both fiber types along the physiological range of membrane deflection. **(C)** Schematic diagram showing the causal chain of influence by which resting membrane capacitance affects charge-dependent internal pressures, sonophore kinematics, effective capacitance variations, and ultimately rheobase excitability.

Both the myelinated and unmyelinated nodes required similar normalized charge build-ups to reach the spiking threshold (5.0 and 5.9 mV respectively), which corresponded to comparable relative variations in effective membrane capacitance (-6.3 and -5.2 %). Moreover, looking at intra-cycle dynamics, the resemblance of these effective cycle-averaged values arose from analogous oscillation profiles of membrane capacitance over an acoustic period (normalized oscillation ranges of 0.32 and 0.30, respectively). Recalling that capacitance is defined here as a deflection-dependent variable (see Methods section), this cross-model analogy could be mapped further back to cavitation profiles. Surprisingly, however, these similar membrane deflections were achieved at significantly different acoustic pressure amplitudes (91 kPa and 28 kPa, respectively). This discrepancy indicates variations in the internal kinetic system regulating sonophore cavitation dynamics in each node model.

Closer inspection of the detailed oscillation profile and resulting signal energy of each internal pressure component at these cell-type-specific amplitudes revealed several interesting features (**Figure 31B**). First, the relatively small cavitation magnitudes and velocities for these threshold levels ($|Z| < 0.5 \text{ nm}$, $\left|\frac{dZ}{dt}\right| < 1 \text{ cm/s}$) did not generate significant viscoelastic stresses on the membrane and surrounding medium. Moreover, this cavitation dynamics allowed for an instantaneous equilibration of gaseous and hydrostatic pressures on both sides of the sonophore cavity through transmembrane gas transport, thereby yielding identical energy levels for these pressure components across the two models. In contrast, both electrical and molecular pressures showed much larger energy levels for the myelinated sonophore model than for its unmyelinated counterpart. More specifically, the molecular pressure profile was shifted towards more positive values and showed higher oscillation amplitudes, whereas the electrical pressure profile was constant across a cycle but shifted towards more negative values. Together, these two pressure components are responsible for the cell-type-specificity of sonophore cavitation kinetics.

These changes in dynamic pressure oscillations can be mapped back to distinct profiles over a reference range of membrane deflections, allowing for the elucidation of the mechanisms of cell-type-specific rheobase excitability:

- The electrical pressure accounts for the attraction forces between the electric ion charges on the membrane leaflets, and is defined as $P_Q(Z, Q_m) = -\frac{S_0}{S(Z)} \frac{Q_m^2}{2\epsilon_0 \cdot \epsilon_r}$. Therefore, both electrical pressure profiles show a weak dependence on membrane deflection, and a constant magnitude ratio across the deflection range ($\frac{P_{Q,myel}}{P_{Q,unmyel}} = 5.8$), corresponding exactly to the square of the ratio of threshold charge densities across the two models ($\frac{Q_{thr,myel}}{Q_{thr,unmyel}} = 2.4$). The latter ratio primarily arises from variations in a fundamental biophysical property: the resting specific membrane capacitance of the myelinated axon is twice as high as that of the unmyelinated axon (see Methods). This increased capacitance allows the myelinated membrane to accumulate twice as much charges for identical transmembrane voltages, thereby increasing the electrical pressure on the membrane and hindering sonophore expansion around threshold levels.
- The intermolecular pressure is defined by a Lennard-Jones expression integrated across the sonophore surface: $P_M(Z) = \frac{1}{S(Z)} \int_0^{2\pi} \int_0^a A_r \cdot (\gamma^x - \gamma^y) dr d\theta$ with $\gamma = \frac{\Delta^*}{2z(r)+4(Q_{m0})}$. All parameters

of this expression are fixed except for Δ^* , the gap between the two membrane leaflets in the absence of charges. This parameter is calculated from a model-specific equilibrium state that depends on resting charge density, and therefore shows cell-type-specificity: the more negative resting charge density of the myelinated axon – mainly resulting from its larger capacitance – results in a smaller computed gap compared to the unmyelinated axon (1.1 nm vs 1.3 nm, respectively). Slight changes in this key parameter have profound implications on the resulting molecular pressure profiles: the smaller gap in the myelinated model reduces the amplitude of the negative (i.e. attractive) peak, and more importantly, shifts the transition towards positive (i.e. repulsive) pressure to a more positive deflection value, thereby producing much larger values of repulsive intermolecular pressure and hindering sonophore compression during an acoustic cycle around threshold levels.

The resting membrane capacitance is thus a crucial parameter that indirectly regulates the rheobase excitability of peripheral axons. This regulation is explained by a causal chain of influence (**Figure 31C**), can be summarized as follows: the resting capacitance influences both the resting value and the variation range of membrane charge density, thereby influencing charge-dependent internal pressures. That is, with larger capacitance, electrical pressure becomes more constraining during expansion phases and intermolecular pressure becomes more repulsive during compression phases. Together, these two pressure amplifications restrict the cavitation dynamics, and thus require higher acoustic pressures to attain similar membrane deflection and resulting relative capacitance oscillation ranges. In terms of cycle-averaged dynamics, higher pressures are needed to reach a given relative drop in effective capacitance, which almost entirely regulates the sub-threshold charge build-up. Given that both axon models require similar relative charge build-ups to reach their spiking threshold, rheobase excitability is then predominantly determined by the electrical modulation of cavitation dynamics, and hence by the resting membrane capacitance. In light of this mechanism, the enhanced excitability of unmyelinated axons for long pulse durations is explained by their smaller resting capacitance.

4.4.6 Pulsed LIFUS robustly modulates axon spiking activity

In the previous sections, we analyzed response and excitability patterns of axon models upon application of isolated ultrasonic pulses. In the following, we investigated how the repeated application of such pulses can be used to modulate the spiking activity of axons over time. To do so, we simulated full axon models (using the standard model parameters defined in previous sections) upon the application of 10 consecutive sonication pulses (setting the stimulus beam width to one fifth of the fiber length), detected propagated APs on membrane charge density traces of axon extremities, and computed the resulting firing rate as the reciprocal of the average inter-spike interval over the simulation window.

We first evaluated the impact of pulsing parameters on spiking activity for a fixed acoustic pressure distribution with a peak amplitude of 300 kPa (a value falling safely above single pulse excitation thresholds of both axon models). Given the important differences in the LIFUS response time constants observed between myelinated and unmyelinated axons, we explored a relevant range of pulse durations around the axon's single pulse chronaxie for each model.

Myelinated axons responded with very low latency but only fired a single spike for each acoustic pulse, followed by a stabilization to a plateau potential regime. As a result, they could be driven very robustly to follow the pulse repetition frequency (PRF) up to approximately 1 kHz over a wide range of pulse durations (**Figure 32A**, inset (i)). At higher stimulus rates, repeated pulses started to interfere with the cell's refractory period, thereby preventing spike generation and / or propagation on average every two pulses, causing the axon to synchronize with the half-PRF (inset (ii)). At even higher stimulus rates, only very short pulses enabled a sustained firing activity, as the axon progressively reached its physiological limit at around 1 kHz (inset (iii)).

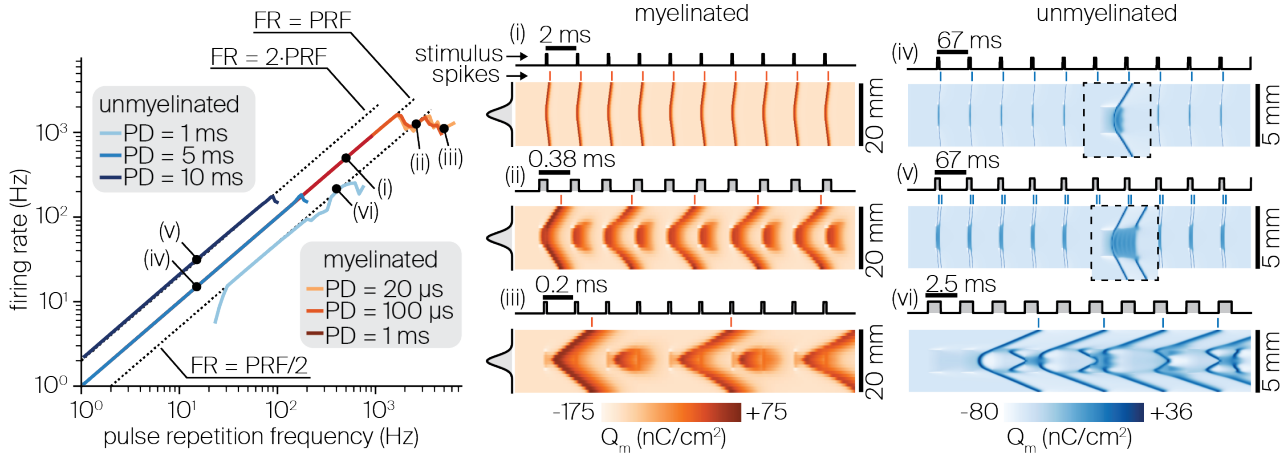
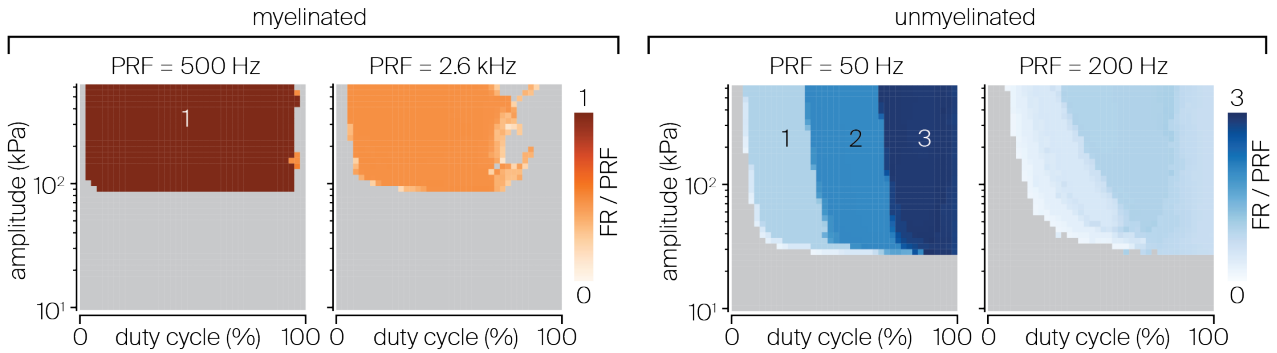
(A) pulsing parameters modulate the firing rate of myelinated and unmyelinated axons**(B) cell-type-specific neuromodulation is robust at low PRFs, and sensitive to stimulus intensity at high PRFs**

Figure 32. Modulation of spiking activity by pulsed sonication in myelinated and unmyelinated axons. (A) Average firing rate elicited in each axon type by a Gaussian acoustic pressure distribution covering one fifth of the fiber length, using default sonophore parameters ($a = 32\text{nm}$, $f_s = 80\%$) and US frequency ($f_{US} = 500\text{ kHz}$), for various pulse durations and pulse repetition frequencies. Dashed lines indicate half, one time and double of the stimulus rate. Detailed spatiotemporal profiles of membrane charge density are indicated for characteristic spiking regimes of each fiber type, along with detailed profiles of the stimulus spatial distribution (vertical) and temporal application (horizontal). **(B)** Average firing rate (normalized by pulse repetition frequency) elicited in each fiber type as a function of duty cycle and peak acoustic pressure amplitude for cell-type-specific pulse repetition frequencies yielding “robust” and “sensitive” spiking behaviors. Numbers on the color maps indicate characteristic regimes of normalized firing rate.

In contrast, unmyelinated axons responded with higher latency, but could fire multiple spikes for prolonged sonication. Consequently, their behavior at low PRFs strongly depended on the pulse duration: short pulses ($PD < 5\text{ ms}$) did not induce any response, intermediate pulses ($5 < PD < 10\text{ ms}$) induced PRF-locking (inset (iv)), and long enough pulses ($PD \geq 10\text{ ms}$) induced spiking activity at double or even higher multiples of the stimulus rate (inset (v)). At intermediate stimulus rates ($20\text{ Hz} < PRF < 100\text{ Hz}$), temporal summation of sub-threshold responses enabled recruitment by short pulses at half the PRF or below. Above 100 Hz , the range of available pulse durations was progressively restricted to shorter values that only allowed the fiber to fire at half the stimulus rate or below (inset (vi)), until a physiological limit was reached around a firing rate of 200 Hz .

Having established that pulsing parameters trigger cell-type-specific patterns of spiking activity, we aimed to investigate whether these neuromodulatory effects also depend on stimulus intensity. Hence, we simulated each axon type across a two-dimensional space of duty cycles (DC, from 0 to 100%) and peak pressure amplitudes (from 10 to 600 kPa), and for each combination, computed the resulting firing rates normalized by the PRF.

At low PRFs allowing a robust pulse-spike synchronization (identified from **Figure 32A** for each axon type), neuromodulatory effects were surprisingly consistent across a wide range of supra-threshold

stimulus amplitudes (**Figure 32B**). The myelinated axon fired exactly one spike per pulse for $DC \in [0.02, 0.95]$ (i.e. for pulses long enough to allow a first response yet distant enough to avoid destructive interaction with the refractory period), independently of stimulus amplitude. In contrast, the unmyelinated axon initiated a first response at slightly larger DCs and then exhibited three distinct spiking regimes with 1, 2 and 3 spikes per pulses as DC increased up to 1. A slight dependency on stimulus amplitude was noted here, as larger pressures shifted transitions between the different spiking regimes to lower duty cycles.

At high PRFs allowing only sub-stimulus rate spiking activity (see again **Figure 32A**), neuromodulatory effects were more intricate, and showed more dependency on stimulus amplitude. In this high-frequency regime (PRF = 2.6 kHz), the myelinated axon's firing rate approached a maximum of 0.5 times the PRF over a wide duty cycle interval ($DC \in [0.04, 0.70]$). At larger duty cycles, spiking was only elicited for sparse DC-amplitude combinations allowing an optimal trade-off between fast depolarization to US stimuli and limited destructive interaction with the refractory period. Surrounding regions did not allow such a trade-off and could only trigger a single spike, after which the axon could not reset to fire again. In contrast, the unmyelinated axon's spiking activity was maximized for an optimal sub-region of intermediate duty cycles where the firing rate approached the stimulus rate (PRF = 200 Hz). Interestingly, larger pressures offered a wider span of this optimal DC interval. Higher duty cycles (up to 100%) also generated spiking activity but also significantly interfered with the axon's ongoing membrane dynamics and were thus less effective.

4.5 Discussion

In this study, we used a novel computational framework to formulate several important predictions on the effects and mechanisms of US neuromodulation by intramembrane cavitation in peripheral fibers. First, single US pulses are capable of inducing *de novo* action potentials in both myelinated and unmyelinated peripheral axons. Second, these two fiber types share a common US recruitment mechanism: the stimulus onset induces a local drop in effective membrane capacitance at the acoustic focus and triggers passive depolarizing currents that raise charge density towards the spiking threshold. Third, while the two fiber types show a robust excitability across a wide range of carrier frequencies and acoustic pressure fields, they exhibit distinct sensitivities to temporal features of US stimuli. Myelinated axons exhibit a low (sub-millisecond) response latency due to their short membrane time constant and can therefore be excited by very short US pulses for which unmyelinated axons are unresponsive. However, for longer stimuli, unmyelinated axons can be excited at lower acoustic intensities than myelinated axons. Interestingly, this enhanced excitability in the rheobase regime is not caused by the absence of myelin, but rather, it is attributable to a smaller specific membrane capacitance ($C_{m0}^{SENN} = 2 \mu\text{F}/\text{cm}^2$, $C_{m0}^{Sundt} = 1 \mu\text{F}/\text{cm}^2$). To the best of our knowledge, the biological origin of this capacitance difference remains undocumented. However, we found the magnitude ratio of this specific parameter to be conserved across a wide collection of biophysical models of myelinated and unmyelinated axons (Frankenhaeuser and Huxley, 1964; McIntyre et al., 2002; Tarnaud et al., 2018b), which supports the reliability of our conclusions. Fourth, the application of repeated US pulses induces a sustained spiking activity in both fiber types, the rate of which can be modulated by adjusting pulsing parameters. Particularly, myelinated axons robustly follow the stimulus rate over a wide range of PRFs, pulse durations and supra-threshold stimulus amplitudes, while unmyelinated axons show more complex dependencies on pulse durations / duty cycle and acoustic intensities. Moreover, both fiber types can be entrained into firing rates that are comparable to those resulting from electrical stimulation (Krauthamer and Crosheck, 2002), with myelinated axons showing a much higher upper limit (FR > 1 kHz) than their unmyelinated counterparts (FR < 180 Hz). The latter finding must be interpreted with caution, as the SENN myelinated axon model ignores subtle spiking adaptation phenomena and hence probably overestimates the physiological limit of the myelinated axon's firing rate. Importantly,

robust neuromodulatory effects can be obtained with both fiber types at relatively low duty cycles (DC < 50%) that prevent significant tissue heating. Together, these predictions define a comprehensive theoretical basis that can guide the design of US neuromodulation protocols.

4.5.1 Applicability of the SONIC paradigm in multi-compartmental models

The SONIC paradigm relies on the assumption that membrane charge density and ion channel kinetics evolve at a much slower speed than microsecond-scale capacitance oscillations, thereby allowing for the accurate integration of neural responses using pre-computed cycle-averaged quantities of fast-oscillating variables. While that assumption is valid for point-neuron models (Lemaire et al., 2019), a recent study using a nanoscale two-compartment model have shown that under tight axial coupling conditions, strong intracellular currents mediate a significant intra-cycle charge redistribution that influences local membrane dynamics in a way that is not captured by the SONIC paradigm, resulting in overestimated sub-threshold charge build-ups and underestimated excitation thresholds (Tarnaud et al., 2020). It was also demonstrated that this numerical inaccuracy could be resolved by taking into account a limited number of Fourier components from precomputed oscillatory variables (as opposed to the SONIC approach that only considers their first component). Those findings raise legitimate concerns about the applicability of the SONIC paradigm in multi-compartmental models and prompted us to examine the conditions of its applicability, and whether it can be accurately used with the axon models of this study.

First, using a generic passive benchmark, we showed that SONIC accuracy is impacted by both intrinsic model properties and stimulus features, but also that this paradigm shows robust convergence if the underlying (membrane and axial) time constants of the considered neuron model are longer than the stimulus periodicity. Second, using axon-specific benchmarks, we demonstrated that the SONIC paradigm can accurately compute passive and active neural responses of both axon models of this study, across a vast majority of the LIFUS parameter space.

In the case of the unmyelinated axon, the axial time constant is a direct product of the spatial discretization of a continuous membrane ($\tau_{ax} = C_{m0}\rho_a \frac{L^2}{D}$, with L the compartment length). Hence, for small enough compartments, this time constant may become smaller than the stimulus periodicity and therefore sensitize the electrical system to intra-cycle variations. However, increasing the model resolution would also eliminate the spatial gradient in acoustic pressure across consecutive compartments, effectively eradicating the axial currents at the origin of SONIC divergence. In fact, the selected compartment length in this study (see Methods section) is in the order of 10^{-2} mm, i.e. already two orders of magnitude smaller than millimeter-scale pressure field variations.

Whether SONIC convergence can extend to other morphological models remains an open question, in particular as neurons of the CNS have a much slower membrane dynamics than peripheral axons (membrane time constants in the order of tens of milliseconds (Pospischil et al., 2008)) but possess tightly connected and heterogeneous morphological sections that may induce significant axial charge redistribution. In this case, a more computationally taxing approach considering extended Fourier decomposition might be required to achieve an acceptable level of accuracy.

4.5.2 Generalizability of the morphoSONIC framework

Due to its intrinsic mechanoelectrical coupling, the NICE model is inherently tedious to simulate. In fact, capacitance oscillations induced by the mechanical membrane resonance introduce a high frequency capacitive displacement current ($I_C = V_m \frac{dC_m}{dt}$) that greatly increases the associated numerical stiffness. We first observed that this stiffness could be reduced by recasting the differential system in terms of charge density (Lemaire et al., 2019). This strategy has since been employed in another study

implementing the NICE model (Tarnaud et al., 2020), and is also at the core of the SONIC paradigm. Unfortunately, neither time-varying capacitance nor charge casting are natively supported by standard neuronal simulation environments such as NEURON. Consequently, computational studies on intramembrane cavitation have been implemented in custom software (Matlab or Python) and restricted to single and two-compartment models, partly because sub-optimal integration routines yield exorbitant simulation times and / or numerical instabilities for larger models.

Here, we derived a hybrid (charge and voltage casted) variant of the cable equation that is numerically reconcilable with both the NICE and SONIC paradigms and implemented it as an independent module that can be seamlessly integrated within the NEURON simulation environment. As such, the proposed approach provides a general solution to the problem of time-varying capacitance that is applicable to a wide variety of model types (single and double cable) and morphological structures (compartment number, branching patterns) seen across the central and peripheral nervous systems. Notably, this approach could also be used with enriched membrane mechanisms including lookup tables for additional Fourier components, as in (Tarnaud et al., 2020). Moreover, the choice of a NEURON-based implementation offers several advantages. First, it leverages NEURON's optimized numerical integration pipelines while offering an appreciable abstraction level to the underlying differential systems. Second, it is applicable to a wide collection of biophysical models – as well as other resources – made available by the NEURON community (McDougal et al., 2017) with limited adaptation effort. Finally, although it has been used here with Gaussian field distributions approximating analytical solutions to simple physical problems, the morphoSONIC framework can easily be combined with finite-element-method (FEM) approaches. This refined multi-scale approach would enable the coupled simulation of complex acoustic propagation, pressure field distribution, and resulting neuronal responses inside anatomically accurate inhomogeneous tissue (such as the brain or the nerve environment).

4.5.3 Comparison with empirical findings

As stated before, one of the major findings of this modeling study is that short US pulses are capable of inducing *de novo* action potentials in both myelinated and unmyelinated peripheral axons. This modeling prediction is in agreement with experimental observations from two recent studies showing that *in vivo* sonication of the mouse intact sciatic nerve directly activates myelinated fibers to induce motor responses (Downs et al., 2018), and that *ex vivo* sonication of unmyelinated crab leg nerve bundles generates compound action potentials (Wright et al., 2017). Interestingly, these studies reported significantly higher excitation thresholds (3.2 MPa and 1.8 MPa peak pressures around the fiber location for myelinated and unmyelinated axons, respectively) than the ones predicted here. Such differences could potentially arise from the intrinsic embedding of fibers within the neural tissue, increasing viscoelastic stresses on the membrane, and therefore hindering its mechanical resonance to acoustic perturbations (Krasovitski et al., 2011), a phenomenon that was not considered here. In fact, active neural responses in the extracted crab leg nerve bundles coincided with the presence of inertial cavitation in the surrounding medium, which may indicate higher thresholds for intramembrane cavitation in this specific environment. Nonetheless, considering that both studies employed minimal stimulus durations that fall within the fibers predicted rheobase regimes (4 ms and 8 ms for the myelinated and unmyelinated cases, respectively), the lower relative range of reported excitation thresholds for unmyelinated fibers corroborates our modeling predictions. Moreover, shorter response latencies were observed in myelinated fibers ($\Delta t < 1$ ms) than in unmyelinated fibers ($\overline{\Delta t} \approx 3.2$ ms), which is also in agreement with our findings. Significant variability in success rate and response latency was observed in the *ex vivo* crab leg nerve preparation, which is a departure from the deterministic nature of single fiber responses predicted by our current model. Nevertheless, the similarities in qualitative behavior between our theoretical results and these empirical observations provide a first indication that intramembrane cavitation could be a physiologically relevant US neuromodulation mechanism also in

the peripheral nervous system. A more definitive answer to that question will require further experimental investigations, including a thorough comparison of excitation thresholds across fiber types and diameters within the same nerve environment and across a wide range of pulse durations and acoustic beam widths.

4.5.4 Therapeutic implications

Beyond mechanistic investigation, our findings further emphasize the potential of LIFUS as a noninvasive neuromodulation technology and its applicability to peripheral structures. In fact, we predict that LIFUS can be used to robustly modulate the spiking activity of both myelinated and unmyelinated fibers, meaning that it could be used to encode sensory information or elicit motor responses. In this context, the lack of clear dependency of LIFUS excitation thresholds on fiber diameter represents a disadvantage, as it excludes the possibility to discriminate across different populations of myelinated fibers and, hence, to target a specific peripheral pathway. However, the ability to selectively target unmyelinated C-fibers, which carry pain and temperature afferent signals, ushers in the possibility to encode new types of sensory information in artificial limbs without interfering with other haptic, i.e. tactile (Petrini et al., 2019; Raspopovic et al., 2014; Valle et al., 2018) and proprioceptive (D’Anna et al., 2019), modalities. To the best of our knowledge, this feature has never been achieved with standard electrical stimulation techniques. The encoding of temperature information would be particularly interesting to enrich the sensory feedback in neuroprosthetic devices and improve user experience (Mendez et al., 2020).

4.6 Conclusion

In this study, we present a novel computational framework to investigate the mechanisms of US neuromodulation by intramembrane cavitation in morphologically realistic neuron models, using the NEURON simulation environment. The new framework is used to predict cell-type-specific responses of myelinated and unmyelinated peripheral axons to acoustic pressure fields. These predictions are in qualitative agreement with recent empirical observations, and open new avenues for the use of US as a neuromodulation technology in the peripheral nervous system. Yet, closer quantitative comparison with experimental data will be necessary to further validate or reject the underlying mechanism. Furthermore, we plan to couple our modular framework with acoustic propagation models to formulate more detailed predictions of neural responses upon sonication by realistic acoustic sources and to inform the development of application-specific ultrasonic devices.

Chapter 5 Confrontation to the experimental setting

Chapter 2 introduces the NICE model, an electromechanical model formulating the hypothesis that ultrasound neuromodulatory effects are mediated – at least partially – by intramembrane cavitation. Chapters 3 and 4 deal with computational investigations to improve the efficiency, interpretability and scalability of the NICE model. Yet, despite their intrinsic value, these investigations remain purely theoretical, and do not provide definite answers about the validity of the underlying biophysical hypothesis.

This chapter presents an attempt at confronting the accumulated modeling predictions to empirical data, and from a more collective standpoint, an effort to elucidate the cellular mechanisms of ultrasound neuromodulation in the experimental setting. To this aim, investigations were carried out on a tractable invertebrate model, the medicinal leech (*Hirudo medicinalis*), that has been heavily used in neurophysiological investigations. Intracellular electrodes were used to record voltage responses of anatomically and functionally identified sensory neurons during ultrasound (and alternatively electrical) stimulation, with the goal of identifying nominal response features and comparing them to modeling predictions.

This empirical investigation – a collective effort led by Dr. Francesca Dedola – constitutes a parallel contribution presented in this thesis.

Sections 5.1 to 5.4 of this chapter are adapted from the manuscript by *Dedola, F., *Severino, F.P.U., Meneghetti, N., **Lemaire, T.**, Cafarelli, A., Ricotti, L., Menciassi, A., Cutrone, A., Mazzoni, A., and Micera, S, “Ultrasound Stimulations Induce Prolonged Depolarization and Fast Action Potentials in Leech Neurons” published in IEEE Open Journal of Engineering in Medicine and Biology 1, 23–32 (2020).

Personal contributions as third author: proposed the experimental setup, designed the experimental protocol, participated in experiments, contributed to writing the manuscript (introduction and discussion).

Section 5.6 provides a more contextual interpretation of the results within the development of this thesis, and the confrontation of empirical data to modeling predictions.

Ultrasound stimulations induce prolonged depolarization and fast action potentials in leech neurons

*Francesca Dedola¹, *Francesco Paolo Ulloa Severino², Nicolò Meneghetti¹, Théo Le-maire³, Andrea Cafarelli¹, Leonardo Ricotti¹, Arianna Menciassi¹, Annarita Cutrone¹, Alberto Mazzoni¹, Silvestro Micera^{1,3}

¹The Biorobotics Institute, Scuola Superiore Sant'Anna (SSSA), Pisa, Italy

²Neuroscience Area, International School for Advanced Studies, Trieste, Italy

³Translational Neural Engineering Laboratory, Center for Neuroprosthetics and Institute of Bioengineering, School of Engineering, École Polytechnique Fédérale de Lausanne (EPFL), Lausanne, Switzerland

5.1 Abstract

Objective: Ultrasound (US) stimulation carries the promise of a selective, reversible, and noninvasive modulation of neural activity without the need for genetic manipulation of neural structures. However, the mechanisms of US-induced generation of action potentials (APs) are still unclear. Here we address this issue by analyzing intracellularly recorded responses of leech nociceptive neurons to controlled delivery of US. **Results:** US induced a depolarization linearly accumulating in time and outlasting the duration of the stimulation. Spiking activity was reliably induced for an optimal US intensity range. Moreover, we found that APs induced by US differ in smaller amplitude and faster repolarization from those induced by electrical stimulation in the same cell but display the same repolarization rate. **Conclusions:** These results shed light on the mechanism by which spikes are induced by US and pave the way for designing more efficient US stimulation patterns.

5.2 Introduction

Ultrasound (US) stimulation is an efficient mean to interact noninvasively with the human body. Beyond its conventional use as an imaging modality (Tanter and Fink, 2014), US is now also applied for therapeutic interventions such as ablation therapies and blood-brain barrier reversible opening for drug delivery (Escoffre and Bouakaz, 2016). Such applications rely on the specific nature of acoustic waves that can be accurately steered through biological tissue, offering the ability to concentrate acoustic energy within small volumes ($\sim\text{mm}^3$) around deep anatomical targets (Kyriakou et al., 2014).

Low-intensity low-frequency ultrasound (LILFU) can elicit APs in ex-vivo mouse brain and hippocampal slice cultures (Tyler et al., 2008). US neuromodulatory effects have been recently studied on various neural targets (Fomenko et al., 2018) with a clear translation path from ex-vivo preparations (Kubanek et al., 2016; Tyler et al., 2008; Wright et al., 2017), to animal models (Gulick et al., 2017; Juan et al., 2014; Kim et al., 2012, 2015; King et al., 2013; Kubanek et al., 2018; Lee et al., 2016a, 2015b) including non-human primates (Deffieux et al., 2013; Wattiez et al., 2017; Yang et al., 2018), and human subjects (Lee et al., 2015a, 2016b, Legon et al., 2014, 2018b, 2018a; Mueller et al., 2014).

However, while the ability of US to modulate neural activity has been extensively confirmed, discrepancies remain about the exact influence of each stimulation parameter (carrier frequency f_c , peak pressure amplitude, stimulation duration, pulse-repetition frequency and duty cycle (DC)) on neural activity, and behavioral responses. Hence, despite a decade of intense investigation, the underlying mechanism of action by which US triggers neuronal excitation/inhibition is still unclear and a predictive model relating the effects on neurons with the US parameters is missing.

Here, in order to tackle these issues, we investigated neural responses to controlled US in a simple nervous system: the medicinal leech (*Hirudo medicinalis*). This invertebrate model can generate a broad range of behaviors (Garcia-Perez, 2007; Mazzoni et al., 2005), but possesses a simple nervous system that can be easily accessed to extract individual ganglia, the anatomical organization of which is highly conserved across specimens (Muller, 1981). Neurons within a ganglion are functionally characterized and identifiable by their position, size, and electrophysiological profile (Kristan et al., 2005; Titlow et al., 2013), and offer very reliable responses to electrical (EL) stimulation. Finally, it is possible to record viable neural responses from an isolated ganglion for extended periods of time (Titlow et al., 2013).

Using this animal model, we systematically explored the US parameter space and recorded direct individual neural responses in isolated leech ganglia, in a controlled environment where the number and influence of external factors was kept to a minimum. We aimed at identifying relevant acoustic parameters governing neural responses, evaluating excitation thresholds, and comparing obtained spike waveforms with that of EL evoked spikes. We focused our analysis on nociceptive (N) mechanosensory cells that exhibit a robust and well-characterized response to EL stimulation, and whose characteristics are predominantly due to the abundance on the membrane of Na⁺ channels, which have been recently indicated to be influenced by US (Kubanek et al., 2016).

5.3 Results

We developed a setup (**Figure 33a-d**) to stimulate cells with ultrasound from isolated leech ganglia (**Figure 33b-c**). We analyzed responses of N mechanosensory neurons to US (see Materials and Methods and **Figure 33e** for details) comparing them to the responses to EL stimulation. We first analyzed US-induced subthreshold depolarization, then US-induced firing activity, and finally US-induced AP characteristics were compared with those of EL triggered spikes.

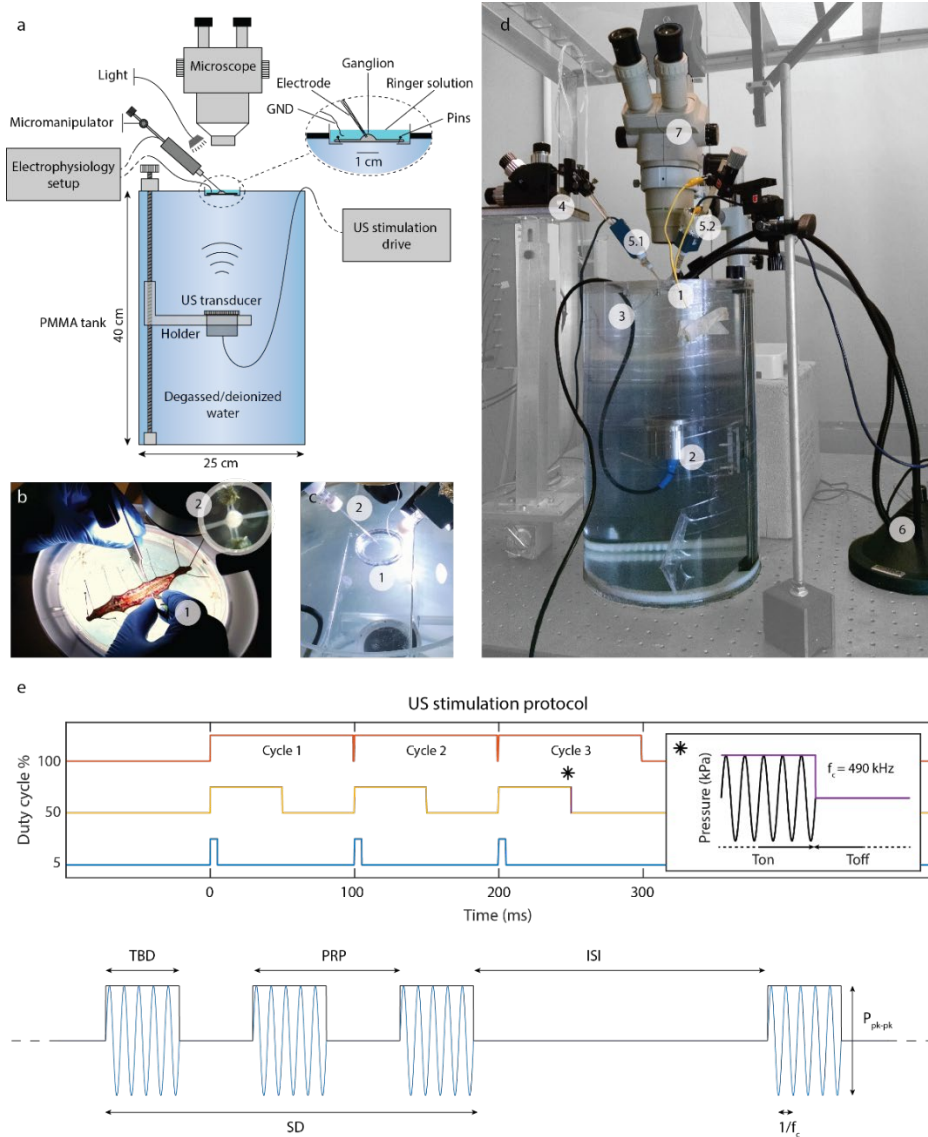


Figure 33. Experimental setup. a) Illustrative scheme of the setup. b) Leech dissection and ganglia chain exposition (1). On the top right corner, a detail of the extracted leech ganglion pinned onto the PDMS substrate (2). c) Focus on the Petri dish with a pinned ganglion (1) and the glass capillary containing the Ag/AgCl electrode for intracellular recording (2). d) The Petri dish with the pinned ganglion was positioned on top of the experimental setup (1). The setup included a US transducer (2) immersed in a tank (3) full of degassed deionized water used for US, and an electrophysiology setup. A micromanipulator (4) allows for fine positioning of the electrodes on ganglion surface. In this configuration two electrodes (5.1 - 5.2) are connected to the electrophysiology setup for recording. A light source (6) and an optical microscope (7) are used for cell identification and impalement. e) Temporal protocol of US: DC 5% (blue), T-on is 5 ms, T-off 95 ms; DC 50% (yellow), T-on 50 ms, T-off 50 ms; DC 100% (brown), T-on 100 ms. The tone burst duration is equal to T-on in case of pulsed stimulation and the pulse repetition period (PRP) is 100 ms; the stimulation duration (SD) is of 300 ms for the 3 temporal protocols. Each stimulation (SD 300 ms) is repeated 3 times during a recording session with an inter stimulation interval (ISI) of 20-30 s. In the inset, temporal evolution of US (violet); transducer central frequency is 490 kHz.

5.3.1 Subthreshold responses to US stimulation

We delivered low-intensity, 490 kHz US in blocks of 3 stimuli of 100 ms each, with a DC of 5, 50 or 100% (continuous stimulation, all reported in **Figure 33e**) and a root mean square pressure (P_{rms}) of 8, 12, 16 or 20 kPa (see Materials and Methods for details). The spatial mapping of the pressure within the acoustic field was measured using a hydrophone and the P_{rms} was evaluated in the Petri dish containing the pinned ganglia (**Figure S2** and **Figure S3**). The response and baseline intervals were defined respectively as the on-state of the stimulation (tone burst duration) and an interval of the same duration preceding the stimulus onset (**Figure 34a**). Note that the US-induced depolarization outlasted

the tone burst duration for pulsed protocols and the duration of continuous stimulation (Figure 34a). Post- and pre- stimulus membrane voltages were compared (Bi, Figure 34a); increase in the membrane potential associated to the stimulus depended on both pressure and DC, but not on their interaction (two-way ANOVA, $p=0.0272$, $p<0.0001$, $p=0.32$ respectively) (Figure 34b). For EL triggers, membrane potential during the 100 ms post-stimulus time was lower than the pre-stimulation level, in stark contrast to what observed for US (Figure S1).

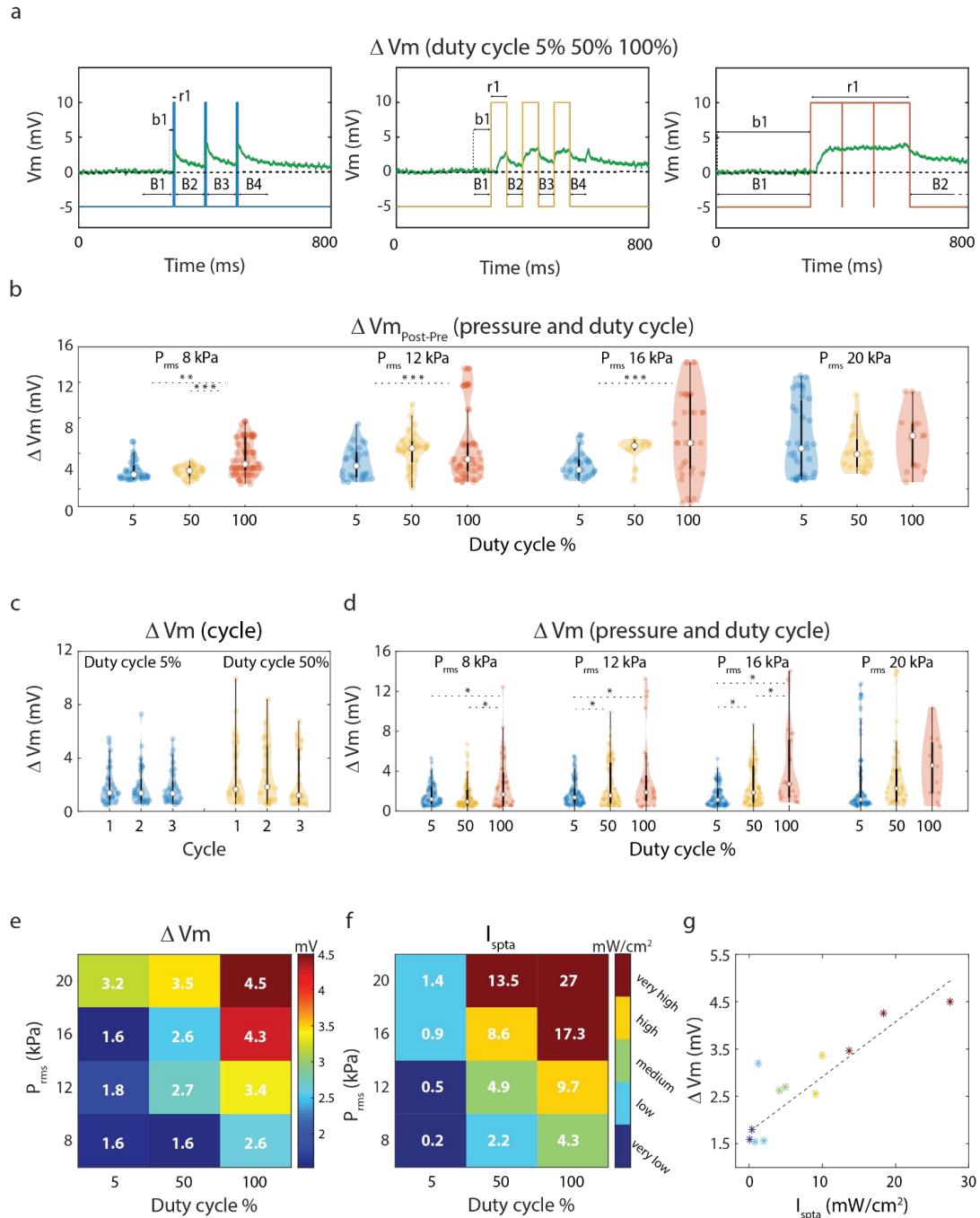


Figure 34. US parameters and membrane depolarization. a) Definition of response and baseline interval for each DC; in case of 100% DC, baseline and response time interval is 300 ms; in case of 5% and 50% DC, baseline and response duration are equal to tone burst duration for each cycle. The membrane potential variation ΔV was defined as the difference between the membrane potential median value during stimulus onset (r1 in the figure) and its median value during the preceding baseline (b1 in the figure). b) Violin plot (Hintze and Nelson, 1998) of baseline variation, defined as the difference between membrane potential pre and post stimulus onset (median B_{i+1} - median B_i), for each pressure amplitude and DC (95 ms at DC 5 %, 50 ms at DC 50 %, 300 ms at DC 100 %). Asterisks indicate post-hoc significant inter-DC differences ($p<0.05$). c) Membrane voltage variation over the three cycles at DC 5% and 50% for pressure 12kPa. d) Membrane potential variation

for each pressure amplitude and DC. e) Median membrane voltage variation for each stimulation protocol setting. f) Stimulation intensity for each experimental protocol. g) Median membrane potential response as a function of the intensity. Color code in f) and g) indicates intensity binning: I_{spta} is binned into five groups: very low $\leq 0.5 \text{ mW/cm}^2$ < low $\leq 2.5 \text{ mW/cm}^2$ < medium $\leq 5 \text{ mW/cm}^2$ < high $\leq 10 \text{ mW/cm}^2$ < very high, with respectively 101, 110, 108, 97, 73 recorded traces.

We also checked whether the membrane potential response to US stimulation (ΔV), defined as the negative difference between the median membrane potential during baseline and its value during the interval with tone burst stimulation (**Figure 34a**), was different across the three consecutive stimulation cycles for 5 and 50 % DC. We found that there was no significant inter-cycle difference in the response for fixed value of pressures. For instance, for 12 kPa (see **Figure 34c**) a two-way ANOVA failed to detect a significant difference in the response across the cycle numbers ($F=0.38$, $p=0.68$) as well as a significant effect of the cycle number x DC interaction ($F=0.17$, $p=0.85$), while there was a significant difference among the DCs ($F=7.19$, $p=0.0082$). Similar results were obtained for all pressure levels (results not shown). Consequently, in the following analysis we will always consider the average response amplitude over all cycles.

The relationship between the stimulation features and the peak membrane potential depolarization was then investigated for the various combinations of pressure and DCs. The membrane potential depolarization response ΔV was found to increase with both DC and pressure parameters (**Figure 34d-e**). This is coherent with the fact that during each stimulation the effect of US on the membrane potential is integrated over time (see for instance **Figure 34a**). A two-way ANOVA with factors DC and P_{rms} detected a significant difference in ΔV across different DCs ($p \ll 0.0001$) and pressures ($p = 0.0002$), as well as for the DC x P_{rms} interaction ($p = 0.021$) (**Figure 34b**).

To measure the total acoustic exposure, taking into account the pulsed protocol, the spatial-peak temporal-average Intensity (I_{spta}) for each stimulation was then computed as

(110)

$$I_{spta} = \frac{P_{rms}^2}{\rho c} DC$$

where ρ and c are approximated to the density and the speed of sound of the water (see the experimental setup in **Figure 33**). It was found that membrane depolarization ΔV associated to US grew linearly with I_{spta} ($R^2=0.78$, $p=0.0001$, **Figure 34g**).

We concluded that the US triggered sub-threshold membrane potential depolarization did not depend simply on the temporal peak stimulation intensity but rather on its integral over time: the effects of the stimulation accumulate linearly. In the following sections, we consider the effect of the stimulations only as a function of I_{spta} .

5.3.2 Spiking activity in response to US stimulation

A key experimental result of our work is that US induced spiking activity in 27 over the 44 recorded N cells (see a representative recorded trace in **Figure 35a**). In order to compare the different spike-triggering mechanisms we alternated US and EL stimulations able to induce firing activity (**Figure 35b**). Note that the latency was longer for US than for EL stimulation, coherently with our hypothesis of a cumulative effect of US, as if the accumulation of the effect over time required to trigger the action potential determined the latency. Coherently with results in **Figure 34**, the success rate (spike elicitation probability) averaged over all neurons depended on both pressure and DC: a two-way ANOVA with factors DC and pressure detected a significant difference between the DCs ($F=6.02$, $p=0.003$) as well as the pressures ($F=2.84$, $p=0.039$), but only a tendency toward DC x pressure interactions ($F=6.18$, $p=0.082$). Indeed, the stimulation success rate was proportional to the intensity ($R^2=0.36$,

$p=0.0442$, **Figure 35c**). Analysis of the spiking activity in the intervals preceding and following the stimulation showed that success rate was always higher than at baseline not only during the stimulation, but also in the following hundreds of ms (**Figure S4**), highlighting the presence of a long-lasting effect of US on spiking activity. Spiking activity during stimulation steadily increased with stimulation intensity ($R^2=0.96$, $p<0.01$) and a similar, although not significant, trend was observed for post-stimulation activity ($R^2=0.59$, $p=0.09$).

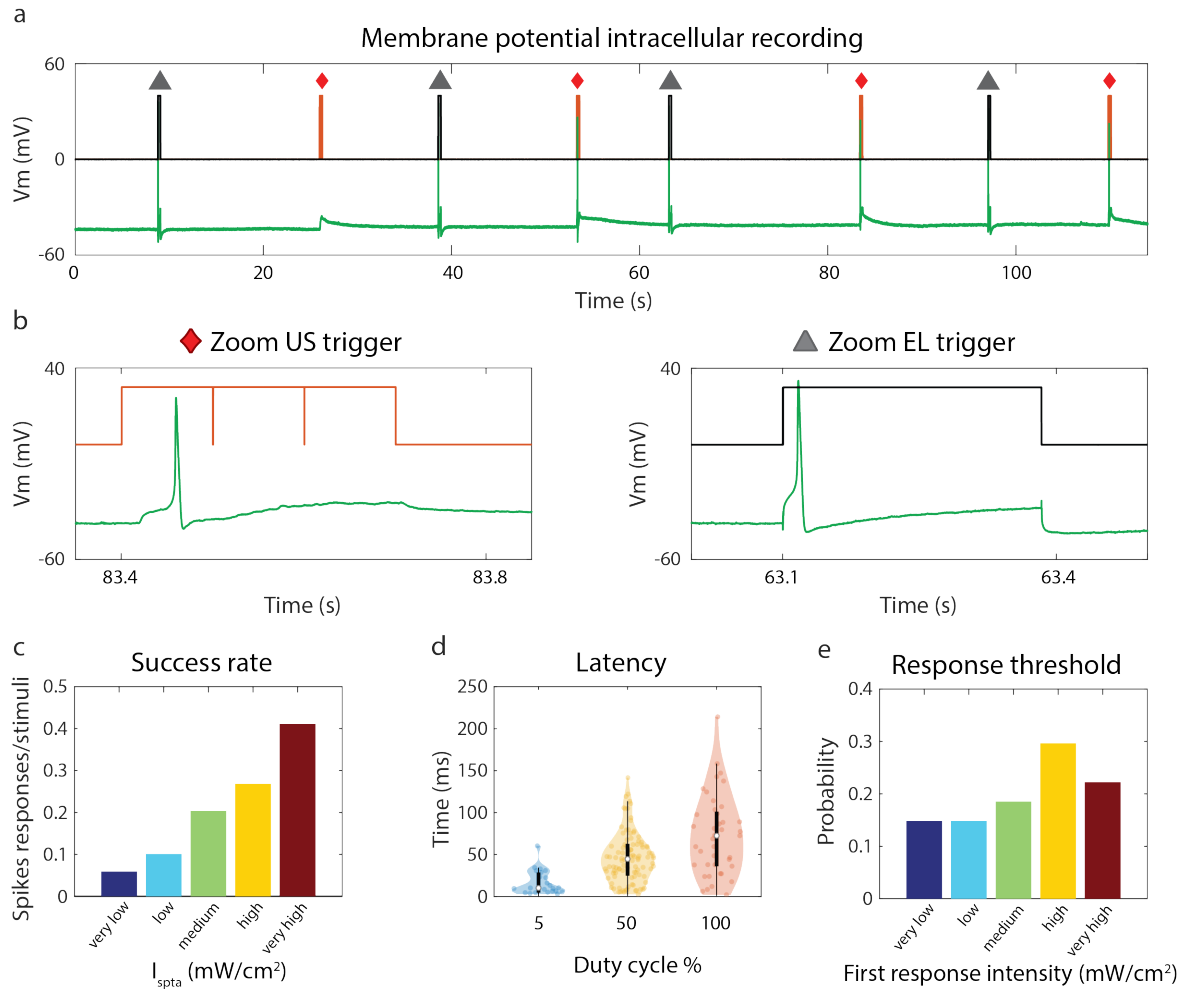


Figure 35. US parameters and firing activity. a) Example of N cell intracellular membrane potential (green) during US (red diamond) or EL (grey triangle) stimulations. Red line indicates US trigger. Black line indicates EL stimulation trigger. The response to EL stimuli is recorded to compare the spikes characteristics with the US induced and to verify cell health. A time interval of 20-30 s between consecutive stimulations allows the cell to recover. b) Zoom of the US trigger signal (red) and the EL triggered signal (black); recorded membrane potential (green). c) Success rate as a function of the intensity, binned into 5 groups. The considered spike detection time window for each stimulation lasted 400 ms from the stimulus onset (stimulus duration of 300 ms + 100 ms post stimulation). d) Distribution of latency as a function of DC of all US-triggered spikes. e) Distribution across neurons of intensity associated to the first response. Intensity ranges are defined as in Fig. 2f: very low $\leq 0.5 mW/cm^2$ < low $\leq 2.5 mW/cm^2$ < medium $\leq 5 mW/cm^2$ < high $\leq 10 mW/cm^2$ < very high.

Another important result came from the latency analysis, measured as the time delay from the tone burst onset to the AP peak. We found that the median of latency distributions increased with the DC (**Figure 35d**), and the most likely value was close to the duration of the tone burst in case of 5% and 50% DC. This is coherent with the fact that the membrane potential grows monotonically during US stimulation, and consequently the highest probability of firing is at the end of the stimulation. Indeed, a shorter duty cycle was associated to a smaller fraction of responding neurons (**Figure 35c**) due to the smaller depolarization associated to the lesser cumulative effect. In other words, when we increased the duty cycle we triggered a far larger number of cells, but all the cells that responded only

with the longer duty cycle will respond at the end of the duty cycle, hence shifting the latency distribution toward larger values. In case of 100% DC the latency was always shorter than stimulation duration, probably because a saturation effect was reached. These results again indicate that the effect of US accumulate over time.

Interestingly, the latency distributions confirmed that a large fraction of spikes was fired after the end of tone bursts indicating that US can induce long lasting effects even tens of ms after its end. This highlights a key difference with EL-triggered spikes, whose peak occurred immediately after current onset as expected (**Figure 35a**, **Figure S1a**).

We also computed the minimal intensity required to elicit spiking activity across all neurons. The resulting distribution showed a maximal probability at moderately high intensities (**Figure 35e**). Several cells indeed exhibited sufferance in the range we labeled as ‘very high’. This suggests that for each cell there might be an intrinsic intensity dependent activation threshold and a higher intensity sufferance threshold; however, there is large variability among tested cells.

We wondered if mechanosensitivity was a sufficient condition to have US-triggered APs. We stimulated then another kind of leech mechanoreceptor, the P cells ($n=23$, see Materials and Methods for details), which is physiologically sensitive to lighter stimuli than the N cells. We found that the membrane potential response was linearly correlated with the intensity of the stimulus also for P cells, ($R^2=0.74$, $p=0.0007$, **Figure S5a**), but such responses were much smaller than those elicited by the same intensities in N cells (paired t-test $p=0.0001$, **Figure S5b**). Due to this weak sensitivity of the membrane potential to US, the occurrence of action potentials was a very rare event ($n=6$ out of 222 stimulations, **Figure S5c**). This shows that, notwithstanding the common function and the presence of mechanosensitive channels in both kind of cells, N cells displayed a significantly stronger sensitivity to US than P cells.

5.3.3 Comparison between US- and EL-induced APs

We established that US is able to modulate membrane potential and trigger APs. To further characterize the specific effect of US, we compared with the same set of stimulations used in the previous section the shape of the APs triggered by US ($n=166$ spikes) and EL ($n=155$ spikes) stimulations. As previously observed (**Figure 34a-b**), US produced long lasting effects on membrane voltage. We thus focused on fast transient characteristics, i.e. AP amplitude and duration, respectively defined as the voltage difference between AP peak and the subsequent minimum, and the duration of the decaying phase at half amplitude, referred as early re-polarization phase (**Figure 36a**).

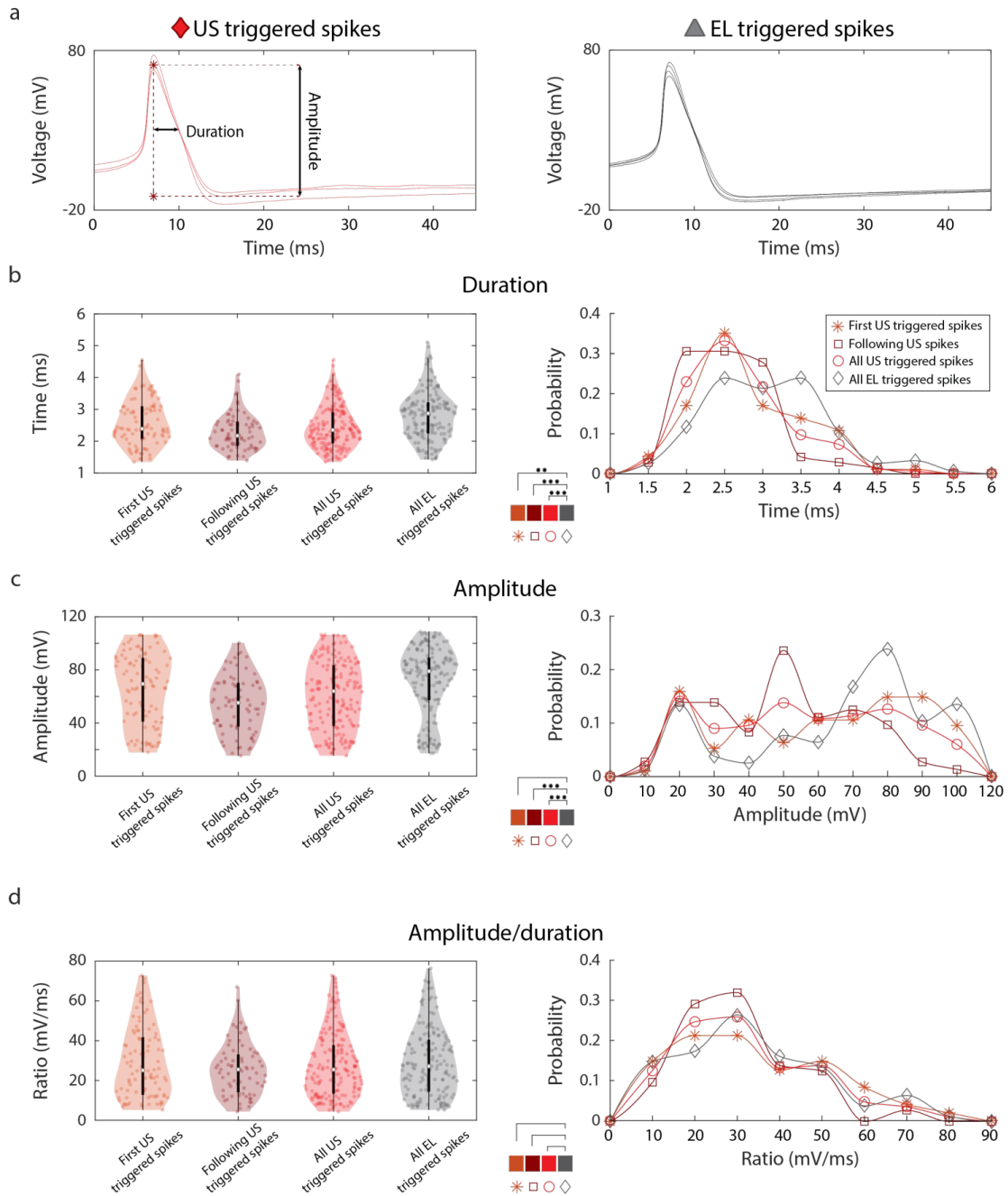


Figure 36. AP features in US and EL stimulation. a) Shape of APs triggered by US (left 5 spikes) and EL (right 3 spikes) stimulation extracted from the trace in Fig. 3a. Left US plot shows definitions of amplitude (from peak to subsequent minimum value) and duration of early repolarization (width at half amplitude of declining phase). b) Left: median, interquartile range and dispersion of first spikes triggered by US (orange), following spikes triggered by USs (brown), the union of the two sets (red), and spike triggered by EL stimulation (grey). Right: comparison between the probability distributions of the durations of the different sets of spikes. Subplot in the center indicates significant differences between distributions. c) Analysis of the distributions of the amplitudes of the four spike categories defined in b). d) Analysis of the distributions of the amplitude/duration ratios of the four spike categories defined in b).

The first APs triggered by US on each stimulus window ($n=94/166$ spikes) and the following were analyzed separately to check for possible memory-effects of US; first-triggered APs do not always correspond to first US stimulus (tone burst during stimulus nor first stimulus on recorded trace). The total dataset of US triggered APs showed significantly shorter duration (2.35 ± 0.45 ms) compared to EL triggered APs (2.87 ± 0.7 ms, KW test, $p = 6 \cdot 10^{-6}$) (**Figure 36b**). We observed that duration of the early repolarization phase of following US triggered APs (2.17 ± 0.4 ms) was shorter than that of first US trig-

gered APs (2.39 ± 0.5 ms, KW test, $p=0.014$). Considered separately, durations of both first and following US triggered APs were significantly shorter than those of EL triggered APs, also with statistically significant differences (respectively $p=0.01$ and $p=4 \cdot 10^{-7}$ KW test). Significant differences were also observed when comparing AP amplitudes (**Figure 36c**). Overall the total dataset of US triggered APs (64 ± 45 mV) showed a significantly smaller amplitude compared to those of EL triggered APs (79 ± 15 mV, $p=1 \cdot 10^{-4}$). The amplitude of the following US triggered APs (55 ± 16 mV) was lower than that of first US triggered APs (70 ± 47 mV), with a statistically significant difference (KW test $p=0.01$). Taken separately, both first and following US triggered APs were significantly smaller than EL triggered APs, although statistically significant difference was only found for the latter comparison (respectively $p=0.14$ and $p=4 \cdot 10^{-7}$). Note that also these differences in AP shape could be associated to the 'long lasting effect' of US compared to the EL (see Conclusions).

We further investigated spiking responses to US taking into account not only the dimensions, but also the shape of the APs, comparing the ratio between amplitude and duration of the AP, which is proportional to the slope of the decay phase of the APs (**Figure 36d**). Interestingly, and coherently with the fact that both amplitude and duration were found to have higher values for EL triggered than US triggered APs, we found that the ratio follows the same trend and belongs to the same distribution. We found no statistically significant difference between the ratios of EL triggered APs (27.4 ± 12 mV/ms) and US triggered APs (25.6 ± 11.5 mV/ms, KW test, $p>0.5$). Moreover, there was no difference between first (25.5 ± 13 mV/ms, KW test, $p>0.5$), and following US-triggered spikes (25.7 ± 9 mV/ms, KW test, $p=0.26$).

5.4 Discussion

Despite the increasing amount of research on the effects of US stimulation on the nervous system, the biophysical dynamics underlying the generation of AP following US stimulation is still unclear. Several small animal models have been used to test US stimulation thanks to the possibility to perform experiments in a very controlled context. We selected the leech *Hirudo Medicinalis* for our studies as it is a consolidated neurophysiological model suitable for the analysis of such complex mechanisms. Moreover, the isolated leech ganglion preparation (**Figure 33**) was found to be suited for performing intracellular recording during US stimulation.

We have shown that US has a direct depolarization effect and elicits spiking activity in leech N neurons. Our work is the first study establishing useful guidelines for US stimulation of excitable cells, showing that the induced activity depends on the applied acoustic I_{spta} (**Figure 34** and **Figure 35**).

More in detail, it was demonstrated that the effects of US leading to increased membrane depolarization for higher pressure amplitude and increasing DC can be summarized by the I_{spta} (**Figure 34f**), and that this metrics linearly modulates sub-threshold depolarization (**Figure 34g**) and is proportional to spike probability (**Figure 35c**). Crucially, sonication produced long lasting effects on membrane voltage (**Figure 34a-b**), leading to increased spiking activity outlasting the stimulation (**Figure S5**, **Figure 35d**).

These results also establish well-defined relationships between US driving parameters and ensuing spiking activity, which might be useful in the design of future experiments. In particular, while duty cycle duration and intensity can be independently modulated, all that matters seem to be their product. This can have practical consequences, as choosing to achieve a given response by doubling the intensity (if a fast response is needed) or by doubling the stimulus duration (to avoid damages to the cell).

Finally, US- and EL-triggered spiking activity were compared by considering fast transient characteristics, i.e. the amplitude and early repolarization duration of the AP. Interestingly, we found that US-induced APs differ from EL-induced ones both in amplitude and early repolarization duration, but not

in the ratio between these two quantities. The combination of these results suggests that the mechanism inducing spikes in the two cases may involve the same ion channels as the waveform shape is preserved. First US triggered APs amplitude is higher than the following ones, probably as a consequence of the residual depolarization effect produced by the sonication.

Several works suggest that US acts on voltage gated ion channels (Kubaneck et al., 2016; Muratore et al., 2009, 2012; Tyler et al., 2008). However, the exact dynamics of this interaction is still unclear. Leech N neurons exhibit standard AP dynamics, with a Na^+ -driven depolarization phase followed by a slow K^+ -driven repolarization phase (Stewart et al., 1989). The fact that US-triggered APs show qualitatively similar waveforms to those of EL-triggered APs (**Figure 35b**) with quantitatively similar repolarization rates (**Figure 36d**), likely indicates that upon sonication, both Na^+ and K^+ channels conserve standard kinetics. It is thus unlikely that US exerts an indistinct, long-lasting action on these ion channels, as that would rather drive membrane voltage towards a stable plateau potential. Hence, a distinct ion channel population likely mediates our observation of US-triggered sub-threshold depolarization (**Figure 34**). As this depolarization linearly depends on the stimulus intensity but not on its specific temporal pattern of application, we hypothesize that the affected channels exhibit a rather slow temporal kinetics, such as that of mechanosensitive channels that are natively expressed in leech N cells. The hypothesis that US can regulate the activity of mechanosensitive ion channels was previously proposed (Kubaneck et al., 2016). Moreover, the possible long-lasting effect of US on such channels could likely explain the observation of an accumulative depolarizing effect during second and third US stimuli, resulting in a lower amplitude of the APs. The fact that more than 50% of the recorded cells responded with spikes to US suggests a threshold mechanism associated to US stimulus intensity. These results are in accordance with *in vitro* studies (Muratore et al., 2009, 2012), which observed in different regions of rat hippocampal slice cultures that US induced intensity dependent responses, and hypothesized a threshold mechanism and a fatigue effect associated to US stimulus intensity. Moreover, the high variability of responses and success rates observed across recorded cells, similarly as in previous studies (Kim et al., 2015; Lee et al., 2016a; Muratore et al., 2009, 2012), could be explained by different densities of mechanosensitive ion channels expressed in the same cell type. Possible future experiments addressing the identification of the channels affected by US could include patch clamp recordings, gene protein expression and channel silencing.

More specifically, a possible explanation to the different sensitivity to US of P and N cells could lie on the recent finding of frequency specificity of the classes of mechanosensory neurons in the leech (Fischer et al., 2017). In this work the authors find that N cells are effectively low-pass filtering voltage oscillations while P cells act as high pass filters. Therefore, as US-induced membrane potential deflections have slow time scales even when the pulses are short lived (**Figure 34a**), the P cells are not sensitive to this stimulation. Moreover, the integration of the depolarizing effect of the US reported in the subthreshold responses of our paper is in line with a low-pass filter voltage membrane behavior. This finding shows that the temporal scale of the stimulation could also have a strong effect even when the cells show an excellent mechanosensitivity and opens the possibility to selectively modulate different mechanoreceptors according to their specific frequency sensitivity.

The parameter set tested in the present work is limited to three DCs (5-50 and 100%) and four low pressure levels (8-12-16-20 kPa), in accordance with ranges considered safe for human US imaging (Lee et al., 2004). Stimulation center frequency has been set to 490 kHz in accordance with previous studies (King et al., 2013; Kubaneck et al., 2016). Further studies are needed to observe the effect of different stimulation protocols. It is in fact likely that the inhibition and excitation effects could have different thresholds, as the stimulation could be more effective on different types of channels, or membrane proteins, which coexist in the same cell.

We achieved so far only a neurophysiological characterization of the responses associated to US in a specific kind of cells, not only providing another proof that US neuronal activity modulation is possible, but also assessing some operational rules that might apply also to other neuronal populations. We are currently conducting studies on other animal preparations to assess the generality of our research and investigate more deeply ion channel dynamics upon US to further understand the working principle that stands behind US neuromodulation.

This work lays the ground for future studies on ultrasonic stimulation and eventually their use in non-invasive neuroengineering biomedical applications.

5.5 Materials and methods

5.5.1 Animals and preparation

Leeches (*Hirudo medicinalis*) were purchased from Ricarimpex (Eysines, France) and kept at 5°C in tap water dechlorinated by aeration for 24 h. They were dissected in chilled Ringer's solution with the following composition (mM): 115.0 NaCl, 1.8 CaCl₂, 4.0 KCl, 12.0 glucose, 10 Tris maleate, buffered to pH 7.4 with NaOH. A longitudinal incision was performed on the dorso-medial side of the animal to expose the chain of ganglia. Surrounding tissues, including the ventral main blood vessel, were carefully removed without touching the nervous tissues (**Figure 33b**). In parallel, a custom recipient was made by removing via laser cut the plastic bottom of a Petri dish and replacing it with a 25 µm thick US transparent polystyrene membrane (Goodfellow, Huntington, Cambridge, UK), subsequently coated with PDMS (ratio of monomer:curing agent = 5:1); the membrane was cut and removed from the bottom after PDMS polymerization. Finally, a ventral ganglion was extracted, fixed ventral side up on the custom recipient via metal pins located on the roots and connectives, and kept in fresh Ringer's solution (**Figure 33a-c**).

Previous attempts to measure membrane voltage with current clamp recordings evidenced the ability of US to elicit action potentials on CA1 pyramidal neurons (Tyler et al., 2008), and on *Xenopus* oocytes (Kubaneck et al., 2016), but the cell seal during sonication was not stable. The authors postulated then that the resonance of the intracellular electrode was responsible for the ineffectiveness of the experiments at low US frequency. Here we observed instead that electrode instability and subsequent cell leakage could also be caused by the induced relative movement of the cultured cells/oocytes (poor adhesion and fluctuation in the medium) with respect to the substrate and the glass capillaries, originating during US. To overcome this limitation, we applied several counter-measures detailed below. To further verify that cell seal was maintained during US sessions, EL stimuli were applied and cell health was monitored; we observed that the EL response in US-irresponsive cells was not affected by the US stimulus and was preserved after the whole protocol execution. To ensure stable cell seal, we secured the micromanipulator for electrophysiology recordings on a rigid support and decided to record from the intact ganglion stretched and secured through metal pins on a thin PDMS substrate. In order to reduce substrate vibrations due to sonication, we increased the crosslinker concentration from 10:1 to 5:1, obtaining a good stability of the sample during the experimental sessions, as no vibration artifacts were observed on the recorded traces.

5.5.2 Intracellular recordings

Nociceptive (N) cells in the isolated ganglion were impaled by a sharp glass capillary filled with 3 M potassium chloride, containing an Ag/AgCl electrode (input resistance ≈ 10 M Ω) to record intracellular potential and deliver electrical pulses (**Figure 33a**, inset). The ground connection was placed at the border of the Petri dish, immersed in the Ringer's solution. Recorded signals were amplified with Ax-

occlamp-2b amplifiers (Axon Instruments, Foster City, CA, USA), digitized, stored in a personal computer and analyzed with the pCLAMP8 software (Axon Instruments, Foster City, CA, USA). Nociceptive (N) cells and pressure (P) cells of leech ganglion were identified in different sessions under optical microscope and impaled. A total of 47 N and 23 P cells were employed in this study.

5.5.3 Ultrasound and electrical stimulation

US was applied on leech ganglion by using a 44 mm diameter PZT (Lead zirconate titanate) unfocused transducer (Precision Acoustics LTD, Dorchester, UK) immersed in a polymethyl methacrylate (PMMA) tank filled with degassed deionized water, atop of which the recipient containing the ganglion was placed. The transducer was driven by a waveform generator (Agilent 33220A Keysight Technologies, Santa Rosa, CA, USA) in series with a 50 dB gain radio frequency power amplifier (240L, Electronics & Innovation, Rochester, NY, USA). The US beam reached the ganglion (placed at a distance of 165 mm from the surface of the transducer) from the dorsal side. Note that the whole ganglion was within the ultrasound field. Sinusoidal tone bursts at 490 kHz, with pressure amplitude from 8 to 20 kPa were delivered at a pulse repetition frequency (PRF=1/PRP) of 10 Hz, for a total stimulus duration of 300 ms. The duty cycle (DC) was fixed at 5%, 50%, 100% (**Figure 33e**), therefore the spatial-peak temporal-average intensity (I_{spta}) varied from 0.2 to 27 mW/cm² (**Figure 34f**). According to our estimates the displacement of the whole ganglion due to ultrasound waves should be at most 6 μm (Obrienjr, 2007).

Each recording session consisted at least of three identical US windows of 300 ms, and electric pulses were used to generate a single spike in N cells prior and after each US. The US protocol was interrupted if no response to electrical stimuli was observed. The considered spike detection time window for each stimulation lasted 400 ms from the stimulus onset (stimulus duration of 300 ms + 100 ms post stimulation). Electrical stimuli were manually provided with a variable duration (ranging from 0.25 to 1 s) and amplitude (current ranging from 1 to 5 nA).

5.5.4 Ultrasound calibration

The US transducer was characterized in free field conditions both in terms of US pressure field mapping and intensity vs. driven voltage calibration.

The acoustic field was mapped by measuring the generated pressure with a 2 mm PVDF needle hydrophone (Precision Acoustics, Dorchester, Dorset, UK) at different locations, using a three-axis step-by-step motorized positioning frame (XYZ BiSlide, Velmex, Bloomfield, NY, USA). A dedicated LabVIEW program (National Instruments, Austin, TX, USA) allowed synchronization between the wave generator, motors and signal acquisition from an oscilloscope (7034 B, InfiniiVision, Agilent Technologies).

Additionally, the root mean square pressure (P_{rms}) and the spatial peak pulse average intensity ($I_{\text{sppa}} = P_{\text{rms}}^2/(\rho c)$) were evaluated at the experimental distance of 165 mm at different driving voltages, where ρ and c are approximated to the density and speed of sound of water, respectively. The driven voltage was measured at the output of the power amplifier. Spatial peak temporal average Intensity (I_{spta}) was easily derived by multiplying the I_{sppa} and the duty cycle (DC) used in the stimulation protocol.

Finally, in order to consider possible acoustic reflection and attenuation phenomena due to the experiment setup configuration, additional intensity measurements were performed by positioning the hydrophone tip inside the custom recipient used during experiments. Free field and the experimental setup measurements are reported in **Figure S2**; transducer characterization results are reported in **Figure S3**.

5.5.5 Data analysis and statistics

The recorded traces were analyzed with MATLAB R2017b (MathWorks, Inc., Natick, MA, USA). No band-pass filtering was applied to the measured intracellular potential to keep the original waveform for each cell; the considered signal window was de-trended (1st order polynomial function) before the peak analysis. Amplitude and early repolarization duration of the spikes were measured: the amplitude is defined as the difference between the peak voltage value and the subsequent minimum; the early repolarization duration is measured at half prominence in the drop phase of the spike, to avoid the possible artifact on membrane potential due to the stimulation start, which is particularly effective on low amplitude spikes. The threshold for spikes detection was set to 15 mV above baseline; subthreshold spikes were also analyzed.

Statistical significance in spike characteristics differences between US and electrically triggered spikes and subthreshold spike analysis (membrane voltage variation between the three stimulation bursts and the difference for each input pressure among duty cycles) was evaluated using the Kruskal-Wallis one-way ANOVA test. A p-value of 0.05 indicated a significant difference in the analyzed distributions; datasets were plotted with the violin plot method (Hintze and Nelson, 1998), which allows for the visualization of the full distribution of the dataset. Response latency, defined as the time difference between the US stimulus start and the subsequent spike peak event, was also analyzed.

5.6 Perspective: confrontation of model predictions to experimental data

The content of this chapter is adapted from a published study by Dedola et al. (Dedola et al., 2020) that aimed at providing a general characterization of LIFUS neuromodulatory effects at the cellular scale, without focusing on a particular mechanistic hypothesis.

Here, I provide a more detailed interpretation of the presented results in the context of the model developments and validation pursued in this thesis.

5.6.1 Limitations of the experimental approach for model validation

Despite revealing interesting features of LIFUS-evoked depolarization and action potential dynamics, the acquired empirical data did not allow to confirm (or infirm) the relevance of intramembrane cavitation as an ultrasound neuromodulation mechanism. This is due to four main experimental constraints:

- First, the use of intracellular electrodes directly impaling the neuronal membrane is prone to yield recording instabilities, as reported by other groups (Collins and Mesce, 2020; Tyler et al., 2008). In fact, by disturbing mechanically the targeted tissue, LIFUS can cause the recording electrode to resonate, resulting in a loosening of the electrode seal, or even a loss of contact with the recorded neuron. This instability has significantly constrained or parametric exploration of pressure amplitudes: first action potentials were observed around 10 kPa, and the recording viability dropped drastically for pressures above 30 kPa. Given the substantial influence of pressure amplitude on neuronal responses predicted by the NICE and SONIC models, the impossibility to reliably assess the influence of that parameter is an important limitation.
- Second, the presence of an air-water interface located just after the biological sample along the acoustic propagation path (**Figure 33a**) is prone to yield significant reflection patterns towards the recording targets, and therefore implies a lack of control of the stimulus delivery. This also hinders a potential comparison with modeling predictions.

- Third, the inter-stimulus interval between electrical and ultrasonic stimuli did not allow for a robust membrane stabilization between all recordings (see for instance **Figure 35a** at time 55s). As a result, confounding factors may well exist that influenced our excitability and action potential dynamics analyses.
- Fourth, we performed these investigations in mature sensory neurons, which is highly relevant from a translation stand-point, but also implies the presence of a multiplicity of membrane elements (including ion channel populations) of which we cannot determine the level of functional expression. As a result, it is very difficult to attribute LIFUS excitability to a particular element.
- Fifth, the absence of comprehensive biophysical characterization of the targeted ganglionic neurons (noxious and pressure cells) in the literature prevents the adaptation of the SONIC model to formulate tailored predictions for these particular cells. Hence, we cannot perform quantitative comparisons between model predictions and experimental data.

5.6.2 Qualitative comparison: similarities and differences between modeling predictions and empirical data

Nevertheless, several qualitative features of recorded neuronal responses agree with the general trends predicted by the NICE and SONIC models:

- First, the gradual accumulation of membrane depolarization during sub-threshold stimulation suggests that neural responses originate from the progressive integration of a depolarizing “force” over time, rather than a stochastic “all-or-nothing” response. This observation correlates with the NICE prediction that the net charge imbalance over an acoustic cycle (resulting from asymmetric membrane deflections) progressively raises the charge density upon sonication.
- Second, the persistence of depolarizing effects after the stimulus offset is reminiscent of the action of T-type Calcium channels present in low-threshold spiking cortical neurons. In fact, the NICE model predicts that those channels offer an additional source of charge build-up during US-OFF periods.
- Third, the distinct (i.e. statistically different) shapes of spikes elicited inside electrical and ultrasonic stimulation windows suggest that those two modalities engage the action potential machinery in different manners. More specifically, while standard electrical pulses raise the membrane potential to activate ion channels, ultrasonic stimulation may offer a more intricate perturbation that effectively modulates the ion channels gating kinetics, and thereby changes the resulting spike shapes. This observation is in line with the predictions of the SONIC model in cortical neurons (see sections 3.4.1 and 3.5.1.1).

Conversely, some experimental observations depart significantly from the predictions of the NICE and SONIC models:

- First and foremost, we did not observe a sharp membrane hyperpolarization upon sonication onsets, which is a universal feature predicted by the NICE model. The absence of recorded hyperpolarization could be explained by the inability of the electrode to detect high-frequency voltage variations, although a low-pass filtered hyperpolarization would still be expected. It could also be explained by a sparse distribution of sonophores across the membrane yielding a strongly dampened capacitance modulation, but here again, a spatially-averaged hyperpo-

larization should be observable. Another potential explanation could be that we recorded action potentials away from the site of their elicitation, in an acoustically unperturbed location. However, that possibility is also unlikely, as our calibration data predicts that the acoustic focus should encompass the entire ganglion (**Figure S3**).

- Second, the variability in neuronal responses across repeated sonication trials within a given cell tends to indicate a stochastic behavior, which departs from the deterministic nature of the NICE and SONIC models. Notably, the inclusion of alternative gating schemes in these models, accounting for the intrinsic stochasticity of ion channels, could provide a more reliable insight regarding the robustness of neuronal responses in the context of intramembrane cavitation (Fox, 1997; Orio and Soudry, 2012).

5.6.3 Implications

Although these empirical findings obtained in an invertebrate model provide valuable insights of LIFUS neuromodulatory effects at the cellular level, they did not allow for a direct comparison with modeling predictions. These limitations emphasize the need to design a more tailored experimental validation approach.

At the same time, the sharp disparities observed between empirical data and modeling predictions highlight the fact that the NICE model, despite its enticing predictive power for large-scale neuromodulatory effects, cannot explain some of the main features observed at the cellular level. In fact, some of our experimental findings seem to point more towards a mechanosensitivity mechanism of LIFUS neuromodulation, which converges with an extensive collection of empirical evidence (see Chapter 1). However, this mechanistic hypothesis, like several others, is still not captured phenomenologically by equivalent biophysical models. Moving forward, the development of such quantitative formalisms to describe these alternative mechanisms will be of crucial importance, in order to provide a more complete picture of LIFUS neuromodulatory effects across neural targets, acoustic environments and sonication parameters.

Chapter 6 Discussion

In this thesis, I aimed at developing a computational framework to investigate the effects of low-intensity ultrasound stimulation (LIFUS) in neuronal structures, focusing on intramembrane cavitation as a mechanistic hypothesis. Building upon the existing NICE model, I developed a multi-layer computational framework enabling the formulation of refined, interpretable and scalable modeling predictions. Using this framework, I investigated the neuromodulatory effects of LIFUS in morphologically realistic peripheral neural structures. Finally, I confronted modeling predictions to experimental data, and discussed the potential implications for the model validity. In what follows, I will discuss these main achievements, inserting them in a broader context and suggesting potential directions for future research.

6.1 Summary and discussion

6.1.1 Motivations for the initial choice of biophysical mechanism

Among several proposed mechanisms for LIFUS evoked neural responses, I focused on the intramembrane cavitation hypothesis and the associated NICE model. Despite a lack of direct empirical observations of the underlying mechanistic hypothesis, and the recent emergence of strong evidence for other mechanisms (Kubaneck et al., 2016; Menz et al., 2019; Yoo et al., 2020), this model provides a unique theoretical framework with the highest level of predictive power about large-scale LIFUS neuromodulatory effects observed up to this day (Plaksin et al., 2016). Moreover, the NICE model constitutes the first notable computational effort at modeling LIFUS-neuron interactions in a quantitative, deterministic manner, and as such, it represents a valuable starting point to more elaborated modeling endeavors.

6.1.2 Methodological achievement 1: substantial improvements of intramembrane cavitation models

The NICE model laid out a valuable theoretical groundwork for computational studies on LIFUS-neuron interactions. Yet, several drawbacks hindered its usability for clinically relevant predictions. First, the computational complexity of the NICE model makes extensive explorations of LIFUS parameter spaces a very tedious process. Second, while offering a highly detailed temporal dynamics of neuronal response profiles, it does not provide the necessary abstraction level to interpret how LIFUS modulates those responses. Chapter 3 describes how we addressed those limitations by implementing the SONIC model. Using a temporal multiscaling approach, we decoupled numerically the two constitutive scales of the NICE model, which resulted in an effective electrical system providing substantial computational gains while guaranteeing numerical accuracy. This enhanced algorithmic efficacy allowed us to carry out extensive, systematic explorations of the LIFUS parameter space with a dense granularity. We could for instance generate cell-type-specific behavior maps for various combinations of stimulation parameters, but also investigate the impact of sonophore dimensions on excitation thresholds. Moreover, the SONIC model depicts neuronal responses in terms of an effective membrane dynamics that can be directly reconciled with classical electrophysiology, thereby enhancing its interpretability. For instance, we could describe how different spiking behaviors can be achieved in cortical neurons by varying LIFUS parameters, and explain how LIFUS modulation of the effective electrical system could affect the resulting spike amplitude and firing rate of neuronal responses. Finally, the reduced computational cost and separation of scales introduced in the SONIC model facilitate its spatial expansion, which we exemplified by introducing the first two-compartment model of intramembrane cavitation, in order to study the impact of partial sonophore coverage on neuronal excitability.

These results constitute a step forward regarding the usability, efficacy and interpretability of biophysical models of LIFUS-neuron interaction.

6.1.3 Methodological achievement 2: expansion of model predictions to the morphological scale

The findings presented in Chapter 3 were, for the most part, limited to the behavior of a single membrane segment lacking spatial extent, thereby providing an incomplete picture of LIFUS-neuron interactions and limiting the accuracy of model predictions. Indeed, typical LIFUS devices typically induce non-uniform pressure fields, the spatial features of which could play a central role in shaping neural excitation, as observed with electrical stimulation (McNeal, 1976; Rattay, 1986). Therefore, I devised a strategy to incorporate the effective SONIC paradigm into multi-compartmental neuron models, and implemented it as a NEURON-based computational framework, termed morphoSONIC (Chapter 4). The choice of NEURON as a development environment was motivated by the popularity of this simulation platform amongst neuroscientists, but also because NEURON features optimized numerical pipelines (in particular, implicit schemes and variable time steps) to handle the stable integration of complex multi-compartmental models formulated as matrix-based differential systems. The latter point is of particular importance in the context of the NICE model, which has proved particularly difficult to expand in the absence of optimized partial differential solvers. Unfortunately, neither charge casting nor time-varying capacitance – two core features of the SONIC paradigm – are natively supported in NEURON. Therefore, I derived a hybrid (charge and voltage casted) variant of the cable equation that is numerically reconcilable with both the NICE and SONIC paradigms and implemented it as an independent module that can be seamlessly integrated within NEURON. This approach provides a general solution to model circuit systems with time-varying capacitance, which is applicable to a wide variety of neuron models, within a reference simulation environment. As such, it also benefits from the wide collection of biophysical models made available by the NEURON community (McDougal et al., 2017), all of which can now be adapted to study LIFUS neuromodulatory effects with minimal effort. Finally, following up on a recent study pointing out limitations of the SONIC paradigm in the presence of tight axial coupling conditions (Tarnaud et al., 2020), I have established the general conditions of its applicability in multi-compartmental models. In particular, I have demonstrated that the SONIC paradigm can be accurately applied in single-cable axon models. Notably, the generalizability of the multi-compartmental modeling approach that I have devised means that it could also be used with more complex representations of the SONIC effective membrane dynamics, as proposed in (Tarnaud et al., 2020), in order to guarantee numerical accuracy across a wider range of axial coupling conditions.

6.1.4 Application: new predictions of LIFUS neuromodulatory effects on peripheral nerve fibers

As a first demonstrative application, I have exploited the morphoSONIC framework to investigate the ultrasound neuromodulation of peripheral nerve fibers with spatially-varying pressure fields (Chapter 4). This study highlighted three main results. First, single LIFUS pulses are capable of inducing *de novo* action potentials in both myelinated and unmyelinated peripheral axons. Second, LIFUS fiber recruitment is driven by a stimulus-evoked drop in effective membrane capacitance at the acoustic focus, which triggers passive depolarizing currents that raise charge density towards the spiking threshold. Third, myelinated and unmyelinated fibers exhibit distinct sensitivities to temporal features of LIFUS stimuli, which allows to selectively recruit either fiber population, a feature that has not yet been achieved by any other stimulation technique. These predictions of fiber-specific excitability offer a certain degree of qualitative agreement with recent empirical observations on both fiber types (Downs et al., 2018; Wright et al., 2017), and constitute an exciting prospect for the use of LIFUS as a selective peripheral neuromodulation technology.

6.1.5 Addressing the challenges identified in Chapter 1

The above results resolve the large majority of the challenges (bullet lists) identified in the introduction of this thesis, particularly section 1.3.4.3 regarding the modeling of intramembrane cavitation as a candidate mechanism for LIFUS neuromodulation, and in section 1.4 concerning issues affecting the maturation and adoption of this technology.

Pursuing the specific objectives defined in section 1.5 has resulted in two main methodological achievements that provide an answer to the central question raised in section 1.4 (*“how can we efficiently model ultrasound neuromodulation across all relevant scales?”*). More specifically, we can now answer some essential questions raised in section 1.4, within the context of a particular mechanistic hypothesis:

- *Given the multiplicity of potential responsive elements in the cellular membrane and their heterogeneous expression across cell types, what sort of cell type specificity can be expected in LIFUS-evoked responses, and how does that specificity affect functional and behavioral outcomes?*

Can these specificities be exploited to induce new forms of neuromodulation?

LIFUS evoked neuronal responses do show a high level of cell-type-specificity both in central and peripheral neural circuits. In the latter case, this specificity can be leveraged to engage a particular neural pathway selectively (e.g. unmyelinated C-fibers for sensory encoding)

- *Within the cell itself, how does the morphological structure affect the location of excitation, the potential integration of the initiated response along a dendritic tree, and its propagation along axonal projections?*

LIFUS-triggered excitation seems to be primarily a local phenomenon mediated by the acoustic perturbation of the cellular membrane, and occurs in morphological segments that contain both active voltage-gated ion channels and enough spared membrane to allow for sonophore cavitation.

6.2 Perspectives

The presented achievements have addressed the main issues raised in the beginning of this thesis. On that basis, we can now envision several perspectives, detailed below.

6.2.1 Experimental validation and model refinement

The value of a modeling framework is strongly dependent on the validity of its inherent assumptions. In that sense, the NICE, SONIC and morphoSONIC ensemble of models would greatly benefit from the experimental validation of the intramembrane cavitation hypothesis. Notably, a recent *in vitro* study employing high-speed imaging and genetically encoded voltage indicators (GEVIs) reported that the mechanical deformations and large scale hyperpolarization of the membrane upon sonication onset predicted by the NICE model could not be observed experimentally (Yoo et al., 2020). However, both methods would arguably fail to detect those mechano-electrical variations if they are sparsely distributed across the neuronal membrane, as would be the case with a low sonophore density. Furthermore, we suggested in Chapter 3 that the intracellular electrical coupling between a sonophore and the surrounding membrane could induce significant depolarizing forces, allowing an isolated sonophore to entrain a larger membrane patch towards the spiking threshold. Hence, I argue that those empirical observations do not completely rule out intramembrane cavitation as a possible neuromodulation mechanism, and suggest here two approaches for a more unequivocal assessment.

Looking closely at the internal dynamics of the NICE model, it appears that leakage channels are the fundamental membrane element that allow neurons to translate the capacitance-mediated hyperpolarization into a depolarizing transmembrane ionic current, in order to bring the membrane charge density (and the transmembrane voltage) toward the spiking threshold. This pivotal role stems from the fact that those leakage channels are constitutively open and can thus conduct across the entire voltage physiological range, while most voltage-gated ion channels are closed in highly hyperpolarized conditions (Plaksin et al., 2014). Therefore, I argue that the validity of the intramembrane cavitation hypothesis could be tested *in vitro* by selectively knocking out leakage channels (through pharmacological or genetic agents) and comparing LIFUS-evoked neural responses to a native condition. Ideally, such an experiment could be performed on a variety of primary cultured neurons, using previously calibrated all optical voltage-sensitive readouts (e.g. GEVIs) allowing robust recordings, and in an acoustically transparent medium allowing for a controlled stimulus delivery and mimicking *in vivo* conditions. Complementarily, a “bottom-up” approach could be devised that involves the genetic expression of leakage channels in non-excitable cells (e.g. HEK293T cells, *Xenopus* oocytes), in order to quantify precisely the impact of these channels on the time course of the transmembrane voltage upon sonication. Moreover, exploiting the quasi-linear voltage dependency of leakage channels, one could easily infer on their functional expression and derive associated parameters such as reversal potential and passive conductance using current clamp techniques. This would allow to construct cell-specific versions of the SONIC model, whose predictions could be tested against experimental readouts of LIFUS-evoked responses.

Furthermore, the morphological expansion of intramembrane cavitation models has enabled the generation of new model predictions at a larger scale, which could be used to design an indirect experimental validation of the mechanism. In particular, our predictions of fiber-specific neural excitability in peripheral structures are easily verifiable using appropriate nerve preparations and recording techniques. In fact, we are planning to use a micro-fabricated “nerve-on-a-chip” platform to record LIFUS-evoked responses from explanted heterogeneous nerve bundles (Gribi et al., 2018), and to assess the differential recruitment of distinct fiber populations by discriminating between their conduction velocities.

6.2.2 Framework application to other neural targets

With SONIC and morphoSONIC, I have presented here two methodological developments that offer an effective way to model one of the mechanistic hypotheses of LIFUS-neuron interaction. So far, this framework has only been applied to peripheral nerve fibers, because of their relatively limited morphological complexity, but also because they constitute prized neuromodulation targets. However, this framework could also be applied to study the effects of ultrasonic waves on other neural targets, particularly in the brain where the correlation between NICE model predictions and empirical data is extensive, and in the spinal cord that remains a largely unexplored LIFUS neuromodulation target. In the former case, it would for instance be highly interesting to investigate which morphological regions of a cortical neuron are most sensitive to LIFUS stimuli and trigger a first response, and how the stimulus can potentially perturb the propagation of an elicited action potential towards other brain areas.

6.2.3 Towards multi-scale modeling

So far, most modeling efforts have focused on investigating LIFUS-neuron interactions in simplified cellular representations, i.e. without morphological considerations. While it allows to predict general trends of elicited effects, this approach fails at providing a full picture of neural responses. By enabling the modeling of a candidate mechanism within morphologically realistic structures with a three-dimensional representation, the morphoSONIC framework addresses that limitation. But also, it enables the realistic modeling of larger-scale neuronal ensembles (along with their synaptic connections) that

portray functionally relevant circuits beyond the individual neuron (e.g. nerve bundles, brain and spinal networks). Such modeling efforts would provide an answer to the remaining central question raised at the beginning of this thesis (*"In the case of highly connected neural circuits of the brain and spinal cord, how does the stimulation of a given area affect other, functionally and anatomically connected areas? How do these network effects scale over time?"*). They would also allow to predict high level LIFUS neuromodulatory effects that are closer to experimental readouts (e.g. compound action potentials, local field potentials, large scale electrical dipoles, fMRI and electro-encephalographic patterns).

6.2.4 Towards hybrid, multi-physics modeling

At the beginning of this thesis, I highlighted the importance of numerical acoustics physics solvers in predicting *where, when, and in which quantity* the acoustic stimulus is delivered. The modeling developments presented in this thesis constitute an optimal complement to these tools, in that their coupling will allow to predict the entire phenomenological chain of events following the application of a given LIFUS stimulus, from the initial acoustic propagation to the large scale functional and / or behavioral outcome, and its eventual experimental readout. As they allow to safely and efficiently explore stimulation parameter spaces, such multi-physics platforms will be instrumental to guide the development of target-specific sonication devices and application-specific LIFUS protocols, in order to obtain refined neuromodulatory effects. In doing so, they will support the translation of LIFUS into the clinical setting.

6.2.5 Therapeutic perspectives

Ultrasound constitutes an optimal energy modality to permeate, perturb, and "communicate" with biological tissue. These enticing physical properties, along with the recently accumulated evidence of ultrasound neuromodulatory effects, emphasize the immense potential of LIFUS as a neuromodulation technology that could be applied in a variety of settings. First and foremost, as a noninvasive brain stimulation technique, where the focusing depth and spatial resolution of LIFUS should allow to probe arbitrary neural circuits to understand their function, but also to treat neurological disorders in both superficial and deep brain regions. In the peripheral nervous system, LIFUS could enable different types of functional selectivity than those enabled by conventional techniques (as highlighted in this work), thereby opening new opportunities for enriched sensory encoding and more effective peripheral neuroprostheses. Looking forward, LIFUS could also be adapted to target pathways of the autonomic nervous system with minimal invasiveness, and therefore offer a valuable neuromodulation technique for various applications in bioelectronic medicine.

Supplementary material for Chapter 5

Supplementary materials display five figures. **Figure S1** (related to **Figure 34**) concerns the estimation of observation time and membrane potential baseline variations for EL stimulation. **Figure S2** and **Figure S3** (related to **Figure 33**) concern US calibration setup and results. **Figure S4** (related to **Figure 35c**) focuses on the analysis of US-APs success rate as a function of acoustic intensity and stimulus onset and offset. **Figure S5** (related to **Figure 34** and **Figure 35**) concerns the comparison between P and N cells in response to ultrasonic stimulation.

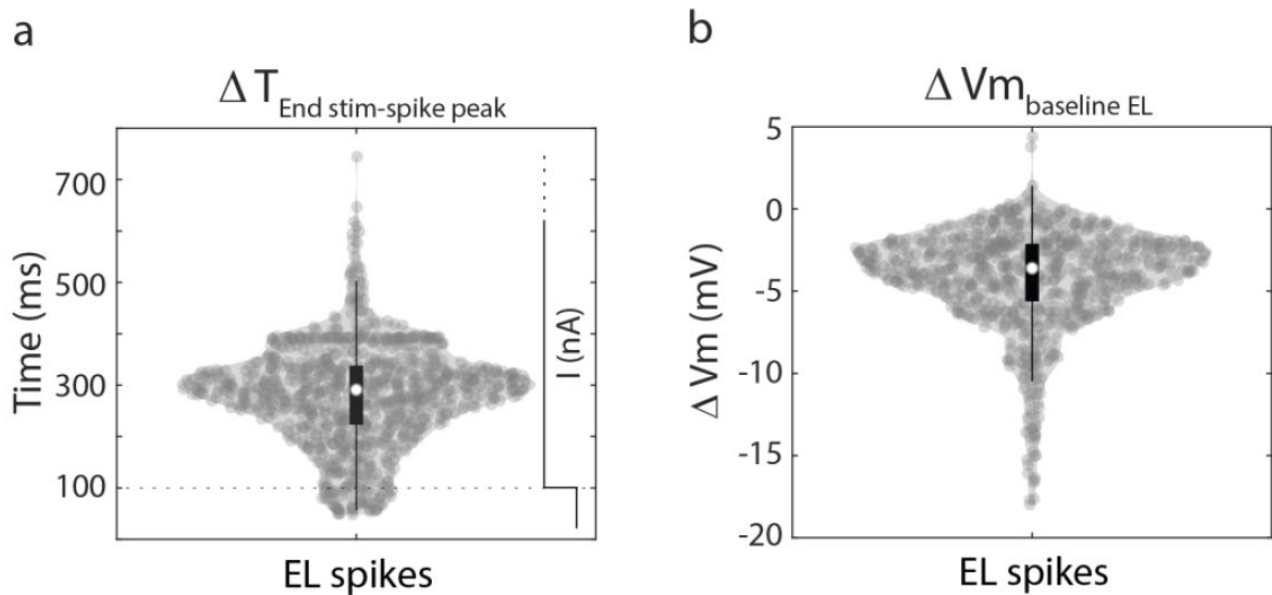


Figure S1 (related to Figure 34). Estimation of observation time and membrane potential baseline variations. a) Analysis of the EL stimulations to estimate the probability of spike detection after the end of the stimulus; only few cells showed spikes during the considered post stimulation time interval (100 ms). The dotted line corresponds to the end of EL trigger. Time measured from 100 ms after trigger end to preceding spike peak. b) Baseline variation on EL stimulation, defined as difference between membrane potential post and pre-current onset. A time window of 100 ms is considered for post and pre-stimulation baseline analysis. Membrane voltage after EL stimulation is lower on the considered observation window.

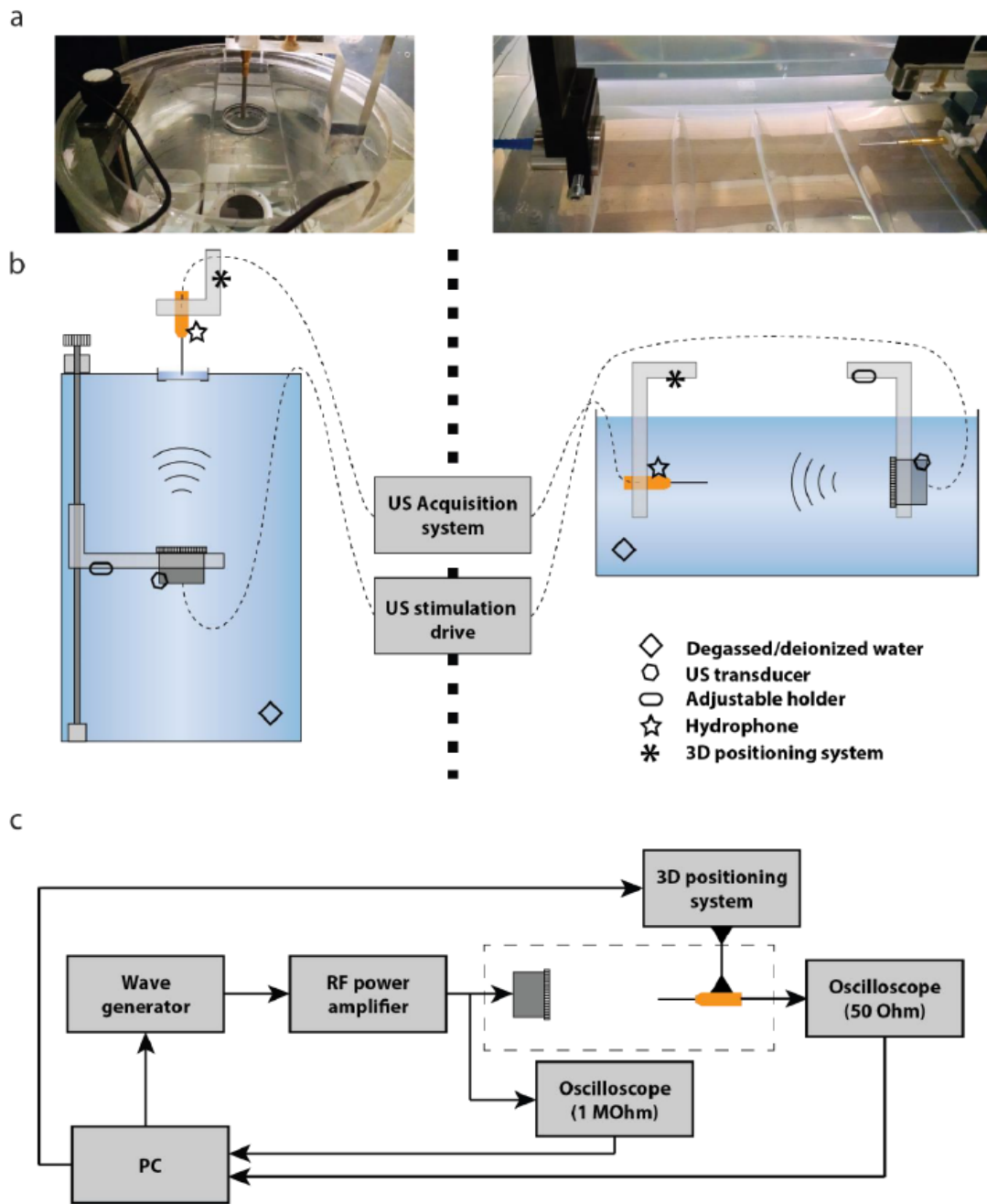


Figure S2 (related to Figure 33). US calibration setup. a) left: calibration into the experimental setup; right: free field calibration setup. b) Scheme of the calibration measurement system. c) Detailed block representation of US/acquisition setup.

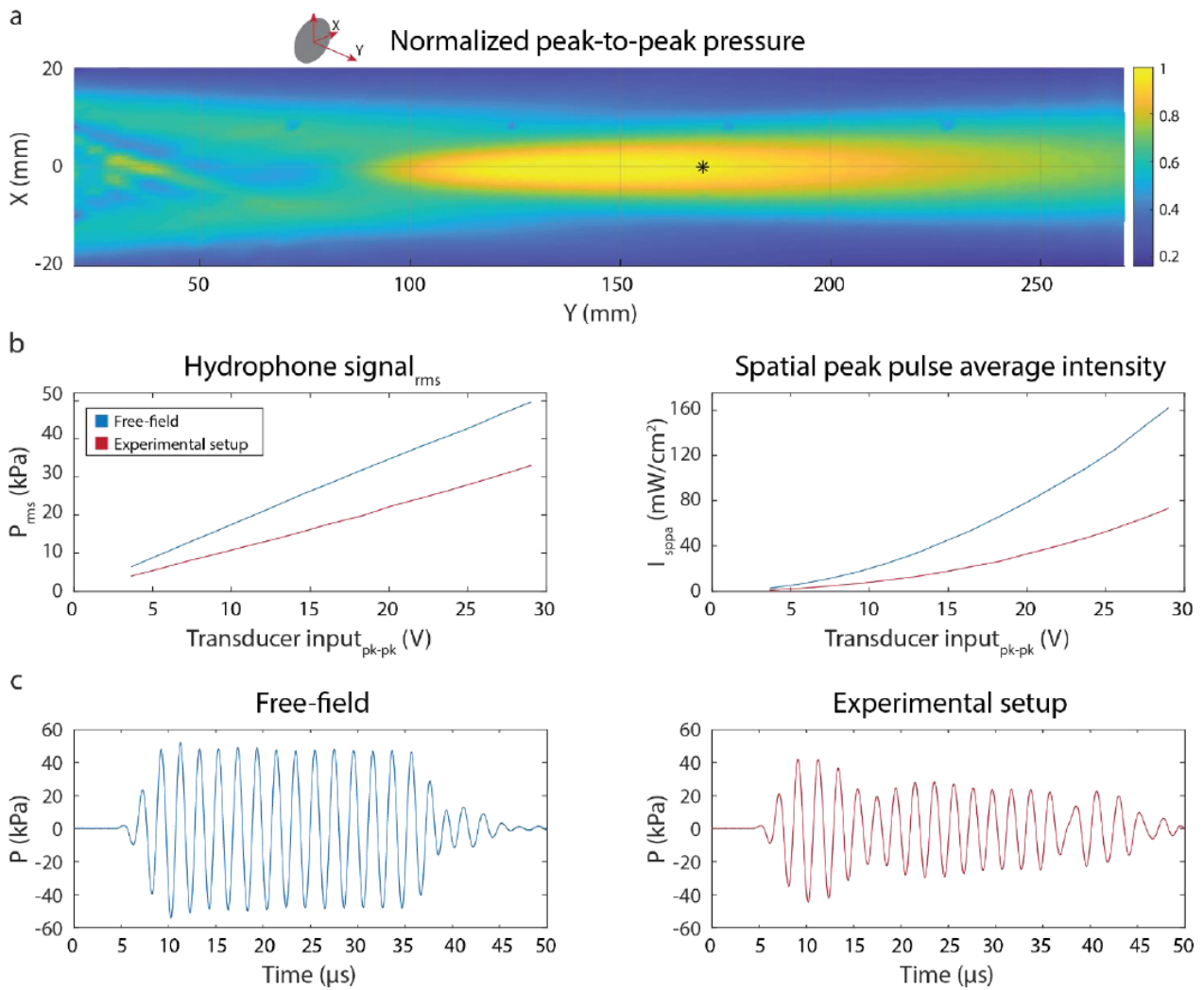


Figure S3 (related to Figure 33). US calibration results. a) 2D spatial mapping of normalized peak-to-peak pressure produced by the transducer in free field. Transducer focus is at 140 mm. Asterisk indicates the distance between the transducer and target employed during experiments, i.e. 165 mm. b) On left, hydrophone root-mean-square pressure (P_{rms}) signal vs driving voltage; low pressure calibration of the transducer shows that pressure is linear with the input voltage. The signal measured in the experimental setup is attenuated with respect to the free field condition. On right, calculation of spatial-peak pulse-average intensity, I_{sppa} ; free field (blue), experimental setup (red). The measure has been conducted at 165 mm from transducer surface. c) Example of time variation of the pressure signal in free-field (blue) and experimental setup (red). It can be observed that the second is attenuated and a post stimulus onset effect is introduced by the experimental setup.

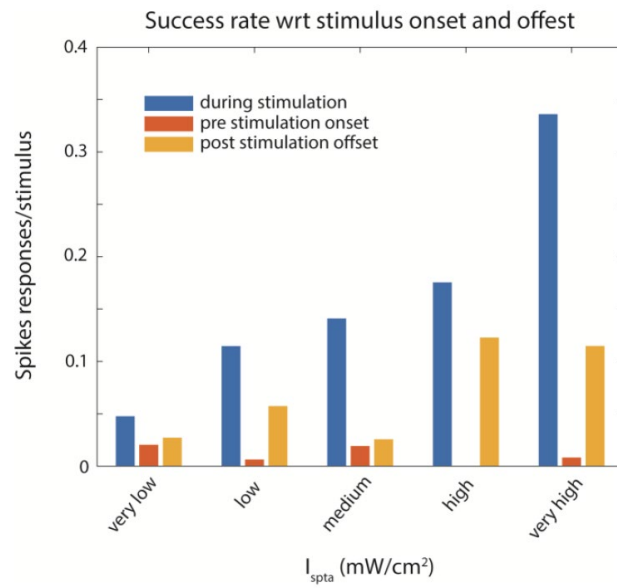


Figure S4 (related to Figure 35c). Action potential success rate as a function of acoustic intensity (binned into 5 groups) and of US stimulus onset and offset. Blue: AP success rate during US stimulus (i.e., during a time window of 300ms following US stimulus onset). Red: AP success rate during a window of length equal to the stimulus duration (i.e., 300 ms) but preceding the stimulus onset. Yellow: AP success rate during a window of length equal to the stimulus duration (i.e., 300 ms) but following the stimulus offset.

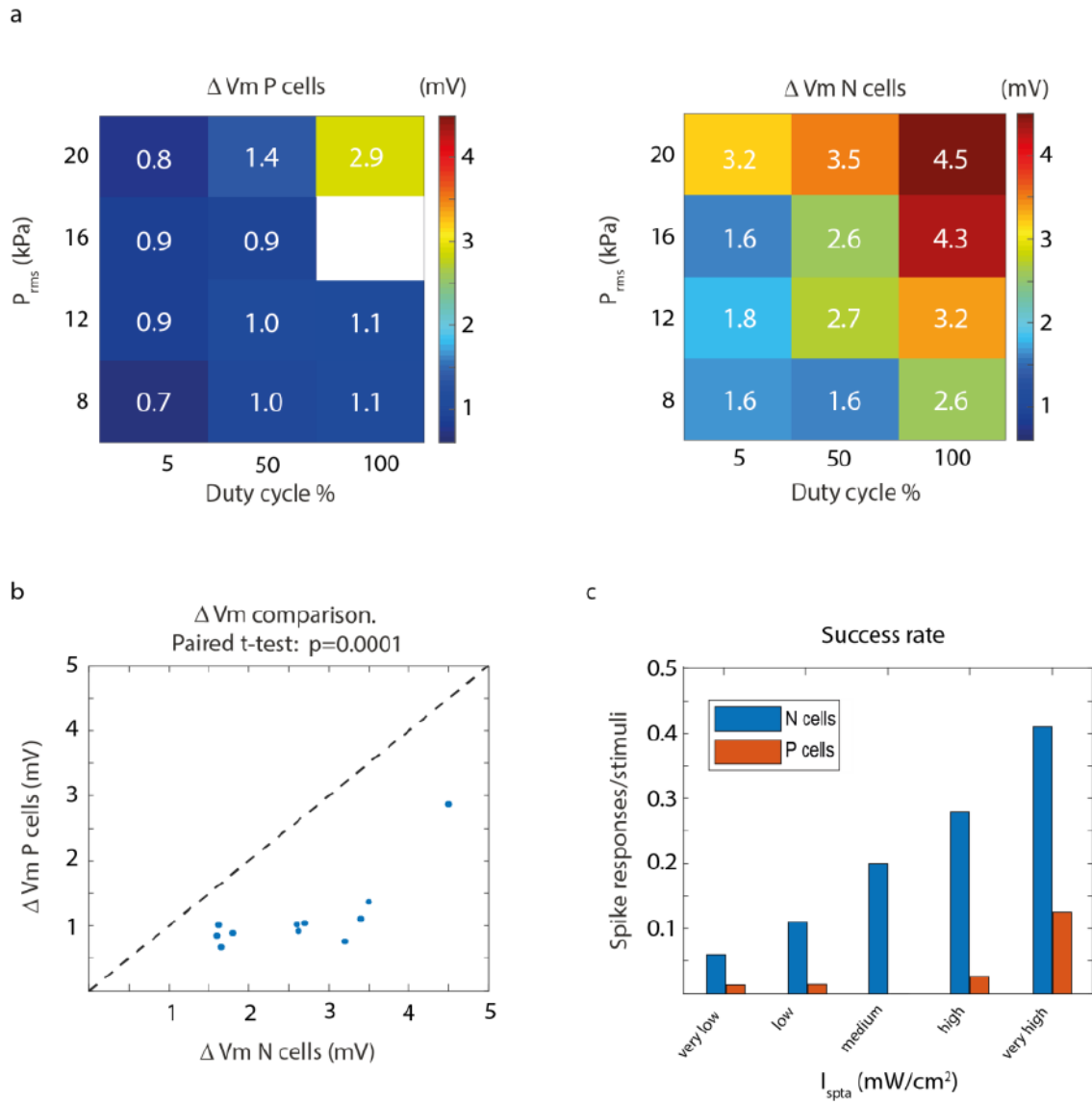


Figure S5 (related to Figure 34 and Figure 35). Comparison between responses to US of P and N mechanoreceptors. a) Left: Same as Figure 2e for P cells stimulation. Empty square indicates that no cell responded to that particular parameters combination. Right: Figure 2e rescaled for clearer comparison. b) Comparison of average membrane potential deflection for P and N cells across stimulation intensities. c) Same as Figure 3c, displaying spike responses from P and N cells.

Bibliography

- Abbott, B.C., and Howarth, J.V. (1973). Heat studies in excitable tissues. *Physiol. Rev.* 53, 120–158.
- Abelson, J.L., Curtis, G.C., Sagher, O., Albucher, R.C., Harrigan, M., Taylor, S.F., Martis, B., and Giordani, B. (2005). Deep brain stimulation for refractory obsessive-compulsive disorder. *Biol. Psychiatry* 57, 510–516.
- Anderson, J.M. (2001). Biological Responses to Materials. *Annu. Rev. Mater. Res.* 31, 81–110.
- Bachtold, M.R., Rinaldi, P.C., Jones, J.P., Reines, F., and Price, L.R. (1998). Focused ultrasound modifications of neural circuit activity in a mammalian brain. *Ultrasound Med. Biol.* 24, 557–565.
- Badia, J., Boretius, T., Andreu, D., Azevedo-Coste, C., Stieglitz, T., and Navarro, X. (2011a). Comparative analysis of transverse intrafascicular multichannel, longitudinal intrafascicular and multipolar cuff electrodes for the selective stimulation of nerve fascicles. *J. Neural Eng.* 8, 036023.
- Badia, J., Boretius, T., Pascual-Font, A., Udina, E., Stieglitz, T., and Navarro, X. (2011b). Biocompatibility of chronically implanted transverse intrafascicular multichannel electrode (TIME) in the rat sciatic nerve. *IEEE Trans. Biomed. Eng.* 58.
- Baldermann, J.C., Schüller, T., Huys, D., Becker, I., Timmermann, L., Jessen, F., Visser-Vandewalle, V., and Kuhn, J. (2016). Deep Brain Stimulation for Tourette-Syndrome: A Systematic Review and Meta-Analysis. *Brain Stimulat.* 9, 296–304.
- Benabid, A.L., Pollak, P., Louveau, A., Henry, S., and de Rougemont, J. (1987). Combined (Thalamotomy and Stimulation) Stereotactic Surgery of the VIM Thalamic Nucleus for Bilateral Parkinson Disease. *Stereotact. Funct. Neurosurg.* 50, 344–346.
- Bhadra, N., and Peckham, P.H. (1997). Peripheral Nerve Stimulation for Restoration of Motor Function: *J. Clin. Neurophysiol.* 14, 378–393.
- Blackmore, J., Shrivastava, S., Sallet, J., Butler, C.R., and Cleveland, R.O. (2019). Ultrasound Neuromodulation: A Review of Results, Mechanisms and Safety. *Ultrasound Med. Biol.*
- Boal, D. (2012). *Mechanics of the Cell* (Cambridge, UK ; New York: Cambridge University Press).
- Boyden, E.S. (2011). Optogenetics: using light to control the brain. *Cerebrum Dana Forum Brain Sci.* 2011, 16.
- Braun, V., Blackmore, J., Cleveland, R.O., and Butler, C.R. (2020). Transcranial ultrasound stimulation in humans is associated with an auditory confound that can be effectively masked. *Brain Stimulat.* 13, 1527–1534.
- Brennen, C.E. (1995). *Cavitation and Bubble Dynamics* (New York: Oxford University Press).
- Brunoni, A.R., Moffa, A.H., Fregni, F., Palm, U., Padberg, F., Blumberger, D.M., Daskalakis, Z.J., Bennabi, D., Haffen, E., Alonzo, A., et al. (2016). Transcranial direct current stimulation for acute

- major depressive episodes: Meta-analysis of individual patient data. *Br. J. Psychiatry* 208, 522–531.
- Buckingham, E. (1914). On Physically Similar Systems; Illustrations of the Use of Dimensional Equations. *Phys. Rev.* 4, 345–376.
- Callier, T., Brantly, N.W., Caravelli, A., and Bensmaia, S.J. (2020). The frequency of cortical microstimulation shapes artificial touch. *Proc. Natl. Acad. Sci.* 117, 1191–1200.
- Capogrosso, M., Wenger, N., Raspopovic, S., Musienko, P., Beauparlant, J., Bassi Luciani, L., Courtine, G., and Micera, S. (2013). A computational model for epidural electrical stimulation of spinal sensorimotor circuits. *J. Neurosci. Off. J. Soc. Neurosci.* 33, 19326–19340.
- Catterall, W.A., Raman, I.M., Robinson, H.P.C., Sejnowski, T.J., and Paulsen, O. (2012). The Hodgkin-Huxley Heritage: From Channels to Circuits. *J. Neurosci.* 32, 14064–14073.
- Chen, H., Garcia-Gonzalez, D., and Jerusalem, A. (2019). Computational model of the mechano-electrophysiological coupling in axons with application to neuromodulation. *Phys. Rev. E* 99, 032406.
- Chen, R., Romero, G., Christiansen, M.G., Mohr, A., and Anikeeva, P. (2015). Wireless magnetothermal deep brain stimulation. *Science* 347, 1477–1480.
- Chow, C.C., and White, J.A. (1996). Spontaneous action potentials due to channel fluctuations. *Biophys. J.* 71, 3013–3021.
- Christensen, M.B., Pearce, S.M., Ledbetter, N.M., Warren, D.J., Clark, G.A., and Tresco, P.A. (2014). The foreign body response to the Utah Slant Electrode Array in the cat sciatic nerve. *Acta Biomater.* 10, 4650–4660.
- Church, C.C. (1995). The effects of an elastic solid surface layer on the radial pulsations of gas bubbles. *J. Acoust. Soc. Am.* 97, 1510–1521.
- Collins, M.N., and Mesce, K.A. (2020). Focused Ultrasound Neuromodulation and the Confounders of Intracellular Electrophysiological Investigation. *ENeuro* 7.
- Colucci, V., Strichartz, G., Jolesz, F., Vykhodtseva, N., and Hynynen, K. (2009). Focused ultrasound effects on nerve action potential in vitro. *Ultrasound Med. Biol.* 35, 1737–1747.
- Crank, J. (2009). *The mathematics of diffusion* (Oxford: Oxford Univ. Press).
- Crema, A., Malesevic, N., Furfaro, I., Raschella, F., Pedrocchi, A., and Micera, S. (2018). A Wearable Multi-Site System for NMES-Based Hand Function Restoration. *IEEE Trans. Neural Syst. Rehabil. Eng.* 26, 428–440.
- Croft, P.G. (1952). The Effect of Electrical Stimulation of the Brain on the Perception of Pain. *J. Ment. Sci.* 98, 421–426.
- D'Anna, E., Valle, G., Mazzoni, A., Strauss, I., Iberite, F., Patton, J., Petrini, F.M., Raspopovic, S., Granata, G., Iorio, R.D., et al. (2019). A closed-loop hand prosthesis with simultaneous intraneural tactile and position feedback. *Sci. Robot.* 4.
- Dedola, F., Severino, F.P.U., Meneghetti, N., Lemaire, T., Cafarelli, A., Ricotti, L., Menciassi, A., Cutrone, A., Mazzoni, A., and Micera, S. (2020). Ultrasound Stimulations Induce Prolonged

- Depolarization and Fast Action Potentials in Leech Neurons. *IEEE Open J. Eng. Med. Biol.* 1, 23–32.
- Deffieux, T., Younan, Y., Wattiez, N., Tanter, M., Pouget, P., and Aubry, J.-F. (2013). Low-intensity focused ultrasound modulates monkey visuomotor behavior. *Curr. Biol. CB* 23, 2430–2433.
- Dionísio, A., Duarte, I.C., Patrício, M., and Castelo-Branco, M. (2018). The Use of Repetitive Transcranial Magnetic Stimulation for Stroke Rehabilitation: A Systematic Review. *J. Stroke Cerebrovasc. Dis.* 27, 1–31.
- Downs, M.E., Lee, S.A., Yang, G., Kim, S., Wang, Q., and Konofagou, E.E. (2018). Non-invasive peripheral nerve stimulation via focused ultrasound in vivo. *Phys. Med. Biol.*
- Escoffre, J.-M., and Bouakaz, A. (2016). Therapeutic ultrasound.
- Fabry, B., Maksym, G.N., Butler, J.P., Glogauer, M., Navajas, D., and Fredberg, J.J. (2001). Scaling the microrheology of living cells. *Phys. Rev. Lett.* 87, 148102.
- Faisal, A.A., White, J.A., and Laughlin, S.B. (2005). Ion-Channel Noise Places Limits on the Miniaturization of the Brain's Wiring. *Curr. Biol.* 15, 1143–1149.
- Famm, K., Litt, B., Tracey, K.J., Boyden, E.S., and Slaoui, M. (2013). Drug discovery: a jump-start for electroceuticals. *Nature* 496, 159–161.
- Fink, M., and Noble, D. (2009). Markov models for ion channels: versatility versus identifiability and speed. *Philos. Trans. R. Soc. Math. Phys. Eng. Sci.* 367, 2161–2179.
- Fischer, L., Scherbarth, F., Chagnaud, B., and Felmy, F. (2017). Intrinsic frequency response patterns in mechano-sensory neurons of the leech. *Biol. Open* 6, 993–999.
- Folloni, D., Verhagen, L., Mars, R.B., Fouragnan, E., Constans, C., Aubry, J.-F., Rushworth, M.F.S., and Sallet, J. (2019). Manipulation of Subcortical and Deep Cortical Activity in the Primate Brain Using Transcranial Focused Ultrasound Stimulation. *Neuron*.
- Fomenko, A., Neudorfer, C., Dallapiazza, R.F., Kalia, S.K., and Lozano, A.M. (2018). Low-intensity ultrasound neuromodulation: An overview of mechanisms and emerging human applications. *Brain Stimulat.*
- Foster, K.R., and Wiederhold, M.L. (1978). Auditory responses in cats produced by pulsed ultrasound. *J. Acoust. Soc. Am.* 63, 1199–1205.
- Fox, R.F. (1997). Stochastic versions of the Hodgkin-Huxley equations. *Biophys. J.* 72, 2068–2074.
- Frankenhaeuser, B., and Huxley, A.F. (1964). The action potential in the myelinated nerve fibre of *Xenopus laevis* as computed on the basis of voltage clamp data. *J. Physiol.* 171, 302–315.
- Fry, W.J., and Fry, R.B. (1950). A possible mechanism involved in the conduction process of thin sheathed nerve fibers. *J. Cell. Physiol.* 36, 229–239.
- Fry, F.J., Ades, H.W., and Fry, W.J. (1958). Production of reversible changes in the central nervous system by ultrasound. *Science* 127, 83–84.

- Garcia-Perez, E. (2007). Spontaneous electrical activity and behavior in the leech *Hirudo medicinalis*. *Front. Integr. Neurosci.* 1.
- Gaur, P., Casey, K.M., Kubanek, J., Li, N., Mohammadjavadi, M., Saenz, Y., Glover, G.H., Bouley, D.M., and Pauly, K.B. (2020). Histologic safety of transcranial focused ultrasound neuromodulation and magnetic resonance acoustic radiation force imaging in rhesus macaques and sheep. *Brain Stimulat.* 13, 804–814.
- Gavrilov, L.R., Gersuni, G.V., Ilyinsky, O.B., Sirotiyuk, M.G., Tsirolnikov, E.M., and Shchekanov, E.E. (1976). The effect of focused ultrasound on the skin and deep nerve structures of man and animal. *Prog. Brain Res.* 43, 279–292.
- Gavrilov, L.R., Tsirolnikov, E.M., and Davies, I. ab I. (1996). Application of focused ultrasound for the stimulation of neural structures. *Ultrasound Med. Biol.* 22, 179–192.
- Gaynes, B.N., Lloyd, S.W., Lux, L., Gartlehner, G., Hansen, R.A., Brode, S., Jonas, D.E., Evans, T.S., Viswanathan, M., and Lohr, K.N. (2014). Repetitive Transcranial Magnetic Stimulation for Treatment-Resistant Depression: A Systematic Review and Meta-Analysis. *J. Clin. Psychiatry* 75, 477–489.
- Geng, M., and Duan, Z. (2010). Prediction of oxygen solubility in pure water and brines up to high temperatures and pressures. *Geochim. Cosmochim. Acta* 74, 5631–5640.
- Ghanouni, P., Pauly, K.B., Elias, W.J., Henderson, J., Sheehan, J., Monteith, S., and Wintermark, M. (2015). Transcranial MRI-Guided Focused Ultrasound: A Review of the Technologic and Neurologic Applications. *Am. J. Roentgenol.* 205, 150–159.
- Giancoli, D.C. (2008). *Physics for scientists & engineers* (Upper Saddle River, NJ: Pearson/Prentice Hall).
- Gribi, S., du Bois de Dunilac, S., Ghezzi, D., and Lacour, S.P. (2018). A microfabricated nerve-on-a-chip platform for rapid assessment of neural conduction in explanted peripheral nerve fibers. *Nat. Commun.* 9.
- Gross, L.C.M., Heron, A.J., Baca, S.C., and Wallace, M.I. (2011). Determining Membrane Capacitance by Dynamic Control of Droplet Interface Bilayer Area. *Langmuir* 27, 14335–14342.
- Grossman, N., Bono, D., Dedic, N., Kodandaramaiah, S.B., Rudenko, A., Suk, H.-J., Cassara, A.M., Neufeld, E., Kuster, N., Tsai, L.-H., et al. (2017). Noninvasive Deep Brain Stimulation via Temporally Interfering Electric Fields. *Cell* 169, 1029–1041.e16.
- Gulick, D.W., Li, T., Kleim, J.A., and Towe, B.C. (2017). Comparison of Electrical and Ultrasound Neurostimulation in Rat Motor Cortex. *Ultrasound Med. Biol.* 0.
- Guo, H., Hamilton, M., Offutt, S.J., Gloeckner, C.D., Li, T., Kim, Y., Legon, W., Alford, J.K., and Lim, H.H. (2018). Ultrasound Produces Extensive Brain Activation via a Cochlear Pathway. *Neuron* 98, 1020–1030.e4.
- Hameroff, S., Trakas, M., Duffield, C., Annabi, E., Gerace, M.B., Boyle, P., Lucas, A., Amos, Q., Buadu, A., and Badal, J.J. (2013). Transcranial ultrasound (TUS) effects on mental states: a pilot study. *Brain Stimulat.* 6, 409–415.
- Harvey, E.N. (1930). The effect of high frequency sound waves on heart muscle and other irritable tissues. *Am. Heart J.* 5, 388.

- Heimburg, T., and Jackson, A.D. (2005). On soliton propagation in biomembranes and nerves. *Proc. Natl. Acad. Sci. U. S. A.* *102*, 9790–9795.
- Helm, C.A., Israelachvili, J.N., and McGuiggan, P.M. (1989). Molecular mechanisms and forces involved in the adhesion and fusion of amphiphilic bilayers. *Science* *246*, 919–922.
- Hindmarsh, A.C. (1983). ODEPACK, A Systematized Collection of ODE Solvers. In *Scientific Computing*, (Amsterdam), pp. 55–64.
- Hindmarsh, A.C., Brown, P.N., Grant, K.E., Lee, S.L., Serban, R., Shumaker, D.E., and Woodward, C.S. (2005). SUNDIALS: Suite of nonlinear and differential/algebraic equation solvers. *ACM Trans. Math. Softw.* *31*, 363–396.
- Hines, M.L., and Carnevale, N.T. (1997). The NEURON simulation environment. *Neural Comput.* *9*, 1179–1209.
- Hintze, J.L., and Nelson, R.D. (1998). Violin plots: A box plot-density trace synergism. *Am. Stat.* *52*, 181–184.
- Hodgkin, A.L., and Huxley, A.F. (1952a). A quantitative description of membrane current and its application to conduction and excitation in nerve. *J. Physiol.* *117*, 500–544.
- Hodgkin, A.L., and Huxley, A.F. (1952d). Currents carried by sodium and potassium ions through the membrane of the giant axon of *Loligo*. *J. Physiol.* *116*, 449–472.
- Hodgkin, A.L., and Huxley, A.F. (1952c). The components of membrane conductance in the giant axon of *Loligo*. *J. Physiol.* *116*, 473–496.
- Hodgkin, A.L., and Huxley, A.F. (1952b). The dual effect of membrane potential on sodium conductance in the giant axon of *Loligo*. *J. Physiol.* *116*, 497–506.
- Hodgkin, A.L., Huxley, A.F., and Katz, B. (1952). Measurement of current-voltage relations in the membrane of the giant axon of *Loligo*. *J. Physiol.* *116*, 424–448.
- Hynynen, K., Clement, G.T., McDannold, N., Vykhodtseva, N., King, R., White, P.J., Vitek, S., and Jolesz, F.A. (2004). 500-element ultrasound phased array system for noninvasive focal surgery of the brain: a preliminary rabbit study with ex vivo human skulls. *Magn. Reson. Med.* *52*, 100–107.
- Ibitoye, M.O., Hamzaid, N.A., Hasnan, N., Abdul Wahab, A.K., and Davis, G.M. (2016). Strategies for Rapid Muscle Fatigue Reduction during FES Exercise in Individuals with Spinal Cord Injury: A Systematic Review. *PLOS ONE* *11*, e0149024.
- Ibsen, S., Tong, A., Schutt, C., Esener, S., and Chalasani, S.H. (2015). Sonogenetics is a non-invasive approach to activating neurons in *Caenorhabditis elegans*. *Nat. Commun.* *6*, 8264.
- Inoue, I., Kobatake, Y., and Tasaki, I. (1973). Excitability, instability and phase transitions in squid axon membrane under internal perfusion with dilute salt solutions. *Biochim. Biophys. Acta BBA - Biomembr.* *307*, 471–477.
- Israelachvili, J.N. (1992). *Intermolecular and surface forces* (London: Academic Press).
- IT'IS Foundation (2015). *Tissue Properties Database V3.0*.

- Johnson, S.M., and Buttress, N. (1973). The osmotic insensitivity of sonicated liposomes and the density of phospholipid-cholesterol mixtures. *Biochim. Biophys. Acta* 307, 20–26.
- Johnson, B.C., Shen, K., Piech, D., Ghanbari, M.M., Li, K.Y., Neely, R., Carmena, J.M., Maharbiz, M.M., and Muller, R. (2018). StimDust: A 6.5mm³, wireless ultrasonic peripheral nerve stimulator with 82% peak chip efficiency. In 2018 IEEE Custom Integrated Circuits Conference (CICC), pp. 1–4.
- Juan, E.J., González, R., Albors, G., Ward, M.P., and Irazoqui, P. (2014). Vagus Nerve Modulation Using Focused Pulsed Ultrasound: Potential Applications and Preliminary Observations in a Rat. *Int. J. Imaging Syst. Technol.* 24, 67–71.
- Kim, H., Taghados, S.J., Fischer, K., Maeng, L.-S., Park, S., and Yoo, S.-S. (2012). Noninvasive transcranial stimulation of rat abducens nerve by focused ultrasound. *Ultrasound Med. Biol.* 38, 1568–1575.
- Kim, H., Chiu, A., Lee, S.D., Fischer, K., and Yoo, S.-S. (2014). Focused Ultrasound-mediated Non-invasive Brain Stimulation: Examination of Sonication Parameters. *Brain Stimulat.* 7, 748–756.
- Kim, H., Park, M.Y., Lee, S.D., Lee, W., Chiu, A., and Yoo, S.-S. (2015). Suppression of EEG visual-evoked potentials in rats through neuromodulatory focused ultrasound. *Neuroreport* 26, 211–215.
- King, R.L., Brown, J.R., Newsome, W.T., and Pauly, K.B. (2013). Effective parameters for ultrasound-induced in vivo neurostimulation. *Ultrasound Med. Biol.* 39, 312–331.
- King, R.L., Brown, J.R., and Pauly, K.B. (2014). Localization of ultrasound-induced in vivo neurostimulation in the mouse model. *Ultrasound Med. Biol.* 40, 1512–1522.
- Klomjai, W., Katz, R., and Lackmy-Vallée, A. (2015). Basic principles of transcranial magnetic stimulation (TMS) and repetitive TMS (rTMS). *Ann. Phys. Rehabil. Med.* 58, 208–213.
- Kobatake, Y., Tasaki, I., and Watanabe, A. (1971). Phase transition in membrane with reference to nerve excitation. *Adv. Biophys.* 2, 1–31.
- Koopman, F.A., Chavan, S.S., Miljko, S., Grazio, S., Sokolovic, S., Schuurman, P.R., Mehta, A.D., Levine, Y.A., Faltys, M., Zitnik, R., et al. (2016). Vagus nerve stimulation inhibits cytokine production and attenuates disease severity in rheumatoid arthritis. *Proc. Natl. Acad. Sci. U. S. A.* 113, 8284–8289.
- Koroleva, V.I., Vykhodtseva, N.I., and Elagin, V.A. (1986). [Spreading depression in the cortex and subcortical structures of the brain of the rat induced by exposure to focused ultrasound]. *Neirofiziologija Neurophysiol.* 18, 55–61.
- Krasovitski, B., Frenkel, V., Shoham, S., and Kimmel, E. (2011). Intramembrane cavitation as a unifying mechanism for ultrasound-induced bioeffects. *Proc. Natl. Acad. Sci. U. S. A.* 108, 3258–3263.
- Krauthamer, V., and Crosheck, T. (2002). Effects of high-rate electrical stimulation upon firing in modelled and real neurons. *Med. Biol. Eng. Comput.* 40, 360–366.
- Kristan, W.B., Calabrese, R.L., and Friesen, W.O. (2005). Neuronal control of leech behavior. *Prog. Neurobiol.* 76, 279–327.

- Kubaneck, J. (2018). Neuromodulation with transcranial focused ultrasound. *Neurosurg. Focus* 44, E14.
- Kubaneck, J., Shi, J., Marsh, J., Chen, D., Deng, C., and Cui, J. (2016). Ultrasound modulates ion channel currents. *Sci. Rep.* 6, 24170.
- Kubaneck, J., Shukla, P., Das, A., Baccus, S.A., and Goodman, M.B. (2018). Ultrasound Elicits Behavioral Responses through Mechanical Effects on Neurons and Ion Channels in a Simple Nervous System. *J. Neurosci.* 38, 3081–3091.
- Kubaneck, J., Brown, J., Ye, P., Pauly, K.B., Moore, T., and Newsome, W. (2020). Remote, brain region-specific control of choice behavior with ultrasonic waves. *Sci. Adv.* 6, eaaz4193.
- Kyriakou (2015). Multi-Physics Computational Modeling of Focused Ultrasound Therapies.
- Kyriakou, A., Neufeld, E., Werner, B., Paulides, M.M., Szekely, G., and Kuster, N. (2014). A review of numerical and experimental compensation techniques for skull-induced phase aberrations in transcranial focused ultrasound. *Int. J. Hyperthermia* 30, 36–46.
- Landau, L.D., Lifšic, E.M., and Landau, L.D. (2011). *Fluid mechanics* (Amsterdam [u.a]: Elsevier/Butterworth Heinemann).
- Lee, W., Garra, B., and American Institute of Ultrasound in Medicine (2004). AIUM Technical Bulletin. How to interpret the ultrasound output display standard for higher acoustic output diagnostic ultrasound devices: version 2. *J. Ultrasound Med. Off. J. Am. Inst. Ultrasound Med.* 23, 723–726.
- Lee, W., Kim, H., Jung, Y., Song, I.-U., Chung, Y.A., and Yoo, S.-S. (2015a). Image-guided transcranial focused ultrasound stimulates human primary somatosensory cortex. *Sci. Rep.* 5, 8743.
- Lee, W., Lee, S.D., Park, M.Y., Foley, L., Purcell-Estabrook, E., Kim, H., Fischer, K., Maeng, L.-S., and Yoo, S.-S. (2016a). Image-Guided Focused Ultrasound-Mediated Regional Brain Stimulation in Sheep. *Ultrasound Med. Biol.* 42, 459–470.
- Lee, W., Kim, H.-C., Jung, Y., Chung, Y.A., Song, I.-U., Lee, J.-H., and Yoo, S.-S. (2016b). Transcranial focused ultrasound stimulation of human primary visual cortex. *Sci. Rep.* 6, 34026.
- Lee, Y.-F., Lin, C.-C., Cheng, J.-S., and Chen, G.-S. (2015b). High-Intensity Focused Ultrasound Attenuates Neural Responses of Sciatic Nerves Isolated from Normal or Neuropathic Rats. *Ultrasound Med. Biol.* 41, 132–142.
- Legon, W., Sato, T.F., Opitz, A., Mueller, J., Barbour, A., Williams, A., and Tyler, W.J. (2014). Transcranial focused ultrasound modulates the activity of primary somatosensory cortex in humans. *Nat. Neurosci.* 17, 322–329.
- Legon, W., Ai, L., Bansal, P., and Mueller, J.K. (2018b). Neuromodulation with single-element transcranial focused ultrasound in human thalamus. *Hum. Brain Mapp.* 39, 1995–2006.
- Legon, W., Bansal, P., Tyshynsky, R., Ai, L., and Mueller, J.K. (2018a). Transcranial focused ultrasound neuromodulation of the human primary motor cortex. *Sci. Rep.* 8, 10007.

- Legon, W., Adams, S., Bansal, P., Patel, P.D., Hobbs, L., Ai, L., Mueller, J.K., Meekins, G., and Gillick, B.T. (2020). A retrospective qualitative report of symptoms and safety from transcranial focused ultrasound for neuromodulation in humans. *Sci. Rep.* 10.
- Lele, P.P. (1963). Effects of focused ultrasonic radiation on peripheral nerve, with observations on local heating. *Exp. Neurol.* 8, 47–83.
- Lemaire, T., Neufeld, E., Kuster, N., and Micera, S. (2019). Understanding ultrasound neuro-modulation using a computationally efficient and interpretable model of intramembrane cavitation. *J. Neural Eng.*
- Leventhal, D.K., Cohen, M., and Durand, D.M. (2006). Chronic histological effects of the flat interface nerve electrode. *J. Neural Eng.* 3, 102–113.
- Lillemeier, B.F., Pfeiffer, J.R., Surviladze, Z., Wilson, B.S., and Davis, M.M. (2006). Plasma membrane-associated proteins are clustered into islands attached to the cytoskeleton. *Proc. Natl. Acad. Sci. U. S. A.* 103, 18992–18997.
- Lubba, C.H., Le Guen, Y., Jarvis, S., Jones, N.S., Cork, S.C., Eftekhari, A., and Schultz, S.R. (2019). PyPNS: Multiscale Simulation of a Peripheral Nerve in Python. *Neuroinformatics* 17, 63–81.
- Mazzoni, A., Garcia-Perez, E., Zoccolan, D., Graziosi, S., and Torre, V. (2005). Quantitative Characterization and Classification of Leech Behavior. *J. Neurophysiol.* 93, 580–593.
- McDougal, R.A., Morse, T.M., Carnevale, T., Marengo, L., Wang, R., Migliore, M., Miller, P.L., Shepherd, G.M., and Hines, M.L. (2017). Twenty years of ModelDB and beyond: building essential modeling tools for the future of neuroscience. *J. Comput. Neurosci.* 42, 1–10.
- McIntyre, C.C., Richardson, A.G., and Grill, W.M. (2002). Modeling the excitability of mammalian nerve fibers: influence of afterpotentials on the recovery cycle. *J. Neurophysiol.* 87, 995–1006.
- McNeal, D.R. (1976). Analysis of a model for excitation of myelinated nerve. *IEEE Trans. Biomed. Eng.* 23, 329–337.
- Mehić, E., Xu, J.M., Caler, C.J., Coulson, N.K., Moritz, C.T., and Mourad, P.D. (2014). Increased anatomical specificity of neuromodulation via modulated focused ultrasound. *PloS One* 9, e86939.
- Mendez, V., Iberite, F., Shokur, S., and Micera, S. (2020). Current Solutions and Future Trends of Robotic Prosthetic Hands. *Annu. Rev. Control Robot. Auton. Syst.*
- Menz, M.D., Ye, P., Firouzi, K., Nikoozadeh, A., Pauly, K.B., Khuri-Yakub, P., and Baccus, S.A. (2019). Radiation force as a physical mechanism for ultrasonic neurostimulation of the ex vivo retina. *J. Neurosci.* 2394–18.
- Micera, S., and Navarro, X. (2009). Bidirectional interfaces with the peripheral nervous system. *Int. Rev. Neurobiol.* 86, 23–38.
- Mihran, R.T., Barnes, F.S., and Wachtel, H. (1990). Temporally-specific modification of myelinated axon excitability in vitro following a single ultrasound pulse. *Ultrasound Med. Biol.* 16, 297–309.

- Min, B.-K., Bystritsky, A., Jung, K.-I., Fischer, K., Zhang, Y., Maeng, L.-S., Park, S.I., Chung, Y.-A., Jolesz, F.A., and Yoo, S.-S. (2011). Focused ultrasound-mediated suppression of chemically-induced acute epileptic EEG activity. *BMC Neurosci.* 12, 23.
- Mohammadjavadi, M., Ye, P.P., Xia, A., Brown, J., Popelka, G., and Pauly, K.B. (2018). Elimination of peripheral auditory pathway activation does not affect motor responses from ultrasound neuromodulation. *BioRxiv* 428342.
- Mohr, P.J., Taylor, B.N., and Newell, D.B. (2008). CODATA recommended values of the fundamental physical constants: 2006. *Rev. Mod. Phys.* 80, 633–730.
- Mueller, J., Legon, W., Opitz, A., Sato, T.F., and Tyler, W.J. (2014). Transcranial focused ultrasound modulates intrinsic and evoked EEG dynamics. *Brain Stimulat.* 7, 900–908.
- Muller, K.J. (1981). *Neurobiology of the leech* (New York: Cold Spring Harbor Pr.).
- Muratore, R., LaManna, J., Szulman, E., Kalisz, M.S.A., Lamprecht, M., Simon, M.S.M., Yu, M.S.Z., Xu, N., Morrison, B., and Ebbini, E.S. (2009). Bioeffective Ultrasound at Very Low Doses: Reversible Manipulation of Neuronal Cell Morphology and Function in Vitro.
- Muratore, R., LaManna, J.K., Lamprecht, M.R., and Morrison III, B. (2012). Hippocampal culture stimulus with 4-megahertz ultrasound. pp. 254–258.
- Neufeld, E., Szczerba, D., Chavannes, N., and Kuster, N. (2013). A novel medical image data-based multi-physics simulation platform for computational life sciences. *Interface Focus* 3, 20120058.
- Obrienjr, W. (2007). Ultrasound–biophysics mechanisms☆. *Prog. Biophys. Mol. Biol.* 93, 212–255.
- Orio, P., and Soudry, D. (2012). Simple, Fast and Accurate Implementation of the Diffusion Approximation Algorithm for Stochastic Ion Channels with Multiple States. *PLoS ONE* 7, e36670.
- Otsuka, T., Abe, T., Tsukagawa, T., and Song, W.-J. (2004). Conductance-Based Model of the Voltage-Dependent Generation of a Plateau Potential in Subthalamic Neurons. *J. Neurophysiol.* 92, 255–264.
- Petrini, F.M., Valle, G., Bumbasirevic, M., Barberi, F., Bortolotti, D., Cvancara, P., Hiairassary, A., Mijovic, P., Sverrisson, A.Ö., Pedrocchi, A., et al. (2019). Enhancing functional abilities and cognitive integration of the lower limb prosthesis. *Sci. Transl. Med.* 11, eaav8939.
- Petrov, A.G. (2002). Flexoelectricity of model and living membranes. *Biochim. Biophys. Acta* 1561, 1–25.
- Petzold, L. (1983). Automatic Selection of Methods for Solving Stiff and Nonstiff Systems of Ordinary Differential-Equations. *Siam J. Sci. Stat. Comput.* 4, 136–148.
- Phillips, R., Ursell, T., Wiggins, P., and Sens, P. (2009). Emerging roles for lipids in shaping membrane-protein function. *Nature* 459, 379–385.
- Plaksin, M., Shoham, S., and Kimmel, E. (2014). Intramembrane Cavitation as a Predictive Bio-Piezoelectric Mechanism for Ultrasonic Brain Stimulation. *Phys. Rev. X* 4.

- Plaksin, M., Kimmel, E., and Shoham, S. (2016). Cell-Type-Selective Effects of Intramembrane Cavitation as a Unifying Theoretical Framework for Ultrasonic Neuromodulation. *ENeuro* 3.
- Plesset, M.S. (1949). The Dynamics of Cavitation Bubbles. *J. Appl. Mech.* 16, 277–282.
- Pospischil, M., Toledo-Rodriguez, M., Monier, C., Piwkowska, Z., Bal, T., Frégnac, Y., Markram, H., and Destexhe, A. (2008). Minimal Hodgkin-Huxley type models for different classes of cortical and thalamic neurons. *Biol. Cybern.* 99, 427–441.
- Pralle, A. (1998). Physical Properties of the Plasma Membrane Studied by Local Probe Techniques.
- Prieto, M.L., Ömer, O., Khuri-Yakub, B.T., and Maduke, M.C. (2013). Dynamic response of model lipid membranes to ultrasonic radiation force. *PloS One* 8, e77115.
- Prieto, M.L., Firouzi, K., Khuri-Yakub, B.T., and Maduke, M. (2017). Activation Of Piezo1 But Not Nav1.2 Channels By Ultrasound at 43 MHz.
- Qiu, Z., Kala, S., Guo, J., Xian, Q., Zhu, J., Zhu, T., Hou, X., Wong, K.F., Yang, M., Wang, H., et al. (2020). Targeted Neurostimulation in Mouse Brains with Non-invasive Ultrasound. *Cell Rep.* 32, 108033.
- Rabut, C., Yoo, S., Hurt, R.C., Jin, Z., Li, H., Guo, H., Ling, B., and Shapiro, M.G. (2020). Ultrasound Technologies for Imaging and Modulating Neural Activity. *Neuron* 108, 93–110.
- Ranck, J.B., and Bement, S.L. (1965). THE SPECIFIC IMPEDANCE OF THE DORSAL COLUMNS OF CAT: AN INISOTROPIC MEDIUM. *Exp. Neurol.* 11, 451–463.
- Raspopovic, S., Capogrosso, M., Petrini, F.M., Bonizzato, M., Rigosa, J., Pino, G.D., Carpaneto, J., Controzzi, M., Boretius, T., Fernandez, E., et al. (2014). Restoring Natural Sensory Feedback in Real-Time Bidirectional Hand Prostheses. *Sci. Transl. Med.* 6, 222ra19–222ra19.
- Rattay, F. (1986). Analysis of models for external stimulation of axons. *IEEE Trans. Biomed. Eng.* 33, 974–977.
- Rawicz, W., Olbrich, K.C., McIntosh, T., Needham, D., and Evans, E. (2000). Effect of chain length and unsaturation on elasticity of lipid bilayers. *Biophys. J.* 79, 328–339.
- Reilly, J.P. (2011). *Electrostimulation: theory, applications, and computational model* (Boston: Artech House).
- Reilly, J.P., Freeman, V.T., and Larkin, W.D. (1985). Sensory effects of transient electrical stimulation--evaluation with a neuroelectric model. *IEEE Trans. Biomed. Eng.* 32, 1001–1011.
- Reismann, H., and Pawlik, P.S. (1991). *Elasticity, Theory and Applications* (Krieger Publishing Company).
- Rinaldi, P.C., Jones, J.P., Reines, F., and Price, L.R. (1991). Modification by focused ultrasound pulses of electrically evoked responses from an in vitro hippocampal preparation. *Brain Res.* 558, 36–42.
- Sander, R. (2015). Compilation of Henry's law constants (version 4.0) for water as solvent. *Atmos Chem Phys* 15, 4399–4981.

- Sanguinetti, J.L., Hameroff, S., Smith, E.E., Sato, T., Daft, C.M.W., Tyler, W.J., and Allen, J.J.B. (2020). Transcranial Focused Ultrasound to the Right Prefrontal Cortex Improves Mood and Alters Functional Connectivity in Humans. *Front. Hum. Neurosci.* *14*.
- Sato, T., Shapiro, M.G., and Tsao, D.Y. (2018). Ultrasonic Neuromodulation Causes Widespread Cortical Activation via an Indirect Auditory Mechanism. *Neuron* *98*, 1031–1041.e5.
- Schlaepfer, T.E., and Bewernick, B.H. (2013). Deep brain stimulation for major depression. In *Handbook of Clinical Neurology*, (Elsevier), pp. 235–243.
- Sens, P., and Safran, S.A. (1998). Pore formation and area exchange in tense membranes. *Europhys. Lett. EPL* *43*, 95–100.
- Seo, D., Carmena, J.M., Rabaey, J.M., Alon, E., and Maharbiz, M.M. (2013). Neural Dust: An Ultrasonic, Low Power Solution for Chronic Brain-Machine Interfaces. *ArXiv13072196 Phys. Q-Bio*.
- Sharif Razavian, R., Ghannadi, B., Mehrabi, N., Charlet, M., and McPhee, J. (2018). Feedback Control of Functional Electrical Stimulation for 2-D Arm Reaching Movements. *IEEE Trans. Neural Syst. Rehabil. Eng.* *26*, 2033–2043.
- Sharpe, A.N., and Jackson, A. (2014). Upper-limb muscle responses to epidural, subdural and intraspinal stimulation of the cervical spinal cord. *J. Neural Eng.* *11*, 016005.
- Stagg, C.J., and Nitsche, M.A. (2011). Physiological Basis of Transcranial Direct Current Stimulation. *The Neuroscientist* *17*, 37–53.
- Stewart, R.R., Nicholls, J.G., and Adams, W.B. (1989). Na⁺, K⁺ and Ca²⁺ currents in identified leech neurones in culture. *J. Exp. Biol.* *141*, 1–20.
- Sukharev, S., and Corey, D.P. (2004). Mechanosensitive channels: multiplicity of families and gating paradigms. *Sci. STKE Signal Transduct. Knowl. Environ.* *2004*, re4.
- Sun, R., Hu, W., and Duan, Z. (2001). Prediction of Nitrogen Solubility in Pure Water and Aqueous NaCl Solutions up to High Temperature, Pressure, and Ionic Strength. *J. Solut. Chem.* *30*, 561–573.
- Sundt, D., Gamper, N., and Jaffe, D.B. (2015). Spike propagation through the dorsal root ganglia in an unmyelinated sensory neuron: a modeling study. *J. Neurophysiol.* *114*, 3140–3153.
- Takagi, S.F., Higashino, S., Shibuya, T., and Osawa, N. (1960). The actions of ultrasound on the myelinated nerve, the spinal cord and the brain. *Jpn. J. Physiol.* *10*, 183–193.
- Tanter, M., and Fink, M. (2014). Ultrafast imaging in biomedical ultrasound. *IEEE Trans. Ultrason. Ferroelectr. Freq. Control* *61*, 102–119.
- Tarnaud, T., Joseph, W., Martens, L., and Tanghe, E. (2018a). Computational Modeling of Ultrasonic Subthalamic Nucleus Stimulation. *IEEE Trans. Biomed. Eng.*
- Tarnaud, T., Joseph, W., Martens, L., and Tanghe, E. (2018b). Dependence of excitability indices on membrane channel dynamics, myelin impedance, electrode location and stimulus waveforms in myelinated and unmyelinated fibre models. *Med. Biol. Eng. Comput.* *56*, 1595–1613.

- Tarnaud, T., Joseph, W., Schoeters, R., Martens, L., and Tanghe, E. (2020). SECONIC: Towards multi-compartmental models for ultrasonic brain stimulation by intramembrane cavitation. *J. Neural Eng.*
- Titlow, J., Majeed, Z.R., Nicholls, J.G., and Cooper, R.L. (2013). Intracellular Recording, Sensory Field Mapping, and Culturing Identified Neurons in the Leech, *Hirudo medicinalis*. *J. Vis. Exp. JoVE*.
- Tomlinson, T., and Miller, L.E. (2016). Toward a Proprioceptive Neural Interface that Mimics Natural Cortical Activity. In *Progress in Motor Control*, J. Laczko, and M.L. Latash, eds. (Cham: Springer International Publishing), pp. 367–388.
- Treeby, B.E., and Cox, B.T. (2010). k-Wave: MATLAB toolbox for the simulation and reconstruction of photoacoustic wave fields. *J. Biomed. Opt.* *15*, 021314.
- Tsirulnikov, E.M., Vartanyan, I.A., Gersuni, G.V., Rosenblyum, A.S., Pudov, V.I., and Gavrilov, L.R. (1988). Use of amplitude-modulated focused ultrasound for diagnosis of hearing disorders. *Ultrasound Med. Biol.* *14*, 277–285.
- Tsui, P.-H., Wang, S.-H., and Huang, C.-C. (2005). In vitro effects of ultrasound with different energies on the conduction properties of neural tissue. *Ultrasonics* *43*, 560–565.
- Tufail, Y., Matyushov, A., Baldwin, N., Tauchmann, M.L., Georges, J., Yoshihiro, A., Tillery, S.I.H., and Tyler, W.J. (2010). Transcranial pulsed ultrasound stimulates intact brain circuits. *Neuron* *66*, 681–694.
- Tufail, Y., Yoshihiro, A., Pati, S., Li, M.M., and Tyler, W.J. (2011). Ultrasonic neuromodulation by brain stimulation with transcranial ultrasound. *Nat. Protoc.* *6*, 1453–1470.
- Tyler, W.J. (2011). Noninvasive neuromodulation with ultrasound? A continuum mechanics hypothesis. *Neurosci. Rev. J. Bringing Neurobiol. Neurol. Psychiatry* *17*, 25–36.
- Tyler, W.J., Tufail, Y., Finsterwald, M., Tauchmann, M.L., Olson, E.J., and Majestic, C. (2008). Remote Excitation of Neuronal Circuits Using Low-Intensity, Low-Frequency Ultrasound. *PLOS ONE* *3*, e3511.
- Valle, G., Mazzoni, A., Iberite, F., D’Anna, E., Strauss, I., Granata, G., Controzzi, M., Clemente, F., Rognini, G., Cipriani, C., et al. (2018). Biomimetic Intraneural Sensory Feedback Enhances Sensation Naturalness, Tactile Sensitivity, and Manual Dexterity in a Bidirectional Prosthesis. *Neuron* *100*, 37–45.e7.
- Velling, V.A., and Shklyaruk, S.P. (1988). Modulation of the functional state of the brain with the aid of focused ultrasonic action. *Neurosci. Behav. Physiol.* *18*, 369–375.
- Verhagen, L., Gallea, C., Folloni, D., Constans, C., Jensen, D.E., Ahnine, H., Roumazeilles, L., Santin, M., Ahmed, B., Lehericy, S., et al. (2019). Offline impact of transcranial focused ultrasound on cortical activation in primates. *ELife* *8*.
- Vierling-Claassen, D., Cardin, J.A., Moore, C.I., and Jones, S.R. (2010). Computational modeling of distinct neocortical oscillations driven by cell-type selective optogenetic drive: separable resonant circuits controlled by low-threshold spiking and fast-spiking interneurons. *Front. Hum. Neurosci.* *4*, 198.

- Wagner, F.B., Mignardot, J.-B., Le Goff-Mignardot, C.G., Demesmaeker, R., Komi, S., Capogrosso, M., Rowald, A., Seáñez, I., Caban, M., Pirondini, E., et al. (2018). Targeted neuro-technology restores walking in humans with spinal cord injury. *Nature* 563, 65–71.
- Warman, E.N., Grill, W.M., and Durand, D. (1992). Modeling the effects of electric fields on nerve fibers: Determination of excitation thresholds. *IEEE Trans. Biomed. Eng.* 39, 1244–1254.
- Wattiez, N., Constans, C., Deffieux, T., Daye, P.M., Tanter, M., Aubry, J.-F., and Pouget, P. (2017). Transcranial ultrasonic stimulation modulates single-neuron discharge in macaques performing an antisaccade task. *Brain Stimul. Basic Transl. Clin. Res. Neuromodulation* 0.
- Wise, D.L., and Houghton, G. (1966). The diffusion coefficients of ten slightly soluble gases in water at 10–60°C. *Chem. Eng. Sci.* 21, 999–1010.
- Wong, H.Y. (1977). *Handbook of essential formulae and data on heat transfer for engineers* (London ; New York: Longman).
- Wright, C.J., Rothwell, J., and Saffari, N. (2015). Ultrasonic stimulation of peripheral nervous tissue: an investigation into mechanisms. *J. Phys. Conf. Ser.* 581, 012003.
- Wright, C.J., Haqshenas, S.R., Rothwell, J., and Saffari, N. (2017). Unmyelinated Peripheral Nerves Can Be Stimulated in Vitro Using Pulsed Ultrasound. *Ultrasound Med. Biol.* 43, 2269–2283.
- Wurth, S., Capogrosso, M., Raspopovic, S., Gandar, J., Federici, G., Kinany, N., Cutrone, A., Piersigilli, A., Pavlova, N., Guiet, R., et al. (2017). Long-term usability and bio-integration of polyimide-based intra-neural stimulating electrodes. *Biomaterials* 122, 114–129.
- Yanagita, T., Kundu, T., and Placko, D. (2009). Ultrasonic field modeling by distributed point source method for different transducer boundary conditions. *J. Acoust. Soc. Am.* 126, 2331–2339.
- Yang, P.-F., Phipps, M.A., Newton, A.T., Chaplin, V., Gore, J.C., Caskey, C.F., and Chen, L.M. (2018). Neuromodulation of sensory networks in monkey brain by focused ultrasound with MRI guidance and detection. *Sci. Rep.* 8, 7993.
- Yang, P.S., Kim, H., Lee, W., Bohlke, M., Park, S., Maher, T.J., and Yoo, S.-S. (2012). Transcranial focused ultrasound to the thalamus is associated with reduced extracellular GABA levels in rats. *Neuropsychobiology* 65, 153–160.
- Yoo, S., Mittelstein, D.R., Hurt, R.C., Lacroix, J.J., and Shapiro, M.G. (2020). Focused ultrasound excites neurons via mechanosensitive calcium accumulation and ion channel amplification. *BioRxiv* 2020.05.19.101196.
- Yoo, S.-S., Bystritsky, A., Lee, J.-H., Zhang, Y., Fischer, K., Min, B.-K., McDannold, N.J., Pascual-Leone, A., and Jolesz, F.A. (2011). Focused ultrasound modulates region-specific brain activity. *NeuroImage* 56, 1267–1275.
- Younan, Y., Deffieux, T., Larrat, B., Fink, M., Tanter, M., and Aubry, J.-F. (2013). Influence of the pressure field distribution in transcranial ultrasonic neurostimulation. *Med. Phys.* 40, 082902.
- Young, R.R., and Henneman, E. (1961). Functional effects of focused ultrasound on mammalian nerves. *Science* 134, 1521–1522.

Curriculum Vitae

Théo Lemaire

Bioengineer • Neuroengineer • Computational Neuroscientist

🏠 Rue des Maraîchers 46 • 1205 Genève • Switzerland

✉️ theo.lemaire1@gmail.com | ☎️ +41 (0)79 629 39 05

EDUCATION

2016 - 2020	PhD in Neuroengineering, Electrical Engineering Ecole Polytechnique Fédérale de Lausanne (EPFL), Switzerland
2013 - 2015	Master in Bioengineering with Minor in Neuroprosthetics Ecole Polytechnique Fédérale de Lausanne (EPFL), Switzerland GPA: 5.34/6
2009 - 2012	Bachelor in Life Sciences and Technologies Ecole Polytechnique Fédérale de Lausanne (EPFL), Switzerland GPA: 4.92/6
2007 - 2009	Scientific baccalauréat Lycée International de Ferney-Voltaire, France, GPA: 18.71/20

PROFESSIONAL EXPERIENCE

Apr 2016 →	Research assistant (Ph.D. candidate) <i>Translational Neural Engineering Lab, EPFL, Switzerland</i> Developing computational models to understand and optimize Ultra-sound Neuromodulation at sub-cellular, cellular and anatomical scales. Teaching assistant for master courses Fundamentals of neuroengineering Sensorimotor neuroprosthetics Student supervision Four semester projects and one master thesis
Nov - Dec 2015	Mathematics Teacher <i>Institution Jeanne d'Arc, Gex, France</i> Managed 3 classes (ca. 75 students, ranging 10-15 years old).
Apr - Aug 2013	Software Engineer Intern <i>Zenith Technologies, Cork, Ireland</i> Designed a C++ application to extract relevant data from a database and provide team leaders with a comprehensive overview of their project's evolution.
Aug 2012 - Jan 2013	Kinesiology Lab Intern <i>Geneva University Hospitals, Geneva, Switzerland</i> Developed a MATLAB framework to analyze biomechanical data from clinical exams, used by lab members for daily reporting and scientific publications.

EXTRACURRICULAR ACTIVITIES

Jan 2013 → **Ski & Snowboard instructor**
Ecole du Ski Français, Monts Jura, France
 Teaching private and collective lessons to skiers of all levels and ages.
 Managed a group of 15 racers for 4 years.
 State diploma training currently underway.

TECHNICAL SKILLS

PYTHON computing & analysis stack (numpy - scipy - pandas - matplotlib) • machine learning (scikit-learn) • PDE systems & FEM models • multi-threading/processing • neuronal simulations in NEURON • Jupyter notebooks • automation tasks • interaction with APIs
[code repository for my PhD project](#)

C++ object-oriented programming • IO streams • XML-querying • GUIs • multi-threading (Boost) • 3D graphics (OpenGL) • mathematical libraries (FFTW, Eigen)

MATLAB scientific computing • machine learning • GUIs • SQL queries

FRONT-END WEB responsive web pages (*Javascript - HTML - CSS - Bootstrap*) • interactive visualizations (*D3JS - Plotly*) • interactive UI components (*React.js - Dash*)
[interactive website for my PhD project](#)

MS OFFICE Word - Excel - Powerpoint • automation with Python / VBA

but also **GIT • ILLUSTRATOR • LATEX • LABVIEW** and more.

LANGUAGES

FRENCH mother tongue
ENGLISH fluent
GERMAN proficient
ITALIAN intermediate
RUSSIAN notions

PUBLICATIONS

Lemaire, T., Neufeld, E., Kuster, N., and Micera, S., “Understanding ultrasound neuromodulation using a computationally efficient and interpretable model of intramembrane cavitation” published in Journal of Neural Engineering, 16, 046007 (2019). [\[doi\]](#)

Dedola, F., Severino, F.P.U., Meneghetti, N., **Lemaire, T.**, Cafarelli, A., Ricotti, L., Menciassi, A., Cutrone, A., Mazzoni, A., and Micera, S. (2020). Ultrasound Stimulation Induces Prolonged Depolarization and Fast Action Potentials in Leech Neurons. IEEE Open Journal of Engineering in Medicine and Biology 1, 23–32. [\[doi\]](#)

Lemaire, T., Vicari E., Neufeld, E., Kuster, N., and Micera, S., “MorphoSONIC: a morphologically realistic in-tramembrane cavitation model reveals fiber specific recruitment by ultrasound”, under review.

ORAL PRESENTATIONS

A Multiscale Modeling Framework to Understand and Optimize Ultrasound Neuromodulation
 Sim4Life Workshop, Society for Neuroscience annual meeting 2018, San Diego (US)